Quantitative analysis of firn meltwater retention on the Greenland ice sheet

Vandecrux, Baptiste

Publication date:
2019

Document Version
Publisher's PDF, also known as Version of record

PhD Thesis R-408
Institut for Byggeri og Anlæg

Quantitative analysis of firn meltwater retention on the Greenland ice sheet

Baptiste Vandecrux

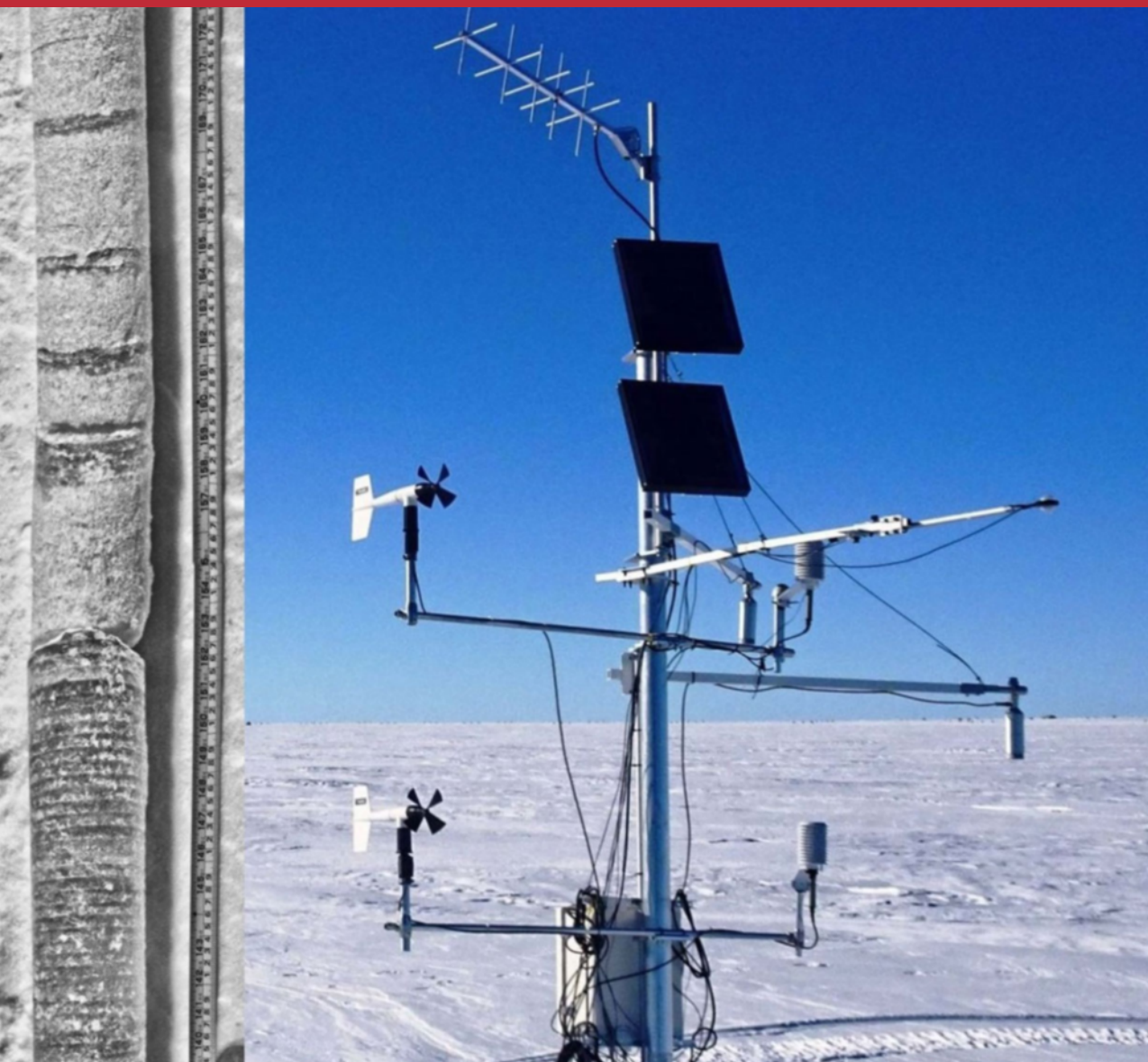

Ph.D. Thesis
Doctor of Philosophy

DTU Civil Engineering
Department of Civil Engineering

Quantitative analysis of firn meltwater retention on the Greenland ice sheet

Baptiste Vandecrux

Kongens Lyngby 2019

DTU

DTU Byg
Department of Civil Engineering
Technical University of Denmark

Brovej Building 118
2800 Kongens Lyngby, Denmark
Phone +45 4525 1700
byg@byg.dtu.dk
www.byg.dtu.dk

Summary

More than half of the Greenland ice sheet mass loss and contribution to sea-level rise originates from surface melt and subsequent runoff. The perennial snow, or firn, that covers ∼80% of the ice sheet, retains a part of this surface melt and hence buffers the ice sheet's sea-level contribution. Yet, the characteristics and processes involved in the meltwater retention in firn are poorly constrained to date.

First, this PhD project contributed to a better understanding of low permeability ice slabs, which are known to prevent meltwater from being retained in the firn. Greenland-wide radar data and repeated firn core observations allowed to map ice slabs in the Greenland firn and climate models were used to estimate their future contribution to global sea-level rise. Firn modelling at an ice slab site using weather station data and a regional climate model also revealed the impact of ice slabs on local runoff and how to represent ice slabs in firn models.

Data from nine weather stations in the Greenland firn area were used to force a firn-evolution model between 1998 and 2015. Increasing summer air temperature and melt was found at all sites. Simulated firn densities, tightly constrained by firn-core observations, increased by about 10% at the two warmest sites and translated into an important (up to 18%) decrease in the volume available for meltwater retention in the firn. Contrastingly, stable firn densities were found at four of the five coldest sites. Simultaneously, summer heat flux from the atmosphere to the firn increased at all sites but one. The subsequent firn warming, however, did not alter the capacity of the firn to refreeze meltwater. Preferential percolation of meltwater was also investigated for its impact on firn heat fluxes and meltwater production.

The analysis of 360 firn-core observations also showed increasing firn density and consequently a $23 \pm 16\%$ decrease of the near-surface firn air content in the warmest and driest 14% of the firn area between 1998 and 2017. The reduced air content indicates a decreasing meltwater retention capacity of the firn. The dataset also describes stable firn densities and air content between 1953 and 2017 in the coldest 74% of the firn area.

Finally, the data collected for this project will provide a baseline for future firn observations and models. The improved understanding of meltwater retention in firn will help to reduce uncertainties when simulating the future mass loss from the Greenland ice sheet and its sea-level contribution.

Resumé på dansk

Oversættelse af R. S. Fausto.

Kvantitative analyser af smeltevands tilbageholdelse i firnen på den Grønlandske Indlandsis

Mere end halvdelen af massetabet fra den Grønlandske Indlandsis og den tilhørende havniveaustigning stammer fra overflade smeltning og afløb. Sne som overlever sommerens smeltning kaldes firn. Firnen dækker ca. 80% af overflade arealet på indlandsisen og virker samtidig som en buffer for smeltevandsafløb, fordi noget af smeltevandet bliver tilbageholdt. Men til dato er egenskaberne og processerne involveret med tilbageholdelse af smeltevand i firn stadig mangelfuldt forstået.

Denne PhD afhandling bidrog til en bedre forståelse af lav permeabilitets islag (isplader), som er kendt for at forhindre smeltevand i at blive tilbageholdt i firnen. Grønlandske radardata og gentagne firn-kerneobservationer blev brug til kortlægning af isplader i den grønlandske firn, hvorefter klimamodeller blev brugt til at estimere deres fremtidige bidrag til den globale stigning i havniveauet. Modellering af firn isplader ved hjælp af vejrstation data og en regional klimamodel afslørede også virkningen af isplader på lokal afstrømning og hvordan man repræsenterer isplader i firn modeller.

Data fra ni vejrstationer fra den Grønlandske firn blev brugt til at forcere en firn model for perioden 1998 og 2015. Der blev fundet en øget sommertemperatur og smeltning ved alle vejrstationer. De simulerede firn densiteter, som var sammenlignet med firn-kerneobservationer, steg med ca. 10% på de to varmeste steder og blev omdannet til et vigtigt (op til 18%) fald i volumet, der var til rådighed for smeltevandsretention i firnen. Modsætningsfuldt blev der fundet stabile firn densiteter ved fire af de fem koldeste steder.

Sommervarmen fra atmosfæren til firnen steg på alle steder pånær et sted. Den efterfølgende opvarmning af firnen ændrede imidlertid ikke kapaciteten af firn til at genfryse smeltevand. Nedsivning af smeltevand blev også undersøgt for dets indvirkning på varme flukse og smeltevandsproduktion. Derudover viste analysen af 360 firn-kerneobservationer også en øget firn densitet og dermed et fald på 24 $\pm$ 16% af luftindholdet i firnen for de varmeste og tørreste 12% af firnområdet mellem 1998 og 2017. Det reducerede luftindhold indikerer en aftagende kapacitet af smeltevandsretention for

firnen. Datasættet beskriver også stabile firn densiteter og luftindhold mellem 1953 og 2017 i det koldeste 74% af firnområdet.

De data der blev indsamlet og brugt i dette projekt vil kunne danne grundlag for fremtidige observationer og modeller. Den forbedrede forståelse af smeltevandsretention i firn vil derved bidrage til at reducere usikkerheden ved simulering af det fremtidige massetab fra Grønland og dets bidrag på havniveauet.

Preface

This PhD thesis was prepared at the department of Civil Engineering at the Technical University of Denmark as part of the completion of the degree of Doctor in Philosophy. The PhD project took place between November 2016 and December 2018 under the supervision of Associate Professor Thomas Ingeman-Nielsen and the co-supervision of Robert S. Fausto, Senior Researcher at the Geological Survey of Denmark and Greenland, department of Glaciology and Climate.

The PhD is part of the *Retain* project, a collaboration between the Technical University of Denmark, the Geological Survey of Denmark and Greenland and the Danish Meteorological Institute, funded by the Danish Council for Independent Research (grant no. 4002-00234) with the support of the Programme for Monitoring of the Greenland Ice Sheet (PROMICE). The PhD project included the participation to two field expeditions to the Greenland ice sheet led by Michael MacFerrin from the University of Colorado.

Kongens Lyngby, April 8, 2019

Baptiste Vandecrux

List of publications

This project fed into the five peer-reviewed articles and two manuscripts presented in this dissertation.

I. MacFerrin, M., H. Machguth, D. Van As, C. Charalampidis, C. M. Stevens, A. Heilig, B. Vandecrux, P. L. Langen, R. Mottram, X. Fettweis, M. R. Van den Broeke, W. Pfeffer, M. Moussavi, and W. Abdalati (2018). "Rapid expansion of Greenland's low-permeability ice slabs". *In review in Nature*

II. Charalampidis, C., D. Van As, P. L. Langen, R. S. Fausto, B. Vandecrux, and J. E. Box (2016a). "Regional climate-model performance in Greenland firn derived from in situ observations". *Geol. Surv. Denmark Greenl. Bull.* 35

III. Fausto, R. S., J. E. Box, B. Vandecrux, D. Van As, K. Steffen, M. J. Macferrin, H. Machguth, W. Colgan, L. S. Koenig, D. McGrath, C. Charalampidis, and R. J. Braithwaite (2018b). "A snow density dataset for improving surface boundary conditions in Greenland ice sheet firn modeling". *Front. Earth Sci.* 6. DOI: 10.3389/feart.2018.00051

IV. Langen, P. L., R. S. Fausto, B. Vandecrux, R. H. Mottram, and J. E. Box (2017). "Liquid Water Flow and Retention on the Greenland Ice Sheet in the Regional Climate Model HIRHAM5: Local and Large-Scale Impacts". *Front. Earth Sci.* 4. DOI: 10.3389/feart.2016.00110

V. Vandecrux, B., R. S. Fausto, P. L. Langen, D. Van As, M. MacFerrin, W. T. Colgan, T. Ingeman-Nielsen, K. Steffen, N. S. Jensen, M. T. Møller, and J. E. Box (2018a). "Drivers of Firn Density on the Greenland Ice Sheet Revealed by Weather Station Observations and Modelling". *J. Geophys. Res. Earth Surf.* DOI: 10.1029/2017JF004597

VI. Vandecrux, B., M. Macferrin, H. Machguth, W. T. Colgan, D. Van As, A. Heilig, L. Koenig, L. N. Montgomery, C. Miège, S. B. Simonsen, and T. Ingeman-nielsen (2019). "Firn data compilation reveals widespread decrease of firn air content in western Greenland". *Cryosph.* 13, pp. 845–859. DOI: 10.5194/tc-13-845-2019

VII. Vandecrux, B., R. S. Fausto, D. Van As, W. T. Colgan, P. L. Langen, K. Sampson, K. Steffen, K. Haubner, T. Ingeman-Nielsen, M. Niwano, and J. E. Box

(2018b). "Heat budget of Greenland firn: observed and simulated changes from 1998-2015". *Manuscript in preparation*

Acknowledgements

I would like to express my gratitude to my supervisors, Thomas Ingeman-Nielsen and Robert S. Fausto for their guidance and support.

I am grateful to Jason E. Box, Peter L. Langen, Horst Machguth and Carl E. Bøggild for making the Retain project possible and for their crucial help at different moments of the PhD. Many thanks to Michael MacFerrin for his invitation to take part in two unforgettable field expeditions.

Thanks to Liam Colgan, Dirk van As, Achim Heilig and Samira Samimi for their help and fruitful scientific discussions.

I would also like to thank Gunvor M. Kirkelund and Lisbeth M. Ottosen for giving me the opportunity to teach in Sisimiut, Martin Kotol for the great moments up there. All my gratitude goes to my colleagues from the Centre for Arctic Technology at DTU and from the department of Glaciology and Climate at GEUS for good collaboration over the past three years.

Finally, many thanks to my family, friends and Elisa for supporting me.

Contents

CHAPTER 1

Introduction

1.0.1 Background

Global sea level has been rising on average by 3 mm every year for the last 25 years and will rise by another 52 to 180 cm by 2100 leading to trillion-dollars-worth flood damages around the world (Nerem et al., 2018; Jevrejeva et al., 2018). This rise stems from atmospheric and oceanic warming as well as mass loss from glaciers and ice caps and undoubtedly results from anthropogenic greenhouse gas emissions (Bindoff et al., 2013; Marzeion et al., 2014; Jevrejeva et al., 2018).

The current mass loss from the Greenland ice sheet is responsible for about 15% of the current sea-level rise and mostly originates from surface melt and subsequent runoff (Van den Broeke et al., 2016). Most of the meltwater discharged into the sea is produced in the low lying ablation area of the ice sheet where melt is sufficient to remove the snow accumulated over the winter and expose the underlying bare ice. In the ice sheet interior, however, some snow survives the summer melt each year and accumulates into an up-to-80-m thick and porous firn layer. The firn has the capacity to retain a part of the surface meltwater and actively buffers the Greenland ice sheet contribution to sea-level rise (Pfeffer et al., 1991; Harper et al., 2012). Yet, as a consequence of atmospheric warming, recent changes in the characteristics of the firn started to alter the meltwater retention capacity of the firn (Van Angelen et al., 2013; Polashenski et al., 2014; De La Peña et al., 2015; Machguth et al., 2016). Thus, understanding and quantifying the meltwater retention processes in firn are necessary to estimate the present and future contribution of the Greenland ice sheet to sea-level rise.

The firn can be seen as a porous matrix of interconnected ice grains that can retain meltwater through two mechanisms (Pfeffer et al., 1991): i) the refreezing of percolating meltwater if the firn is cold enough and ii) the retention of liquid water through capillary suction within the firn pores. Any excess water is available for percolation to greater depth or, if downward movement is impeded for instance by an ice layer, moves down-slope until it is retained or reaches the sea after transiting through an efficient surface drainage system (Smith et al., 2015) or a slower firn aquifer (Forster et al., 2014; Miller et al., 2018). Meltwater refreezing is controlled primarily by the firn temperature, which determines if refreezing can occur. The meltwater retention in pores is on the other hand limited by the firn air content, which represent the maximum volume available for water retention and is closely related to the firn density. Pfeffer et al. (1991) first studied

the dependency between firn temperature, air content and firn meltwater retention in Greenland. But their approach relied on simplifying assumptions such as a constant firn density across the ice sheet as well as melt, snowfall and firn temperature estimates derived from relatively sparse observations.

To overcome this lack of field observations, regional climate models (RCM) have been commonly used in combination with snow and firn models to quantify the melt and refreezing in the Greenland firn (Janssens and Huybrechts, 2000; Reijmer et al., 2012; Van Angelen et al., 2013; Fettweis et al., 2017; Langen et al., 2017; Ligtenberg et al., 2018; Niwano et al., 2018; Noël et al., 2018). Nevertheless, these RCMs still present many issues such as limited spatio-temporal resolution, the misrepresention of key processes driving the ice sheet surface melt (Fausto et al., 2016) or the overestimation of firn density in the lower accumulation area (Steger et al., 2017a; Ligtenberg et al., 2018).

Over the last three decades, the deployment of weather stations (e.g. Steffen et al., 1996; Ahlstrøm et al., 2008) allows to describe the surface energy budget (SEB) and consequently to improve estimations of meltwater production at the weather station locations (e.g. Charalampidis et al., 2015; Niwano et al., 2015; Fausto et al., 2016; Miller et al., 2017). Additionally, repeated field investigations (e.g. Mosley-Thompson et al., 2001; Polashenski et al., 2014; De La Peña et al., 2015; Machguth et al., 2016; Graeter et al., 2018), airborne surveys (Lewis et al., 2017) and data compilation (Montgomery et al., 2018) also allow to describe the current state of the firn in a more precise way than ever before. Yet, thorough assessment of the meltwater retention processes in the Greenland firn using these observational datasets is still missing.

These observations and recent laboratory work also lead to significant improvement in the predictive modelling of snow and firn properties from weather station or RCM data. Current multilayer models account for firn compaction, homogeneous or heterogeneous melt-water percolation, meltwater refreezing and subsequent latent heat release (e.g. Vionnet et al., 2012; Van Pelt et al., 2012; Niwano et al., 2015; Wever et al., 2016; Marchenko et al., 2017). They nevertheless need constant evaluation against observations in natural environment and improvement as these same snow and firn models are used for future projections of ice sheet contribution to sea-level rise.

In addition to the firn refreezing capacity and available air content, a necessary criteria for meltwater retention is that the firn can be accessed by the meltwater generated at the surface. Recently Mikkelsen et al. (2015) and Machguth et al. (2016) brought to light the emergence of thick ice slabs within the near-surface firn in western Greenland. Both studies could establish how these ice slabs impede downward meltwater percolation into the firn and how they contributed to the unprecedented runoff seen from the western Greenland ice sheet in 2012. However the mapping of these ice slabs, the evaluation of firn models performance at these sites and the simulation of their evolution in the coming decades were still unexplored. The discovery of the ice slabs in the firn

of western Greenland also triggered increased attention to firn processes and provided a prime motivation for this PhD project.

In addition to its meltwater retention capacity, the Greenland firn is studied for two other reasons. Firstly, the accurate modelling of the firn characteristics is necessary to derive the ice sheet mass balance from repeated satellite observations of the ice sheet's surface elevation, a.k.a. altimetry (Zwally et al., 1989; Sørensen et al., 2011; Kuipers Munneke et al., 2015a). Indeed satellite observations of ice sheet thinning or thickening can only be interpreted as mass loss or gain after taking into account the evolution of the firn density which depends on the firn's physical, thermal and hydrological characteristics (Zwally and Jun, 2002; Reeh, 2008; Simonsen, 2013). Secondly, understanding how snow and firn compacts into ice, trapping chemical compounds within their ice matrix and air bubbles, is necessary to reconstruct past climate from ice cores (Schwander et al., 1997; Goujon et al., 2003). Although this PhD project focuses on meltwater retention in firn, altimetry and ice core sciences also benefit from the increased understanding of the firn characteristics and processes.

1.0.2 Objectives of the project and structure

The aim of this PhD project is to describe and quantify the key firn characteristics and processes that influence the firn meltwater retention on the Greenland ice sheet in a changing climate.

The objective of this project is to provide better insights on:

1. The existence of low permeability ice slabs in the lower accumulation area of the ice sheet and their effect on runoff (Paper I, II, IV).

2. The magnitude of meltwater production at the surface as well as its percolation through the snow (Paper II, IV, V, VII).

3. The spatio-temporal variability of firn density and firn air content as an indicator of the firn meltwater retention capacity (Paper III, V, VI, VII).

4. The evolution of firn temperature and its control of the firn refreezing capacity (Paper II, IV, VII).

Our work on these four research items is presented according to the following structure. The seven scientific articles on which this dissertation is based are summarized in Chapter 2 and illustrated in Figure 1.1 while their transcriptions are available in Appendix A to G. Chapter 3 presents work in progress on the observation and modelling of heterogeneous percolation in snow. Chapter 4 discusses how the presented studies feed into each other, how they complement each other and give perspective on future work.

Finally Chapter 5 summarizes our findings and how the presented work addressed the research objectives.

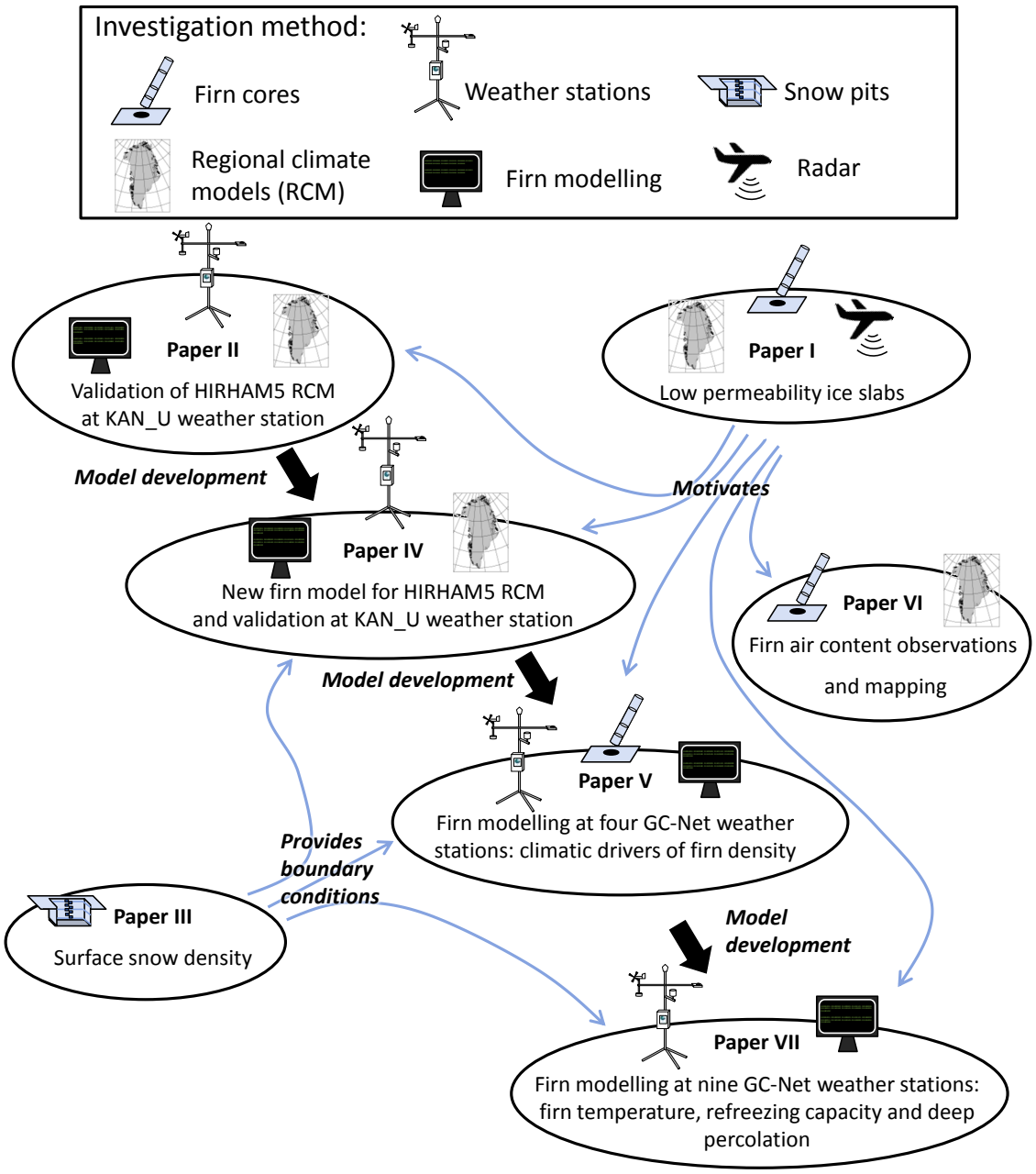

Figure 1.1: Overview of the presented studies and of their interrelations.

CHAPTER 2
Summary of articles

In this chapter, the seven articles on which the present work is based are summarized. The papers are ordered according to their interrelation as shown in Figure 1.1. Paper I to IV are collaboration work providing the foundation to Paper V, VI and VII, which represent the core of the produced work. A short description of the personal contribution to each co-authored publication is made when needed.

2.1 Paper I

MacFerrin, M., H. Machguth, D. Van As, C. Charalampidis, C. M. Stevens, A. Heilig, B. Vandecrux, P. L. Langen, R. Mottram, X. Fettweis, M. R. Van den Broeke, W. Pfeffer, M. Moussavi, and W. Abdalati (2018). "Rapid expansion of Greenland's low-permeability ice slabs". *In review in Nature*

Mikkelsen et al. (2015) and Machguth et al. (2016) first described the existence of low permeability ice slabs, ice layers thicker than 1 m formed through the repeated refreezing of meltwater, on the lower percolation area in the western part of the Greenland ice sheet. They showed how the ice slabs prevented the meltwater from accessing the underlying firn where it could have been retained. Consequently, Mikkelsen et al. (2015) and Machguth et al. (2016) found that ice slab played a key role in the extreme runoff from the western ice sheet in the summer of 2012.

In Paper I, we map these ice slabs across the ice sheet using extensive airborne radar measurements from the Operation IceBridge, as well as surface ground penetrating radar and firn core observations. We find that they currently cover 3.9-4.6% of the Greenland ice sheet surface or 4.9 - 5.8% of its firn area.

Using a set of RCMs, we calculate the annual excess melt, that is defined as the difference between annual liquid water input (melt + rain) and the retention capacity of the snow accumulated each year. Excess melt is traditionally used as a criteria to describe the exhaustion of meltwater retention capacity and the subsequent runoff (Pfeffer et al., 1991). We find that ice slabs are characterized as the areas that have received, according to RCMs, about 266-573 mm w.e. yr^{-1} of excess melt for more than 10 years before the ice slabs mapping in 2013. RCMs forced by general circulation models provide projections

of future excess melt that can then be used to estimate the expected evolution of ice slabs under two emission scenarios: RCP4.5 and RCP 8.5 (Meinshausen et al., 2011). We find that the extent of the ice slabs is expected to increase between 40 to 800% by 2100 depending on the climate model and emission scenario. Using the simulated excess melt we recalculate the amount of meltwater that cannot be stored below these newly formed ice slabs and runs off the ice sheet. The ice-slab related runoff represents an additional 10-73 mm to the end-of-century sea level in the RCP4.5 scenario. This additional runoff is multiplied by 2.4 in the high emission RCP8.5 scenario.

My contribution to this publication was to participate to the 2016 and 2017 field expeditions during which 21 new firn cores were drilled. At KAN_U and BAB_U ice slabs were found to grow few centimetres thicker since these sites were first investigated in 2013 and 2015. The accretion of new ice at the top of the ice slab indicates the transition of these sites to superimposed ice areas. I also curated the firn density and stratigraphy dataset collected since 2013 by several field teams, and compared recent cores to older measurements. I additionally discussed the methods and commented the manuscript. This study sets the scene for the rest of the PhD project and provide the prime motivation for understanding better firn processes that could lead to the creation of ice slabs.

2.2 Paper II

Charalampidis, C., D. Van As, P. L. Langen, R. S. Fausto, B. Vandecrux, and J. E. Box (2016a). "Regional climate-model performance in Greenland firn derived from in situ observations". *Geol. Surv. Denmark Greenl. Bull.* 35

The aim of this paper was to use the subsurface temperature dataset produced by Charalampidis et al. (2015) at KAN_U, an ice slab site on the Greenland ice sheet, over the 2009-2013 period to validate the simulated melt, refreezing and firn temperature in the HIRHAM5 output presented in Langen et al. (2015). The presence of water within the firn is inferred from firn temperature measurements.

We find that HIRHAM5 overestimates the meltwater percolation depth and consequently overestimates firn temperatures by 6 to 7 °C on average at 6 m below the surface. HIRHAM5's estimate of melt was similar to the one calculated from the weather station data by Charalampidis et al. (2015), however, the treatment of meltwater percolation, refreezing and runoff inaccurately distributed the percolating meltwater in the subsurface. In the simulation from Charalampidis et al. (2015) the ice layers were present between 2 and 5 m below the surface since the model initiation in 2009. These ice layers subsequently grew in the simulation and impeded meltwater percolation in 2012, triggering runoff in concordance with firn-core estimation of ice-slab-induced runoff presented by Machguth et al. (2016). In HIRHAM5, the growth of such ice layers was not simulated,

both because of the subsurface model formulation but also because the simulation was initiated in 1980 and the inaccurate simulation of past climate may have lead to the absence of ice slab at KAN_U in 2012 in the simulation.

Our findings show the importance of simulating the emergence of ice layers within the firn before an extreme melt event occurs. The misrepresentation of these ice layers significantly impact runoff calculations and therefore local mass balance and contribution to sea-level rise.

This study took place early in the PhD project and introduced me to the challenges of firn modelling in an ice slab context. Discussing the manuscript, the interpretation of the results, and questioning the various modules within the firn models allowed me to identify potential improvements to the firn models as described in Section 4.

2.3 Paper III

Fausto, R. S., J. E. Box, B. Vandecrux, D. Van As, K. Steffen, M. J. Macferrin, H. Machguth, W. Colgan, L. S. Koenig, D. McGrath, C. Charalampidis, and R. J. Braithwaite (2018b). "A snow density dataset for improving surface boundary conditions in Greenland ice sheet firn modeling". *Front. Earth Sci.* 6. DOI: 10.3389/feart.2018.00051

Contemporary snow and firn models typically have centimetre vertical resolution close to the surface and/or are often run on sub-daily time steps. These temporal and vertical resolutions imply that models have to add centimetres of newly fallen snow at a specified density to their subsurface scheme (e.g. Van Pelt et al., 2012; Charalampidis et al., 2015; Fettweis et al., 2017). Inaccurate surface snow density potentially lead to inadequate simulation of firn density or to the tuning of firn densification routines to compensate the inaccurate boundary conditions. To constrain this surface snow density, we collect 200 previously published snow density measurements for which we calculate the average density of the top 10, 20 and 50 cm of the snowpack.

We find that the parametrization of the surface snow density from Reeh et al. (2005) and Kuipers Munneke et al. (2015a), currently used in RCMs, overestimate by 17-19% the top 10 cm snow density, mainly because they were designed to give the average density of the top meter of snow. Additionally, our collection of density measurements do not show a strong correlation with annual air temperature nor with elevation indicating the predominance of other environmental factors such as wind speed and time since last snowfall. Our best recommendation for the regional climate modelling community is to use the average density of 315 $\pm$ 44 kg m^{-3} found in our dataset, as new snow density. Our estimate indicates that many existing snow and firn models currently use inaccurate surface snow density. Finally, the PhD project directly benefited from this

study's output as this surface snow density was used in all the following papers, either as boundary to our firn model (Paper IV, V, VII) or to gap fill observed firn density profiles (Paper VI).

My input to this study was a significant share of the statistical analysis, the interpretation of the results as well as the discussion of the manuscript.

2.4 Paper IV

Langen, P. L., R. S. Fausto, B. Vandecrux, R. H. Mottram, and J. E. Box (2017). "Liquid Water Flow and Retention on the Greenland Ice Sheet in the Regional Climate Model HIRHAM5: Local and Large-Scale Impacts". *Front. Earth Sci.* 4. DOI: 10.3389/feart.2016.00110

Regional climate models such as HIRHAM5 are powerful tools to estimate surface and subsurface conditions over the entire ice sheet. However, it is important to validate their performance before they are applied onto climate projections. In this study we use the HIRHAM5 RCM (Lucas-Picher et al., 2012), forced at its boundary by the ERA-Interim reanalysi, to drive an updated firn model. We test the performance of the model using either the remotely sensed surface albedo or the internally calculated albedo. We also test a new implementation of meltwater percolation using Darcy's law, replacing the bucket scheme previously used. Finally, we investigate the sensitivity of the model to the prescription of the firn irreducible water content (the amount of water that can be retained in the firn by capillary forces) and to the way ice content of a subsurface model layer is allowed to decrease the hydraulic conductivity of that layer.

The study presents a thorough assessment of the model performance by comparing its output to: 68 ice-core derived accumulation records, 1041 in-situ SMB observations, 25 years of remotely sensed melt area, 6 years of firn temperature measurements at KAN_U, a PROMICE station located in the western part of the lower accumulation area of the ice sheet, and 75 firn density profiles observations.

We found that the model versions using MODIS-derived albedo gave the best match against SMB measurements, but the model using the internally calculated albedo compared better with the firn temperature measurements from the KAN_U site, in particular by reproducing the creation of a thick ice layer, or ice slabs, preventing deep percolation of meltwater at that site. The large difference in calculated meltwater input at the surface depending on which albedo was used made it impossible to determine the best settings for the new meltwater percolation scheme. But the sensitivity experiment nevertheless allowed us to identify the impact of these parameters.

My contribution to this publication was the validation of HIRHAM5's firn density

against 75 firn density observations, of the simulated firn temperature at KAN_U site, the writing of the related sections of the article as well as the discussion of all the other parts of the study.

2.5 Paper V

Vandecrux, B., R. S. Fausto, P. L. Langen, D. Van As, M. MacFerrin, W. T. Colgan, T. Ingeman-Nielsen, K. Steffen, N. S. Jensen, M. T. Møller, and J. E. Box (2018a). "Drivers of Firn Density on the Greenland Ice Sheet Revealed by Weather Station Observations and Modelling". *J. Geophys. Res. Earth Surf.* DOI: 10.1029/2017JF004597

In the firn area, representing about 80% of the ice sheet, few weather stations currently monitor the surface conditions and can be used to estimate surface melt, precipitation and firn evolution. These stations are left unattended for most of the year in the harshest climate and their data need intensive filtering and processing because of measurement errors and sensor failure.

In this study, we process and gap-filled data spanning from 1998 to 2015 from four GC-Net weather stations located in the firn area: Crawford Point, Dye-2, NASA-SE and Summit. We calculate the surface energy budget and determined hourly energy and mass fluxes at the surface. We then update the discretization and the parametrizations used for calculating the firn's hydraulic conductivity, heat capacity and thermal conductivity in the multi-layer firn model from Paper III and use this firn model to simulate the evolution of the firn properties. The simulated firn densities are compared with 22 firn core observations which ensure the accuracy of the model. We finally relate the hourly evolution of the near-surface firn density to its climatic and internal drivers such as surface melt, sublimation, snowfall and firn densification calculated from the station data.

We find that increasing summer air temperatures and turbulent heat fluxes lead to a slight increase of summer melt at all sites. The firn model could accurately simulate firn density within measurement uncertainty. Finally we detail how both annual and daily variability of internal firn densification, surface melt, sublimation and snowfall impacts changes in modelled firn density. We find that sublimation and firn densification do not drive changes in the firn density at any of our sites during the 1998-2015 period. It is common knowledge that intense melt densifies the firn layer and that important snowfall would decrease the firn's density. However we show that for our study sites and periods, years with below-average snowfall can lead to an important increase of firn density just as above-average snowfall can counterbalance the densification due to intense melt and refreezing. The sensitivity of the firn density budget to the variability of both melt and snowfall calls for caution when relating observed firn density change to changes in melt

only.

2.6 Paper VI

Vandecrux, B., M. Macferrin, H. Machguth, W. T. Colgan, D. Van As, A. Heilig, L. Koenig, L. N. Montgomery, C. Miège, S. B. Simonsen, and T. Ingeman-nielsen (2019). "Firn data compilation reveals widespread decrease of firn air content in western Greenland". *Cryosph.* 13, pp. 845–859. DOI: 10.5194/tc-13-845-2019

The firn air content (FAC) represents the maximum volume available for meltwater retention in the firn and is therefore crucial for runoff calculation. The FAC is also needed to convert satellite observations of ice sheet volume change into mass change. In this study, we collect 360 firn density measurements from which we calculate the FAC of the top 10 m of firn (FAC_{10}) and estimate the FAC_{tot}, the air content of the entire firn column. We divide the firn area into three regions where FAC_{10} show consistent behaviours relative to the long-term average air temperature ($\overline{T_a}$) and precipitation ($\bar{\dot{c}}$).

The dry snow area (DSA), defined as the region where $\overline{T_a}$ < -19 °C, represents 74% of the firn area. In these cold regions, melt seldom occurs and the main process controlling the near-surface firn density, and therefore the FAC is dry firn compaction. The percolation area contains relatively warm areas ($\overline{T_a}$ > -19 °C) and is located at lower latitude and/or elevation than the DSA. In these regions, more melt occurs each summer part of which is refrozen into the firn, thus decreasing its air content. Here, we identify two subregions: First, the low accumulation ($\bar{\dot{c}} < 600$ mm w.eq. yr^{-1}) percolation area, or LAPA, covers 14% of the firn area. In the LAPA, moving down-slope to warmer climates leads to an increase of melt and refreezing and as a result a decrease of FAC until exhaustion at the firn line. The high accumulation ($\bar{\dot{c}} \geq 600$ mm w.eq. yr^{-1}) percolation area, or HAPA, covers the 12% of the firn area. Here, the FAC_{10} decreases only slightly with increasing $\overline{T_a}$ and can be up to five times higher than in the LAPA for similar $\overline{T_a}$. The higher FAC_{10} in the HAPA indicates, in line with firn aquifer studies, that wintertime meltwater refreezing is hindered by the high accumulation rates. Meltwater either percolates deeper than 10 m and refreezes there, or runs off down-slope. Unfortunately, few measurements are available from that region.

Using functions of $\overline{T_a}$ and $\bar{\dot{c}}$ fitted to FAC_{10} observations, we map the spatial distribution of FAC_{10} and when possible its temporal evolution. These maps are also converted to map FAC_{tot} as well as the firn retention capacity over the top 10 m and whole depth of the firn layer. Finally, we compare both our dataset and our FAC maps to outputs from three RCMs (MAR3.9, HIRHAM5 and RACMO2.3p2).

From our dataset, FAC maps and comparison to RCMs we find:

- That the FAC and consequently the retention capacity of the firn remained stable, within measurement uncertainty, in the DSA over the 1953-2017 period.

- That the FAC decreased in the LAPA leading to a loss of 170 ± 120 km^3 of air from the top 10 m of firn and a loss of up to 700 ±490 km^3 of air from the whole firn layer between the 1998-2008 and 2010-2017 period.

- This loss translate into a decreasing retention capacity of the firn ranging between 150 ± 100 Gt to 540 ± 440 Gt.

- The regional climate models present mixed performance when compared to our FAC dataset and maps. More importantly they all underestimate FAC_{10} in the LAPA and all calculate a decreasing FAC in the DSA in contradiction with our finding.

2.7 Paper VII

Vandecrux, B., R. S. Fausto, D. Van As, W. T. Colgan, P. L. Langen, K. Sampson, K. Steffen, K. Haubner, T. Ingeman-Nielsen, M. Niwano, and J. E. Box (2018b). "Heat budget of Greenland firn: observed and simulated changes from 1998-2015". *Manuscript in preparation*

In this paper, we process the data from five GC-Net weather stations: Saddle, South Dome, NASA-E, NASA-U and TUNU-N. We use them along with the four GC-Net stations (Crawford Point, Dye-2, NASA-SE and Summit) used for Paper V. At these nine stations, we calculate the surface energy budget and run the firn model presented in Paper V. We additionally process the firn temperature observations available at these 9 stations: we remove erroneous measurements and estimate at each hourly time step the location of each temperature sensor below the surface accounting for snowfall, melt, sublimation and internal compaction.

Observations show increasing summer air temperatures at all sites except NASA-SE, with rates ranging from 0.2 to 1.26 °C per decade. In combination with other contributors to the surface energy budget, increased heat transfer from the air to the snow surface, calculated at all sites but two, lead to increasing calculated annual melt at all stations. We find record-low surface albedo at all stations but two during the extreme melt summer of 2012, illustrating the so-called melt-albedo feedback. We also calculate a slightly decreasing snow accumulation at six sites out of nine.

Firn temperature observations reveal a negative bias in the simulated firn temperature. Implementing the meltwater deep percolation parametrization from Marchenko et al. (2017) improves the performance of the model at sites where melt is frequent in

summer. We also find that accounting for deep percolation can reduce the heat transferred from the subsurface to the surface by up to 30% at Dye-2. Indeed, when the meltwater percolates deeper into the firn and refreeze there, the latent heat released remains at depth and does not have the time to be conducted toward the surface. We also find that the standard percolation scheme produces up to 8% more melt than when using the deep percolation parametrization. We attribute this difference to the fact that meltwater concentrated near the surface takes a longer time to refreeze compared to water homogeneously distributed at depth by the deep percolation scheme. As a consequence, the near-surface firn more frequently remains at higher temperature over the night which makes it easier to warm up and melt the following days.

Nevertheless, the tuning parameters of the deep percolation scheme are poorly constrained and were previously determined from a firn site in Svalbard. On the other hand, both model versions have a cold bias at stations where melt is seldom. This indicates that our calculation may underestimate the heat transfer from the atmosphere to the surface and potentially melt. Further quantification of meltwater deep percolation in the Greenland firn and improved estimation of surface energy budget will be needed to better understand the feedbacks between meltwater percolation, heat transfer between the firn and the atmosphere and surface melt.

CHAPTER 3

Work in progress

3.1 Introduction

Meltwater movement in snow has been described as a combination of a gravity driven, spatially homogeneous percolation and preferential flow along channels, also called fingers or pipes (Figure 3.1), routing water ahead of the homogeneous percolation front (e.g. Marsh and Woo, 1984b). In seasonal snowpacks, preferential flow affects for example the timing and magnitude of meltwater delivery to the ground and the growth of ice layers (e.g. Colbeck, 1979; Wever et al., 2016).

Preferential flow has been widely observed on the Greenland ice sheet, either in firn temperature observations (e.g. Pfeffer and Humphrey, 1996; Pfeffer and Humphrey, 1998; Humphrey et al., 2012; Charalampidis et al., 2016b) or through the observation of ice columns left after the preferential flow channel refroze (e.g. Benson, 1962; Jezek et al., 1994). Several studies indicated the potential utility of accounting preferential flow within snow and firn models on the Greenland ice sheet. For instance, Rignot et al. (1993) find that the presence of ice columns within the snow affect radar observations of the Greenland ice sheet. Marchenko et al. (2017) and our Paper VII both find that parameterizing deep preferential percolation within firn models reduces the deviation between simulated and observed firn temperature. Steger et al. (2017a) also hypothesize that accounting for preferential flow may be important for the recharge of south-east Greenland firn aquifers. Yet, preferential flow has not been widely adopted in firn models used on the Greenland ice sheet. A first reason for this is the computational cost of complex models currently used for seasonal snowpacks (Wever et al., 2016; Hirashima et al., 2014) . Another reason is the lack of distributed in-situ observations of preferential flow in the firn of the Greenland ice sheet to calibrate simpler models such as the ones from Colbeck (1979), Marsh and Woo (1984a) or Marchenko et al. (2017). As a result it is still unsure whether preferential water flow can have a significant impact on the mass balance and sea-level contribution of the Greenland ice sheet.

In this chapter, Section 3.2 first presents a simple and portable procedure to detect refreezing of preferentially percolated meltwater. The protocol is then used to constrain key characteristics of preferential flow in firn using existing firn temperature measurements on the Greenland ice sheet. Secondly, Section 3.3 details how these information can be used in a probabilistic parametrization of preferential flow in firn which is tested

at a site in the lower accumulation area of western Greenland.

3.2 Detecting preferential meltwater flow from firn temperature observations

3.2.1 Conceptual model and previous work

Laboratory experiments and in-situ observations showed that preferential flow originates either at the surface from heterogeneous surface melt or below the surface above flow-impeding horizons such as fine-to-coarse-snow boundary or ice lenses (e.g. Conway and Benedict, 1994; Waldner et al., 2004; Katsushima et al., 2013). Once formed, the grain growth within the flow channel is enhanced by the presence of water (Brun, 1989) and subsequently augment the pipe's hydraulic conductivity and flow rates (Calonne et al., 2011). Additionally, the cylindrical shape of the flow path limits the surface of contact with the surrounding subfreezing snow and the snow's low thermal conductivity reduces lateral heat losses from the pipe.

As soon as the preferential flow channel reaches a flow-impeding stratigraphic boundary, ice layer or coarser snow, the water will start to move according to the pressure head gradient: away from the water source and along the stratigraphic boundary slope (Conway and Benedict, 1994). On the ice sheet, slopes are typically small and the water will spread in different directions as a sheet-like flow over the flow-impeding horizon (Figure 3.1). This new flow type presents a greater area for thermal exchange between the water and the subfreezing snow or with the thermally conductive ice layer. This enhanced thermal exchange triggers meltwater refreezing and the release of latent heat.

According to this conceptual description, preferential flow can be assumed to have the following three characteristics:

- They originate from meltwater present at the surface or at flow-impeding horizons.
- They percolate through subfreezing snow in a pipe-shaped channel without important heat dispersion.
- If they reach a flow-impeding boundary, then percolation transitions to a sheet-like flow, intensifying refreezing and latent heat release, until a path down is found or the meltwater supply dries out.

As a consequence, important meltwater release and refreezing from preferential flowpath disruption show as a localized and transient firn warming at depth and can be tracked using firn temperature measurements.

Marchenko et al. (2017) used an array of 9 thermistor strings to derive preferential flow characteristics at a firn site in Svalbard. Unfortunately, no similar experimental set up is available on the Greenland ice sheet. Other studies in Greenland compared single-string firn temperature observations to simulations of heat conduction through firn in order to quantify meltwater refreezing and preferential flow (Pfeffer and Humphrey, 1996; Cox et al., 2014; Humphrey et al., 2012; Charalampidis et al., 2016b). Yet, this procedure is sensitive to firn temperature measurement accuracy and noise, to the accurate forcing and initialization of the heat conduction model and to the assumption that meltwater refreezing is homogeneous horizontally.

To overcome these challenges, we here present a method to detect meltwater refreezing after preferential percolation from single-string firn temperature observations and without the help of heat conduction models. The detection protocol is tested on the firn temperature observations from Humphrey et al. (2012) (Table 3.1) and used to gather information about the frequency and depth of preferential flow at these sites.

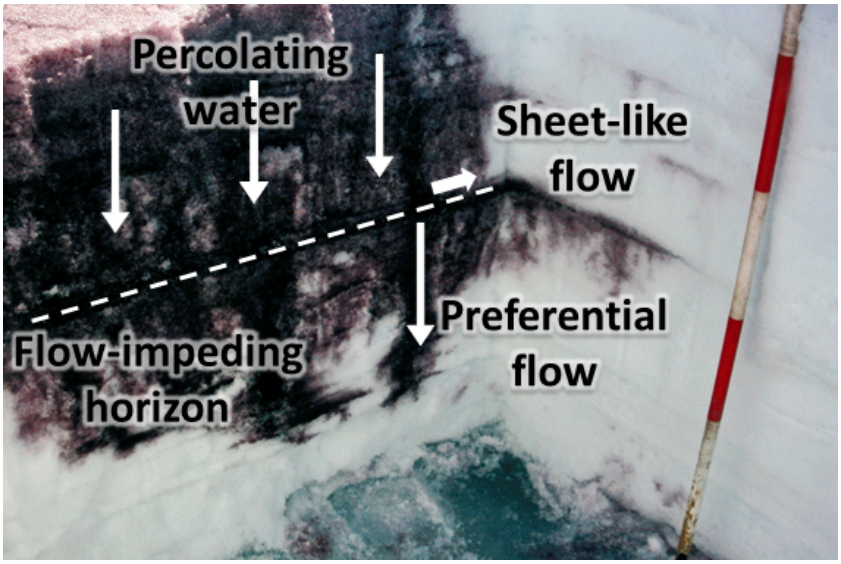

Figure 3.1: Dye tracer experiment with illustration of preferential and sheet-like water flow around a flow-impeding horizon. Photo courtesy of Robert S. Fausto.

3.2.2 Detection method

Given firn temperature observations from several sensors buried in the firn, the first step is to identify all the transient firn warming, i.e. periods during which the firn temperature at a certain level is seen to increase, reach a maximum and decrease. So for each temperature sensor k providing a temperature time series $T_k(t)$, we look for the time steps t_m that are either: i) giving a higher temperature than at the preceding and following time steps ($T_k(t_m) > T_k(t_m - 1)$ and $T_k(t_m) > T_k(t_m + 1)$); or ii) located at the leading edge of a flat maximum ($T_k(t_m) > T_k(t_m - 1)$ and $T_k(t_m) = T_k(t_m + 1) =$

... = $T_k(t_m + N - 1)$ and $T_k(t_m) > T_k(t_m + N)$). To remove small temperature peaks resulting from sensor noise, we filter out peaks with prominence lower than 1 °C. One consequence of this necessary filtering is that it is not possible to detect transient firn warming of magnitude equal to or smaller than the noise present in the temperature record.

In a second step, the temperature maxima $T_k(t_m)$ that also represent a temperature maximum compared to measurements from the upper and lower neighbouring sensors ($T_k(t_m) > T_{k-1}(t_m)$ and $T_k(t_m) > T_{k+1}(t_m)$) are selected. Thereby, only the punctual release of latent heat at depth (defined as the thermal signature of preferential flow in Section 3.2.1) are isolated while warming events from heat conduction or from homogeneous meltwater percolation are filtered out.

3.2.3 Results and discussion

The observed firn temperatures and results from the detection algorithm are presented in Figure 3.2. The stations did not monitor the evolution of surface height, so all the reported depth in the following are related to the surface level when the temperature strings were installed. At each of the 12 locations up to 35 local maxima in firn temperature were detected. They were located between few centimetres below the surface to 8-9 m deep.

We find that 50% of the detected events occur between the initial surface level and 3 m depth and that 90% of the events are located within 6 m from the initial surface level. As discussed in the next section, most of the detected peaks below 6 m are the results of noise.

These results agree well with the preferential flow characteristics derived by Humphrey et al. (2012) at the same sites. But the presented protocol has the advantage of not requir-

Station name	Time coverage	Latitude (°N)	Longitude (°E)	Elevation (m a.s.l.)
CP	May 2007 – May 2008	69.88	47.01	1997
T3	May 2007 – May 2008	69.78	47.67	1819
T2	May 2007 – May 2009	69.76	47.88	1750
T1old & new	May 2008 – May 2009	69.74	48.06	1710
H163	May 2008 – May 2009	69.73	48.19	1680
H1	May 2008 – May 2009	69.74	48.24	1660
H165	May 2008 – May 2009	69.72	48.27	1644
H2	May 2008 – May 2009	69.71	48.34	1555
H3	May 2008 – May 2009	69.69	48.50	1540
H4	May 2008 – May 2009	69.66	48.69	1401

Table 3.1: Firn temperature data used for the tracking of preferential water flow.

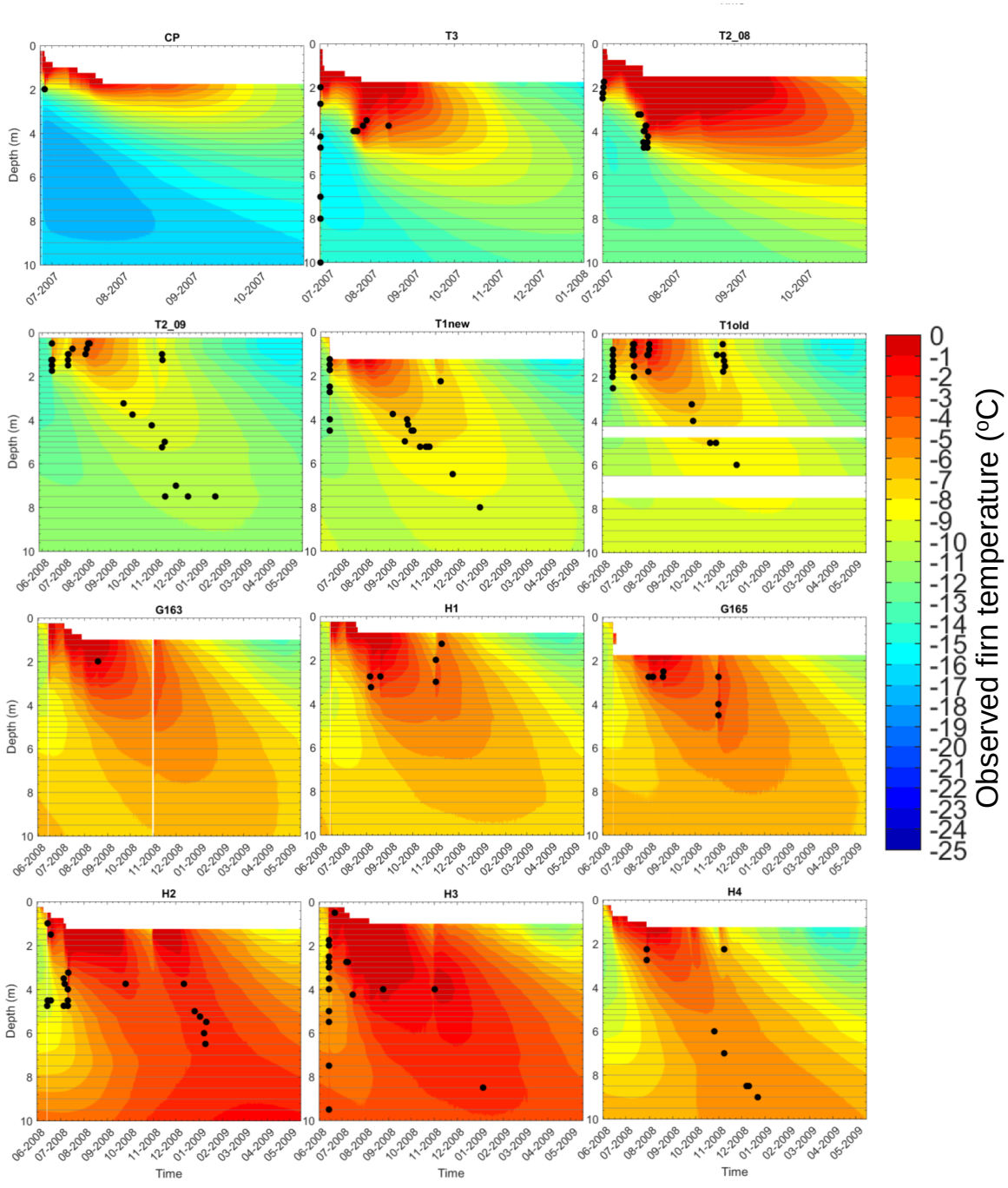

Figure 3.2: Automatic detection of thermal maximum in thermistor string data. The black dots indicate the detection of a local maximum in firn temperature.

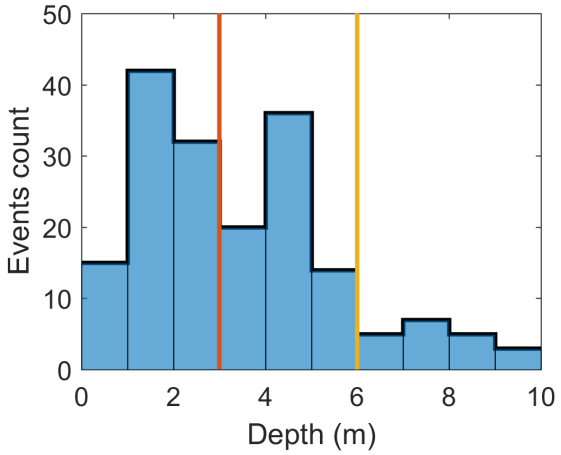

Figure 3.3: Distribution of the detected firn temperature peaks. The blue line indicates the 50% percentile and the orange line indicates the 90% percentile.

ing any heat conduction model, forcing data or other assumptions needed by Humphrey et al. (2012). As a consequence, this detection method is immediately portable to study preferential flow at other sites where firn temperature is available (see next Section). The price for this increased portability is that the presented technique cannot estimate the amount of water that was refrozen in the detected events.

3.2.3.1 Portability to other datasets

The portability of our detection protocol is tested on the firn temperature data from the PROMICE KAN_U station processed in Paper II and IV. Three heat release events were detected ahead of the wetting front over the 2012 melt season (Figure 3.4). In agreement with the analysis of Charalampidis et al. (2016a), percolation events are also detect below the thick ice layer located 2 m below the surface (Figure 3.4).

3.2.3.2 Effect of noise

Our technique can be very sensitive to the noise present in the temperature records. At the string T2_09 (Figure 3.2), piping was detected down to 8 m deep throughout the autumn and winter which we consider unlikely to be linked with meltwater transport. It also appeared problematic when applied on GC-Net thermistor data which are more noisy than the ones from Humphrey et al. (2012). Finer tuning of the threshold value on temperature peak prominence as well as improved pre-processing of the temperature records could help to remove the unwanted noise.

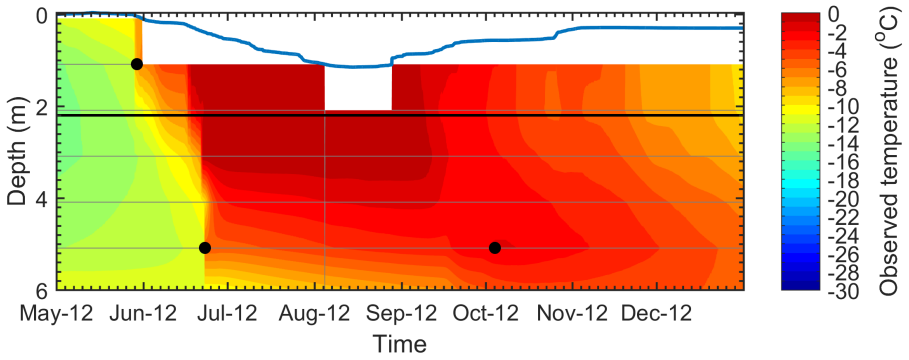

Figure 3.4: Automatic detection of thermal maximum in KAN_U thermistor string data. The black dots indicate the detection of a local maximum in firn temperature. The horizontal black line marks the surface of a 3- to 5-m-thick ice layer.

3.2.3.3 Percolation along the temperature string

Drilling a borehole for the installation of a temperature string disrupts the firn stratigraphy and potentially provides a preferential path for meltwater percolation. This obvious risk is usually discarded by assuming that those backfilled boreholes are a natural barrier to percolation (Pfeffer and Humphrey, 1998; Humphrey et al., 2012). However Charalampidis et al. (2016b) mentioned the occurrence of such events which shows the absence of consensus on this question.

In a recent study of near-surface ice temperature conducted in the western bare-ice area of the Greenland ice sheet, Hills et al. (2018) monitored suspicious short-lived subsurface warming events while they were observing englacial temperature (Figure 3 in Hills et al. (2018)). We find very similar events in the data from Humphrey et al. (2012) as shown in Figure 3.5.

There are potential reasons for subsurface heat release both in ice, such as meltwater refreezing in cracks or crevasses, and in firn, such as migrating pore water. Nevertheless, we interpret these very similar events as percolation of meltwater along the temperature string for the following reasons:

- These warming events are seen by several temperature sensors and thus do not fit with the punctual release of latent heat at the disruption of a preferential flow path when it meets a flow-impeding boundary.
- They are much deeper than all the other detected percolation events.
- They usually occur at the onset of melt and do not reappear later in the season, potentially indicating that the percolating meltwater refroze, sealed the borehole and prevents any further percolation along the temperature string.

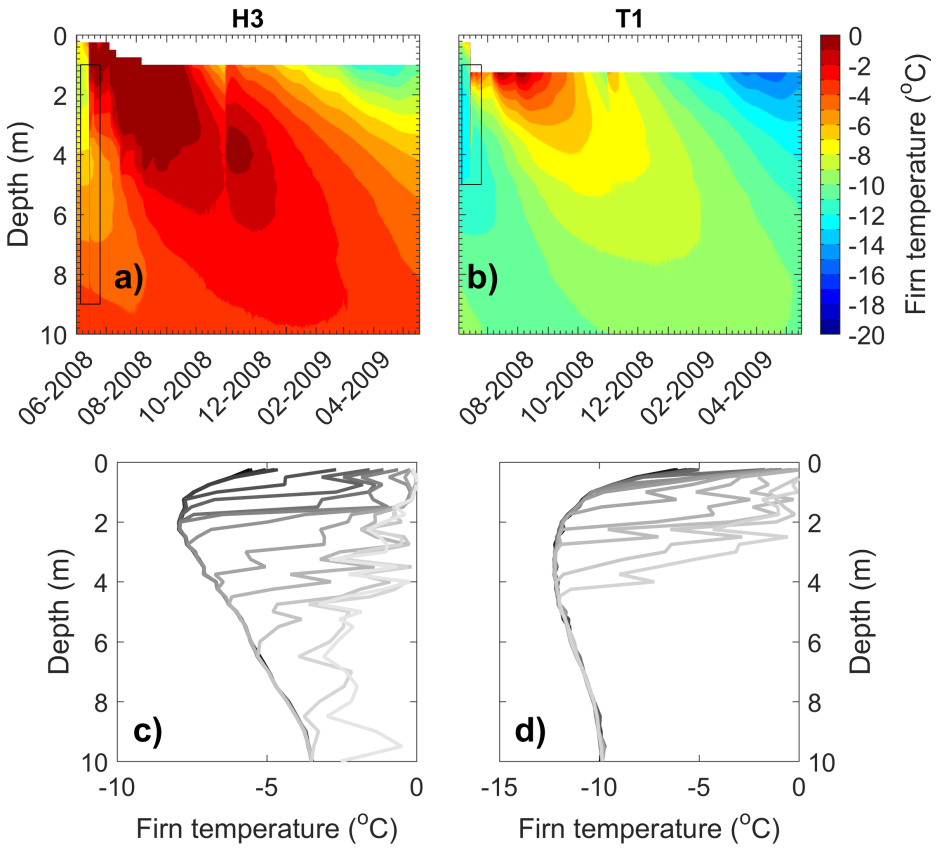

Figure 3.5: Suspicious short-lived warming event in firn interpreted as percolation along the sensor cable at H3 and T1. In panels c and d, firn temperatures are displayed from dark to light gray at 90 min interval..

- The occurrence of such events both in ice and firn indicate that they are more probably linked to their common measuring technique rather than linked to two different processes taking place either in ice or firn which would have the same thermal signature.

We therefore consider that meltwater percolation along the temperature string is common both in ice and firn in contradiction with the arguments from Humphrey et al. (2012). The impact of such events on the overall thermal state of the ice or firn is limited by their typical briefness (Charalampidis et al., 2016b). It consequently does not question the results presented by Humphrey et al. (2012) and Hills et al. (2018). Yet percolation along the temperature string raises questions regarding our preferential flow detection procedure: How many of the detected events operated through the borehole? How many of them take place in the undisturbed snow surrounding the temperature string? We are unable to answer these questions yet. However, future field testing could investigate the backfilling procedure that would prevent along-string percolation. Also innovative wireless sensors such as the ETracer (Bagshaw et al., 2018) would pre-

vent the disruption of stratigraphy or help to evaluate how much temperature string measurements are affected by along-string meltwater percolation.

3.3 Modelling of preferential flow using a probabilistic approach

3.3.1 Background

Until recently, all operational snow models, i.e. models being used in avalanche forecast or glacier and ice sheet mass balance models, describe meltwater percolation as a homogeneous front with various levels of complexity: from bucket schemes (Kuipers Munneke et al., 2015a) to Darcy flow (Langen et al., 2017) and now using Richards' equation (Wever et al., 2014).

Colbeck (1979) and Marsh and Woo (1984a) integrated preferential flow channels, or fingers, into snow models based on a reduced number of parameters derived from observation: the cross-sectional area covered by fingers and the proportion of total water flux flowing into the fingers. The water flux in both homogeneous wetting front and fingers were then calculated according to gravity flow.

Recently, Wever et al. (2016) used the same dual-domain approach to describe the preferential flow: Whenever water from a homogeneous matrix flow ponds on a flow-impeding horizon, a grain-size-dependant fraction of it is moved to a preferential flow domain with higher saturation allowing water to cross the horizon. Water movement in both matrix flow and preferential flow domains was calculated using Richards' equations. Although they simulate more thoroughly the dynamics of preferential flow and use recent laboratory experiments, their model still rely on a number of unconstrained parameters accounting for some of the flow fingers characteristics. Also, their preferential flow routine requires solving Richards' equation which is computationally more demanding than other percolation schemes.

Marchenko et al. (2017) also provided an alternative by modifying a homogeneous meltwater percolation scheme so that the meltwater is not added at the surface but instantaneously distributed to the snow and firn at depth. A prescribed function then determined how much meltwater was assigned to each subsurface level between the surface and maximum depth to which preferential flow was assumed to reach. The shape of this redistribution function and maximum depth of preferential flow was then adjusted to fit the simulated firn temperatures to thermistor string observations. Their approach reduces considerably the number of parameters to be tuned and is very computationally efficient. However they neglect the time needed for water to percolate through the snow, even in preferential flow channels. They also consider a rather homogeneous redistribution of meltwater at depth, as opposed to the punctual release of meltwater from

preferential flow disruption presented in Section 3.2.1. Finally, they used a background flow routine (the so-called bucket scheme) that is known to overestimate percolation depth (Paper I and II).

We can also note that high-resolution 3D model from Hirashima et al. (2014) showed promising results in comparison to preferential flow observed in laboratory. However their set-up remains computationally expensive and is yet to be tested in natural environments.

It appears that improvements are still possible in the modelling of heterogeneous flow. We here present a probabilistic approach for including preferential flow into the firn model developed in Paper II and III.

3.3.2 Methods

We use the same model set up as in Paper V. However, at each time step, before the standard Darcy flow is being applied, the model tests for each layer if there is water in excess of the layer's irreducible water content, i.e. water available for movement. The model then draws from a binomial probability function of probability p_{piping} whether piping occurs. If it does, a fraction f_{piping} is taken from the layer's available water and allocated for preferential flow. The model then searches through the underlying layers until it reaches a layer satisfying a preferential flow disruption criteria. Here we used as criteria any layer density above 800 kg m^{-3} but future development can include as a criteria a certain gradient in grain size, the existence of saturated conditions or a layer with ice fraction exceeding a certain threshold. The water available for preferential flow is then allocated to the layer located above the one that met the preferential flow disruption criteria. If these criteria are not met within a maximum percolation distance d_{max}, the water is distributed homogeneously to all the layers located within d_{max} of the water's starting point.

For illustration and proof of concept, we apply this model to the 2012 melt year at the KAN_U PROMICE station. The value used for each parameter of the heterogeneous meltwater percolation scheme are listed in Table 3.2

p_{piping}	0.2
f_{piping}	0.5
d_{max}	10

Table 3.2: Values of the parameters used in the preferential flow scheme.

3.3.3 Results and discussion

The firn temperature produced by our preferential flow scheme mimics successfully the localised heat release described as the thermal signature of piping in Section 3.2.1

(Figure 3.6a). These heat releases are located at the surface of an ice layer located 2 m below the surface. For comparison, we also present the simulated firn temperature from the firn model elaborated in Paper V, henceforth called standard model (Figure 3.6b), and the version of our model which uses the deep percolation scheme from Marchenko et al. (2017) as developed in Paper VII (Figure 3.6c). As expected, the standard model produces a homogeneous wetting front. The model using Marchenko's scheme homogeneously warms the top 5 m of snow and ice before the wetting front reaches that depth.

Although our procedure manages to mimic the heat release from preferential flow disruption, all the simulated temperature profiles differ significantly from the temperature strings observations (Figure 3.4). Additionally the result presented in the previous section does not allow to constrain the various parameters that our preferential flow scheme requires. Nevertheless future data could potentially describe the probability of a pipe to form and to be disrupted based on the snow characteristics. Finally the horizontal resolution to which we want to apply the snow model may not require the modelling of individual piping events but rather their cumulated effect.

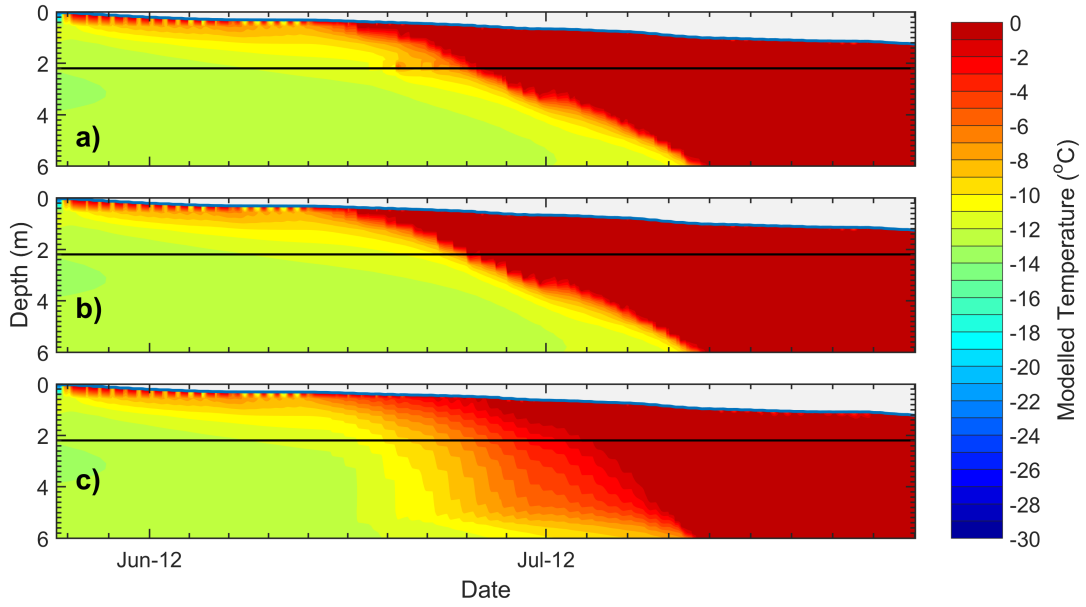

Figure 3.6: Simulated firn temperature using our preferential flow scheme (a), our standard model from Paper V (b) and the model from Paper VII with the deep preferential percolation parametrization from Marchenko et al. (2017) .

CHAPTER 4

Discussion

In this section, we discuss the specific elements that came across the published and unpublished material enclosed in this dissertation. The discussion of each specific study can be found in the respective articles in Appendices A to G.

By presenting the first evidence of low permeability ice slabs in western Greenland and describing how they may enhance runoff at a regional scale, Machguth et al. (2016) triggered increased attention to the firn processes within the scientific community. Paper I further increase the understanding of these ice slabs by mapping their extent and inferring their contribution to future runoff from the ice sheet. Paper I also gave yet another justification to better constrain the meltwater retention capacity of the firn in a changing climate. However, both Machguth et al., 2016 and Paper I could only give either qualitative or model-dependant descriptions of the conditions that may lead to the development of ice slabs. They therefore encouraged both the collection of relevant climate and firn information to better characterize the conditions and firn processes that are responsible for the emergence of ice slabs.

The KAN_U site, located in the accumulation area and where a thick ice slab was found about 2 m below the surface, quickly became an iconic site for the study of firn processes. A PROMICE weather station operates at KAN_U since 2009. Unfortunately, the installation of KAN_U is not long enough before the discovery of the ice slab in 2012 to describe the climatic history leading to the creation of the ice slab. Yet, KAN_U station can help to document the current effect of the ice slab on the local surface energy and mass balance (Charalampidis et al., 2015; Charalampidis et al., 2016b). KAN_U station can also help to evaluate RCMs and snow models and ensure that they simulate adequately these features. In Paper II, we used KAN_U station data to identify key features in the subsurface modules of both HIRHAM5 RCM and Charalampidis et al., 2015 that needed to be improved. The bucket scheme in HIRHAM5, for example, led to too deep meltwater percolation and to too warm subsurface and was consequently changed for a Darcy-flow percolation scheme in Paper IV. The new simulations presented in Paper IV, also evaluated at KAN_U station, compared much better to observations than in Paper II: simulation of the growth of a percolation impeding ice layer in certain model configurations leading to water ponding on top of the ice layer and running off laterally.

Simultaneously, the collection of surface snow density observations presented in

Paper III gives a constrain to a crucial boundary condition in HIRHAM5's firn model (Paper IV) and to all subsequent development of this firn model (Paper IV and VII). Indeed inaccurate surface snow density prescription had already been identified as a potential source of firn density overestimation in firn models by Steger et al. (2017a) and setting surface snow density to 320 kg m^{-3}, close to the estimation Paper III, was found to improve simulated firn densities over previously used parameterizations (Steger et al., 2017b, p. 7). Although the sensitivity of firn models to the choice of surface snow density alone was not explicitly calculated, the surface snow density estimated in Paper III certainly participated to the satisfactory comparison between modelled and observed firn density in Paper IV (root mean squared error inferior to 30 kg m^{-3}, close to the uncertainty of applying density measurements). Additionally, Papers IV and VII quantified the impact of firn density on the meltwater retention capacity of the firn. Consequently, the constrain on surface snow density given in Paper III indirectly participates to more realistic estimations of meltwater retention in firn and ultimately to runoff and sea-level contribution from the firn area.

Nevertheless, in spite of all the efforts made in Paper IV to improve HIRHAM5's subsurface module, it appeared that surface characteristics such as albedo had a much more drastic impact on the model performance. Indeed, in certain regions, annual runoff could change by more 1000 mm depending on the choice of albedo (Paper IV, Figure 11). One surprising finding was that, at the KAN_U site, the HIRHAM5 version using internally calculated albedo was giving a more realistic subsurface temperature than when using remotely-sensed MODIS albedo. Although MODIS albedo carries inaccuracies, it is still expected to be closer to the true albedo than the internally calculated albedo from HIRHAM5. Paper IV showed, for that specific site, that HIRHAM5 could match better observations by using a less realistic albedo. It appeared that, first, improvement of the internally calculated albedo was necessary to match better MODIS-derived albedo, and second, that more observation-derived melt records were needed to assess the performance of the subsurface scheme and of its representation of meltwater retention. Another flaw in HIRHAM5's firn model identified in Paper IV was the discretization strategy that had an undesirable diffusive effect on the firn properties.

As a result, intensive efforts were made to further improve HIRHAM5's firn model as well as to process data from existing weather stations in the firn area. In Paper V, we processed and gap-filled climate records from four GC-Net stations. We updated the subsurface scheme of HIRHAM5 to avoid the above mentioned diffusion issue and forced it with station-derived surface energy and mass fluxes. The simulated firn density tightly matched firn density measurements, indicating that the model updates improved the model performance. It then appeared that the simulation, forced by observed weather at the surface and tightly constrained by firn density observations, could be used to describe the firn history at each of the sites: the increasing near-surface firn density and temperature at lower sites and consequently decreasing meltwater retention capacity. Surprisingly, the higher stations presented a stable modelled and observed firn density. This contradicts results from RCMs (Van Angelen et al., 2013, see Figure S8 showing

pore space decrease above 2000 m a.s.l. between 1995 and 2020) and the common idea that the warming observed in the firn area (McGrath et al., 2013) may accelerate firn densification and and lead to firn density increase (Kuipers Munneke et al., 2015b).

In that context, Paper VI built upon the firn core validation dataset from Paper IV and newly acquired firn observations, and attempted to expand the point-wise conclusions from Paper V to a Greenland-wide estimation of the firn meltwater retention capacity. And as mentioned in Section 2.6, a stable firn density, air content and retention capacity was found in the coldest region of the firn area while the lower regions saw their firn densifying over recent decades and their retention capacity consequently declined by about 23%. This could be expected when considering the long term average accumulation and air temperature at the weather stations used in Paper V and comparing them to the different snow areas that we defined in Paper VI (Figure 4.1).

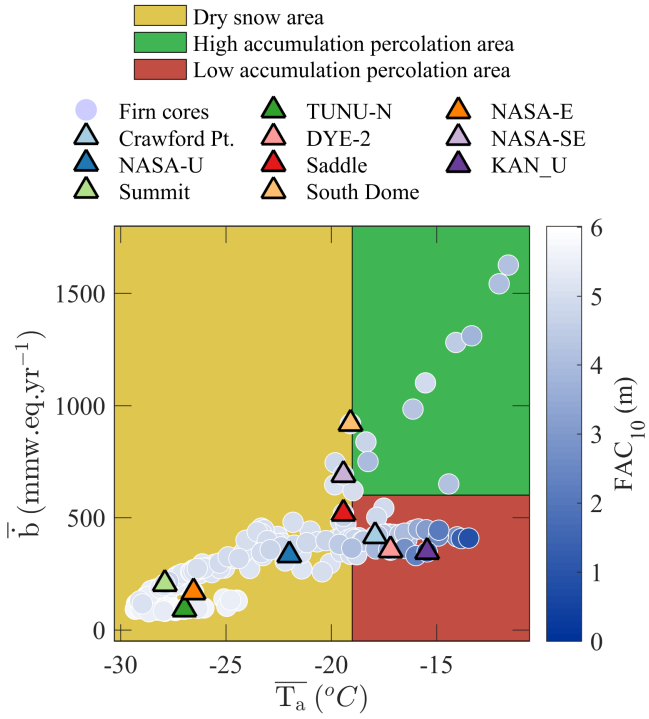

Figure 4.1: Location of the firn observations and weather stations in the long-term average temperature and accumulation space.

We also use these dataset and maps to evaluate three RCMs. They all presented acceptable overall performance, but they can underestimated the firn air content (FAC) by up to 100% in certain sites of the western lower accumulation area of the ice sheet. RCMs also simulate a decrease of FAC in the dry snow area that does not match with observations of stable FAC in the dry snow area. Once again, just like in Paper II and IV, it was shown that RCM are still subject to many biases which may affect their

current estimation of the retention capacity of the firn as well as its future evolution. Beyond the model intercomparison conducted in Paper VI, the FAC dataset as well as the weather-station-derived melt and precipitation records calculated in Paper V, can be used for the evaluation and improvement of future climate and firn model.

Another by product of Paper VI was the 2000-2017 firn extent that we determined from the end-of-summer snow maps of Fausto et al. (2018a). This firn line is compared to the ice slabs map from Paper I (Figure 4.2). In Paper I, ice slabs were detected in airborne radar data. So to produce a gap-free map of ice slab, interpolation between flight lines is conducted in the following way. In a 5x5 km grid covering the ice sheet, every cell where ice slabs were detected in the radar data is categorize as "ice slab". This ice slab area is then grown and shrunk by one cell to fill remaining small gaps.

As expected, the ice slabs in central western Greenland stretch over 50 km-wide band up-glacier of the firn line (Figure 4.2d). More surprisingly, ice slabs are being identified down-glacier of the firn line in north-eastern and north-western Greenland (Figure 4.2b,c). A possible explanation would be that ice slabs in these northern regions were exposed during an extreme melt event and were classified as bare ice at least once between 2000 and 2017 by Fausto et al. (2018a). They would then wrongly fall outside of the firn area delineated in Paper VI although firn existed below the ice slab.

In theory, the FAC map from Paper VI can be compared to the ice slab map (Figure 4.2) to quantify the deep pore space effectively isolated under the ice slab. Unfortunately, the estimation of FAC_{tot} comes with high relative uncertainty in the ice slab areas (see Paper VI Figure 3) and makes such calculation highly uncertain at the moment.

Paper V and VI focused on firn density and its corollary the firn air content, but did not address the thermodynamics of meltwater refreezing in the firn. Paper VII aims at filling that gap by describing the firn temperature and density, quantifying the firn refreezing capacity which is the amount of meltwater that needs to be refrozen to bring the near-surface firn to melting point and finally the firn capacity which is the amount of meltwater that can be possibly be stored in the firn pore volume. The simulated density at the five new sites remained stable or had relatively low density increase (<+5%) over the 1996-2015 period. These relatively stable near-surface firn densities agrees with the stable firn air content, and therefore densities, that was found in firn cores (Paper VI) in regions where average air temperature was below -19°C, known as the dry snow area (Figure 4.1). But more surprising was the ∼8% increase of refreezing capacity at DYE-2 and Crawford Point in spite of a slight (∼0.5 °C) warming of the firn at 10 m depth. This increase in refreezing capacity stems from the 5-10% increase in the top 20 m firn density at DYE-2 and Crawford Point which means that more mass is contained in a given volume of firn and therefore more energy is needed to bring the firn to melting temperature. The slight increase in refreezing capacity yet does not compensate for the 13-15% decrease of retention capacity and firn pore volume at these two sites. This surprising but logical sensitivity of the firn refreezing capacity to an increase of firn

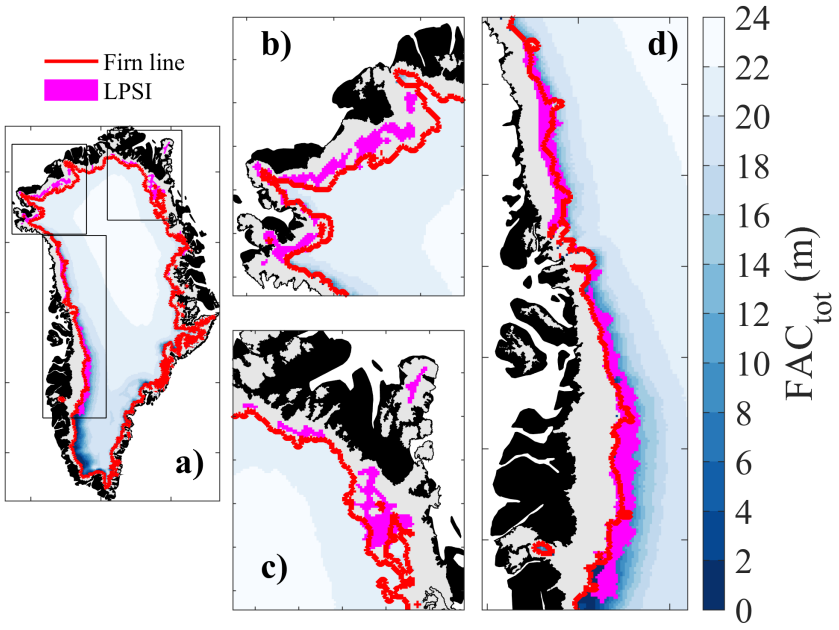

Figure 4.2: Estimated location of the low permeability ice slabs and total firn capacity (FAC_{tot}).

density reminds us of the fine coupling between firn temperature, density, refreezing and retention capacity.

Paper VII also discusses the impact of the choice of meltwater percolation scheme on the calculated melt and energy fluxes. For instance, using the deep percolation parameterization from Marchenko et al. (2017) in combination to the Darcy flow meltwater routing scheme (Paper IV and V) decreases melt by up to 8% and improves the model performance compared to the model with Darcy flow alone. Nevertheless, the deep percolation scheme depends on characteristics (meltwater distribution function and maximum percolation depth) that has not been documented for the Greenlandic firn. An attempt was made to quantify the characteristics of deep percolation in Section 3.2 using firn temperature observations but faced technical issues with meltwater percolation along the sensors' cable. Additionally, the deep percolation parameterization from Marchenko et al. (2017) assumes that i) deep percolation only initiates at the surface, ii) deep percolation occurs at every time step and iii) deep percolation redistributes the meltwater at depth according to a function fixed in time. The first assumption disregards observations of preferential flow initiation within the snow pack when meltwater ponds over a flow-impeding horizon (Figure 3.1). The second assumption can be justified when working at a spatial and temporal resolution for which a preferential flow initiates from the surface at every time step. Yet the spacing and frequency of preferential flow is still insufficiently understood to define these spatial and temporal scales. The third assump-

tion disregards the ability of ice features and abrupt transition between firn of different grain size to stop the deep percolation (Machguth et al., 2016; Katsushima et al., 2013). To circumvent these limitations we developed a probabilistic parameterization of preferential flow in Section 3.3. The approach presented here allows to set the probability of preferential flow initiation, how far it percolates, and in which conditions it stops. The probabilities defining the occurrence and conditions of preferential flow can, in the future, be changed to empirical laws based on the firn characteristics and meltwater input. Nevertheless, insufficient data is available so far to constrain the probability laws applying on preferential flow.

The investigation of various meltwater percolation schemes throughout the present project also indicates the issue that is now facing the firn modelling community. Indeed, after identifying the bucket scheme as insufficiently related to the physical laws dictating water flow in porous media, Darcy's equation was implemented HIRHAM5's firn model (Paper IV). Although it allowed some improvement such as an even better match between simulated and observed firn densities, the new model still cannot reproduce observed ice layers in firn (Paper V) and presents negative bias in firn temperature (Paper VII). As a consequence, we investigate empirical but relatively unconstrained deep percolation schemes (Paper VII and Section 3.3) somehow similar to the simple percolation scheme we moved away from in the first place. New knowledge is gained at each step of this trial and error approach. Yet, the lack of direct and distributed observations still limits the understanding of meltwater movement in snow and firn and consequently the development of numerical models.

Future work

Although technological advances allow always finer and faster climate and snow models, the presented work shows the importance of contemporary and historical in-situ observations to understand the firn characteristics and processes. We revealed that the south-western region of the Greenlandic firn area was almost blank of firn measurements, making it difficult to understand which processes drive the firn conditions there. Additionally, low permeability ice slabs were detected in north-east and north-west Greenland. Yet, no ground measurement is available to ascertain that these areas in north Greenland transitioned to superimposed ice area, as it was seen in central-western Greenland. More firn density observations would allow to fill these knowledge gaps. Finally, tracking vertical but also horizontal meltwater movement through snow and firn is a challenge on both the observation and modelling side. Future laboratory experiments (e.g. Katsushima et al., 2013; Avanzi et al., 2016), novel field measurements (e.g. Heilig et al., 2018; Bagshaw et al., 2018) and/or the compilation of existing observations could help to understand the firn hydrology better.

All automatic weather stations on the Greenland ice sheet are so far divided between the long-term ablation area and the long-term accumulation area, at the exception of

KAN_U. Additional weather stations at or just above the firn line would allow to understand the firn line dynamic in a warming climate.

The firn line is also an important variable for the firn retention capacity (Paper VI). Fausto et al., 2018a provided a first estimate from MODIS satellite observations but did not discuss thoroughly the regional implications of their dataset and the the accuracy of their algorithm. Additionally, other satellites platforms are available and could potentially increase the resolution and temporal span of remotely sensed firn line.

Snow and firn models already started to implement heterogeneous percolation schemes which, in the absence of appropriate data, may be difficult to tune. However, sensitivity analysis could be conducted to investigate the impact of such schemes on the simulated long-term ice sheet mass balance.

Using the extensive climate and firn observations collected for this project, the various snow and firn models currently used can be compared on common ground. The meltwater Retention Model Intercomparison Project, initiated in October 2017 in Copenhagen aims at pursuing this goal and should give results in the months following the submission of the present thesis.

CHAPTER 5

Conclusion

Meltwater retention in firn on the Greenland ice sheet is a combination of various processes which depend on the physical characteristics of firn and on the local climate history.

The first motivation throughout the PhD project was to better understand firn processes leading to the emergence of low permeability ice slabs, known for blocking meltwater from being retained in part of the firn. To understand their impact on current runoff, the ice slabs were mapped over 3.9-4.6% of the ice sheet (Paper I) and studied at a specific site (Paper II). Simulations indicated that their extent may double by 2100, potentially adding 10-73 mm to global sea level compared to a scenario where future melt is allowed to be retained in the firn (Paper I). Subsequently, the percolation scheme of HIRHAM5 was evaluated at an ice slab site (Paper II) and updated to enable the regional climate model (RCM) to simulate the emergence of an impermeable ice layer at that site and to reproduce the runoff observed there over the 2012 melt season (Paper IV). This improvement, in addition to the other evaluations conducted in Paper IV, builds confidence in the capacity of HIRHAM5 to simulate adequately the hindering effect of ice slabs on meltwater retention in firn as well as the impact of ice slabs on the current and future Greenland ice sheet contribution to sea level.

The second objective of the project was to better quantify the meltwater production, which appeared crucial in the simulation of ice slabs in Paper IV. Consequently, the surface energy budget (SEB) was calculated at nine GC-Net weather stations (Paper VI and VII). Surface melt was seen to increase at all sites as a response to trends in summer near-surface air temperatures ranging from 0.22 to 1.26°C (Paper VII). At these sites, all meltwater is retained in the firn and a firn model is used to describe the impact of meltwater percolation (Paper V, VII). For instance, implementation of deep meltwater percolation in the firn model was found, through the routing of water away from the surface, to decrease the calculated surface meltwater production by up to 8% at the warmest site. However, work in progress to quantify the magnitude and frequency of deep meltwater percolation faced technical challenges related to the perturbation of the firn when observing firn water movement.

The third research item was to give spatio-temporal perspective on firn air content which represent the volume available for meltwater retention, and its corollary the firn density. An important prerequisite to the study of firn density is the understanding of

surface snow density that was found to be on average 315 ± 44 kg m^{-3} across the ice sheet in a collection of 200 observations (Paper III). The firn air content (respectively firn density) was found to decrease (resp. increase) by 23% in the warmest and driest regions of the ice sheet, either when comparing firn cores collected in 1998-2008 to cores collected in 2010-2017 (Paper VI) or firn modelling at nine weather stations between 1997 and 2015 (Paper VII). Contrastingly, relatively stable firn air content and consequently meltwater retention capacity was found in the coldest regions of the ice sheet from 1954 to 2017 (Paper V, VI, VII). Understanding the firn retention capacity in the higher stations in Paper V and VII or in the dry snow area in Paper VI helps to understand how these regions may react to future warming and increased melting.

Finally, the study of meltwater movement and retention in firn could not be done without detailing the evolution of firn temperature (Paper II, IV, VII). Firn temperature observations were first used to track meltwater movement in firn and evaluate firn models (Paper II and IV). The impact of surface energy budget and meltwater refreezing on the firn heat budget were subsequently detailed in Paper VII. Interestingly, we find that the refreezing capacity of the top 20 m of firn, i.e. the amount of water that needs to be refrozen to bring the firn to melting point, remained stable even at sites where heat input to the firn had recently increased. Indeed the simultaneous firn densification increased the mass of firn present in the top 20 m which then represents more subfreezing mass that needs to be brought to the melting temperature. Hence the dynamics of firn density and temperature both have to be accounted for when describing the current and future retention of meltwater in the firn.

Far from exhausting the topic, this project highlighted the complexity and the prime importance of meltwater retention in the firn for current and future estimation of the Greenland ice sheet to sea level rise. Further modelling and monitoring efforts are therefore recommended.

Postface

As a final remark, the study of the sea-level contribution of the Greenland ice sheet is driven by the wish of the civil society to estimate the impact of man-made climate change on coastal infrastructures, natural and human systems. The risks of such climate perturbations for our societies and future generations have long been documented in successive scientific reports, of which IPCC (2018) is the latest one. Consequently, the scientific community, from which these warnings arose, should be taking exemplary actions towards the reduction of carbon emissions such as the reduction of air travel, meat consumption, car usage, waste production, as well as putting pressure on decision makers. Then researchers will not only be documenting the problem but also be part of the solution.

Bibliography

Ahlstrøm, A. P., P. Gravesen, S. B. Andersen, D. van As, M. Citterio, R. S. Fausto, S. Nielsen, H. F. Jepsen, S. S. Kristensen, E. L. Christensen, L. Stenseng, R. Forsberg, S. Hanson, D. Petersen, and P. P. Team (2008). "A new programme for monitoring the mass loss of the Greenland ice sheet". *Geol. Surv. Denmark Greenl. Bull.* 15, pp. 61–64.

Avanzi, F., C. De Michele, S. Morin, C. M. Carmagnola, A. Ghezzi, and Y. Lejeune (2016). "Model complexity and data requirements in snow hydrology: seeking a balance in practical applications". *Hydrol. Process.* 30.13, pp. 2106–2118. DOI: 10.1002/hyp.10782. arXiv: AcevesLozano1999.

Bagshaw, E. A., N. B. Karlsson, L. B. Lok, B. Lishman, L. Clare, K. W. Nicholls, S. Burrow, J. L. Wadham, O. Eisen, H. Corr, P. Brennan, and D. Dahl-Jensen (2018). "Prototype wireless sensors for monitoring subsurface processes in snow and firn". *J. Glaciol.* Pp. 1–10. DOI: 10.1017/jog.2018.76.

Benson, C. S. (1962). "Stratigraphic Studies in the Snow and Firn of the Greenland Ice Sheet. Research Report 70. Reprinted August 1996 with revision of Cold Regions Research Laboratory (CRRL)". August, p. 93.

Bindoff, N., P. Stott, K. AchutaRao, M. Allen, N. Gillett, D. Gutzler, K. Hansingo, G. Hegerl, Y. Hu, S. Jain, I. Mokhov, J. Overland, J. Perlwitz, R. Sebbari, and X. Zhang (2013). "Detection and attribution of climate change: From global to regional". *Clim. Chang. 2013 Phys. Sci. Basis Work. Gr. I Contrib. to Fifth Assess. Rep. Intergov. Panel Clim. Chang.* DOI: 10.1017/CBO9781107415324.022. arXiv: arXiv:1011.1669v3.

Brun, E. (1989). "Investigation on wet-snow metamorphism in respect of liquid-water content". *Ann. Glaciol.* 13, pp. 22–26. DOI: 10.1017/S0260305500007576.

Calonne, N., F. Flin, S. Morin, B. Lesaffre, S. R. Du Roscoat, and C. Geindreau (2011). "Numerical and experimental investigations of the effective thermal conductivity of snow". *Geophys. Res. Lett.* 38.23, pp. 1–6. DOI: 10.1029/2011GL049234.

Charalampidis, C., D. Van As, J. E. Box, M. R. Van den Broeke, W. T. Colgan, S. H. Doyle, A. L. Hubbard, M. MacFerrin, H. Machguth, and C. J. P. Smeets (2015). "Changing surface-atmosphere energy exchange and refreezing capacity of the lower accumulation area, West Greenland". *Cryosphere* 9.6, pp. 2163–2181. DOI: 10.5194/tc-9-2163-2015.

Charalampidis, C., D. Van As, P. L. Langen, R. S. Fausto, B. Vandecrux, and J. E. Box (2016a). "Regional climate-model performance in Greenland firn derived from in situ observations". *Geol. Surv. Denmark Greenl. Bull.* 35.

Charalampidis, C., D. Van As, W. T. Colgan, R. S. Fausto, M. Macferrin, and H. Machguth (2016b). "Thermal tracing of retained meltwater in the lower accumulation area of the Southwestern Greenland ice sheet". *Ann. Glaciol.* 57.72, pp. 1–10. DOI: 10.1017/aog.2016.2.

Colbeck, S. C. (1979). "Grain clusters in wet snow". *J. Colloid Interface Sci.* 72.3, pp. 371–384. DOI: 10.1016/0021-9797(79)90340-0.

Conway, H. and R. Benedict (1994). "Infiltration of water into snow". *Water Resour. Res.* DOI: 10.1029/93WR03247.

Cox, C., N. Humphrey, and J. Harper (2014). "Quantifying meltwater refreezing along a transect of sites on the Greenland Icesheet". *Cryosph. Discuss.* 8.5, pp. 5485–5509. DOI: 10.5194/tcd-8-5485-2014.

De La Peña, S., I. M. Howat, P. W. Nienow, M. R. van den Broeke, E. Mosley-Thompson, S. F. Price, D. Mair, B. Noël, and A. J. Sole (2015). "Changes in the firn structure of the western Greenland Ice Sheet caused by recent warming". *Cryosphere* 9.3, pp. 1203–1211. DOI: 10.5194/tc-9-1203-2015.

Fausto, R. S., S. B. Andersen, A. P. Ahlstrøm, D. Van As, J. E. Box, D. Binder, M. Citterio, W. Colgan, K. Haubner, K. Hansen, N. B. Karlsson, K. D. Mankoff, A. Ø. Pedersen, A. Solgaard, and B. Vandecrux (2018a). "The Greenland ice sheet – snowline elevations at the end of the melt seasons from 2000 to 2017". *Geol. Surv. Denmark Greenl. Bull.* 41, pp. 71–74.

Fausto, R. S., J. E. Box, B. Vandecrux, D. Van As, K. Steffen, M. J. Macferrin, H. Machguth, W. Colgan, L. S. Koenig, D. McGrath, C. Charalampidis, and R. J. Braithwaite (2018b). "A snow density dataset for improving surface boundary conditions in Greenland ice sheet firn modeling". *Front. Earth Sci.* 6. DOI: 10.3389/feart.2018.00051.

Fausto, R. S., D. van As, J. E. Box, W. Colgan, P. L. Langen, and R. H. Mottram (2016). "The implication of nonradiative energy fluxes dominating Greenland ice sheet exceptional ablation area surface melt in 2012". *Geophys. Res. Lett.* DOI: 10.1002/2016GL067720.

Fettweis, X., J. E. Box, C. Agosta, C. Amory, C. Kittel, C. Lang, D. Van As, H. Machguth, and H. Gallée (2017). "Reconstructions of the 1900-2015 Greenland ice sheet surface mass balance using the regional climate MAR model". *Cryosphere* 11.2, pp. 1015–1033. DOI: 10.5194/tc-11-1015-2017.

Forster, R. R., J. E. Box, M. R. Van den Broeke, C. Miège, E. W. Burgess, J. H. Van Angelen, J. T. Lenaerts, L. S. Koenig, J. Paden, C. Lewis, S. P. Gogineni, C. Leuschen, and J. R. McConnell (2014). "Extensive liquid meltwater storage in firn within the Greenland ice sheet". *Nat. Geosci.* 7.2, pp. 95–98. DOI: 10.1038/ngeo2043.

Goujon, C., J.-M. Barnola, and C. Ritz (2003). "Modeling the densification of polar firn including heat diffusion: Application to close-off characteristics and gas isotopic fractionation for Antarctica and Greenland sites". *J. Geophys. Res. Atmos.* 108.D24, n/a–n/a. DOI: 10.1029/2002JD003319.

Graeter, K. A., E. C. Osterberg, D. G. Ferris, R. L. Hawley, H. P. Marshall, G. Lewis, T. Meehan, F. McCarthy, T. Overly, and S. D. Birkel (2018). "Ice Core Records of West Greenland Melt and Climate Forcing". *Geophys. Res. Lett.* 45.7, pp. 3164–3172. DOI: 10.1002/2017GL076641.

Harper, J., N. Humphrey, W. T. Pfeffer, J. Brown, and X. Fettweis (2012). "Greenland ice-sheet contribution to sea-level rise buffered by meltwater storage in firn". *Nature* 491.7423, pp. 240–243. DOI: 10.1038/nature11566.

Heilig, A., O. Eisen, M. MacFerrin, M. Tedesco, and X. Fettweis (2018). "Seasonal monitoring of melt and accumulation within the deep percolation zone of the Greenland Ice Sheet and comparison with simulations of regional climate modeling". *Cryosph. Discuss.* 2011.January, pp. 1–26. DOI: 10.5194/tc-2017-277.

Hills, B. H., J. T. Harper, T. W. Meierbachtol, J. V. Johnson, N. F. Humphrey, and P. J. Wright (2018). "Processes influencing near-surface heat transfer in Greenland's ablation zone". *Cryosph. Discuss.* May, pp. 1–22. DOI: 10.5194/tc-12-3215-2018.

Hirashima, H., S. Yamaguchi, and T. Katsushima (2014). "A multi-dimensional water transport model to reproduce preferential flow in the snowpack". *Cold Reg. Sci. Technol.* 108, pp. 80–90. DOI: 10.1016/j.coldregions.2014.09.004.

Humphrey, N. F., J. T. Harper, and W. T. Pfeffer (2012). "Thermal tracking of meltwater retention in Greenland's accumulation area". *J. Geophys. Res. Earth Surf.* 117.1, pp. 1–11. DOI: 10.1029/2011JF002083.

IPCC (2018). *Global warming of 1.5°C. An IPCC Special Report on the impacts of global warming of 1.5°C above pre-industrial levels and related global greenhouse gas emission pathways, in the context of strengthening the global response to the threat of climate change*. Ed. by V. Masson-Delmotte, P. Zhai, H. O. Pörtner, D. Roberts, J. Skea, P. Shukla, A. Pirani, W. Moufouma-Okia, C. Péan, R. Pidcock, S. Connors, J. B. R. Matthews, Y. Chen, X. Zhou, M. I. Gomis, E. Lonnoy, T. Maycock, M. Tignor, and T. Waterfield. World Mete. Geneva, Switzerland.

Janssens, I. and P. Huybrechts (2000). "The treatment of meltwater retention in mass-balance parametrizations of the Greenland ice sheet". *Ann. Glaciol.* Pp. 133–140.

Jevrejeva, S., L. P. Jackson, A. Grinsted, D. Lincke, and B. Marzeion (2018). "Flood damage costs under the sea level rise with warming of 1.5 ∘C and 2 ∘C". *Environ. Res. Lett.* 13.074014.

Jezek, K. C., P. Gogineni, and M. Shanableh (1994). "Radar measurements of melt zones on the Greenland Ice Sheet". *Geophys. Res. Lett.* 21.1, pp. 33–36. DOI: 10.1029/93GL03377.

Katsushima, T., S. Yamaguchi, T. Kumakura, and A. Sato (2013). "Experimental analysis of preferential flow in dry snowpack". *Cold Reg. Sci. Technol.* 85, pp. 206–216. DOI: 10.1016/j.coldregions.2012.09.012.

Kuipers Munneke, P., S. R. Ligtenberg, B. P. Noël, I. M. Howat, J. E. Box, E. Mosley-Thompson, J. R. McConnell, K. Steffen, J. T. Harper, S. B. Das, and M. R. Van Den Broeke (2015a). "Elevation change of the Greenland ice sheet due to surface mass balance and firn processes, 1960-2013". *Cryosph. Discuss.* 9.3, pp. 3541–3580. DOI: 10.5194/tcd-9-3541-2015.

Kuipers Munneke, P., S. R. Ligtenberg, E. A. Suder, and M. R. Van Den Broeke (2015b). "A model study of the response of dry and wet firn to climate change". *Ann. Glaciol.* 56.70, pp. 1–8. DOI: 10.3189/2015AoG70A994.

Langen, P. L., R. S. Fausto, B. Vandecrux, R. H. Mottram, and J. E. Box (2017). "Liquid Water Flow and Retention on the Greenland Ice Sheet in the Regional Climate Model HIRHAM5: Local and Large-Scale Impacts". *Front. Earth Sci.* 4. DOI: 10.3389/feart.2016.00110.

Langen, P. L., R. H. Mottram, J. H. Christensen, F. Boberg, C. B. Rodehacke, M. Stendel, D. Van As, A. P. Ahlstrøm, J. Mortensen, S. Rysgaard, D. Petersen, K. H. Svendsen, G. Adalgeirsdóttir, and J. Cappelen (2015). "Quantifying energy and mass fluxes controlling Godthåbsfjord freshwater input in a 5-km simulation (1991-2012)". *J. Clim.* 28.9, pp. 3694–3713. DOI: 10.1175/JCLI-D-14-00271.1.

Lewis, G., E. Osterberg, R. Hawley, B. Whitmore, H. P. Marshall, and J. Box (2017). "Regional Greenland accumulation variability from Operation IceBridge airborne accumulation radar". *Cryosphere* 11.2, pp. 773–788. DOI: 10.5194/tc-11-773-2017.

Ligtenberg, S. R., P. K. Munneke, B. P. Noël, and M. R. Van Den Broeke (2018). "Brief communication: Improved simulation of the present-day Greenland firn layer (1960-2016)". *Cryosphere* 12.5, pp. 1643–1649. DOI: 10.5194/tc-12-1643-2018.

Lucas-Picher, P., M. Wulff-Nielsen, J. H. Christensen, G. Aoalgeirsdóttir, R. Mottram, and S. B. Simonsen (2012). "Very high resolution regional climate model simulations over Greenland: Identifying added value". *J. Geophys. Res. Atmos.* 117.2, pp. 1–16. DOI: 10.1029/2011JD016267.

MacFerrin, M., H. Machguth, D. Van As, C. Charalampidis, C. M. Stevens, A. Heilig, B. Vandecrux, P. L. Langen, R. Mottram, X. Fettweis, M. R. Van den Broeke, W. Pfeffer, M. Moussavi, and W. Abdalati (2018). "Rapid expansion of Greenland's low-permeability ice slabs". *In review in Nature.*

Machguth, H., M. Macferrin, D. Van As, J. E. Box, C. Charalampidis, W. Colgan, R. S. Fausto, H. A. Meijer, E. Mosley-Thompson, and R. S. Van de Wal (2016). "Greenland meltwater storage in firn limited by near-surface ice formation". *Nat. Clim. Chang.* 6.4, pp. 390–393. DOI: 10.1038/nclimate2899.

Marchenko, S., W. J. J. Van Pelt, B. Claremar, V. Pohjola, R. Pettersson, H. Machguth, and C. Reijmer (2017). "Parameterizing Deep Water Percolation Improves Subsurface Temperature Simulations by a Multilayer Firn Model". *Front. Earth Sci.* 5.March. DOI: 10.3389/feart.2017.00016.

Marsh, P. and M. K. Woo (1984a). "Wetting Front Advance and Freezing of Meltwater within a Snow Cover .2. a Simulation-Model". *Water Resour. Res.* 20.12, pp. 1865–1874.

Marsh, P. and M. .-. Woo (1984b). "Wetting front advance and freezing of meltwater within a snow cover: 1. Observations in the Canadian Arctic". *Water Resour. Res.* 20.12, pp. 1853–1864. DOI: 10.1029/WR020i012p01853.

Marzeion, B., J. G. Cogley, K. Richter, and D. Parkes (2014). "Attribution of Past Glacier Mass Loss to Anthropogenic and Natural Climate Forcing". *Science (80-.).* 345.6199, pp. 919–921. DOI: 10.1093/jhered/esq036.

McGrath, D., W. Colgan, N. Bayou, A. Muto, and K. Steffen (2013). "Recent warming at Summit, Greenland: Global context and implications". *Geophys. Res. Lett.* 40.10, pp. 2091–2096. DOI: 10.1002/grl.50456.

Meinshausen, M., S. J. Smith, K. Calvin, J. S. Daniel, M. L. Kainuma, J. Lamarque, K. Matsumoto, S. A. Montzka, S. C. Raper, K. Riahi, A. Thomson, G. J. Velders, and D. P. van Vuuren (2011). "The RCP greenhouse gas concentrations and their extensions from 1765 to 2300". *Clim. Change*. DOI: 10.1007/s10584-011-0156-z.

Mikkelsen, A. B., A. Hubbard, M. MacFerrin, J. Box, S. Doyle, A. Fitzpatrick, B. Hasholt, and H. Bailey (2015). "Extraordinary runoff from the Greenland Ice Sheet in 2012 amplified by hypsometry and depleted firn-retention". *Cryosph. Discuss.* 9.5, pp. 4625–4660. DOI: 10.5194/tcd-9-4625-2015.

Miller, N. B., M. D. Shupe, C. J. Cox, D. Noone, P. O. G. Persson, and K. Steffen (2017). "Surface energy budget responses to radiative forcing at Summit, Greenland". *Cryosphere* 11.1, pp. 497–516. DOI: 10.5194/tc-11-497-2017.

Miller, O., D. K. Solomon, C. Miège, L. Koenig, R. Forster, N. Schmerr, S. R. Ligtenberg, and L. Montgomery (2018). "Direct Evidence of Meltwater Flow Within a Firn Aquifer in Southeast Greenland". *Geophys. Res. Lett.* 45.1, pp. 207–215. DOI: 10.1002/2017GL075707.

Montgomery, L., L. Koenig, and P. Alexander (2018). "The SUMup dataset : compiled measurements of surface mass balance components over ice sheets and sea ice with analysis over Greenland", pp. 1959–1985.

Mosley-Thompson, E., J. R. McConnell, R. C. Bales, Z. Li, P. N. Lin, K. Steffen, L. G. Thompson, R. Edwards, and D. Bathke (2001). "Local to regional-scale variability of annual net accumulation on the Greenland ice sheet from PARCA cores Regional Climate Assessment opportunity to assess local to regional variability of annual accumulation rates over the Greenland ice sheet . PARCA co". *J. Geophys. Res. Atmos.* 106. DOI: 10.1029/2001JD900067.

Nerem, R. S., B. D. Beckley, J. T. Fasullo, B. D. Hamlington, D. Masters, and G. T. Mitchum (2018). "Climate-change–driven accelerated sea-level rise detected in the altimeter era". *Proc. Natl. Acad. Sci.* DOI: 10.1073/pnas.1717312115.

Niwano, M., T. Aoki, S. Matoba, S. Yamaguchi, T. Tanikawa, K. Kuchiki, and H. Motoyama (2015). "Numerical simulation of extreme snowmelt observed at the SIGMA-A site , northwest Greenland , during summer 2012". 2012, pp. 971–988. DOI: 10.5194/tc-9-971-2015.

Niwano, M., T. Aoki, A. Hashimoto, S. Matoba, S. Yamaguchi, and T. Tanikawa (2018). "NHM – SMAP : spatially and temporally high-resolution nonhydrostatic atmospheric model coupled with detailed snow process model for Greenland Ice Sheet", pp. 635–655.

Noël, B., W. J. Van de Berg, J. M. Van Wessem, E. Van Meijgaard, D. Van As, J. T. M. Lenaerts, S. Lhermitte, P. Kuipers Munneke, C. J. P. P. Smeets, L. H. Van Ulft, R. S. W. Van de Wal, and M. R. Van den Broeke (2018). "Modelling the climate and surface mass balance of polar ice sheets using RACMO2 – Part 1: Greenland (1958–2016)". *Cryosphere* 12, pp. 811–831. DOI: 10.5194/tc-12-1479-2018.

Pfeffer, W. T., M. F. Meier, and T. H. Illangasekare (1991). "Retention of Greenland Runoff by Refreezing: Implications for Projected Future Sea-Level Rise". *J. Geophys. Res.* 96.C12, pp. 22117–22124. DOI: 10.1029/91JC02502.

Pfeffer, W. T. and N. F. Humphrey (1996). "Determination of timing and location of water movement and ice-layer formation by temperature measurements in sub-freezing snow". *J. Glaciol.* 42.141, pp. 292–304. DOI: 10.1017/S0022143000004159.

— (1998). "Formation of ice layers by infiltration and refreezing of meltwater". *Ann. Glaciol.* Pp. 83–91. DOI: 10.1017/S0260305500014610.

Polashenski, C., Z. Courville, C. Benson, A. Wagner, J. Chen, G. Wong, R. Hawley, and D. Hall (2014). "Warming and Implications for Runoff Production". *Geophys. Res. Lett.* 41, pp. 1–9. DOI: 10.1002/2014GL059806.Received.

Reeh, N. (2008). "A nonsteady-state firn-densification model for the percolation zone of a glacier". *J. Geophys. Res. Earth Surf.* 113.3, pp. 1–13. DOI: 10.1029/2007JF000746.

Reeh, N., D. A. Fisher, R. M. Koerner, and H. B. Clausen (2005). "An empirical firn-densification model comprising ice lenses". *Ann. Glaciol.* 42, pp. 101–106. DOI: 10.3189/172756405781812871.

Reijmer, C. H., M. R. van den Broeke, X. Fettweis, J. Ettema, and L. B. Stap (2012). "Refreezing on the Greenland ice sheet: A comparison of parameterizations". *Cryosphere* 6.4, pp. 743–762. DOI: 10.5194/tc-6-743-2012.

Rignot, E. J., S. J. Ostro, J. J. Van Zyl, and K. C. Jezek (1993). "Unusual radar echoes from the Greenland ice sheet". *Science (80-.).* 261.5129, pp. 1710–1713. DOI: 10.1126/science.261.5129.1710.

Schwander, J., T. Sowers, J.-M. Barnola, T. Blunier, A. Fuchs, and B. Malaizé (1997). "Age scale of the air in the summit ice: Implication for glacial-interglacial temperature change". *J. Geophys. Res. Atmos.* DOI: 10.1029/97JD01309.

Simonsen, S. B. (2013). "PhD Thesis The state of the Greenland Ice Sheet - Firn-induced surface elevation change".

Smith, L. C., V. W. Chu, K. Yang, C. J. Gleason, L. H. Pitcher, A. K. Rennermalm, C. J. Legleiter, A. E. Behar, B. T. Overstreet, S. E. Moustafa, M. Tedesco, R. R. Forster, A. L. LeWinter, D. C. Finnegan, Y. Sheng, and J. Balog (2015). "Efficient meltwater drainage through supraglacial streams and rivers on the southwest Greenland ice sheet". *Proc. Natl. Acad. Sci.* DOI: 10.1073/pnas.1413024112.

Sørensen, L. S., S. B. Simonsen, K. Nielsen, P. Lucas-Picher, G. Spada, G. Adalgeirsdottir, R. Forsberg, and C. S. Hvidberg (2011). "Mass balance of the Greenland ice sheet (2003-2008) from ICESat data - The impact of interpolation, sampling and firn density". *Cryosphere* 5.1, pp. 173–186. DOI: 10.5194/tc-5-173-2011.

Steffen, K., J. E. Box, and and W. Abdalati (1996). "Greenland Climate Network: GC-Net". *CRREL 96-27 Spec. Rep. Glaciers, Ice Sheets Volcanoes, trib. to M. Meier.* DOI: 10.1016/j.aprim.2017.09.001.

Steger, C. R., C. H. Reijmer, M. R. van den Broeke, N. Wever, R. R. Forster, L. S. Koenig, P. Kuipers Munneke, M. Lehning, S. Lhermitte, S. R. M. Ligtenberg, C. Miège, and B. P. Y. Noël (2017a). "Firn Meltwater Retention on the Greenland Ice Sheet: A Model Comparison". *Front. Earth Sci.* 5.January. DOI: 10.3389/feart.2017.00003.

Steger, C. R., C. H. Reijmer, and M. R. Van Den Broeke (2017b). "The modelled liquid water balance of the Greenland Ice Sheet". *Cryosphere* 11.6, pp. 2507–2526. DOI: 10.5194/tc-11-2507-2017.

Van Angelen, J. H., J. T. Lenaerts, M. R. Van den Broeke, X. Fettweis, and E. Van Meijgaard (2013). "Rapid loss of firn pore space accelerates 21st century Greenland mass loss". *Geophys. Res. Lett.* 40.10, pp. 2109–2113. DOI: 10.1002/grl.50490.

Van den Broeke, M. R., E. M. Enderlin, I. M. Howat, P. Kuipers Munneke, B. P. Noël, W. Jan Van De Berg, E. Van Meijgaard, and B. Wouters (2016). "On the recent contribution of the Greenland ice sheet to sea level change". *Cryosphere* 10.5, pp. 1933–1946. DOI: 10.5194/tc-10-1933-2016. arXiv: arXiv:1011.1669v3.

Van Pelt, W. J., J. Oerlemans, C. H. Reijmer, V. A. Pohjola, R. Pettersson, and J. H. Van Angelen (2012). "Simulating melt, runoff and refreezing on Nordenskiöldbreen, Svalbard, using a coupled snow and energy balance model". *Cryosphere* 6.3, pp. 641–659. DOI: 10.5194/tc-6-641-2012.

Vandecrux, B., R. S. Fausto, P. L. Langen, D. Van As, M. MacFerrin, W. T. Colgan, T. Ingeman-Nielsen, K. Steffen, N. S. Jensen, M. T. Møller, and J. E. Box (2018a). "Drivers of Firn Density on the Greenland Ice Sheet Revealed by Weather Station Observations and Modelling". *J. Geophys. Res. Earth Surf.* DOI: 10.1029/2017JF004597.

Vandecrux, B., R. S. Fausto, D. Van As, W. T. Colgan, P. L. Langen, K. Sampson, K. Steffen, K. Haubner, T. Ingeman-Nielsen, M. Niwano, and J. E. Box (2018b). "Heat budget of Greenland firn: observed and simulated changes from 1998-2015". *Manuscript in preparation*.

Vandecrux, B., M. MacFerrin, H. Machguth, W. T. Colgan, D. van As, A. Heilig, C. M. Stevens, C. Charalampidis, R. S. Fausto, E. M. Morris, E. Mosley-Thompson, L. Koenig, L. N. Montgomery, C. Miège, S. B. Simonsen, T. Ingeman-Nielsen, and J. E. Box (2018c). "Firn data compilation reveals the evolution of the firn air content on the Greenland ice sheet". *Cryosph. Discuss.* Pp. 1–19. DOI: 10.5194/tc-2018-172. *In review*.

Vandecrux, B., M. Macferrin, H. Machguth, W. T. Colgan, D. Van As, A. Heilig, L. Koenig, L. N. Montgomery, C. Miège, S. B. Simonsen, and T. Ingeman-nielsen (2019). "Firn data compilation reveals widespread decrease of firn air content in western Greenland". *Cryosph.* 13, pp. 845–859. DOI: 10.5194/tc-13-845-2019.

Vionnet, V., E. Brun, S. Morin, A. Boone, S. Faroux, P. Le Moigne, E. Martin, and J. M. Willemet (2012). "The detailed snowpack scheme Crocus and its implementation in SURFEX v7.2". *Geosci. Model Dev.* 5.3, pp. 773–791. DOI: 10.5194/gmd-5-773-2012.

Waldner, P. A., M. Schneebeli, U. Schultze-Zimmermann, and H. Flühler (2004). "Effect of snow structure on water flow and solute transport". *Hydrol. Process.* 18.7, pp. 1271–1290. DOI: 10.1002/hyp.1401.

Wever, N., C. Fierz, C. Mitterer, H. Hirashima, and M. Lehning (2014). "Solving Richards Equation for snow improves snowpack meltwater runoff estimations in detailed multi-layer snowpack model". *Cryosphere* 8.1, pp. 257–274. DOI: 10.5194/tc-8-257-2014.

Wever, N., S. Würzer, C. Fierz, and M. Lehning (2016). "Simulating ice layer formation under the presence of preferential flow in layered snowpacks". *Cryosphere* 10.6, pp. 2731–2744. DOI: 10.5194/tc-10-2731-2016.

Zwally, H. J., A. C. Brenner, J. A. Major, R. A. Bindschadler, and J. G. Marsh (1989). "Growth of Greenland ice sheet: Measurement". *Science (80-.).* DOI: 10.1126/science.246.4937.1587.

Zwally, H. J. and L. Jun (2002). "Seasonal and interannual variations of firn densification and ice-sheet surface elevation at the Greenland summit". *J. Glaciol.* 48.161, pp. 199–207. DOI: 10.3189/172756502781831403.

APPENDIX A

Paper I

Rapid expansion of Greenland's low-permeability ice slabs

MacFerrin, M.[*1], Machguth, H.[2,3], van As, D.[4], Charalampidis, C.[5], Stevens, C.[6], Heilig, A.[7], Vandecrux, B.[4], Langen, P.[8], Mottram, R.[8], Fettweis, X.[9], Van den Broeke, M. R. [10], Pfeffer, W.T.[11], Moussavi, M.[1,12], Abdalati, W.[1]

Summary

In recent decades, meltwater runoff has accelerated to become the Greenland ice sheet's dominant mechanism for mass loss[1,2]. Across Greenland's high-elevation interior, porous snow and firn accumulate on the ice which can absorb surface meltwater and inhibit runoff[3], but this buffering effect is limited if enough water refreezes near the surface to hinder percolation[4,5]. How strongly refreezing affects meltwater runoff from the Greenland ice sheet remains largely unquantified. Here we present firn cores[4,6], radar observations[4,7], and regional climate models[2,8,9] to demonstrate that meters-thick low permeability "ice slabs" already cover 3.9–4.6 % of Greenland's ice and have significantly expanded its runoff area since the early 2000s. Continued ice slab growth may expand Greenland's runoff area to more than double its present size by the year 2100, contribute an additional 10–73 mm to global sea-level rise, and play a progressively more significant role in the ice sheet's future hydrology. We calculate that total runoff from ice slabs by 2100 is 2.4 times higher under a high-emissions future than moderate emissions. With

* Corresponding author
[1] Cooperative Institute for Research in Environmental Sciences, 216 UCB, University of Colorado, Boulder, CO 80309, USA
[2] Department of Geography, University of Zurich, Winterthurerstrasse 190, 8057 Zurich, Switzerland
[3] Department of Geosciences, University of Fribourg, Chemin du Musée 4, 1700 Fribourg, Switzerland
[4] Geological Survey of Denmark and Greenland, Øster Voldgade 10, DK-1350 Copenhagen, Denmark
[5] Bavarian Academy of Sciences and Humanities, Alfons-Goppel-Straße 11, 80539 Munich, Bavaria, Germany
[6] Department of Earth and Space Sciences, 4000 15th Ave NE, University of Washington, Seattle, WA 98195, USA
[7] Department of Earth and Environmental Sciences, Ludwig-Maximilians-University, Theresienstr. 41, 80333 Munich, Germany
[8] Department of Civil Engineering, Technical University of Denmark, Brovej B118, 2800 Kgs. Lyngby, Denmark
[9] Department of Geography, University of Liège, Clos Mercator, n°3, 4000 Liège, Belgium
[10] Institute for Marine and Atmospheric Research, Utrecht University, Princetonplein 5, 3584CC Utrecht, the Netherlands
[11] Department of Civil Engineering, 428 UCB, University of Colorado, Boulder, CO 80309, USA
[12] National Snow and Ice Data Center, 449 UCB, University of Colorado, Boulder, CO 80309, USA

the effect of ice slabs considered, today's greenhouse gas emissions pathways will have an increasingly significant effect on sea level rise from Greenland in a warming climate.

(Main Text)

In Greenland's high-elevation accumulation area, a porous layer of firn up to 80 m thick overlays the ice sheet[11], created by the gradual compression of snow into glacial ice. Meltwater can refreeze inside this firn layer, acting as a temporary buffer to runoff[3]. A Spring 2012 field campaign at the KAN_U field site at 1840 m elevation in southwest Greenland's accumulation area found layers of refrozen meltwater 3–5 meters thick just below the seasonal snow layer[4,5]. The record-breaking 2012 Greenland summer melt[12,13] caused meltwater to run off from KAN_U for the first time on record rather than refreeze locally in porous firn. These thick ice layers resulted in approximately 14±3 % more runoff in that region of southwest Greenland than would have occurred without the blocking effect of subsurface ice[4].

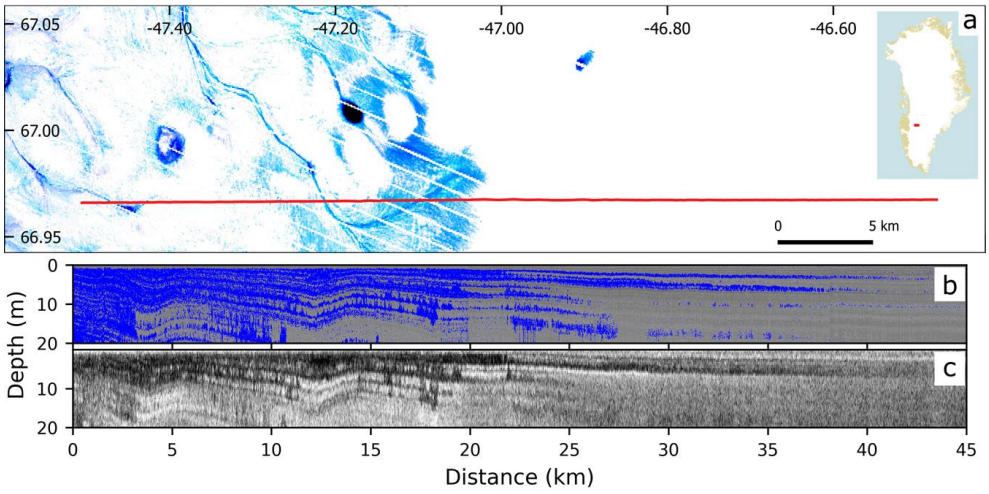

Figure 1 | Illustration of meltwater runoff over low-permeability ice slabs in southwest Greenland. (a) ACT-13 transect path (red) overlaid on a LandSat-7 image from July 16, 2012 (contrast-enhanced to show surface water in blue), lat/lon ticks. (b) ACT-13 in situ 800 MHz GPR with ice slabs colored blue. (c) A coincident transect of NASA's Operation IceBridge Accumulation Radar.

The Spring 2013 Arctic Circle Traverse (ACT-13) in southwest Greenland mapped a continuous, 40 kilometer long, multi-meter thick "ice slab" along an uphill transect in Greenland's Russell Glacier catchment (Figure 1). In summer 2012, meltwater saturated the limited snow/firn layer on top of this continuous ice slab, moving the runoff line ~22 km further uphill than previously observed.

This work distinguishes between ice "lenses" and thicker "slabs." Lenses refer to thin (0-10 cm) refrozen ice layers that form in a single melt season[11,14]. Meltwater can percolate through and around lenses[15] along preferential flow paths, sometimes reaching significant depths of 10 m or more before refreezing[16]. Low-permeability ice "slabs" refer to thicker layers (≥1 m) that form when water refreezes among preexisting lenses, annealing them together. Slabs form over multiple years, can span horizontally for tens of kilometers, and cause the measured permeability of the near-surface firn layer to approach zero[17]. This work focuses solely upon ice slabs in Greenland's firn that block deep percolation and affect wide-scale runoff.

Results

Shallow firn cores drilled along the ACT-13 route contain thick ice slabs (≥ 1 m) within firn at the lowest-elevation sites of the transect (Fig. S1, cores 1-3)[4]. Ice slabs at KAN_U have grown progressively thicker; in five years, ice volume-content of the top 10 meters grew from 54% in 2012 to 73% in 2017 (Fig S2), with nearby locations experiencing similar growth (Fig. S3).

In situ ground-penetrating radar (GPR) shows ice slabs begin at approximately 1690 m above sea level (a.s.l.) along the ACT-13 transect (Figure 1b). Ice slabs detected from a spatially-coincident transect of NASA IceBridge's airborne Accumulation Radar[7] flown three weeks before the ACT-13 transect closely match results in the top 20 meters of firn with a −14.9 to +6.7

% error rate, underestimating ice volume to a small degree. Data resolution, noise filtering, suboptimal flight conditions, adverse weather, variable surface topography and other collection issues sometimes weaken the airborne radar signal, causing ice slab presence and thickness to be slightly under-detected in IceBridge radar compared to the in situ radar. Portions of Greenland's lower accumulation area lack IceBridge coverage altogether. A map of ice slab thickness in Greenland using IceBridge Accumulation Radar (Figure 2) should be therefore be interpreted as a "minimum observed extent" of ice slabs in Greenland rather than an exhaustive map.

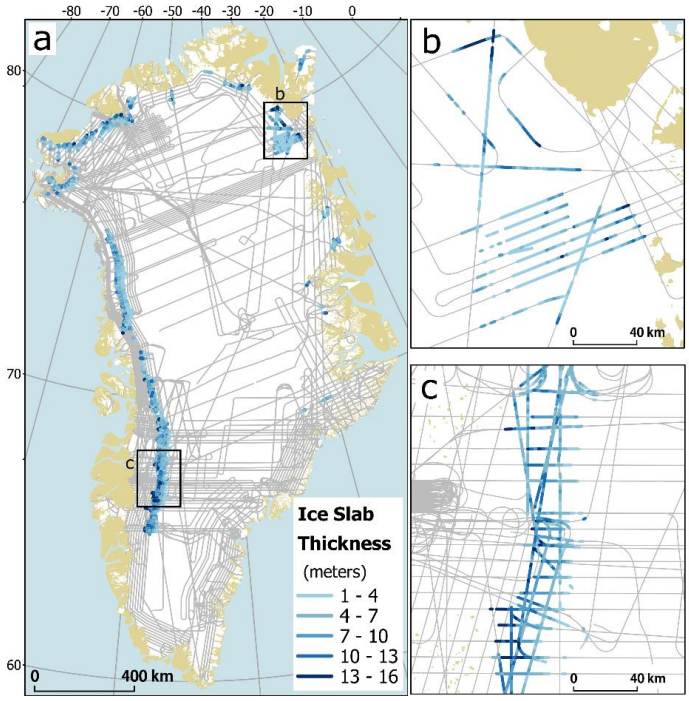

Figure 2 | Low-permeability Ice Slabs on the Greenland ice sheet and peripheral ice caps detected by IceBridge Accumulation Radar. Ice slabs detected in Greenland (a) with 6x-zoomed insets in northeast Greenland (b) and southwest Greenland (c).

Observations of ice slabs (Figure 2) cover approximately 69,400 km^2, and are not present in regions of high accumulation where surface meltwater is trapped in perennial firn aquifers

instead of refreezing[18]. Regional climate models overlaying the IceBridge transects suggest that ice slabs are observed in locations with annual accumulations below 572 mm w.e. (1.85 m snowfall at 340 kg m^{-3}) at a 95 % confidence threshold, consistent with firn models showing aquifers that form in regions with annual accumulation rates exceeding ~600 mm w.e.[19].

Regional climate models[2,8,9] (RCMs) forced at their boundaries by atmospheric reanalysis data[20,21] show that ice slabs have formed in regions receiving 266–573 mm w.e. yr^{-1} excess melt for a decade or more (Fig. S16). Here, "excess melt" refers to the amount of meltwater exceeding the seasonal snow's capacity to store and refreeze it (see Methods), which would inevitably occupy firn pore volume at depth faster than new pore volume is being added at the surface. The upper value of that range of excess melt (573 mm w.e. a^{-1}) would fill a porous firn layer (density 500 kg m^{-3}) into refrozen ice with bubbles (density 873 kg m^{-3}) to a thickness of 15.4 meters in ten years, in close agreement with the maximum thickness of 16 meters used when detecting ice slabs with IceBridge radar. RCMs show that excess melt slowly increased since the 1990s in regions where ice slabs currently exist (Fig. S17) and rapidly increased after 2001 when annual rates of ice slab formation jumped tenfold or more (Table 1 & Fig. 3a). At the end of 2013, RCMs estimate that ice slabs in Greenland cover 62,100–78,900 km^2 above Greenland's pre-1990 runoff area. Maps of simulated ice slabs at end-of-year 2013 (Fig 3b-e) are consistent with one another, as well as with the extent observed using IceBridge radar (Figure 2).

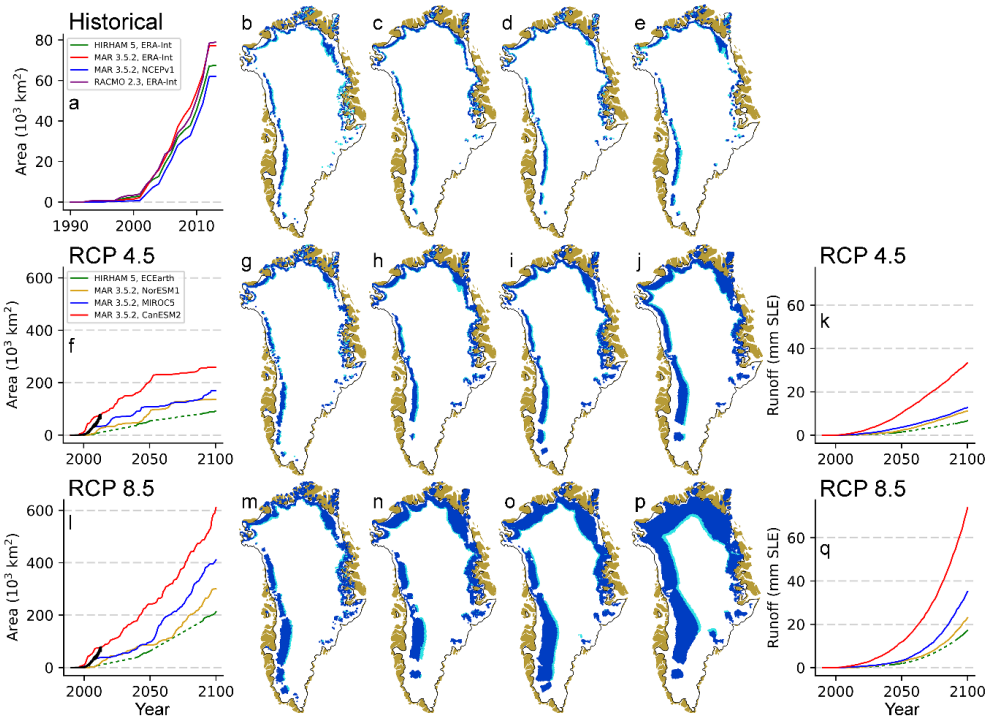

Figure 3 | Ice slab growth and runoff computed by outputs from regional climate models. Top row (a-e) show growth from historically-run RCMs forced by reanalysis data through 2013, and are directly comparable to spring-2010-2014 observations of ice slabs in Figure 2. Maps in (b-e) are affiliated with model results from end-of-year 2013 in the order listed in the legend of panel (a). The bottom two rows show 21st century RCM results forced by GCMs, each forced by RCP 4.5 (f-k) and 8.5 (l-q) emissions pathways (respectively). Ice slab area on the left (f and l) each have a black span representing historical ice slab grown from panel (a) for comparison. Maps (g-j) and (m-p) show ice slab extents in 2100 simulated by the RCMs in the order listed in the legend of panel (f). Runoff estimates on the right-hand panels (k and q) show 21st century runoff from atop ice slab regions, not including contributions from Greenland's historical runoff area or from dynamic ice loss.

RCMs forced by general circulation models[22–26] (GCMs) until the year 2100 show the area of ice slabs across Greenland is likely to expand moderately through 2050 under both Representative Concentration Pathway (RCP) 4.5 and 8.5 forcing (Fig 3f & l, respectively), approximately doubling in area compared to present-day extent. Most GCM-forced RCMs underestimate present-day ice slab extent when compared to reanalysis-forced RCMs, in part because GCMs haven't yet captured changing atmospheric circulation patterns over Greenland

that have contributed to recent summer melt increases[27]. Models forced by the RCP 4.5 "moderate emissions" scenario show a relative leveling-off of ice slab extent after 2050 through 2100 (Fig. 3f). Under the RCP 8.5 "high emissions" scenario, the formation of new ice slabs will accelerate from their 1990-2050 growth (1240–4160 $km^2\ a^{-1}$) to approximately double that rate of growth (2890–7130 $km^2\ a^{-1}$) in the latter half of the century (Fig. 3l). On average by 2100, RCMs show ice slab area and surface runoff being 2.32 and 2.42 times higher, respectively, following a high-emissions pathway than moderate-emissions.

Under linear warming conditions, ice slab growth follows an approximate quadratic increase consistent with the ice sheet's parabolic hypsometry, where step-changes in elevation cover increasingly large areas as they progress further onto the ice sheet's flat interior[5,28]. Runoff atop ice slabs also shows a divergence after 2050 between moderate- and high-emissions pathways, with both the rates and accelerations of runoff increasing through the end of model simulations in 2100 under high emissions (Table 1). In all cases, pre-2050 and post-2050 trends are statistically significant ($p < 0.02$).

Discussion

Excess melt production and runoff calculated in this study do not account for darkening of the snow surface from newly-formed summer slush fields, formed as meltwater saturates near-surface firn and increases absorption of solar radiation (Fig. 1). Slush fields significantly increased local melt atop ice slabs in the summer of 2012[29]; not accounting for them may cause runoff estimates presented here to be biased low. Other uncertainties include potential changes in the amount of local runoff that refreezes downstream before exiting the ice sheet[30]. Future work is needed to study these effects in more detail and narrow the range of future estimates of sea level rise from Greenland's high-elevation interior.

The global impact of an extra 10–73 mm sea level rise coming from regions of the Greenland ice sheet that did not previously produce runoff is itself significant, but the saturation of the ice sheet's surface over large areas of Greenland's high-elevation interior is likely to impact the ice sheet's hydrology, dynamics and other glaciological processes. Some regions showing significant future ice slab growth, especially in northern Greenland, currently have a perennially frozen bed[31] which could change if concentrations of surface water are able to find their way to the bed. If greater amounts of surface meltwater enter moulins at higher elevations, cryo-hydrologic warming[32] could alter the thermal structure of interior ice and potentially increase dynamic flow. Potential downstream effects of ice slabs to the future behavior of the ice sheet are beyond the scope of this paper, but will need to be considered in greater detail to accurately predict Greenland's future contributions to global sea level.

Ice slab extent differs by Significant differences in ice slab extent between moderate- and high-emissions pathways demonstrate the significant role that the present-day choices of emissions pathways have on the future of the Greenland ice sheet.

Methods

Firn Cores and In Situ GPR

Cores were drilled at 100 m elevation intervals between 1840 and 2350 meters along the ACT-13 ground-penetrating radar (GPR) transect (Fig. S1, Table S1), with two cores drilled at KAN_U approximately 3 km north of the main transect where a 1x1 km GPR grid was collected and two more cores at the Dye-2 site, 40 km south of the main transect. Cores were logged for stratigraphy at 1 cm resolution and cut into 10 cm intervals to record density. Using core sections

with clean cuts consisting of purely refrozen ice, we observed a density of refrozen "bubbly" ice in firn to be 873±25 kg m^{-3} in the cores[4].

In situ GPR was collected in a 1 km grid at KAN_U adjacent to cores 1 and 2, in select tracks at Dye-2 near cores 5 and 6, and along the main transect line adjacent to the remaining coring sites. GPR data were first pre-processed to combine individual files into continuous transects and resampled for constant 1.5 m trace spacing. We applied a de-wow filter to remove low-frequency artifacts and an exponential gain filter to eliminate the majority of depth-dependent signal attenuation. We then processed the traces with a moving window to compute local variance in the GPR signal, which is significantly lower in thick refrozen ice than in porous firn[4]. We applied an adaptive linear-gain filter to eliminate residual depth attenuation that still remained after post-processing the data. We converted radar two-way travel time to depth using a correlation function that maximized the negative correlation between core density and local signal variance. We chose a cutoff for local signal variance to identify refrozen ice layers within the firn, to minimize both Type-1 (commission) and Type-2 (omission) errors compared with to adjacent cores. A chosen cutoff of $10^{5.0}$ [16-bit raw GPR value, unitless] in local variance of the GPR signal was able to identify ice slabs ≥50 cm thick with an average error of –13.4 to +3.2 % compared to adjacent cores. Ice thickness estimates derived from this GPR technique should be considered "lower bound" estimates, only able to reliably identify ice layers that are both thick and spatially continuous, consistent with the purpose of this study. Specific details sufficient to reproduce results in other GPR transects are available in the Supplementary Methods.

Operation IceBridge GPR

NASA Operation IceBridge Level 1B Accumulation Radar (AR) files[7] for years 2010–2014 were acquired from the Center for Remote Sensing of Ice Sheets (CReSIS) public FTP

website. We filtered flight lines to cover the extent of Greenland's ice using the Greenland Ice Mapping Project (GIMP)[33] land classification data set. Since we are only interested in firn processes, we additionally subset the data to include only returns above the long-term equilibrium line altitude where past long-term average melt does not exceed long-term accumulation, and within the percolation area where melt exceeds 10 % of accumulation in an average year, using the HIRHAM v5 regional climate model outputs for 1980–1990 forced on its boundary by ERA-interim.

IceBridge radar data were post-processed to improve the smoothness of surface selections in the radar and minimize artifacts introduced by a poorly-chosen surface. Artifacts are minimized using assumptions of surface continuity to identify and eliminate false returns, primarily caused by strong echoes in the radar signal along some flight lines.

Airborne radar data strength is significantly affected when the aircraft rolls during a turn, often causing anomalously weak returns based solely upon the geometry of the flight line. To correct this, we apply a depth-dependent roll-correction factor to each flight line. In 2012, aircraft roll data were not provided with the radar data, and we use a calculation of aircraft path curvature as a substitute, which matches strongly with aircraft roll in high-roll scenarios >5°, when the IceBridge radar data are most affected.

Surface lakes are known to occasionally remain unfrozen through a winter season[34], as are firn aquifers buried in high-accumulation regions[18]. Liquid water stored within the firn causes a bright reflection at the water's surface and a rapid extinction of the signal to depth, making GPR samples unsuitable for detecting ice slabs beneath the water table. Although lakes can form atop ice slabs (113 such lakes were identified during this work), radar lines were manually

193 filtered to eliminate locations which included lakes and aquifers before the data was further
194 processed.

195 The return strength of radar decays approximately exponentially with depth through a
196 medium[35], so a depth-correction must be applied in order to reliably quantify artifacts within the
197 firn using signal strength. Using the same time-to-depth conversion calculated for the in-situ
198 GPR, we selected pixels in the top 50 meters below the surface of the firn and performed a
199 depth-homogenization to provide relatively homogeneous signal strength by dividing by a best-
200 fit exponential decay curve on each file and correcting for signal decay. Through this process, we
201 also normalized the data by flight line, giving each final return a mean value of 0 and a standard
202 deviation of 1. Before normalization, the signal strength of original AR data in the top 50 meters
203 differs by up to 5 orders of magnitude between flight lines, caused by different aircraft and
204 instrument configurations from year to year. After depth-correction and normalization, the
205 IceBridge data are standardized to have consistent return strengths which can be further
206 processed using constant thresholds that do not depend upon individual flight lines.

207 After IceBridge AR files have been rescaled and normalized for consistent return
208 strength, we use a threshold cutoff to identify radar samples below the threshold, where the
209 return signal is weaker from relatively homogeneous ice than from surrounding firn. We apply a
210 simple noise filter to eliminate small-scale (1-2 pixel) noise from the images, and the apply a
211 continuity filter to remove small disconnected groups of pixels from the image and leave only
212 spatially-continuous regions of identified pixels identified as ice slabs. The noise-filtering steps
213 eliminate false-positives in porous firn, where pixels below the threshold are scattered rather than
214 contiguous. We use a 2-dimensional minimization search to validate the reference track
215 “20130409_01_010_012” against the 800 MHz in situ GPR line and choose sensitivity and

continuity thresholds which minimize errors. A sensitivity threshold of -0.45 (normalized dB) and a continuity threshold of 350 pixels minimized the sum of Type-1 and Type-2 errors when compared to ice identified in the in situ GPR (Fig. S6). IceBridge traces with more than 16 m of ice in the top 20 m of firn were discarded to eliminate false-positive Type-1 identifications of ice slabs where there is solid ice to depth with little or no firn in the entire column (i.e. the long-term saturation and ablation areas). The IceBridge data estimates ice content in the firn with a –16.5 to +5.0 % error rate with respect to the in situ GPR. The IceBridge radar generally underestimates total ice content due to limits of the data's resolution. Some thinner ice slabs (50–100 cm) are identified with in situ GPR that IceBridge radar does not see. Combined with in situ GPR accuracy of –13.2% to +3.2% compared to core data (previous section), we estimate the root sum squared error of the IceBridge data to be –21.1% to +5.9% accurate when identifying >50 cm thick solid ice volumes in the top 20 meters of firn, compared to the "truth" in coincident firn cores. Generally speaking, IceBridge radar underestimates total ice content in the firn compared with firn cores drilled at the same location. The IceBridge AR reference track was a straight flight line (<1° aircraft roll) with relatively high data quality. IceBridge AR data may be considerably less accurate over flight lines with low data quality due to aircraft roll, pitch, or other variables, resulting in data gaps in Figure 2, where ice slabs in the firn are not identified (Type-2 omission errors).

Excess Melt Calculations

"Excess melt" refers to meltwater beyond a threshold which has overwhelmed the seasonal snow's pore-space and refreezing capacity, resulting in excess water that must either fill surrounding firn layers faster than accumulation is replenishing near-surface pore space, or run off to lower elevations. We modify a previously-defined relationship for this threshold[36] to

include rain water, which affects firn in a similar manner to meltwater and is projected to increase across Greenland's accumulation area in a warming climate[37]. We calculate the amount of excess melt M_e (kg m^{-2}) as

$$M_e = \left(\frac{M+R}{C} - \left[\left(\frac{\mathbb{c}}{L}T_f + \frac{\rho_r - \rho_c}{\rho_c}\right)\left(1 + \frac{\rho_r - \rho_c}{\rho_c}\right)^{-1}\right]\right) \cdot C \quad (1)$$

where M = melt (kg m^{-2}), C = accumulation (kg m^{-2}), R = rain (kg m^{-2}), $\mathbb{c}$ = heat capacity of ice (J °K^{-1} kg^{-1}), L = latent heat refreezing capacity of ice (J kg^{-1}), T_f = temperature of underlying firn (positive °K below freezing) derived from mean annual air temperature, ρ_r = density of refrozen ice (kg m^{-3}), and ρ_c = density of fresh accumulation (kg m^{-3}). We calculate the density of fresh snow accumulation (ρ_c) with a geographically-based parameterization used in surface mass balance models[38] that provides accumulation density values between 300–380 kg m^{-3}, a range consistent with independent observations[6]. We use 873 kg m^{-3} for the density of refrozen ice (ρ_r) as found in firn cores[4]. Excess melt calculations are generally insensitive to reasonable variations in ρ_r and ρ_c, consistent with prior literature[36]. For this work, excess melt is calculated on a 10-year running mean (i.e. mean values in 2001 are calculated from 1992–2001, inclusive) to compute decadal averages and to smooth inter-annual variability when considered for the formation of ice slabs. In the main text, excess melt is presented in mm water-equivalent, functionally equivalent to the kg m^{-2} units in Eq. 1. A more detailed derivation of Eq. 1 is presented in Supplemental Materials.

Mapping Ice Slabs

We used three regional climate models forced by two different reanalysis datasets (Table 1) to determine the range of decadal excess melt volumes that have caused ice slabs to form within the firn as identified by IceBridge AR data in 2010–2014. We use a subset of IceBridge

flight lines which transect ice slab areas in straight "downhill to uphill" orientations, where both the "bottom" and "top" extent of ice slabs is identified. A range of 266–573 mm w.e. during the full decade prior to observations fits the observations of current ice slabs with good agreement between the models (Fig. S18). Areas which averaged this amount of excess melt or more during the prior "baseline" period prior to 1990 are masked out as being in the long-term ablation area where porous firn would not exist in appreciable volume. Regions with enough annual accumulation to form perennial firn aquifers are masked out and not included in ice slab calculations.

We applied identical thresholds to RCMs forced at their boundaries by GCMs under the RCP 4.5 "moderate emissions" and RCP 8.5 "high emissions" climate scenarios[10] (Table 1). For the HIRHAM 5 RCM, data was not available to compute a pre-1990 baseline period, and 1990–1999 was used instead with ice slabs growing after the year 2000, which may bias the results slightly low for that particular RCM. GCM time periods using historical forcings were combined with each respective 21st-century forcing to form a continuous datasets to predict the growth of ice slabs.

Runoff Calculations

Inter-annual variability in melt and accumulation are high in Greenland, with some years demonstrating exceptional melt while others demonstrating relatively low levels of melt and runoff. As calculated in Equation 1, excess melt refers to the amount of meltwater beyond which pore volume from annual snow accumulation is able to absorb it. When excess melt is negative, it represents the amount of pore volume (absence of melt) added at a given location. After an ice

slab forms on/near the ice-sheet surface, pore volume added atop the slab is tallied on an annual basis from RCM results. Surface melt in future years much occupy all accumulated pore volume before runoff occurs. Runoff from the top of ice slabs is tallied on an annual basis and presented in Fig. 3 as a running sum-total. Means and trends are outlined in Table 1.

Data Availability

Firn cores presented in supplemental Figures S1–S3 are available in the 2018 release of Greenland's SumUp Dataset[6]. Post-processed in-situ and IceBridge radar transects, shapefiles and CSV-summaries are publicly available in Figshare project "Greenland Ice Slab Runoff" at https://figshare.com/projects/*XXXX*. Code for post-processing cores, in-situ GPR, IceBridge GPR, and RCM model data are available at https://github.com/mmacferrin/*YYYY*. RCM model outputs are available from respective online data repositories for each model, and/or upon request from co-authors of this manuscript. [*Note to editors and reviewers: datasets and code are currently available at any point upon request. Online archives will be made public and URLs posted upon publication of the manuscript.*]

References

1. van den Broeke, M. R. *et al.* On the recent contribution of the Greenland ice sheet to sea level change. *The Cryosphere* **10,** 1933–1946 (2016).
2. Fettweis, X. *et al.* Reconstructions of the 1900–2015 Greenland ice sheet surface mass balance using the regional climate MAR model. *The Cryosphere* **11,** 1015–1033 (2017).
3. Harper, J., Humphrey, N., Pfeffer, W. T., Brown, J. & Fettweis, X. Greenland ice-sheet contribution to sea-level rise buffered by meltwater storage in firn. *Nature* **491,** 240–243 (2012).

4. Machguth, H. *et al.* Greenland meltwater storage in firn limited by near-surface ice formation. *Nat. Clim. Change* **6,** 390–393 (2016).
5. Mikkelsen, A. B. *et al.* Extraordinary runoff from the Greenland ice sheet in 2012 amplified by hypsometry and depleted firn retention. *The Cryosphere* **10,** 1147–1159 (2016).
6. Montgomery, L., Koenig, L. & Alexander, P. The SUMup Dataset: Compiled measurements of surface mass balance components over ice sheets and sea ice with preliminary analysis over Greenland. *Earth Syst. Sci. Data Discuss.* 1–31 (2018). doi:https://doi.org/10.5194/essd-2018-21
7. Leuschen, C. *Operation IceBridge Accumulation Radar L1B Geolocated Radar Echo Strength Profiles*. (NASA DAAC at that National Snow and Ice Data Center, 2014).
8. Christensen, O. *et al. The HIRHAM regional climate model version 5 (β). Danish Meteorological Institute Technical Report 06-17*. (2007).
9. Noël, B. *et al.* Evaluation of the updated regional climate model RACMO2.3: summer snowfall impact on the Greenland Ice Sheet. *The Cryosphere* **9,** 1831–1844 (2015).
10. IPCC. *Climate Change 2013: The Physical Science Basis. Contribution of Working Group 1 to the Fifth Assessment Report of the Intergovernmental Panel on Climate Change [Stocker, T.F., D. Qin, G.-K. Plattner, S.K. Allen, J. Boschung, A. Nauels, Y. Xia, V. Bex and P.M. Midgley (eds.)]*. (2013).
11. Benson, C. S. *Stratigraphic Studies in the Snow and Firn of the Greenland Ice Sheet*. (U.S. Army Snow, Ice and Permafrost Research Establishment, Corps of Engineers, 1962).
12. Nghiem, S. V. *et al.* The extreme melt across the Greenland ice sheet in 2012. *Geophys. Res. Lett.* **39,** L20502 (2012).

13. Tedesco, M. *et al.* Evidence and analysis of 2012 Greenland records from spaceborne observations, a regional climate model and reanalysis data. *The Cryosphere* **7,** 615–630 (2013).
14. Brown, J., Harper, J., Pfeffer, W. T., Humphrey, N. & Bradford, J. High-resolution study of layering within the percolation and soaked facies of the Greenland ice sheet. *Ann. Glaciol.* **52,** 35–42 (2011).
15. Heilig, A., Eisen, O., MacFerrin, M., Tedesco, M. & Fettweis, X. Seasonal monitoring of melt and accumulation within the deep percolation zone of the Greenland Ice Sheet and comparison with simulations of regional climate modeling. *The Cryosphere* **12,** 1851–1866 (2018).
16. Humphrey, N. F., Harper, J. T. & Pfeffer, W. T. Thermal tracking of meltwater retention in Greenland's accumulation area. *J. Geophys. Res.* **117,** 11 PP. (2012).
17. Sommers, A. N. *et al.* Inferring Firn Permeability from Pneumatic Testing: A Case Study on the Greenland Ice Sheet. *Front. Earth Sci.* **5,** (2017).
18. Forster, R. R. *et al.* Extensive liquid meltwater storage in firn within the Greenland ice sheet. *Nat. Geosci.* **7,** 95–98 (2014).
19. Munneke, P. K., M. Ligtenberg, S. R., van den Broeke, M. R., van Angelen, J. H. & Forster, R. R. Explaining the presence of perennial liquid water bodies in the firn of the Greenland Ice Sheet. *Geophys. Res. Lett.* **41,** 476–483 (2014).
20. Dee, D. P. *et al.* The ERA-Interim reanalysis: configuration and performance of the data assimilation system. *Q. J. R. Meteorol. Soc.* **137,** 553–597 (2011).
21. Kalnay, E. *et al.* The NCEP/NCAR 40-Year Reanalysis Project. *Bull. Am. Meteorol. Soc.* **77,** 437–471 (1996).

22. Hazeleger, W. *et al.* EC-Earth: A Seamless Earth-System Prediction Approach in Action. *Bull. Am. Meteorol. Soc.* **91,** 1357–1363 (2010).
23. Chylek, P., Li, J., Dubey, M. K., Wang, M. & Lesins, G. Observed and model simulated 20th century Arctic temperature variability: Canadian Earth System Model CanESM2. *Atmos Chem Phys Discuss* **2011,** 22893–22907 (2011).
24. Watanabe, M. *et al.* Improved Climate Simulation by MIROC5: Mean States, Variability, and Climate Sensitivity. *J. Clim.* **23,** 6312–6335 (2010).
25. Bentsen, M. *et al.* The Norwegian Earth System Model, NorESM1-M – Part 1: Description and basic evaluation of the physical climate. *Geosci Model Dev* **6,** 687–720 (2013).
26. Collins, W. J. *et al.* Evaluation of the HadGEM2 model. *Met Off. Hadley Cent. Tech. Note* (2008).
27. Hanna, E., Fettweis, X. & Hall, R. J. Recent changes in summer Greenland blocking captured by none of the CMIP5 models. *Cryosphere Discuss.* 1–8 (2018). doi:https://doi.org/10.5194/tc-2018-91
28. van As, D. *et al.* Hypsometric amplification and routing moderation of Greenland ice sheet meltwater release. *The Cryosphere* **11,** 1371–1386 (2017).
29. Charalampidis, C. *et al.* Changing surface–atmosphere energy exchange and refreezing capacity of the lower accumulation area, West Greenland. *The Cryosphere* **9,** 2163–2181 (2015).
30. Rennermalm, A. K. *et al.* Evidence of meltwater retention within the Greenland ice sheet. *The Cryosphere* **7,** 1433–1445 (2013).
31. MacGregor, J. A. *et al.* A synthesis of the basal thermal state of the Greenland Ice Sheet. *J. Geophys. Res. Earth Surf.* **121,** 1328–1350 (2016).

32. Phillips, T., Rajaram, H. & Steffen, K. Cryo-hydrologic warming: A potential mechanism for rapid thermal response of ice sheets. *Geophys. Res. Lett.* **37,** (2010).
33. Howat, I. M., Negrete, A. & Smith, B. E. The Greenland Ice Mapping Project (GIMP) land classification and surface elevation data sets. *The Cryosphere* **8,** 1509–1518 (2014).
34. Koenig, L. S. *et al*. Wintertime storage of water in buried supraglacial lakes across the Greenland Ice Sheet. *The Cryosphere* **9,** 1333–1342 (2015).
35. Jol, H. M. *Ground Penetrating Radar Theory and Applications*. (Elsevier, 2008).
36. Pfeffer, W. T., Meier, M. F. & Illangasekare, T. H. Retention of Greenland runoff by refreezing: Implications for projected future sea level change. *J. Geophys. Res.* **96,** 22117–22,124 (1991).
37. Doyle, S. H. *et al.* Amplified melt and flow of the Greenland ice sheet driven by late-summer cyclonic rainfall. *Nat. Geosci.* **8,** 647–653 (2015).
38. Langen, P. L., Fausto, R. S., Vandecrux, B., Mottram, R. H. & Box, J. E. Liquid Water Flow and Retention on the Greenland Ice Sheet in the Regional Climate Model HIRHAM5: Local and Large-Scale Impacts. *Front. Earth Sci.* **4,** (2017).

Supplementary Information

Supplementary information containing firn cores and validation plots between cores, GPR, and RCMs, and detailed GPR-processing methods descriptions is available at [*URL of Supplementary Information upon publication*].

Acknowledgements

Authors would like to acknowledge National Aeronautics and Space Administration (NASA) awards NNX10AR76G and NNX15AC62G for funding the majority of the work including field seasons. Authors would like to thank the dozens of additional field team members for their contributions to field data collection in years 2012–2017.

Author Information

Reprints and permissions information is available at www.nature.com/reprints. The authors declare no external competing interests related to this manuscript. Correspondence and requests for materials should be addressed to Michael.MacFerrin@Colorado.edu.

Author Contributions

MM1 conceived of the study question, processed the core data, in situ radar data, airborne radar data, post-processed the RCM output data and was primary author of the main manuscript and supplement. All authors contributed to the manuscript text and revisions. MM1, HM, and DA planned, organized and undertook field campaigns dedicated to the data presented in this paper. CC, CS, BV, and AH were instrumental to collecting, interpreting, and/or plotting field data. PL, RM, XF, and MvdB provided regional climate model outputs for the study and assisted with their results and interpretations. WTP helped formulate and interpret the excess melt model. MM2 performed remote sensing validation of runoff over ice slabs. WA supervised and oversaw the direction and formulation of the manuscript and project.

Tables

Table 1. **Regional Climate Model results of ice slab growth and runoff.** Historical results available 1990-2013, 21st Century results from 1990-2100.

RCM, Forcing	Area Trend	Area Total	Runoff Trend	Runoff Accel.	Runoff Total	Area Trend	Area Total	Runoff Trend	Runoff Accel.	Runoff Total
Units:	$km^2\ a^{-1}$	km^2	$GT\ a^{-1}$	$GT\ a^{-2}$	GT	$km^2\ a^{-1}$	km^2	$GT\ a^{-1}$	$GT\ a^{-2}$	GT
Historical	**1990 - 2000**	**2000**	**1990 - 2000**	**1990 - 2000**	**2000**	**2001 - 2013**	**2013**	**2001 - 2013**	**2001 - 2013**	**2013**
HIRHAM 5, ERA-Int.	234	2500	0.099	0.055	1.42	5540	67500	13.7	2.28	166
MAR 3.5.2, ERA-Int.	148	1410	0.079	0.040	1.07	6510	77300	18.5	3.19	222
MAR 3.5.2, NCEP v1	53.3	491	0.025	0.013	0.35	5300	62100	12.5	2.48	153
RACMO 2.3, ERA-Int.	330	3310	0.209	0.070	2.35	6310	78900	16.2	2.74	200
21st Century RCP 4.5	**1990 - 2050**	**2050**	**1990 - 2050**	**1990 - 2050**	**2050**	**2051 - 2100**	**2100**	**2051 - 2100**	**2051 - 2100**	**2100**
HIRHAM 5, ECEarth*	1080	53500	9.67	0.556	514	817	91700	34.9	0.531	2380
MAR 3.5.2, NorESM 1	1280	85400	11.9	0.698	822	945	135000	66.4	0.432	3970
MAR 3.5.2, MIROC 5	1980	108000	21.6	0.957	1330	1200	170000	66.0	0.834	4570
MAR 3.5.2, CanESM 2	3520	205000	59.5	2.51	3660	762	258000	166	1.03	12000
RACMO 2.1, HadGEM 2‡	3970	216000	46.5	1.96	2810	3095	344000	172	2.35	11000
21st Century RCP 8.5	**1990 - 2050**	**2050**	**1990 - 2050**	**1990 - 2050**	**2050**	**2051 - 2100**	**2100**	**2051 - 2100**	**2051 - 2100**	**2100**
HIRHAM5, ECEarth*	1240	62900	13.4	0.672	682	2890	212000	95.6	2.97	6170
MAR 3.5.2, NorESM 1	1780	85500	16.6	0.787	1010	4740	301000	143	5.34	8300
MAR 3.5.2, MIROC 5	1610	97900	17.9	0.842	1150	6220	410000	229	7.48	12700
MAR 3.5.2, CanESM 2	4160	243000	67.3	3.13	4250	7130	610000	440	12.9	26600

*HIRHAM 5 21st-Century model results only available in three periods: 2000-2010, 2040-2050, and 2090-2100. 1900-2050 results are computed using 2000-2010 and 2040-2050 combined data; 2051-2100 results are computed using 2041-2050 and 2090-2100 combined data.

‡RACMO 2.1 21st-Century model results conclude 2098; 2050-2100 results are computed from 2051-2098. RACMO 2.1 results are only available for RCP 4.5, which are included here but not in the moderate- vs high-emissions visual comparison in Figure 3.

APPENDIX B

Paper II

Regional climate-model performance in Greenland firn derived from *in situ* observations

Charalampos Charalampidis, Dirk van As, Peter L. Langen, Robert S. Fausto, Baptiste Vandecrux and Jason E. Box

Recent record-warm summers in Greenland (Khan *et al.* 2015) have started affecting the higher regions of the ice sheet (i.e. the accumulation area), where increased melt has altered the properties of firn (i.e. multi-year snow). At high altitudes, meltwater percolates in the porous snow and firn, where it refreezes. The result is mass conservation, as the refrozen meltwater is essentially stored (Harper *et al.* 2012). However, in some regions increased meltwater refreezing in shallow firn has created thick ice layers. These ice layers act as a lid, and can inhibit meltwater percolation to greater depths, causing it to run off instead (Machguth *et al.* 2016). Meltwater at the surface also results in more absorbed sunlight, and hence increased melt in the accumulation area (Charalampidis *et al.* 2015). These relatively poorly understood processes are important for ice-sheet mass-budget projections.

Regional climate models (RCMs) simulate energy fluxes and mass transfer between the atmosphere and the ice-sheet surface. Their accuracy depends on model physics and numerical sophistication, as well as on the atmospheric forcing implemented at their boundaries based on global weather reanalyses or general circulation models (see below). Ice-sheet mass-budget calculations using RCMs therefore need to be validated against observations. In this study, we evaluate the performance of the subsurface scheme of the HIRHAM5 RCM (Christensen *et al.* 2006) by comparing it with firn temperatures measured at the KAN_U weather station from April 2009 to September 2013 (Charalampidis *et al.* 2016). We determine the reasons for temperature biases by comparing HIRHAM5 with a validated surface energy balance (SEB) model over the same period (Charalampidis *et al.* 2015).

Firn temperature measurements

Situated 1840 m above sea level (a.s.l.), KAN_U is the uppermost automatic weather station at an elevation transect of meteorological and mass-budget monitoring sites in the south-western part of the Greenland ice sheet (Charalampidis *et al.* 2015; 67°0′N, 47°1′W). The long-term equilibrium line altitude, where summer ablation balances winter accumulation, is 1553 m a.s.l. (Van de Wal *et al.* 2012). KAN_U is located above that, and thus monitors melt, percolation and refreezing in firn. Established in April 2009, the KAN_U record includes the high melt seasons of 2010, 2011 and 2012 (Charalampidis *et al.* 2015).

The subsurface temperature analysis by Charalampidis *et al.* (2016) revealed that in the 2010 and 2011 high melt summers, meltwater occupied the pore volume between 2 and 3 m below the surface (Fig. 1A). The continued refreezing of this temporarily retained, near-surface liquid water until after the end of both the 2010 and 2011 melt seasons contributed to the merging of superimposed annual ice layers. These ice layers were observed at depths between 2.5 and 5.5 m in May 2012 (Machguth *et al.* 2016). Subsequently, meltwater by the end of August 2012 was confined in the upper 2.5 m relative to the May 2012 surface, with subsequent runoff in response to the intense surface lowering. By September 2012, after the onset of cold atmospheric conditions, refreezing occurred below 2.5 m by meltwater percolation to the limited available pore volume between the ice layers. The latent heat release by refreezing at depth in autumn 2012 resulted in a high December–January–February average firn temperature of –6.1°C between 2 and 5 m depth (Charalampidis *et al.* 2016), while the accumulating snow cover provided thermal insulation from the cold winter atmosphere.

The HIRHAM5 regional climate model

We use HIRHAM5 at 5 × 5 km horizontal resolution, which has demonstrated good results for the climate of the Greenland ice-sheet margin (e.g. Langen *et al.* 2015). It uses 31 vertical atmospheric levels and a time step of 90 seconds. At the lateral boundaries, the model is forced at 6-hour intervals with wind, temperature, specific humidity and atmospheric pressure from the ERA-Interim weather reanalysis (Dee *et al.* 2011). The model computes processes in the atmosphere, including clouds, solar radiation attenuation, longwave radiation emission and precipitation. These variables then determine the energy balance and mass budget at the surface. Daily-smoothed, MODIS-derived surface albedo regulates solar radiation absorption (Box *et al.* 2012).

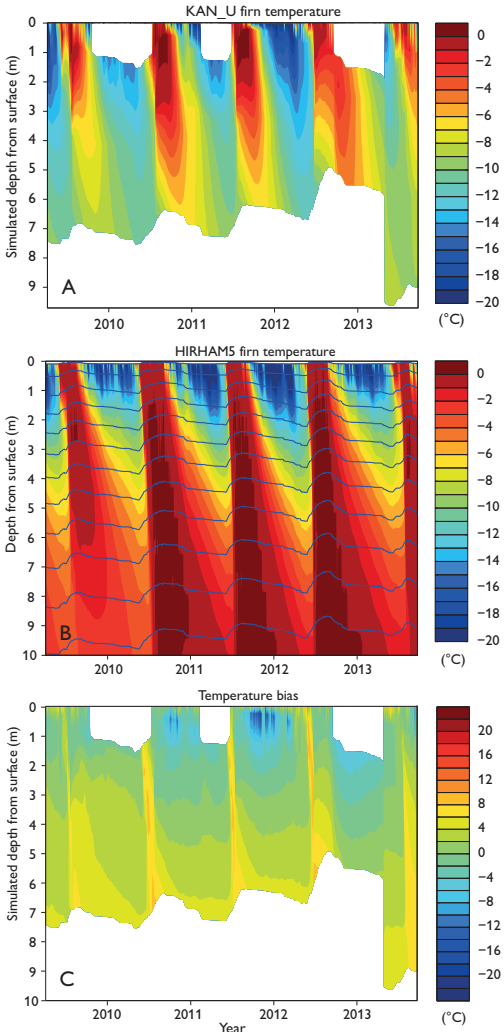

Fig. 1. **A**: Firn temperatures observed at KAN_U (Charalampidis *et al.* 2016). **B**: HIRHAM5-simulated firn temperatures at the location of KAN_U, with the blue lines indicating the simulated depth of the mid-point of each layer. **C**: The difference between the two (B minus A).

The subsurface scheme (version 7.11) uses 25 layers with a total depth of 70 m water equivalent (*c.* 78 m physical distance at KAN_U). It accounts for heat diffusion, vertical water transport and refreezing, as well as temperature, and pressure-dependent densification of snow and firn after Vionnet *et al.* (2012). Each layer can hold liquid water corresponding to 2% of the snow pore volume and excess water percolates downward to the next layer. Water is assumed to run off when it encounters a layer of pore close-off density (i.e. 830 kg/m^3; Herron & Langway 1980). Before runoff occurs, the water is available for superimposed ice formation onto the ice layer.

Simulated versus observed firn temperatures

The HIRHAM5-simulated firn temperature evolution at KAN_U is shown in Fig. 1B. A seasonality following surface forcing is evident: 0°C from summer melting and about –20°C near the surface in winter. During the melt season, the simulation shows maximum firn temperature at depths *c.* 2 m in 2009 and *c.* 9 m in 2010, and even deeper in the following years. Accordingly, the extent of the simulated temperate layer (i.e. temperatures between –1 and 0°C) increases from 6 m in summer 2009 to more than 10 m in 2010 and the following melt seasons. The propagation of the temperate conditions at depth suggests concurrent meltwater percolation, refreezing and latent heat release. However, the observed temperate layer did not extend below 3 m at any point (Fig. 1A).

The firn temperature bias (simulated minus observed) is shown in Fig. 1C by comparing the interpolated HIRHAM5 values at observational depths with the observed ones. The model bias is mostly positive and increases with depth. Typical differences for the deepest measurements range between +6 and +12°C. Negative differences occur during winter at depths less than 2 m in all years except 2012. In winter 2012, the RCM underestimates firn temperatures as deep as 3 m.

Table 1 shows the average summer and winter HIRHAM5 firn temperatures at specific depths, and the biases. The summer difference averaged over all available depths is +5.7°C. Better agreement between HIRHAM5 and observations is found for winter with an average difference of +3.2°C. In winter 2012, HIRHAM5 agreement is best, and is the only instance in the comparison when model bias at any of the listed depths was negative. This agreement is indicative of the abnormally warm conditions that persisted in the top 2–5 m firn after the extreme 2012 melt season, but also of the efficiency of the HIRHAM5 simulation of surface-heat transfer into firn.

Explaining the bias

Subsurface differences between RCM and the observations can be due to differences in surface melt, quantity and depth of meltwater percolation and the timing of refreezing.

Table 1. Average HIRHAM5 firn temperatures, linearly interpolated to specific depths (left columns) and biases (right columns) at KAN_U (Charalampidis *et al.* 2016)

Depth	2009		2010		2011		2012		2013	
Summer temperatures (°C; June–July–August)										
2 m	–2.9	+3.1	–0.4	+4.3	–1.9	+3.5	–0.3	+5.3	–4.2	+3.5
3 m	–3.6	+4.7	–1.0	+5.5	–2.3	+4.7	–1.1	+5.9	–4.4	+4.5
4 m	–3.6	+6.1	–1.5	+6.5	–2.3	+6.0	–1.4	+6.9	–4.1	+5.1
5 m	–3.6	+6.3	–1.7	+7.1	–2.1	+6.8	–1.3	–	–3.6	+5.7
6 m	–3.4	+6.7	–1.8	+7.9	–1.7	+7.7	–1.2	–	–3.0	+6.4
Following winter temperatures (°C; December–January–February)										
2 m	–9.5	+3.2	–8.9	+0.7	–12.2	+0.3	–8.7	–2.0	–	–
3 m	–6.5	+4.6	–5.9	+1.7	–8.4	+2.2	–6.0	+0.1	–	–
4 m	–4.6	+5.1	–3.8	+3.2	–5.5	+4.1	–4.0	+1.9	–	–
5 m	–3.4	+5.9	–2.3	+4.7	–3.3	+5.7	–2.6	+3.2	–	–
6 m	–2.7	+6.4	–1.2	+5.8	–1.9	+6.4	–1.6	–	–	–

The comparison of HIRHAM5 with a validated SEB model forced by *in situ* observation data (Charalampidis *et al.* 2015) shows good agreement in simulated melt estimates (Fig. 2A). HIRHAM5 slightly underestimates melt in all years (differences less than 31 MJ/m^2) except 2011 (excess of 7 MJ/m^2). The cumulative difference in melt energy between the two models over the course of five melt seasons amounts to 68 MJ/m^2, approximately equal to the total melt in July 2013. This suggests that the positive firn temperature biases are not due to exaggerated melt.

HIRHAM5 substantially underestimates refreezing (Fig. 2B). The differences are less than 15% in all years except 2012, when the difference is 44% and approximately equal to total refreezing in 2013 (380 kg/m^2). With well-simulated melt and underestimated refreezing by HIRHAM5, the firn temperature bias is due to prolonged wintertime refreezing at great depth. As a result of the overestimated latent heat release at depth during every year, HIRHAM5 wintertime low temperature extremes remain at depths no greater than *c.* 3 m (Fig. 1B).

Both HIRHAM5 and Charalampidis *et al.* (2015) overestimate the percolation depth. As analysed by Charalampidis (2016), the SEB model captures the thermal evolution of firn well. The model was initialised on 4 April 2009 based on firn temperature observations, and height-corrected 2012 firn densities, thus calculating realistic cold content (i.e. the required energy to raise firn temperature at 0°C) and heat diffusion estimates throughout the 4.5-year simulation. The SEB model does not calculate liquid water retention, thus all percolating meltwater is refrozen at every time step, which is incorrect close to the surface (2–3 m depth; Fig. 1A). However, no refreezing (i.e. no latent heat release) after the melt season at depth results in more realistic wintertime cooling of deep firn.

HIRHAM5 was initiated more than two decades before 2009. Additionally, the current subsurface scheme of HIRHAM5 cannot reproduce ice layers. This inability results in unrealistic representation of firn stratigraphy, and thus estimation of cold content, which is dependent on firn temperature and density. On 4 April 2009, the thermal state of the subsurface in HIRHAM5 is the integrated result of all previous simulation years, and is already on average 4.6°C too warm in the upper 10 m of firn (Fig. 1C). The associated cold content integrated over the first 10 m is 72 MJ/m^2. By

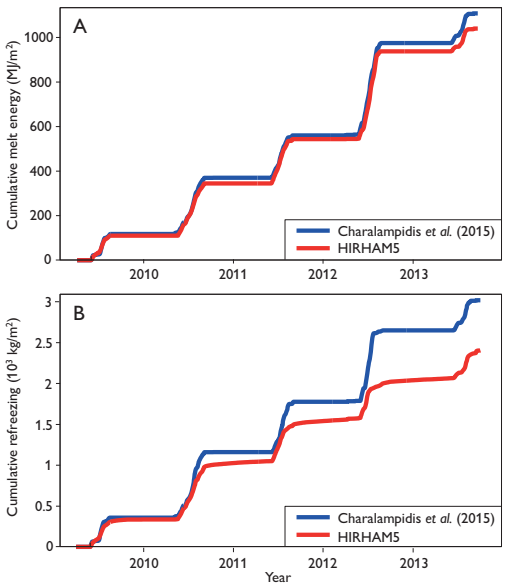

Fig. 2. Cumulative melt energy (**A**) and total refreezing (**B**) at KAN_U by HIRHAM5 and Charalampidis *et al.* (2015).

comparison, the cold content on the same day in Charalampidis *et al.* (2015) is 151 MJ/m^2. One third of the difference in cold content is due to differences in firn density.

Near-complete cold content depletion (i.e. firn temperature at 0°C) of the first 10 m of firn is simulated by HIRHAM5 for 2010. Thereafter, this temperate firn retains liquid water, which refreezes during winter under the influence of subfreezing conditions diffused from the surface. This results in wintertime latent heat release at depth that in 2010 to 2012 is sustained until the beginning of the following melt season (Fig. 2B). Eventually, this premature depletion of cold content leads to overestimation of the percolation depth, liquid water retention and heat in firn.

Concluding remarks

Judging from the simulation of wintertime firn temperatures in the period April 2009 to September 2013, HIRHAM5 is able to realistically reproduce subsurface processes when heat conduction dominates. Yet the comparison of HIRHAM5 with observations and SEB model output reveals an overestimation of the percolation depth, liquid water retention and heat input from refreezing.

For April 2009, HIRHAM5 calculates less than half of the cold content estimate based on observations in the first 10 m of firn. This is the result of the 1989 initialisation of HIRHAM5 and thus the cumulative effect of the imprecise determination of heat diffusion, as HIRHAM5 is unable to adequately represent ice-layer formation in firn. A HIRHAM5 subsurface scheme with improved accounting of shallow firn stratigraphy would greatly improve heat diffusion estimates over long simulation periods, and thus provide more reliable simulations.

Acknowledgements

The KAN_U weather station is funded by the Greenland Analogue Project, with contributions from the Programme for Monitoring of the Greenland Ice Sheet (PROMICE). This is a PROMICE publication and contribution number 76 of the Nordic Centre of Excellence SVALI, 'Stability and Variations of Arctic Land Ice', funded by the Nordic Top-level Research Initiative (TRI). The study has been supported by the Danish Council for Independent research (DFF) project 4002-00234 'Understanding and predicting non-linear change in the permeability of Greenland firn'.

References

Box, J.E., Fettweis, X., Stroeve, J.C., Tedesco, M., Hall, D.K. & Steffen, K. 2012: Greenland ice sheet albedo feedback: thermodynamics and atmospheric drivers. The Cryosphere **6**, 821–839.

Charalampidis, C. 2016: Climatology and firn processes in the lower accumulation area of the Greenland ice sheet. Digital comprehensive summaries of Uppsala Dissertations from the Faculty of Science and Technology **1372**, 81 pp. Acta Universitatis Upsaliensis, Uppsala, Sweden.

Charalampidis, C., van As, D., Box, J.E., van den Broeke, M.R., Colgan, W.T., Doyle, S.H., Hubbard, A.L., MacFerrin, M., Machguth, H. & Smeets, C.J. 2015: Changing surface–atmosphere energy exchange and refreezing capacity of the lower accumulation area, West Greenland. The Cryosphere **9**, 2163–2181.

Charalampidis, C., van As, D., Colgan, W.T., Fausto, R.S., Macferrin, M. & Machguth, H. 2016: Thermal tracing of retained meltwater in the lower accumulation area of the southwestern Greenland ice sheet. Annals of Glaciology, available on CJO2016, *http://dx.doi.org/10.1017/aog.2016.2*

Christensen, O.B., Drews, M., Christensen, J.H., Dethloff, K., Ketelsen, K., Hebestadt, I. & Rinke, A. 2006: The HIRHAM regional climate model version 5. Danish Meteorological Institute Technical Report **06–17**, 22 pp. Copenhagen: Danish Meteorological Institute.

Dee, D.P. *et al.* 2011: The ERA-Interim reanalysis: configuration and performance of the data assimilation system. Quarterly Journal of the Royal Meteorological Society **137**, 553–597.

Harper, J., Humphrey, N., Pfeffer, W.T., Brown, J. & Fettweis, X. 2012: Greenland ice-sheet contribution to sea-level rise buffered by meltwater storage in firn. Nature **491**, 240–243.

Herron, M.M. & Langway, C.C. 1980: Firn densification: an empirical model. Journal of Glaciology **25**(93), 373–385.

Khan, S.A., Aschwanden, A., Bjørk, A.A., Wahr, J., Kjeldsen, K. & Kjær, K. 2015: Greenland ice sheet mass balance: a review. Reports on Progress in Physics **78**(4), 046801.

Langen, P.L. *et al.* 2015: Quantifying energy and mass fluxes controlling Godthåbsfjord freshwater input in a 5-km simulation (1991–2012). Journal of Climate **28**, 3694–3713.

Machguth, H., MacFerrin, M., van As, D., Box, J.E., Charalampidis, C., Colgan, W., Fausto, R.S., Meijer, H.A.J., Mosley-Thompson, E. & van de Wal, R.S.W. 2016: Greenland meltwater storage in firn limited by near-surface ice formation. Nature Climate Change **6**, 390–393.

Van de Wal, R.S.W., Boot, W., Smeets, C.J.P.P., Snellen, H., van den Broecke, M.R. & Oerlemans, J. 2012: Twenty-one years of mass balance observations along the K-transect, West Greenland. Earth System Science Data **4**, 31–35.

Vionnet, V., Brun, E., Morin, S., Boone, A., Faroux, S., Le Moigne, P., Martin, E. & Willemet, J.-M. 2012: The detailed snowpack scheme Crocus and its implementation in SURFEX v7.2. Geoscientific Model Development **5**, 773–791.

Authors' addresses

C.C., D.v.A., R.S.F., B.V. & J.E.B., *Geological Survey of Denmark and Greenland, Øster Voldgade 10, DK-1350 Copenhagen K.* E-mail: *cc@geus.dk*

P.L.L., *Climate and Arctic Research, Danish Meteorological Institute, Lyngbyvej 100, DK-2100 Copenhagen Ø, Denmark.*

C.C., also at: *Department of Earth Sciences, Uppsala University, Villavägen 16, SE-752 36 Uppsala, Sweden.*

B.V., also at: *Arctic Technology Centre (ARTEK), Technical University of Denmark, Brovej, byg. 118, DK-2800 Kgs. Lyngby, Denmark.*

APPENDIX C

Paper III

frontiers in Earth Science

METHODS
published: 07 May 2018
doi: 10.3389/feart.2018.00051

A Snow Density Dataset for Improving Surface Boundary Conditions in Greenland Ice Sheet Firn Modeling

Robert S. Fausto[1], Jason E. Box[1], Baptiste Vandecrux[1,2], Dirk van As[1], Konrad Steffen[3,4,5], Michael J. MacFerrin[6], Horst Machguth[7,8], William Colgan[1,6], Lora S. Koenig[9], Daniel McGrath[10], Charalampos Charalampidis[11] and Roger J. Braithwaite[12]*

[1] Geological Survey of Denmark and Greenland, Copenhagen, Denmark, [2] Arctic Technology Centre, Technical University of Denmark, Lyngby, Denmark, [3] Swiss Federal Research Institute WSL, Birmensdorf, Switzerland, [4] Swiss Federal Institute of Technology, Zurich, Switzerland, [5] Swiss Federal Institute of Technology, Lausanne, Switzerland, [6] Cooperative Institute for Research in Environmental Sciences, University of Colorado Boulder, Boulder, NV, United States, [7] Department of Geography, University of Zurich, Zurich, Switzerland, [8] Department of Geosciences, University of Fribourg, Fribourg, Switzerland, [9] National Snow and Ice Data Center, University of Colorado, Boulder, NV, United States, [10] Geosciences Department, Colorado State University, Fort Collins, CO, United States, [11] Bavarian Academy of Sciences and Humanities, Munich, Germany, [12] University of Manchester, Manchester, United Kingdom

OPEN ACCESS

Edited by:
Timothy C. Bartholomaus, University of Idaho, United States

Reviewed by:
Xavier Fettweis, University of Liège, Belgium
Marco Möller, University of Bremen, Germany
Clément Miège, University of Utah, United States

***Correspondence:**
Robert S. Fausto
rsf@geus.dk

Specialty section:
This article was submitted to Cryospheric Sciences, a section of the journal Frontiers in Earth Science

Received: *13 October 2017*
Accepted: *18 April 2018*
Published: *07 May 2018*

Citation:
Fausto RS, Box JE, Vandecrux B, van As D, Steffen K, MacFerrin MJ, Machguth H, Colgan W, Koenig LS, McGrath D, Charalampidis C and Braithwaite RJ (2018) A Snow Density Dataset for Improving Surface Boundary Conditions in Greenland Ice Sheet Firn Modeling. Front. Earth Sci. 6:51. doi: 10.3389/feart.2018.00051

The surface snow density of glaciers and ice sheets is of fundamental importance in converting volume to mass in both altimetry and surface mass balance studies, yet it is often poorly constrained. Site-specific surface snow densities are typically derived from empirical relations based on temperature and wind speed. These parameterizations commonly calculate the average density of the top meter of snow, thereby systematically overestimating snow density at the actual surface. Therefore, constraining surface snow density to the top 0.1 m can improve boundary conditions in high-resolution firn-evolution modeling. We have compiled an extensive dataset of 200 point measurements of surface snow density from firn cores and snow pits on the Greenland ice sheet. We find that surface snow density within 0.1 m of the surface has an average value of 315 kg m^{-3} with a standard deviation of 44 kg m^{-3}, and has an insignificant annual air temperature dependency. We demonstrate that two widely-used surface snow density parameterizations dependent on temperature systematically overestimate surface snow density over the Greenland ice sheet by 17–19%, and that using a constant density of 315 kg m^{-3} may give superior results when applied in surface mass budget modeling.

Keywords: snow surface density, firn, Greenland, parameterization, surface mass budget, model boundary condition

INTRODUCTION

The mass budget of the Greenland ice sheet has grown increasingly negative during the past two decades (e.g., Kjeldsen et al., 2015; Van den Broeke et al., 2016). There is a strong impetus to constrain critical processes in order to reduce uncertainties in mass balance estimates (e.g., Shepherd et al., 2012; IPCC, 2013; Khan et al., 2015). In particular, an improved understanding of

ice-sheet-wide snow and firn properties can reduce uncertainties in: remotely-sensed or modeled ice sheet mass budget (e.g., Van den Broeke et al., 2016), identifying internal layers for calculating accumulation rates from combined radar and firn core surveys (Hawley et al., 2006, 2014; de la Peña et al., 2010; Miège et al., 2013; Karlsson et al., 2016; Koenig et al., 2016; Overly et al., 2016; Lewis et al., 2017), and quantifying meltwater retention (Harper et al., 2012; Humphrey et al., 2012; Machguth et al., 2016) and accumulation rates (López-Moreno et al., 2016; Schaller et al., 2016) from firn cores and snow pits. Improved estimates of surface snow density, which serves as an important boundary condition in firn densification modeling, can reduce uncertainties in mass budget studies (e.g., Sørensen et al., 2011; Csatho et al., 2014; Hurkmans et al., 2014; Morris and Wingham, 2014; Colgan et al., 2015) that convert remotely-sensed volume changes to mass changes based on either depth-density profile relations or surface snow density parameterizations. Ice sheet models that assess the surface mass budget, such as SICOPOLIS (Greve et al., 2011) or PISM (Aschwanden et al., 2012), are also limited by uncertainties in surface snow density. Fausto et al. (2009) found that the inclusion of firn densification in SICOPOLIS through a physical description of the retention capacity yields a 10% increase in the accuracy of the present-day surface mass budget.

Regional climate models calculate firn densification (e.g., Vionnet et al., 2012; Langen et al., 2015; Steger et al., 2017), but are limited by uncertainties in surface snow density feeding into their subsurface schemes. Some models use surface snow density parameterizations based on temperature to implicitly account for spatiotemporal variability (e.g., Reeh et al., 2005; Kuipers Munneke et al., 2015). Other models use parameterizations that depend on wind speed (e.g., Gallée et al., 2013) or a combination of air temperature and wind speed (e.g., Vionnet et al., 2012), while for instance Langen et al. (2015) used a constant surface snow density value.

The parameterizations based on temperatures rely on *in-situ* firn measurements with a coarse vertical resolution. For instance, Reeh et al. (2005) used a firn model to infer surface snow density from the 10-m firn temperature and depth-density profiles, while Kuipers Munneke et al. (2015) used the average density of the top meter of snow/firn, which would systematically overestimate surface snow density in regional climate model studies (Steger et al., 2017) if interpreted as the surface value. Most firn-evolution models operate at a centimeter-scale vertical resolution, requiring a surface snow density boundary condition derived at a resolution finer that 1 m. Using observational data sampled at high vertical resolution, one can derive the true surface value and avoid systematically overestimating surface snow density and consequently the density of the entire firn column. More accurate firn density-depth profiles yield improvements for mass budget studies of the Greenland ice sheet (e.g., Li and Zwally, 2011; Ligtenberg et al., 2011; Simonsen et al., 2013; Csatho et al., 2014; Overly et al., 2016; Steger et al., 2017).

The aim of this study is to present a spatially extensive density dataset for the Greenland ice sheet derived from 200 density-profile measurements, and to investigate the observed spatiotemporal variability for the top 0.1 m of snow/firn. In an application of this dataset, we quantify the performance of the observation-based temperature-dependent surface snow density parameterizations by Kuipers Munneke et al. (2015) and Reeh et al. (2005) that are often used as boundary conditions in surface mass budget studies of the Greenland ice sheet (e.g., Csatho et al., 2014; Steger et al., 2017).

METHODS

Dataset

Our surface density dataset consists of 200 point observations, along with the geographic location, annual air temperature and annual accumulation rate for these locations. The oldest surface density data were collected by Benson (1962) in 1954 in Northwest Greenland at latitudes between 70° to 77° N (Appendix C). These measurements include annual accumulation rates and 10 m firn temperatures reported by Mock and Weeks (1965) (Appendix A). Data from both the percolation and ablation areas of the southern and western ice sheet sections near 61.3° N (Nordbo Gletscher) and 69.7° N (Paakitsoq), respectively, were collected by Braithwaite et al. (1982, 1994). Our dataset also includes data from the Program for Arctic Regional Climate Assessment (PARCA) (Mosley-Thompson et al., 2001; Thomas and Investigators, 2001). Further, the SUrface Mass balance and snow depth on sea ice working grouP (SUMuP) provided accumulation rates, snow depths and density values at various sites on the ice sheet (Koenig et al., 2013; Montgomery et al., 2018), including observations from a study of Greenland accumulation (Hawley et al., 2014) and firn aquifers (Forster et al., 2013; Koenig et al., 2014; Miège et al., 2016). We gathered annual air temperatures, accumulation rates, and density observations from snow pits and firn cores from the Greenland Climate Network (GC-Net) (Steffen et al., 1996), the Programme for Monitoring of the Greenland Ice Sheet (PROMICE) (Van As et al., 2016b), and the Arctic Circle Traverses (ACTs) (e.g., Machguth et al., 2016). Lastly, we also included observations by Schaller et al. (2016) from the NEEM to EGRIP traverse, and from the López-Moreno et al. (2016) Greenland circumnavigation. Accumulation rates in the database are not long-term averages, but represent the preceding year's snowfall. **Figure 1** provides a map of all measurement locations. All data are available as Supplementary Material. **Figure 2a** illustrates that 28% of the observations were taken in the mid-1950s, only 2% were taken in the 1980s and 1990s, while 70% were obtained between 1999 and 2016. 94% of the measurements were gathered at elevations exceeding 1,000 m above sea level (**Figure 2d**).

Defining the surface layer as the upper 0.1 m of snow yields that in most cases the surface layer was deposited in multiple snowfall events, except for areas located at relatively low elevations in the south and southeast of the ice sheet, where individual precipitation events typically produce more than 0.1 m of snow (Burgess et al., 2010). Where possible, the annual air temperature was calculated as the average over the 365 days prior to the date for which the surface snow density was determined. Where air temperature measurements are not available, i.e., for the older data by Benson (1962) and Braithwaite et al. (1994),

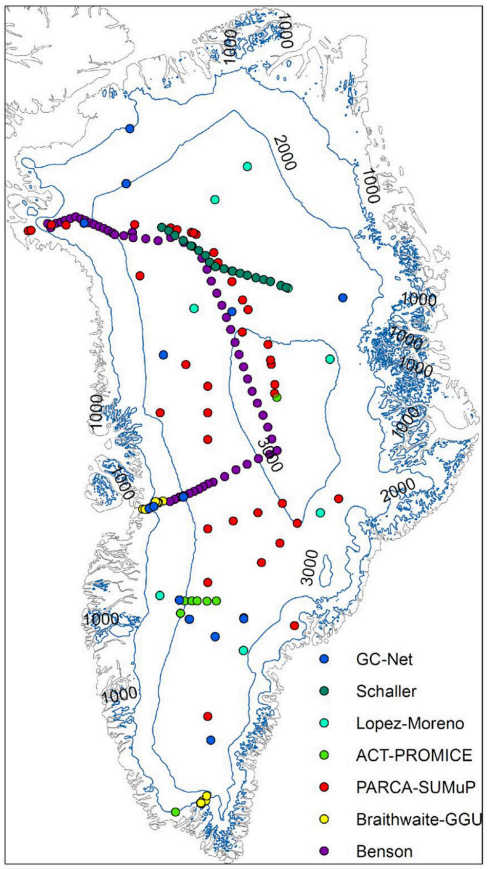

FIGURE 1 | Locations of all surface snow density measurement locations in our dataset. Contours lines indicate elevations in meters above sea level.

but firn-core temperatures were, we use 10 m firn temperature as annual air temperature following e.g., Reeh et al. (2005), Polashenski et al. (2014), and Kuipers Munneke et al. (2015). This is a fair approximation since 10 m firn temperatures reflect the conductive temperature wave propagation in places with little or no melt (Benson, 1962). Though valid for the earlier observations in our dataset, recent increases in ice sheet melt area have reduced the dry snow facies of the ice sheet (McGrath et al., 2013) and therefore the applicability of this methodology.

Commonly, snow/firn was sampled in snow pits using a fixed volume cutter at 0.05–0.1 m vertical resolution. These samples were weighed using a variety of scales. When density data were derived from a core, the snow was extracted from the core barrel and typically sub-sampled into 0.1 m sections before being weighed. Conger and McClung (2009) investigated measurement errors of several different density cutters and conclude that measurement accuracy was within 3–12%. They also conclude that the absolute measurement uncertainty is within 11% of true density. A discussion of density cutters by Proksch et al. (2016) reaches a similar uncertainty of 9%. For the data in our database, sampling uncertainty is not documented in any of the field campaigns, however it seems reasonable to assume that surface snow density is known within 10%. Typically, this measurement uncertainty is smaller than the spatial variability in surface snow density in the vicinity of the measurement location (e.g., Proksch et al., 2015). We argue that the point measurements in our dataset do not represent fresh snow, as the persistent katabatic winds in Greenland compact surface snow within days after snowfall (e.g., Liston et al., 2007).

Firn Model Initialization

We test a surface snow density parameterization for the Greenland ice sheet that is dependent on temperature, similar to commonly used parameterizations by Kuipers Munneke et al. (2015) and Reeh et al. (2005). We assume a linear dependence of surface snow density (ρ) in kg m^{-3} on annual air temperature (T_a) in °C, in what we refer to as parameterization P1:

$$\rho = A + B \cdot T_a \quad (1)$$

We determine the fit coefficients by orthogonal linear regression to all available T_a values in our dataset, and find a best fit for A = 362.1 and B = 2.78 (**Table 1**) for the top 0.1 m of snow. Kuipers Munneke et al. (2015) determined the coefficients of Equation (1) using annual surface temperature T_s in °C simulated by RACMO2.3 and the average density of the uppermost 1 m of snow/firn, and found what we here refer to as parameterization P2:

$$\rho_{KM15} = 481 + 4.834 \cdot T_s \quad (2)$$

Reeh et al. (2005) derived surface snow density as a function of the 10-m firn temperature (T_f) from the near-surface part of their depth-density profiles by determining the load at 5 m depth, as calculated by their model, so that it fits the corresponding load derived from the measured depth-density profiles (parameterization P3):

$$\rho_{R05} = 625 + 18.7 \cdot T_f + 0.293 \cdot T_f^2 \quad (3)$$

There is a ca. 40% overlap between our dataset and the data feeding into the Kuipers Munneke et al. (2015) and Reeh et al. (2005) parameterizations that stems from them also using the Benson (1962), Braithwaite et al. (1994), and PARCA (Mosley-Thompson et al., 2001) datasets.

To highlight the importance of sampling depth ranges in producing an observationally-based boundary condition for firn models in Greenland, we also test P1 (Equation 1) using the average density of the top 0.2 and 0.5 m of snow/firn in our analysis (**Table 1**). We theorize that, by using density data obtained as close to the surface as possible, we avoid introducing a systematic bias due to compaction. Yet by focusing only on the top layer of snow/firn, we likely introduce more scatter in our results due to additional variability by single weather events. We investigate such considerations below.

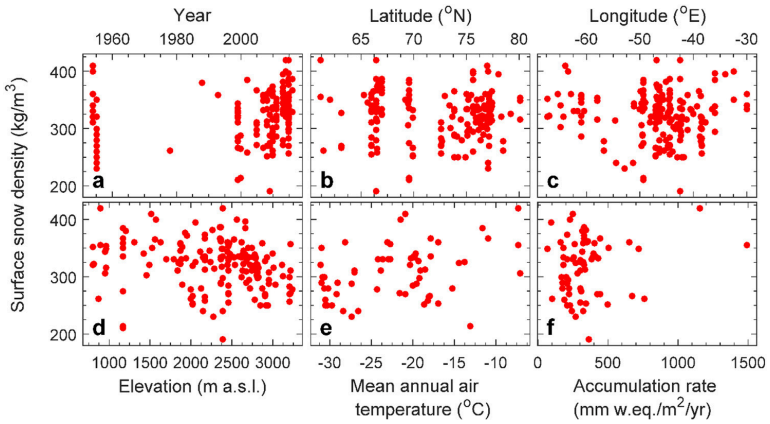

FIGURE 2 | Density of the top 0.1 m of snow plotted against site- and campaign-specific parameters: **(a)** year, **(b)** latitude, **(c)** longitude, **(d)** elevation, **(e)** annual mean near-surface air temperature, and **(f)** accumulation rate.

TABLE 1 | Fit coefficients and statistics for parameterization P1 (Equation 1).

Depth range (m)	A	B	Correlation (R^2)	Number of observations
0–0.1	362.1	2.78	0.12	91
0–0.2	363.0	2.21	0.14	91
0–0.5	358.4	1.30	0.08	91

RESULTS

Surface snow density in our 200-value database ranges between 190 and 420 kg m^{-3}, with an average of 315 kg m^{-3} and associated standard deviation of 44 kg m^{-3} (**Figure 3**, **Table 2**). Using the 10% measurement uncertainty range chosen in the methods section, we determine the average uncertainty to be ± 32 kg m^{-3}. The measurement uncertainty is smaller than the 44 kg m^{-3} standard deviation, which demonstrates a significant natural variability in the top 0.1 m of snow most likely due to differences in precipitation events and influences from weather in general. Yet the variability in surface snow density could also depend on location or annual air temperature as investigated below.

There is no significant temporal trend in surface snow density (**Figure 2a**), indicating that the relatively large timespan over which measurements were collected does not introduce a bias. **Figure 2** also illustrates that surface snow density is not significantly correlated with latitude, longitude, elevation, nor annual accumulation rate. Remarkably, also annual air temperature does not prove to be a strong predictor of surface snow density (**Figure 2e**). Even in a stepwise linear regression we find that no combination of variables in our database adequately predicts the surface snow density (results not presented). We quantify the poor predictive skill of annual air temperature in all three parameterizations in **Table 3**, showing root mean square error (RMSE) values for the top 0.1 m of snow to be 42–84 kg m^{-3}, with mean biases of + 19% (P2) and +17% (P3). For the 0–0.1 m depth range, RMSE values for P2 and P3, are respectively a factor of 2.0 and 1.8 higher than those for our P1 parameterization (**Table 3**).

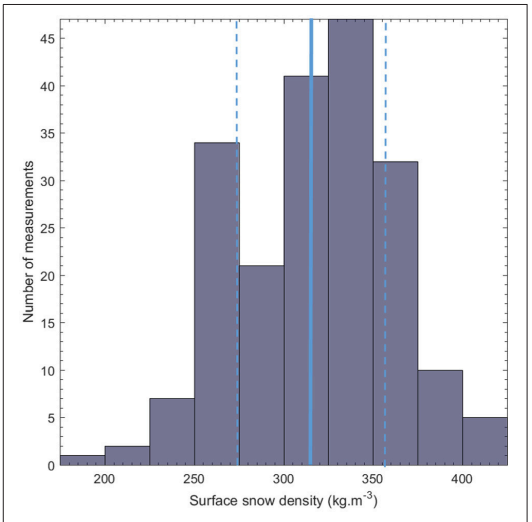

FIGURE 3 | Number of surface snow density measurements over the Greenland ice sheet. Blue solid and dashed lines indicate the average and standard deviation of the dataset, respectively.

TABLE 2 | Surface snow density dataset metadata for three depth ranges.

Depth range (m)	0–0.1	0–0.2	0–0.5
Number of observations	200	206	231
Minimum (kg m^{-3})	191	170	256
Maximum (kg m^{-3})	420	478	510
Average (kg m^{-3})	315	324	341
Median (kg m^{-3})	321	325	336
Standard deviation (kg m^{-3})	44	41	37

TABLE 3 | Root-mean-square error (RMSE), mean bias and RMSE ratio values for parameterizations using annual mean air temperature: P1 (this study), P2 (Kuipers Munneke et al., 2015) and P3 (Reeh et al., 2005).

ρ parameterization	Depth range (m)	RMSE (kg m^{-3})	Mean bias (kg m^{-3})	RMSE ratio P2/P1	RSME ratio P3/P1
P1	0–0.1	42	0	2.0	1.8
P1	0–0.2	30	0	2.2	2.1
P1	0–0.5	24	0	2.2	2.1
P2	0–0.1	84	72 (19%)	–	–
P2	0–0.2	67	58 (15%)	–	–
P2	0–0.5	53	42 (11%)	–	–
P3	0–0.1	76	62 (17%)	–	–
P3	0–0.2	63	48 (13%)	–	–
P3	0–0.5	50	32 (8%)	–	–

Average snow/firn density increases from 315 to 341 kg m^{-3} as the averaging depth range increases from 0.1 to 0.5 m (**Table 2**). Simultaneously, the standard deviation decreases indicative of a reduction in small-scale spatial variability (**Table 2**), i.e., differences in snow/firn density profiles are growing smaller due to compaction and as the relative influence of single weather events reduces. As a result of using larger depth ranges yielding larger average densities, the performance of parameterizations P2 and P3 increases judging from reducing RMSE values, but they still overestimate the average density of the top 0.5 m of snow/firn by 11% (P2) and 8% (P3) (**Table 3**). Even taking into account that T_a (Equation 1) typically exceeds T_s (Equation 2) by a few degrees does not make up for more than 10 kg m^{-3} of the P2 overestimate.

Figure 4 illustrates the dependence of surface snow density on annual air temperature for the top 0.1, 0.2, and 0.5 m of snow/firn, confirming that (1) air temperature is a poor predictor of surface snow density, (2) variability of surface snow density decreases with increasing depth range, (3) existing temperature-based parameterizations tend to overestimate surface snow density, (4) especially for snow density nearest the surface, and revealing that (5) the predictive skill of parameterizations P2 and P3 is poorest for annual temperatures exceeding −20°C. Consequently, we judge that using a single constant value to represent surface snow density on the Greenland ice sheet may be preferred over using a temperature-dependent parameterization.

DISCUSSION

Depth Range

We use a smaller depth range to better represent surface snow density than previous studies. Assessing density closer to the surface is important for producing a more accurate upper boundary condition to be used in firn evolution models that would produce too high firn densities along the entire depth profile. **Figure 4**, **Table 3** confirm that using relatively large depth ranges in determining a surface snow density parameterization results in overestimated values by Kuipers Munneke et al. (2015) and Reeh et al. (2005). Our smallest tested depth range of 0–0.1 m reveals larger natural variability, but would not introduce a considerable systematic bias in firn evolution modeling even if a vertical grid resolution finer than 0.1 m is used. In surface mass balance modeling, the choice of vertical resolution of the subsurface directly influences the calculation of key variables, such as the meltwater retention capacity of the snow/firn column. The more variable density in the top 0.1 m of snow compared to the top 0.2 m (factor of 1.4 more variable) or 0.5 m (1.8), is due to the influence of single precipitation events and subsequent weather forcing. We contend that this increased variability is preferable over the introduction of a systematic bias in surface mass balance modeling.

The top of the snowpack compacts rapidly after snowfall (e.g., Brun et al., 1997; Liston et al., 2007), as the crystal structure of freshly deposited snow breaks down within days due to wind and redistribution of drifting snow (e.g., Kotlyakov, 1961; Kojima, 1967; Pahaut, 1976). Surface snow densification by wind, which generally only influences the top 0.1 m, becomes insignificant after a few days (Brun et al., 1997). For most or all observations in our dataset, we can safely assume that wind compaction has occurred already. Therefore, our dataset and resulting products should not be used in models to prescribe or validate fresh snow densities (e.g., Vionnet et al., 2012), but rather to define the upper boundary condition (i.e., minimum density) in firn evolution models that do not calculate micro-scale snow physics and densification by wind, snow drift and redistribution.

In regions where large snowfall events occur, such as in south Greenland, density measurements of the top 0.1 m of snow may reflect the conditions during one snowfall event and subsequent weather-dependent densification prior to measurement. All of the snow-density measurements in our database were taken in spring and summer, meaning that our average and parameterization may be seasonally biased. Dibb and Fahnestock (2004) investigated the seasonality of the surface snow density at Summit in Greenland, and found a seasonal standard deviation of 30% in density in the top 0.03 m of snow as determined from 22 measurements during a two-year period. However, seasonal variation in the surface snow density is likely to increase with elevation (Brun et al., 1997) with standard deviation values lower than 30% in regions away from the three dome sites in Greenland where persistent katabatic winds and their influence on snow compaction do not occur (e.g., Noël et al., 2014). In general, katabatic winds are strongest in winter due to surface radiative cooling, and at lower elevations (below 2,000 m above sea level) due to larger surface slopes (e.g., Van As et al., 2013; Noël et al.,

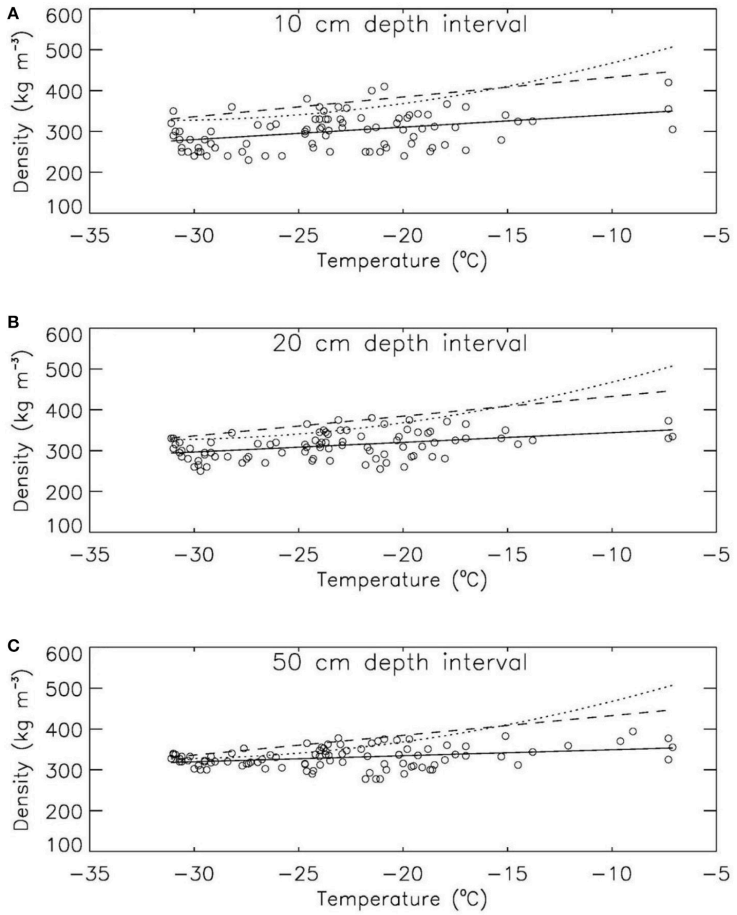

FIGURE 4 | Orthogonal linear regression fits (solid lines) for temperature-dependent parameterization P1 (**Table 1**) for **(A)** depth range 0–0.1 m, **(B)** depth range 0–0.2 m, and **(C)** depth range 0–0.5 m. Circles represent our observational dataset. Parameterizations by Kuipers Munneke et al. (2015) and Reeh et al. (2005) are plotted as dashed and dotted lines, respectively.

2014), resulting in wind-packing of fresh surface snow within days.

Temperature Dependence

Higher air temperatures result in higher snow and firn densities through increased compaction (Zwally and Li, 2002). It is therefore desirable to ensure that parameterizations of surface snow density remain appropriate even as the climate changes (e.g., Reeh et al., 2005; Morris and Wingham, 2014). Studies of Greenland accumulation rates and firn properties document a recent densification in the overall firn column and attribute it to climate warming (e.g., de la Peña et al., 2015; Charalampidis et al., 2016a; Machguth et al., 2016; Overly et al., 2016). If we assume that temperature-dependent densification processes are responsible for the transformation of freshly-fallen snow to the surface snow densities of our dataset, the inclusion of temperature as a variable in a parameterization (Equation 1) explicitly accounts for atmospheric warming. In this case, a parameterization is better capable of representing changing surface conditions due to climate variability. For instance, our temperature-dependent parameterization suggests that the observed 2.7°C warming at Summit over the period 1982–2011 (McGrath et al., 2013) had lead to a local surface snow density increase of 8 kg m^{-3}. But even a large temperature increase of 10°C anywhere in Greenland would only cause a densification of 28 kg m^{-3} in the top 0.1 m of snow, which

is smaller than the 32 kg m^{-3} measurement uncertainty and 44 kg m^{-3} standard deviation of the dataset (**Table 2**). For larger depth ranges the temperature sensitivity (*B*-values in P1, see **Table 2**) is considerably smaller and thus more insignificant given the measurement uncertainty and natural variability. The insignificant densification as a result of warming supports the notion that temperature is a poor predictor of the variability of surface snow density in the top 0.1, 0.2, and 0.5 m of snow/firn, and that using a constant value may be preferable in some applications.

Modeling Implications and Limitations

The choice of a surface snow density boundary condition influences calculations of available pore space by models simulating the surface mass budget of the Greenland ice sheet. Steger et al. (2017) discussed the limitations and inaccuracies of their Greenland ice sheet surface mass budget simulations by regional climate model RACMO2.3, and conclude that the Kuipers Munneke et al. (2015) parameterization systematically overestimates surface snow density, impacting pore space available for refreezing at depth. Langen et al. (2015) and Charalampidis et al. (2016b) applied a constant surface snow density value of 330 kg m^{-3} in regional climate model HIRHAM5, while Langen et al. (2017) applied a parameterization depending on latitude, longitude and elevation, derived from our dataset, in a new model version. The latter study found that the parameterization yields an ice-sheet-wide average of surface snow density that is 7% lower than using a constant density value of 330 kg m^{-3}, signifying a higher meltwater retention capacity in the snow and firn. Langen et al. (2017) also documented that the firn density profiles simulated by HIRHAM5 using their parameterization satisfactorily resemble measured profiles. Yet based on our own findings we suspect that using a constant surface snow density value of 315 $\pm$ 32 kg m^{-3} as boundary condition, a value 5% lower than that used by Langen et al. (2015), should perform equally well in Greenland-wide surface mass budget simulations.

Using our dataset for the top 0.1 m of snow, as opposed to using those for larger depth ranges, comes at the cost of a higher variability (standard deviation in **Table 2**) due to a larger influence of meteorology-dependent processes like snow drift (Brun et al., 1997; Hörhold et al., 2011; Koenig et al., 2016). The larger variability could also stem from snowfall events depositing more than 0.1 m of snow. Layers below the top 0.1 m are not much influenced by wind compaction, snow drift and redistribution, and will primarily be subject to the less efficient densification through rounding or settling of snow grains from vapor fluxes in the subsurface layers (e.g., Albert and Shultz, 2002). Surface mass budget models using our constant value of 315 kg m^{-3} for the top 0.1 m of snow may therefore misrepresent relatively low-density layers below 0.1 m depth deposited during large snowfall events. Regions where snowfall may exceed 0.1 m in single events are typically located at lower elevations on the southern and southeastern parts of the ice sheet (e.g., Burgess et al., 2010).

Our dataset has sparse coverage in the northern and eastern sectors of the ice sheet, possibly introducing a spatial bias in our results. **Figure 5** illustrates that the elevation distribution of our measurement locations broadly reflects the overall area-elevation distribution of the ice sheet as determined from the GIMP digital elevation model (Howat et al., 2014). Some lower elevation ranges (1,000–1,750 m above sea level) are relatively underrepresented in our dataset, while some higher elevation ranges are comparatively overrepresented. Our parameterization could benefit from acquiring additional measurements from elevations between 1,000 and 1,750 m above sea level, i.e., in the lower percolation area of the ice sheet (Benson, 1962). The lower percolation area is considered crucial for properly determining the surface mass budget, as firn properties influencing meltwater retention capacity vary substantially across the ice sheet (Van As et al., 2016a; Langen et al., 2017).

CONCLUSIONS

We constructed a dataset of surface snow density for the top 0.1, 0.2, and 0.5 m of snow/firn on the Greenland ice sheet based on 200 *in situ* measurements collected during the 1953–2016 timespan. We found that only the annual air temperature has a weak predictive skill of surface snow density in the construction of a temperature-dependent parameterization. Our parameterization yields surface snow densities of 32–72 kg m^{-3} (8–19%) lower than earlier parameterizations do, thus beyond the 32 kg m^{-3} measurement uncertainty range. Yet since the natural variability in surface snow density is found to be large with e.g., a 44 kg m^{-3} standard deviation for the top 0.1 m of snow, the temperature sensitivity of surface snow density is not found to be significant, indicating that an average surface snow density of 315 kg m^{-3} could be the preferred choice as a boundary

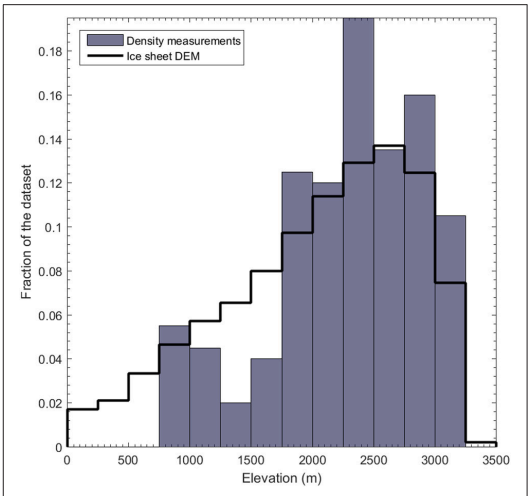

FIGURE 5 | Elevation distribution of the surface snow density measurement locations compared to the area-elevation distribution of the entire Greenland ice sheet.

condition for models calculating the surface mass budget of the Greenland ice sheet.

AUTHOR CONTRIBUTIONS

RF conceived the study and wrote the manuscript; BV and RF did the statistical analysis. All authors contributed with field data and continuously discussed the results and developed the analysis further.

ACKNOWLEDGMENTS

This work was supported by the Danish Research Council Grant FNU 4002-00234 and the Programme for Monitoring of the Greenland Ice Sheet (www.promice.dk). The author team would like to thank all the reviewers and scientific editor, T. Bartholomaus, for help and constructive criticism, which improved the manuscript significantly. We acknowledge J. T. M. Lenaerts for a collegial review and valuable comments. LK was supported by NASA Cryospheric Sciences program NASA Award NNX1 5AC62G.

SUPPLEMENTARY MATERIAL

The Supplementary Material for this article can be found online at: https://www.frontiersin.org/articles/10.3389/feart.2018.00051/full#supplementary-material

Data Sheet 1 | Surface density dataset consists of point observations (0–10, 0–20, 0–50 cm), along with the geographic location, annual air temperature and annual accumulation rates.

REFERENCES

Albert, M. R., and Shultz, E. F. (2002). Snow and firn properties and air-snow transport processes at Summit, Greenland. *Atmos. Environ.* 36, 2789–2797. doi: 10.1016/S1352-2310(02)00119-X

Aschwanden, A., Bueler, E., Khroulev, C., and Blatter, H. (2012). An enthalpy formulation for glaciers and ice sheets. *J. Glaciol.* 58, 441–457. doi: 10.3189/2012JoG11J088

Benson, C. S. (1962). Stratigraphic studies in the snow and firn of the Greenland ice sheet. *SIPRE. Res. Rep.* 70, 1–93.

Braithwaite, R. J., Clement, P., and Clausen, H. (1982). Inferences from a 19 m firn core, Nordbogletscher, South Greenland. *Rapp. Grønlands Geol. Unders.* 110, 96–98.

Braithwaite, R. J., Laternser, M., and Pfeffer, W. T. (1994). Variations of near-surface firn density in the lower accumulation area of the Greenland ice sheet, Pakitsoq, West Greenland. *J. Glaciol.* 40, 477–485. doi: 10.1017/S002214300001234X

Brun, E., Martin, E., and Spiridonov, V. (1997). Coupling a multi-layered snow model with a GCM. *Ann. Glaciol.* 25, 66–72. doi: 10.3189/S0260305500013811

Burgess, E. W., Forster, R. R., Box, J. E., Mosley-Thompson, E., Bromwich, D. H., Bales, R. C., et al. (2010). A spatially calibrated model of annual accumulation rate on the Greenland ice sheet (1958–2007). *J. Geophys. Res. Earth Surf.* 115:F02004. doi: 10.1029/2009JF001293

Charalampidis, C., Van As, D., Colgan, W. T., Fausto, R. S., Macferrin, M., and Machguth, H. (2016a). Thermal tracing of retained meltwater in the lower accumulation area of the Southwestern Greenland ice sheet. *Ann. Glaciol.* 57, 1–10. doi: 10.1017/aog.2016.2

Charalampidis, C., Van As, D., Langen, P. L., Fausto, R. S., Vandecrux, B., and Box, J. E. (2016b). Regional climate-model performance in Greenland firn derived from *in situ* observations. *Geol. Surv. Denmark Greenland Bull.* 35, 75–78.

Colgan, W., Abdalati, W., Citterio, M., Csatho, B., Fettweis, X., Luthcke, S., et al. (2015). Hybrid glacier inventory, Gravimetry and Altimetry (HIGA) mass balance product for Greenland and the Canadian Arctic. *Rem. Sens. Environ.* 168, 24–39. doi: 10.1016/j.rse.2015.06.016

Conger, S. M., and McClung, D. M. (2009). Comparison of density cutters for snow profile observations. *J. Glaciol.* 55, 163–169. doi: 10.3189/002214309788609038

Csatho, B. M., Schenk, A. F., Van der Veen, C. J., Babonis, G., Duncan, K., Rezvanbehbahani, S., et al. (2014). Laser altimetry reveals complex pattern of Greenland ice sheet dynamics. *Proc. Nat. Acad. Sci. U.S.A.* 111, 18478–18483. doi: 10.1073/pnas.1411680112

de la Peña, S., Howat, I. M., Nienow, P. W., Van den Broeke, M. R., Mosley-Thompson, E., Price, S. F., et al. (2015). Changes in the firn structure of the western Greenland ice sheet caused by recent warming. *Cryosphere* 9, 1203–1211. doi: 10.5194/tc-9-1203-2015

de la Peña, S., Nienow, P., Shepherd, A., Helm, V., Mair, D., Hanna, E., et al. (2010). Spatially extensive estimates of annual accumulation in the dry snow zone of the Greenland ice sheet determined from radar altimetry. Cryosph*ere* 4, 467–474. doi: 10.5194/tc-4-467-2010

Dibb, J. E., and Fahnestock, M. (2004). Snow accumulation, surface height change, and firn densification at Summit, Greenland: insights from 2 years of *in situ* observation. *J. Geophys. Res.* 109:D24113. doi: 10.1029/2003JD004300

Fausto, R. S., Ahlstrøm, A., Van As, D., Johnsen, S. J., Langen, P. L., and Steffen, K. (2009). Improving surface boundary conditions with focus on coupling snow densification and meltwater retention in large-scale ice-sheet models of Greenland. *J. Glaciol.* 55, 869–878. doi: 10.3189/002214309790152537

Forster, R. R., Box, J. E., Van den Broeke, M. R., Miège, C., Burgess, E. W., Van Angelen, J. H., et al. (2013). Perennial liquid water discovered in Greenland firn layer. *Nat. Geosci.* 7, 95–98. doi: 10.1038/ngeo2043

Gallée, H., Trouvilliez, A., Agosta, C., Genthon, C., Favier, V., and Naaim-Bouvet, F. (2013). Transport of snow by the wind: a comparison between observations in Adélie Land, Antarctica, and simulations made with the regional climate model MAR. *Bound Lay. Meteorol.* 146, 133–147. doi: 10.1007/s10546-012-9764-z

Greve, R., Saito, F., and Abe-Ouchi, A. (2011). Initial results of the SeaRISE numerical experiments with the models SICOPOLIS and IcIES for the Greenland Ice Sheet. *Ann. Glaciol.* 52, 23–30. doi: 10.3189/172756411797252068

Harper, J., Humphrey, N., Pfeffer, W. T., Brown, J., and Fettweis, X. (2012). Greenland ice-sheet contribution to sea-level rise buffered by meltwater storage in firn. *Nature* 491, 240–243. doi: 10.1038/nature11566

Hawley, R. L., Courville, Z. R., Kehrl, L. M., Lutz, E. R., Osterberg, E. C., Overly, T. B., et al. (2014). Recent accumulation variability in Northwest Greenland from GPR and shallow cores along the Greenland inland traverse. *J. Glaciol.* 60, 375–382. doi: 10.3189/2014JoG13J141

Hawley, R. L., Morris, E. M., Cullen, R., Nixdorf, U., Shepherd, A. P., and Wingham, D. J. (2006). ASIRAS airborne radar resolves internal annual layers in the dry-snow zone of Greenland. *Geophys. Res. Lett.* 33:L04502. doi: 10.1029/2005GL025147

Hörhold, M. W., Kipfstuhl, S., Wilhelms, F., Freitag, J., and Frenzel, A. (2011). The densification of layered polar firn. *J. Geophys. Res.* 116:F01001. doi: 10.1029/2009JF001630

Howat, I. M., Negrete, A., and Smith, B. E. (2014). The Greenland Ice Mapping Project (GIMP) land classification and surface elevation datasets. *Cryosphere* 8, 1509–1518. doi: 10.5194/tc-8-1509-2014

Humphrey, N. F., Harper, J. T., and Pfeffer, W. T. (2012). Thermal tracking of meltwater retention in Greenland's accumulation area. *J. Geophys. Res. Earth Surf.* 117:F01010. doi: 10.1029/2011JF002083

Hurkmans, R. T. W. L., Bamber, J. L., Davis, C. H., Joughin, I. R., Khvorostovsky, K. S., Smith, B. S., et al. (2014). Time-evolving mass loss of the Greenland ice sheet from satellite altimetry. *Cryosphere* 8, 1725–1740. doi: 10.5194/tc-8-1725-2014

IPCC. (2013). *Climate Change 2013: the Physical Science Basis*. Contribution of Working Group I to the Fifth Assessment Report of the Intergovernmental Panel on Climate Change, eds T. F. Stocker, D. Qin, G.-K. Plattner, M. Tignor, S. K. Allen, J. Boschung et al. (Cambridge, New York, NY: Cambridge University Press), 1535.

Karlsson, N. B., Eisen, O., Dahl-Jensen, D., Freitag, J., Kipfstuhl, S., Lewis, C., et al. (2016). Accumulation rates during 1311-2011 CE in north-central Greenland derived from air-borne radar data. *Front. Earth Sci.* 4:97. doi: 10.3389/feart.2016.00097

Khan, S. A., Aschwanden, A., Bjørk, A. A., Wahr Kjeldsen, K. K., and Kjær, K. H. (2015). Greenland ice sheet mass balance: a review. *Rep. Prog. Phys.* 78:046801. doi: 10.1088/0034-4885/78/4/046801

Kjeldsen, K. K., Korsgaard, N. J., Bjørk, A. A., Khan, S. A., Box, J. E., Funder, S., et al. (2015). Spatial and temporal distribution of mass loss from the Greenland ice sheet since AD 1900. *Nature* 528, 396–400. doi: 10.1038/nature16183

Koenig, L., Box, J., and Kurtz, N. (2013). Improving surface mass balance over ice sheets and snow depth on sea ice. *Eos Trans. AGU* 94:100. doi: 10.1002/2013EO100006

Koenig, L. S., Ivanoff, A., Alexander, P. M., MacGregor, J. A., Fettweis, X., Panzer, B., et al. (2016). Annual Greenland accumulation rates (2009–2012) from airborne snow radar. *Cryosphere* 10, 1739–1752. doi: 10.5194/tc-10-1739-2016

Koenig, L. S., Miège, C., Forster, R. R., and Brucker, L. (2014). Initial *in situ* measurements of perennial meltwater storage in the Greenland firn aquifer. *Geophys. Res. Lett.* 41, 81–85. doi: 10.1002/2013GL058083

Kojima, K. (1967). "Densification of seasonal snow cover," in *Physics of Snow and Ice*, ed. H. Oura (Sapporo: Institute of Low Temperature Science, Hokkaido University), 929–952.

Kotlyakov, V. M. (1961). Results of a study of the process of formation and structure of the upper layer of the ice sheet in eastern Antarctica. *Antarctic Glaciol.* 55, 88–99.

Kuipers Munneke, P., Ligtenberg, S. R. M., Noël, B. P. Y., Howat, I. M., Box, J. E., Mosley-Thompson, E., et al. (2015). Elevation change of the Greenland ice sheet due to surface mass balance and firn processes 1960–2014. *Cryosphere* 9, 2009–2025. doi: 10.5194/tc-9-2009-2015

Langen, P. L., Fausto, R. S., Vandecrux, B., Mottram, R. H., and Box, J. E. (2017). Liquid water flow and retention on the Greenland ice sheet in the regional climate model HIRHAM5: local and large-scale impacts. *Front. Earth Sci.* 4:110. doi: 10.3389/feart.2016.00110

Langen, P. L., Mottram, R. H., Christensen, J. H., Boberg, F., Rodehacke, C. B., Stendel, M., et al. (2015). Quantifying energy and mass fluxes controlling Godthåbsfjord freshwater input in a 5 km simulation (1991–2012). *J. Climate*. 28, 3694–3713. doi: 10.1175/JCLI-D-14-00271.1

Lewis, G., Osterberg, E., Hawley, R., Whitmore, B., Marshall, H. P., and Box, J. E. (2017). Regional Greenland accumulation variability from operation IceBridge airborne accumulation radar. *Cryosphere* 11, 773–788. doi: 10.5194/tc-11-773-2017

Li, J., and Zwally, H. J. (2011). Modeling of firn compaction for estimating ice-sheet mass change from observed ice-sheet elevation change. *Ann. Glaciol.* 52, 1–7. doi: 10.3189/172756411799096321

Ligtenberg, S. R. M., Helsen, M. M., and Van den Broeke, M. R. (2011). An improved semi-empirical model for the densification of Antarctic firn. *Cryosphere* 5, 809–819. doi: 10.5194/tc-5-809-2011

Liston, G. E., Haehnel, R. B., Sturm, M., Hiemstra, C. A., Berezovskaya, S., and Tabler, R. D. (2007). Simulating complex snow distributions in windy environments using SnowTran-3D. *J. Glaciol.* 53, 241–256. doi: 10.3189/172756507782202865

López-Moreno, J. I., Olivera-Marañón, M., Zabalza, J., and Larramendi, R. H. (2016). Snowpack observations from a circumnavigation of the Greenland Ice Sheet. *Cuad. Invest. Geográf.* 42, 369–381.

Machguth, H., MacFerrin, M., Van As, D., Box, J. E., Charalampidis, C., Colgan, W., et al. (2016). Greenland meltwater storage in firn limited by near-surface ice formation. *Nat. Clim. Change* 6, 390–393. doi: 10.1038/nclimate2899

McGrath, D., Colgan, W., Bayou, N., Muto, A., and Steffen, K. (2013). Recent warming at Summit, Greenland: global context and implications. *Geophys. Res. Lett.* 40, 2091–2096. doi: 10.1002/grl.50456

Miège, C., Forster, R. R., Box, J. E., Burgess, E. W., McConnell, J. R., Pasteris, D. R., et al. (2013). Southeast Greenland high accumulation rates derived from firn cores and ground-penetrating radar. *Ann. Glaciol.* 54, 322–332. doi: 10.3189/2013AoG63A358

Miège, C., Forster, R. R., Brucker, L., Koenig, L. S., Solomon, D. K., Paden, J. D., et al. (2016). Spatial extent and temporal variability of Greenland firn aquifers detected by ground and airborne radars. *J. Geophys. Res. Earth Surf.* 121, 2381–2398. doi: 10.1002/2016JF003869

Mock, S. J., and Weeks, W. F. (1965). The distribution of ten-meter snow temperatures on the Greenland ice sheet. *CRREL Rep*. 170, 1–44.

Montgomery, L., Koenig, L., and Alexander, P. (2018). The SUMup Dataset: compiled measurements of surface mass balance components over ice sheets and sea ice with preliminary analysis over Greenland. *Earth Syst. Sci. Data Discuss*. doi: 10.5194/essd-2018-21

Morris, E. M., and Wingham, D. J. (2014). Densification of polar snow: measurements, modeling, and implications for altimetry. *J. Geophys. Res. Earth Surf.* 119, 349–365. doi: 10.1002/2013JF002898

Mosley-Thompson, E., McConnell, J. R., Bales, R. C., Li, Z., Lin, P.-N., Steffens, K., et al. (2001). Local to regional scale variability of annual net accumulation on the Greenland ice sheet from PARCA cores. *J. Geophys. Res.*106, 33839–33851. doi: 10.1029/2001JD900067

Noël, B., Fettweis, X., Van de Berg, W. J., Van den Broeke, M. R., and Erpicum, M. (2014). Sensitivity of Greenland ice sheet surface mass balance to perturbations in sea surface temperature and sea ice cover: a study with the regional climate model MAR. *Cryosphere* 8, 1871–1883. doi: 10.5194/tc-8-1871-2014

Overly, T. B., Hawley, R. L., Helm, V., Morris, E. M., and Chaudhary, R. N. (2016). Greenland annual accumulation along the EGIG line, 1959-2004, from ASIRAS airborne radar and neutron-probe density measurements. *Cryosphere* 10, 1679–1694. doi: 10.5194/tc-10-1679-2016

Pahaut, E. (1976). *La Métamorphose des Cristaux de Neige (Snow crystal metamorphosis), 96, Monographies de la Météorologie Nationale*. Paris: Météo France.

Polashenski, C., Courville, Z., Benson, C., Wagner, A., Chen, J., Wong, G., et al. (2014). Observations of pronounced Greenland ice sheet firn warming and implications for runoff production. *Geophys. Res. Lett.* 41, 4238–4246. doi: 10.1002/2014GL059806

Proksch, M., Löwe, H., and Schneebeli, M. (2015). Density, specific surface area, and correlation length of snow measured by high-resolution penetrometry. *J. Geophys. Res. Earth Surf.* 120, 346–362, doi: 10.1002/2014JF003266

Proksch, M., Rutter, N., Fierz, C., and Schneebeli, M. (2016). Intercomparison of snow density measurements: bias, precision, and vertical resolution .*Cryosphere* 10, 371–384. doi: 10.5194/tc-10-371-2016

Reeh, N., Fisher, D. A., Koerner, R. M., and Clausen, H. B. (2005). An empirical firn-densification model comprising ice lenses. *Ann. Glaciol.* 42, 101–106. doi: 10.3189/172756405781812871

Schaller, C. F., Freitag, J., Kipfstuhl, S., Laepple, T., Steen-Larsen, H. C., and Eisen, O. (2016). A representative density profile of the North Greenland snowpack. *Cryosphere* 10, 1991–2002. doi: 10.5194/tc-10-1991-2016

Shepherd, A., Ivins, E. R., Geruo, A., Barletta, V. R., Bentley, M. J., Bettadpur, S., et al. (2012). A reconciled estimate of ice-sheet mass budget. *Science* 338, 1183–1189. doi: 10.1126/science.1228102

Simonsen, S. B., Stenseng, L., Adalgeirsdóttir, G., Fausto, R. S., Hvidberg, C. S., and Lucas-Picher, P. (2013). Assessing a multilayered dynamic firn-compaction model for Greenland with ASIRAS radar measurements. *J. Glaciol.* 59, 545–558. doi: 10.3189/2013JoG12J158

Sørensen, L. S., Simonsen, S. B., Nielsen, K., Lucas-Picher, P., Spada, G., Adalgeirsdottir, G., et al. (2011). Mass balance of the Greenland ice sheet (2003–2008) from ICESat data: the impact of interpolation, sampling and firn density. *Cryosphere* 5, 173–186. doi: 10.5194/tc-5-173-2011

Steffen, K., Box, J. E., and Abdalati, W. (1996). "Greenland climate network: GC-Net," in *CRREL 96-27 Special Report on Glaciers, Ice Sheets and Volcanoes*, ed S. C. Colbeck, 98–103.

Steger, C. R., Reijmer, C. H., Van den Broeke, M. R., Wever, N., Forster, R. R., Koenig, L. S., et al. (2017). Firn meltwater retention on the Greenland ice sheet: a model comparison. *Front. Earth Sci.* 5:3. doi: 10.3389/feart.2017.00003

Thomas, R. H., and PARCA Investigators (2001). Program for Arctic Regional Climate Assessment (PARCA): goals, key findings, and future directions. *J. Geophys. Res.* 106, 33691–33705. doi: 10.1029/2001JD900042

Van As, D., Box, J. E., and Fausto, R. S. (2016a). Challenges of quantifying meltwater retention in snow and firn: an expert elicitation. *Front. Earth Sci.* 4:101. doi: 10.3389/feart.2016.00101

Van As, D., Fausto, R. S., Cappelen, J., Machguth, H., Van de Wal, R. S. W., and the PROMICE project team (2016b). Placing Greenland ice sheet ablation measurements in a multi-decadal context. *Geol. Surv. Denmark Greenland Bull.* 35, 71–74.

Van As, D., Fausto, R. S., Colgan, W. T., Box, J. E., Ahlstrøm, A. P., Andersen, S. B., et al. (2013). Darkening of the Greenland ice sheet due to the melt albedo feedback observed at PROMICE weather stations. *Geol. Surv. Denmark Greenland Bull.* 28, 69–72.

Van den Broeke, M. R., Enderlin, E. M., Howat, I. M., Kuipers Munneke, P., Noël, B. P. Y., Van de Berg, W. J., et al. (2016). On the recent contribution of the Greenland ice sheet to sea level change. *Cryosphere* 10, 1933–1946. doi: 10.5194/tc-10-1933-2016

Vionnet, V., Brun, E., Morin, S., Boone, A., Faroux, S., Le Moigne, P., et al. (2012). The detailed snowpack scheme Crocus and its implementation in SURFEX v7. 2. *Geosci. Model. Dev.* 5, 773–791. doi: 10.5194/gmd-5-773-2012

Zwally, H. J., and Li, J. (2002). Seasonal and interannual variations of firn densification and ice-sheet surface elevation at the Greenland summit. *J. Glaciol.* 48, 199–207. doi: 10.3189/172756502781831403

Conflict of Interest Statement: The authors declare that the research was conducted in the absence of any commercial or financial relationships that could be construed as a potential conflict of interest.

The reviewer, CM, declared a past collaboration with two of the authors, JB and LK, to the handling editor.

APPENDIX D

Paper IV

frontiers in Earth Science

METHODS
published: 12 January 2017
doi: 10.3389/feart.2016.00110

Liquid Water Flow and Retention on the Greenland Ice Sheet in the Regional Climate Model HIRHAM5: Local and Large-Scale Impacts

Peter L. Langen[1], Robert S. Fausto[2], Baptiste Vandecrux[2,3], Ruth H. Mottram[1] and Jason E. Box[2]*

[1] Climate and Arctic Research, Danish Meteorological Institute, Copenhagen, Denmark, [2] Geological Survey of Denmark and Greenland, Copenhagen, Denmark, [3] Arctic Technology Centre (ARTEK), Technical University of Denmark, Lyngby, Denmark

OPEN ACCESS

Edited by:
Marco Tedesco,
NASA Goddard Institute for Space Studies-Columbia University, USA

Reviewed by:
Michiel Van Den Broeke,
Utrecht University, Netherlands
Xavier Fettweis,
University of Liège, Belgium
Patrick Alexander,
NASA Goddard Institute for Space Studies, USA

****Correspondence:***
Peter L. Langen
pla@dmi.dk

Specialty section:
This article was submitted to Cryospheric Sciences, a section of the journal Frontiers in Earth Science

Received: *04 October 2016*
Accepted: *22 December 2016*
Published: *12 January 2017*

Citation:
Langen PL, Fausto RS, Vandecrux B, Mottram RH and Box JE (2017) Liquid Water Flow and Retention on the Greenland Ice Sheet in the Regional Climate Model HIRHAM5: Local and Large-Scale Impacts. Front. Earth Sci. 4:110. doi: 10.3389/feart.2016.00110

To improve Greenland Ice Sheet surface mass balance (SMB) simulation, the subsurface scheme of the HIRHAM5 regional climate model was extended to include snow densification, varying hydraulic conductivity, irreducible water saturation and other effects on snow liquid water percolation and retention. Sensitivity experiments to investigate the effects of the additions and the impact of different parameterization choices are presented. Compared with 68 accumulation area ice cores, the simulated mean annual net accumulation bias is −5% (correlation coefficient of 0.90). Modeled SMB in the ablation area compares favorably with 1041 PROMICE observations with regression slope of 0.95–0.97 (depending on model configuration), correlation coefficient of 0.75–0.86 and mean bias −3%. Weighting ablation area SMB biases at low- and high-elevation with the amount of runoff from these areas, we estimate ice sheet-wide mass loss biases in the ablation area at −5 and −7% using observed (MODIS-derived) and internally calculated albedo, respectively. Comparison with observed melt day counts shows that patterns of spatial (correlation ∼0.9) and temporal (correlation coefficient of ∼0.9) variability are realistically represented in the simulations. However, the model tends to underestimate the magnitude of inter-annual variability (regression slope ∼0.7) and overestimate that of spatial variability (slope ∼1.2). In terms of subsurface temperature structure and occurrence of perennial firn aquifers and perched ice layers, the most important model choices are the albedo implementation and irreducible water saturation parameterization. At one percolation area location, for instance, the internally calculated albedo yields too high subsurface temperatures below 5 m, but when using an implementation of irreducible saturation allowing higher values, an ice layer forms in 2011, reducing the deep warm bias in subsequent years. On the other hand, prior to the formation of the ice layer, observed albedos combined with lower irreducible saturation give the smallest bias. Perennial firn aquifers and perched ice layers occur in varying thickness and area for

different model parameter choices. While the occurrence of these features has an influence on the local-scale subsurface temperature, snow, ice and water fields, the Greenland-wide runoff and SMB are—in the model's current climate—dominated by the albedo implementation.

Keywords: liquid water percolation in firn, regional climate model, HIRHAM5 subsurface scheme, Greenland ice sheet runoff, Greenland ice sheet surface mass balance, Greenland ice sheet perched ice layers, Greenland ice sheet perennial firn aquifer

INTRODUCTION

Greenland ice sheet mass budget changes are among the largest sources of uncertainty in estimates of sea level rise under climate change (Church et al., 2013; Gregory et al., 2013). A key uncertainty in the mass budget is the degree of meltwater retention due to refreezing and capillary forces (e.g., Janssens and Huybrechts, 2000; Harper et al., 2012; Vernon et al., 2013; van As et al., 2016). As the climate has warmed, the zone where melt and rainfall occurs over the snowpack has expanded to higher elevations in the last decade (Howat et al., 2013; de la Peña et al., 2015). Observations from Polashenski et al. (2014) confirm that firn warming is a both long-term (>50 years) and widespread effect. Successive warm summers have also led to the formation of reduced permeability ice lens complexes that expand runoff into the accumulation area, e.g., at the KAN-U site at 1840 m a.s.l (above sea level) in 2012 (Machguth et al., 2016a). Accounting realistically for firn permeability will likely become increasingly important with continued climate warming, and we focus in this paper on representing the pathways of liquid water in snow and firn in a surface mass balance (SMB) model.

When melt or rainfall occurs at the surface of the snowpack, the water typically percolates deeper down and may be stored as liquid water or refrozen in the form of ice lenses (Benson, 1962; Braithwaite et al., 1992). The process by which water percolates in the snowpack was comprehensively described in a Darcian type flow model by Colbeck (1972). Melt percolation has been identified and observed across many glaciers, particularly in the Alps and the Arctic, where deep snow packs often exist overlying glacier ice (e.g., Müller, 1976; Braithwaite et al., 1994; Parry et al., 2007; Wright et al., 2007; Humphrey et al., 2012; Gascon et al., 2013; Polashenski et al., 2014). The meltwater penetration depth is controlled by the temperature and density of the snowpack. Snow/firn density controls the hydraulic conductivity, the pore spaces where water can be contained, and the thermal conductivity of the snow. Subsurface temperature has an important control on densification rate and, via layer cold content, determines if and how much liquid water will freeze.

Once liquid water is in the snowpack, if there is sufficient cold content, the water may refreeze, forming ice layers and pipes. Ice lenses appear to reduce percolation, acting as a barrier to "deep percolation," i.e., percolation below the previous year's accumulation (Machguth et al., 2016a). Refreezing releases latent heat and acts to warm the snowpack, a phenomenon that has been observed in the Greenland firn over the last 50 years (Polashenski et al., 2014) and seen in modeled snow packs in regional climate simulations (e.g., van den Broeke et al., 2009). However, under high accumulation rate and in locations with low surface slope, meltwater may remain unfrozen and locked in perennial firn aquifers (Forster et al., 2014; Koenig et al., 2014; Kuipers Munneke et al., 2014). Along with refrozen water, perennial firn aquifers have a potentially important delaying effect on sea level rise from Greenland ice in a warming world (Pfeffer et al., 1991). Percolation of meltwater into the snowpack is, however, limited by available pore space (Harper et al., 2012) and future projections by van Angelen et al. (2013) suggest that this pore space may be filled after just a few decades, leading to an acceleration of runoff.

The importance of accounting for these processes has driven the development of snow and firn models within SMB models. As liquid water retention and refreezing are spatially heterogeneous processes and occur at sub-grid scale, early models used parameterizations. Reeh (1989) assumed a fixed percentage of the winter accumulation was retained. Janssens and Huybrechts (2000), Pfeffer et al. (1991) and others developed parameterizations to quantify meltwater retention from a reduced number of variables. Only more recently have meltwater percolation and retention been physically described in firn and snowpack models both at ice sheet scale and in alpine environments (CROCUS, Vionnet et al., 2012; SNOWPACK, Wever et al., 2015). Similar physically-based representations have also been adapted into regional climate models RACMO and MAR (Fettweis, 2007; van den Broeke et al., 2009; Reijmer et al., 2012). The version of HIRHAM5 described in Langen et al. (2015) used a simplified representation of liquid water retention and refreezing.

Declining surface albedo feeding back with temperature and melt plays an important role for the mass balance (e.g., Box et al., 2012; van Angelen et al., 2014). The darkening may be associated both with a general warming (Tedesco et al., 2016) and with increasing amounts of light-absorbing impurities transported to the ice sheet (Dumont et al., 2014; Keegan et al., 2014) or from exposure of "dirty ice" (Tedesco et al., 2016). In any case, the representation of and interplay between albedo processes and subsurface meltwater and refreezing has important effects on the mass balance in a warming climate (van Angelen et al., 2012) including the lower accumulation area (Charalampidis et al., 2015).

In this paper we present results from a HIRHAM5 subsurface scheme which accounts for snow/firn density evolution and hydraulic conductivity and employs two different albedo implementations (described in Section Model Description and Simulations), allowing for formation of firn aquifers and perched impermeable ice layers. In Section Model Evaluation

Using Observations, we compare model results to observed net accumulation, SMB in the ablation area, melt extent and subsurface density profiles at multiple ice sheet locations. In addition, we compare simulations with observed subsurface temperature evolution at a single site in West Greenland. We then perform sensitivity tests and discuss the choices made in the model which are particularly important (Section Sensitivity Results). Conclusions are given in Section Conclusions.

MODEL DESCRIPTION AND SIMULATIONS

The regional climate model HIRHAM5 combines the dynamical core of the HIRLAM7 numerical weather forecasting model (Eerola, 2006) with physics schemes from the ECHAM5 general circulation model (Roeckner et al., 2003). Details of the configuration are in Christensen et al. (2006). In the all-Greenland domain employed here after Lucas-Picher et al. (2012), HIRHAM5 is run on a horizontal $0.05^\circ \times 0.05^\circ$ rotated-pole grid corresponding roughly to 5.5 km resolution. The atmosphere has 31 levels in the vertical and a 90 s time step. On the lateral boundaries, the ERA-Interim reanalysis (Dee et al., 2011) provides 6 h atmospheric model-level fields of wind, temperature and humidity as well as surface pressure. Across ocean grid points, ERA-Interim sea surface temperatures and sea ice concentration are prescribed. The experiment covers 35 years (1980-2014).

Subsurface Scheme

At the surface, snow mass is updated with snowfall, rainfall, melt and deposition/sublimation at each subsurface scheme time step (1 h). Likewise, the surface temperature is updated via energy budget closure with radiative and turbulent surface energy exchange above and diffusive and advective heat exchange with subsurface layers. If the surface temperature exceeds 0°C, it is reset to 0°C and the excess energy supplies heat for melting (Langen et al., 2015).

The current subsurface model has a number of additions and extensions after the original five-layer ECHAM5 surface scheme (Roeckner et al., 2003) modified for use over glaciers and ice sheets by Langen et al. (2015). Advancements include densification, snow grain growth, snow state-dependent hydraulic conductivity, superimposed ice formation and irreducible water saturation as well as accommodation for water retention in excess of the irreducible saturation. In the following, we describe the details of the new features.

Vertical Discretization

The new subsurface scheme consists of a horizontal grid of non-interacting columns with 32 layers of time-constant water equivalent thicknesses. Each layer's thickness is divided into contributions from snow (p_s), ice (p_i), and liquid water (p_w); each having m w.e. units. While their relative magnitudes can vary through time, the sum of these three parameters equals the layer thickness and remains constant. The layer thicknesses increase exponentially with depth to increase resolution near the surface (N'th layer thickness $D_N = D_1\lambda^{N-1}$, with $D_1 = 0.065$ m and $\lambda = 1.173265$ chosen to give a full model depth of 60 m w.e. minimizing impacts of lower boundary conditions). The uppermost 2.2 m w.e. are thus represented by 12 layers with thicknesses varying from 6.5 to 37 cm w.e., while the top 10.4 m w.e. has 21 layers with thicknesses up to 1.6 m w.e. The lowest subsurface layer has a thickness of 9.2 m w.e.

As mass is added on top of the subsurface model (via snow, rainfall, condensation or deposition), the scheme advects mass downward to ensure the constant w.e. layer thicknesses. Likewise, when mass is removed from the column by runoff, evaporation or sublimation, mass is shifted up from an infinite ice reservoir below into the lowest model layer. This up- and down mass flux is accompanied by an associated vertical transfer of sensible heat, snow density, grain size and snow, water and ice fractions.

Temperature, Refreezing, and Superimposed Ice Formation

The original ECHAM5 heat diffusion solver (Roeckner et al., 2003) is modified to accommodate a density dependent snow thermal conductivity (Yen, 1981; Vionnet et al., 2012),

$$k_s = k_{ice}\left(\frac{\rho_s}{\rho_w}\right)^{1.88} \quad (1)$$

where k_{ice} is the ice thermal conductivity (in W m^{-1} K^{-1}) and ρ_s and ρ_w are, respectively, the densities of snow and water. The layer bulk thermal conductivity is calculated through a volume-weighted blending of k_s and k_{ice}. Accumulating snow is assumed to have the temperature of the upper layer, while rain is assumed have 0°C temperature, T_f. The possible energy source from rain with temperature above T_f is thus disregarded. The infinite sublayer, with which the lowest model layer exchanges heat, is set to the simulated local long-term mean near-surface air temperature. This infinite sublayer choice may lead to a slight overestimation of refreezing since the model-bottom will be kept cooler than near-surface layers in case of latent heat release from refreezing. Since the subsurface model is 60 m w.e. deep, the vertical temperature gradient and resulting heat diffusion associated with this bottom cooling will be minor.

The cold content, i.e., the energy required to heat the snow and ice mass to T_f, in each layer is used to freeze liquid water, transferring mass to the ice fraction. Refreezing is assumed to be instantaneous, thereby freezing as much water as is available or as cold content allows within a single time step. The temperature of the layer is raised by latent heat release to conserve energy. Superimposed ice formation occurs when liquid water resides in a temperate layer above an impermeable layer (description below) with a temperature below the freezing point. A downward heat flux at the layer interface is then calculated assuming that the cold, impermeable layer has a linear temperature profile between T_f at the interface and the mean layer temperature at the layer mid-point. This downward heat flux allows superimposed ice to form in the temperate layer and heats the impermeable layer beneath.

Water Saturation

The water saturation, S_w, is the volume of water per pore space volume and may be written in terms of masses as

$$S_w = \frac{p_w}{p_s}\frac{\rho_s\rho_i}{\rho_w(\rho_i-\rho_s)} \quad (2)$$

where $\rho_i = 917\,\mathrm{kg\,m^{-3}}$ is taken to be the density of ice and p_w and p_s are the layer masses of water and snow. The maximum water saturation that can be sustained by snow grain capillary tension is termed the irreducible water saturation, S_{wi}, with values employed in models varying widely. Colbeck (1974) found a value of 0.07 experimentally and Yamaguchi et al. (2010) found a value of 0.02, both for snow with a density of about $550\,\mathrm{kg\,m^{-3}}$. Coleou and Lesaffre (1998) experimented with variable densities and found an approximate relationship between porosity, $P = 1-\rho_s/\rho_i$, and the water per snow-plus-water mass irreducible liquid water content, W_{mi}:

$$W_{mi} = 0.057\frac{P}{1-P} + 0.017 = 0.057\frac{\rho_i-\rho_s}{\rho_s} + 0.017 \quad (3)$$

The quantity W_{mi} may be converted to S_{wi} through the relation

$$S_{wi} = \frac{W_{mi}}{(1-W_{mi})}\frac{\rho_s\rho_i}{\rho_w(\rho_i-\rho_s)} \quad (4)$$

As ρ_s increases, S_{wi} calculated in this manner initially decreases from ∼0.10 at $100\,\mathrm{kg\,m^{-3}}$ to ∼0.07 at $300\,\mathrm{kg\,m^{-3}}$. S_{wi} then increases to about ∼0.085 at $600\,\mathrm{kg\,m^{-3}}$ and ∼0.17 near $810\,\mathrm{kg\,m^{-3}}$ (**Figure 1**).

Vionnet et al. (2012) used an irreducible water saturation value of 0.05 in the Crocus/SURFEX model. As described by Reijmer et al. (2012), SOMARS/RACMO used 0.02 while Crocus/MAR used 0.06. Kuipers Munneke et al. (2014) used the Coleou and Lesaffre (1998) approach in their study of perennial firn aquifers with the Ligtenberg et al. (2011) firn model. To test the sensitivity toward this choice, we perform experiments with a fixed value of 0.02 along with values calculated based on the Coleou and Lesaffre (1998) parameterization.

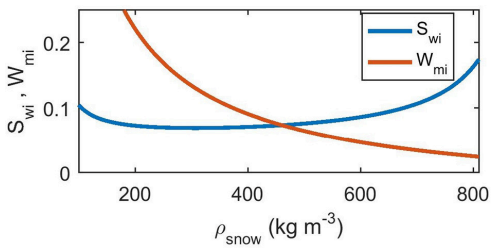

FIGURE 1 | Irreducible saturation, S_{wi}, and irreducible liquid water content, W_{mi} (water per snow-plus-water mass), as a function of snow density following the parameterization by Coleou and Lesaffre (1998).

Finally, given values of S_w and S_{wi}, we may calculate the effective liquid saturation,

$$\Theta = \frac{S_w - S_{wi}}{1-S_{wi}} \quad (5)$$

which becomes positive when the snow contains more water than can be permanently held by capillary forces alone.

Downward Flow of Liquid Water

In our treatment of vertical flow of liquid water through the snowpack, we closely follow the implementation by Hirashima et al. (2010). The governing equation for water flow, q ($\mathrm{m\,s^{-1}}$), is Darcy's law,

$$q = K\left(\frac{dh}{dz}+1\right) \quad (6)$$

where dh/dz is the vertical gradient in capillary suction, h (m units), and the second term (+1) represents gravity. The vertical coordinate, z, increases downwards. The hydraulic conductivity, K ($\mathrm{m\ s^{-1}}$), and the capillary suction are parameterized in terms of snow grain diameter, d_g (mm units), effective liquid saturation, Θ, and snow density, ρ_s, as follows. The hydraulic conductivity of snow is the product of the saturated and unsaturated conductivities, $K_{snow} = K_s K_r$, the former of which was determined by Shimizu (1970) to follow:

$$K_s = 0.077\frac{g}{\nu_w}\left(\frac{d_g}{1000}\right)^2 \exp(-0.0078\rho_s) \quad (7)$$

Here, g is the acceleration due to gravity and ν_w is the kinematic viscosity of water ($1.787\cdot10^{-6}\ \mathrm{m^2\ s^{-1}}$). Note that d_g has mm units. We thus divide by 1000 to get the diameter in m units in accordance with Calonne et al. (2012). In the van Genuchten (1980) parameterization of K_r and h used by Hirashima et al. (2010), two parameters (α and n) must be calculated,

$$\alpha = 7.3\,d_g + 1.9,\ n = 15.68\exp(-0.46\,d_g) + 1 \quad (8)$$

With these, and the quantity $m = 1 - 1/n$, we calculate,

$$K_r = \Theta^{\frac{1}{2}}\left[1-\left(1-\Theta^{\frac{1}{m}}\right)^m\right]^2 \quad (9)$$

$$h = \frac{1}{\alpha}\left(\Theta^{-\frac{1}{m}}-1\right)^{\frac{1}{n}} \quad (10)$$

As the layers in our subsurface model contain both snow and ice, we need to take into account the hydraulic conductivity reduction resulting from the presence of ice. Colbeck (1975) developed an analytical model for a snowpack with interspersed ice layers, and we employ it here for model layers with some ice fraction. The bulk hydraulic conductivity of the entire model layer is

$$K = K_{snow}\left[f_{snow} + (1-f_{snow})\frac{1+\frac{w_h}{w_{ice}}}{\frac{K_{ice}}{K_{snow}}+\frac{w_h}{w_{ice}}}\right] \quad (11)$$

where $f_{snow} = H_s/(H_s+H_i)$ is the fraction of the physical layer thickness which is snow (here, $H_s = p_s\rho_w/\rho_s$ and $H_i = p_i\rho_w/\rho_i$

are the physical thicknesses of the snow and ice fractions). The hydraulic conductivity of ice, K_{ice}, is assumed zero, and the fraction w_h/w_{ice} is the ratio between the width of holes in the ice and the width of the ice. A value of 1 for this fraction means that when ice is present in a layer, it has a horizontal extent of half the unit area. Here, it is essentially a tuning parameter that can decrease the hydraulic conductivity in the presence of ice and we perform experiments with w_h/w_{ice} values of 1 and 0.1.

Hirashima et al. (2010) introduced an implementation of Darcy's law that allows for longer time-steps at the cost of considering only downward flow, and the same is adopted here. The instantaneous flux, q_0, evaluated using beginning-of-time-step values for all the above quantities influencing K and h, will change during a long time step and taking $q_0\Delta t$ as the time-step total flux will be an overestimate; the total flux into a given layer will at most equal all the water beyond irreducible saturation in the layer above, or it will equal the amount that increases the vertical h-gradient sufficiently to obtain balance between the two terms in Darcy's law (Equation 6). That limiting amount, q_{lim}, is estimated iteratively and allows for calculation of the time-step integrated flux $q_{lim}\left[1-\exp\left(-\frac{q_0}{q_{lim}}\Delta t\right)\right]$ (Hirashima et al., 2010).

During our sensitivity experiments, we also employ a "NoDarcy" version of the code which ignores the delaying effect of hydraulic conductivity on the vertical flow, allowing all water in excess of the irreducible saturation to fully percolate within a single time step.

Impermeable Layers and Runoff

A layer is considered impermeable if its bulk dry density,

$$\rho_{bulk} = (p_s + p_i)/\left(\frac{p_s}{\rho_s} + \frac{p_i}{\rho_i}\right) \tag{12}$$

exceeds a threshold of 810 kg m^{-3}. This value is lower than the classical value of pore close-off density at 830 kg m^{-3} (Cuffey and Paterson, 2010), since field studies (Gregory et al., 2014) show that in high-accumulation areas such as West Antarctic Ice Sheet (WAIS) divide (and presumably Greenland), impermeability occurs over a range of densities (780–840 kg m^{-3}) centered around an average of 810 kg m^{-3}. No water is allowed to flow to an impermeable layer from above and the same applies if a layer has its entire pore space filled ($S_w = 1$). For a layer above an impermeable layer, water that would otherwise have flowed downwards, through either the Darcy or NoDarcy mechanisms described above, becomes available to run off. However, it does not run off immediately. Instead, runoff, Q_{RO}, per time-step is calculated from the water in excess of the irreducible saturation, p_{liqex}, as:

$$Q_{RO} = p_{liqex}\frac{\Delta t}{\tau_{RO}} \tag{13}$$

where $\tau_{RO} = c_{RO,1} + c_{RO,2}\exp(-c_{RO,3}S)$ is a characteristic local runoff time-scale that increases as the surface slope, S (unit m m^{-1}), tends to zero (Zuo and Oerlemans, 1996). The coefficients $c_{RO,1}$, $c_{RO,2}$ and $c_{RO,3}$ are set to 0.33 day, 25 days and 140, respectively (as in CROCUS/MAR, Lefebre et al., 2003). With this delayed runoff, water in excess of irreducible saturation may linger in a layer until it forms superimposed ice on the layer beneath, runs off or refreezes.

There is currently no representation of horizontal flow or routing of meltwater in HIRHAM5. Once water runs off as described above, it exits the model domain.

Densification and Grain Growth

Re-writing Equation (5) in Vionnet et al. (2012), the time evolution of the snow density, ρ_s, is given as

$$\frac{d\rho_s}{dt} = \frac{\rho_s\sigma}{\eta} \tag{14}$$

where σ is the overburden pressure and η is the snow viscosity, parameterized as in Vionnet et al. (2012) Equation (7):

$$\eta = f_1 f_2 \eta_0 \frac{\rho_s}{c_\eta}\exp\left[a_\eta\,(T_f - T) + b_\eta\rho_s\right] \tag{15}$$

Here, $\eta_0 = 7.62237 \cdot 10^6$kg s^{-1}, $a_\eta = 0.1$ K^{-1}, $b_\eta = 0.023$ m^3 kg^{-1}, $c_\eta = 250$ kg m^{-3} are identical to Vionnet et al. (2012), while f_2 is taken to be a constant of 4, neglecting the reduction in η for grain sizes smaller than about 0.3 mm. The effect of liquid water on viscosity and compaction rate enters in f_1 as,

$$f_1 = \frac{1}{1 + 60\frac{p_w}{p_s}\frac{\rho_s}{\rho_w}} \tag{16}$$

Freshly-fallen snow has an initial density parameterized through a linear regression of surface density observations onto surface elevation, z_{srf} (m a.s.l.), latitude, φ (degrees north), and longitude, λ (degrees east):

$$\rho_{s,f} = a_\rho + b_\rho z_{srf} + c_\rho\varphi + d_\rho\lambda \tag{17}$$

with $a_\rho = 328.35$ kg m^{-3}, $b_\rho = -0.049376$ kg m^{-4}, $c_\rho = 1.0427$ kg m^{-3} deg^{-1} and $d_\rho = -0.11186$ kg m^{-3} deg^{-1} (Fausto et al., in preparation).

The snow grain size diameter, d_g (in mm), used in the calculation of hydraulic conductivity is modeled following Katsushima et al. (2009) and Hirashima et al. (2010) in terms of the mass liquid water content in percent, $L = p_w/p_s \times 100$, as

$$\frac{d}{dt}d_g = \frac{1}{d_g^2}\min\left(\frac{2}{\pi}\left[1.28\cdot 10^{-8}\text{mm}^3\text{s}^{-1} + 4.22\cdot 10^{-10}\text{mm}^3\text{s}^{-1}\times L^3\right],\ 6.94\cdot 10^{-8}\text{mm}^3\text{s}^{-1}\right) \tag{18}$$

The first option, increasing with L^3, follows Brun (1989) for low liquid water content, while the second option depends only on the d_g^{-2} factor. As in Katsushima et al. (2009), we choose an initial value of 0.1 mm for the grain size diameter of freshly fallen snow.

Experimental Design

We perform sensitivity tests with multiple subsurface scheme versions and parameter settings, running the subsurface scheme offline from the HIRHAM5 atmospheric code by saving 6 h fields of surface fluxes of energy (downward short- and longwave radiation, latent and sensible heat fluxes) and snowfall, rainfall and sublimation mass fluxes from HIRHAM5. These fields are in turn read in to the offline subsurface code and interpolated to the 1 h time step employed there. The upward short- and longwave fluxes are calculated in the offline code based on albedo (see below) and surface temperature. Spin-up of the subsurface model is performed by taking an initial condition from a previous experiment and repeating the decade 1980-1989 (chosen since it precedes the warming in later decades) until transients in decadal means of runoff and subsurface temperatures have ceased, typically 50–100 years. A separate spin-up is performed for each sensitivity experiment. After spin-up, the transient 1980-2014 experiment is started from the final model state.

Surface albedo is crucial to determining melt energy and in turn the supply of subsurface liquid water and runoff. We perform sensitivity tests with two different implementations: (i) MODIS-derived daily gridded fields of observed surface albedo after Box et al. (2012, see Section Observational Data), hereafter "MOD," and (ii) surface albedo computed internally as in Langen et al. (2015), hereafter "LIN" referring to the linear function of temperature. The internally computed albedo thus employs a linear ramping of snow albedo between 0.85 below −5°C and 0.65 at 0°C for the upper-level temperature. The albedo of bare ice is constant at 0.4. Ice and snow albedos are blended for small snow depths using an exponential transition with an e-folding depth of 3.2 cm (as in Oerlemans and Knap, 1998).

Table 1 lists the sensitivity experiments with different combinations of albedo, water percolation mechanism, parameterization of S_{wi} and choice of w_h/w_{ice}. The experiments MOD-ref and LIN-ref, corresponding to a model with Darcy flow, S_{wi} parameterized following Coleou and Lesaffre (1998) and w_h/w_{ice} set to 1 (with either MODIS-derived or internally calculated albedo), are considered the reference setting.

TABLE 1 | Overview of sensitivity experiments with different choices of albedo implementation (MODIS-derived or linear formulation), water percolation mechanism (Darcy or NoDarcy), parameterization of irreducible water saturation, S_{wi} (fixed value of 0.02 or Coleou and Lesaffre, 1998, parameterization) and choice of w_h/w_{ice} (used in Equation 11).

Experiment	Darcy vs. NoDarcy	S_{wi}	w_h/w_{ice}	Albedo
MOD-ref	Darcy	CL	1.0	MODIS
MOD-w01	Darcy	CL	0.1	MODIS
MOD-Swi02	Darcy	0.02	1.0	MODIS
MOD-NoDarcy	NoDarcy	CL	–	MODIS
LIN-ref	Darcy	CL	1.0	Linear
LIN-Swi02	Darcy	0.02	1.0	Linear

The parameter w_h/w_{ice} is not relevant in NoDarcy.

MODEL EVALUATION USING OBSERVATIONS

In the following, we compare simulated and observed surface accumulation, SMB and surface melt day counts (Section Surface Mass Balance and Melt Extent) as well as subsurface temperature development at a single Programme for Monitoring of the Greenland Ice Sheet (PROMICE) site and subsurface density profiles at a collection of sites (Section Subsurface Temperature and Density). Throughout this study, we use the term SMB for the sum of surface accumulation and ablation, including internal accumulation within the surface snowpack due to refreezing and superimposed ice formation. We note that this term is sometimes also referred to as climatic mass balance (e.g., Cogley et al., 2011). The surface accumulation (and to some extent also ablation) is external to the subsurface model in the sense that accumulation is provided exclusively from the HIRHAM5 atmospheric model. The ablation is a result of the downward energy fluxes from HIRHAM5, but also the albedo calculated in the LIN simulations and specified in the MOD simulations at the top of the subsurface model. It furthermore depends on the subsurface energy flows and thus also on the other model choices.

Observational Data

MODIS Albedo

The Moderate Resolution Imaging Spectroradiometer (MODIS) MOD10A1 surface albedo used in the model is de-noised and smoothed as described by Box et al. (2012), whereby residual cloud artifacts are identified and rejected using running 11-day statistics in each pixel. Values that differ by more than two standard deviations from the 11-day mean are rejected unless they are within 0.04 of the median. Finally, the 11-day running median is used as the daily value. Given that data are only available since 2000, a daily MODIS-climatology based on the pre-darkening period 2000-2006 (see Tedesco et al., 2016) is used prior to 2000 (as in Fausto et al., 2016b).

Accumulation

A compilation of 86 ice cores providing annual w.e. net accumulation rate is available from Box et al. (2013), and spans elevations between 311 and 3188 m a.s.l. Here we select cores overlapping in time with our experiments and having elevations above 1000 m a.s.l. This gives a total of 68 cores (red circles in **Figure 2** and Supplementary Table S1) providing a sample across elevations and east-west and north-south differences.

Surface Mass Balance

Historical and contemporary SMB observations from all regions of Greenland compiled by Machguth et al. (2016b) under PROMICE are compared to daily simulated SMB. We use observations that overlap with our experiments and exclude sites that fall outside the model's glacier mask. The selection yields 1041 observations from 351 sites (blue circles in **Figure 2**). The time span of the SMB observations varies from months to years, although a full year or a 3-month ablation season are the most common. In our analyses (see **Table 2** and **Figure 4**) these

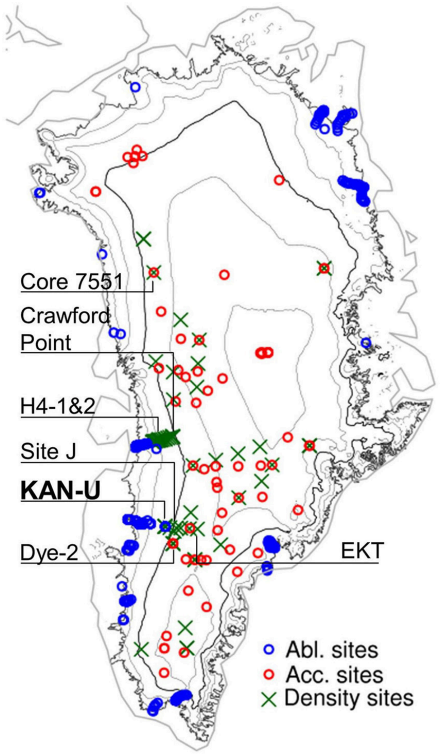

FIGURE 2 | The position of the 68 ice cores used for accumulation evaluation (red circles), 351 SMB observation sites in the ablation area (blue circles) and 75 firn cores used in density evaluation (names of 7 sites included in Figure 7 are shown) with elevation contours (1000-3000 m a.s.l. in steps of 500 m with 2000 m a.s.l. highlighted) and outline of the contiguous ice sheet.

observations (in m w.e.) of varying time span enter with equal weights.

Automatic Weather Stations

Interpretation of model-observation discrepancies is aided by the use of automatic weather station data from the PROMICE network (Ahlstrøm et al., 2008, see Supplementary Table S2). From these stations we use near-surface air temperature, surface temperature, downwelling longwave, downwelling shortwave, net incoming shortwave and albedo.

Surface Melt

We use the MEaSUREs Greenland Surface Melt Daily 25 km EASE-Grid 2.0 data set (Mote, 2014) from 1988 to 2012 to compare with modeled melt extent. After 1987, the product has daily resolution and derives from brightness temperatures measured with the Special Sensor Microwave Imager (SSM/I) and

TABLE 2 | Statistics of comparison between 1041 observed (Machguth et al., 2016b) and simulated SMBs from 351 ablation area sites.

Experiment	Slope	Intcpt (m w.e.)	R^2	RMSE (m w.e.)	Bias (m w.e.)	Bias (%)
MOD-ref	0.97	0.00	0.74	0.74	0.04	−3
MOD-w01	0.97	0.00	0.74	0.74	0.05	−3
MOD-Swi02	0.97	−0.01	0.74	0.74	0.04	−3
MOD-NoDarcy	0.97	0.00	0.74	0.74	0.04	−3
LIN-ref	0.95	−0.02	0.57	0.98	0.04	−3
LIN-Swi02	0.95	−0.02	0.57	0.98	0.05	−3

*Slope and intercept are of orthogonal linear fits (as in **Figure 4**). Biases (in m w.e. and in %) are mean model minus observation. Since SMBs are mostly negative, a positive bias (in m w.e.) indicates that the net mass loss is underestimated and the relative bias (%) is accordingly negative.*

Special Sensor Microwave Imager/Sounder (SSMIS) on board Defense Meteorological Satellite Program (DMSP) satellites. Measured brightness temperatures are compared to thresholds found using a microwave emission model to simulate brightness temperatures of a melting snowpack (Mote and Anderson, 1995; Mote, 2007). The result is a daily melt or no-melt field on the 25 km resolution Equal-Area Scalable Earth (EASE) grid.

Subsurface Temperature

Subsurface temperatures were recorded at the western ice sheet percolation area PROMICE site KAN-U (67.0003 N, 47.0243 W, marked in bold in **Figure 2**) 1840 m above sea level. The station has a thermistor string measuring subsurface temperature to 8–10 m depth (Charalampidis et al., 2015) and we use temperatures interpolated linearly between the thermistors. The depth of each sensor is calculated from maintenance reports and observed surface height changes from acoustic height sensors on the station boom and on a stake assembly few meters away. Between May and August 2012, the stake assembly tilted severely and the station was standing on (and lowering along with) the surface meaning that neither of them could monitor ablation accurately. For that period, we use five firn cores drilled at KAN-U in May 2012 and April 2013 and derive surface lowering between those two dates as the vertical offset that maximizes the correlation of their density profiles (Machguth et al., 2016a).

Density

Simulated subsurface density is evaluated against field measurements using a total of 75 firn cores spanning 1989 to 2013 (green crosses in **Figure 2** and Supplementary Table S4). This dataset comprises 14 cores from the Arctic Circle Traverse 2009 to 2013 (Machguth et al., 2016a), 32 cores from the PARCA campaigns in 1997-1998 (Mosley-Thompson et al., 2001), one core drilled at Site J in 1989 (Kameda et al., 1995) and 28 cores from 2007 to 2008 along the EGIG line (Harper et al., 2012). Resolution and accuracy vary for each dataset and are detailed in the studies above. Each core was compared to the modeled density profile of the grid cell it is located in. Different cores can

therefore be compared to the same modeled density profile and illustrate within-cell variability of firn density.

Surface Mass Balance and Melt Extent

The observed annual w.e. net accumulation rates compare with simulated net accumulation (calculated in the model as snowfall-minus-sublimation) with an average model bias of −5%, correlation coefficient of 0.90 and orthogonal linear regression slope of 1.01 indicating that the average magnitude and spatial variations are reliably reproduced by the model (**Figure 3**). Biases are locally both positive and negative and nearly cancel out in the mean but give a 25% root-mean-square-error, with no clear pattern in the distribution of positive and negative biases with elevation.

Figure 4 and **Table 2** compare the Machguth et al. (2016b) SMB measurements to nearest-neighbor interpolated simulated daily SMB sums over the dates reported in the observations. The MOD-ref experiment compares favorably with observations (slope 0.97, intercept 0.00 m w.e., R^2 0.74 and relative bias −3%, i.e., underestimated net mass loss). The LIN-ref experiment compares almost as well (slope 0.95, intercept −0.02 m w.e., R^2 0.57 and relative bias −3%). Comparing across model versions using MOD albedo in **Table 2**, they are all similar and no clear winner may be identified. The same applies across the two LIN albedo experiments.

To investigate the elevation dependence of the SMB comparison, statistics are redone for sites above and below 700 m a.s.l. (above 700 m shown in blue in **Figure 4**). At high elevation sites, the MOD-ref and LIN-ref experiments on average underestimate the net mass loss by 8 and 16%, respectively. At low elevation sites, they overestimate net mass loss by 1 and 7%, respectively. The small negative bias found for all sites (−3%), is thus a result of cancelation of under- and overestimates at high and low elevation sites. To gauge the overall impact of the low- and high-elevation biases, we calculate the total long-term runoff deriving from elevations above and below 700 m a.s.l. in the MOD-ref and LIN-ref experiments. We find that in both experiments, about 38% of the total ice sheet-wide runoff derives from below 700 m a.s.l. Considering the biases (+1 and +7% at low elevations for MOD and LIN, and −8 and −16% at high) together with 38% runoff from low areas and 62% from high, suggests weighted mean ice sheet-wide mass loss biases in the ablation area of −5 and −7% for the MOD and LIN cases, respectively.

For the very largest negative observed SMBs, the model has a pronounced tendency to underestimate the mass loss, see e.g., the leftmost points in both panels of **Figure 4** corresponding to the PROMICE QAS_L site in southern Greenland [see Supplementary Table S2). In fact, considering solely the lower ablation area PROMICE sites (KAN_L, KPC_L, NUK_L, NUK_N, QAS_L, SCO_L, TAS_L, and UPE_L, situated at 468 ± 240 m a.s.l. (mean ± stddev)] yields mean underestimates of 29 and 37% for MOD and LIN, respectively.

Reasons for the significant ablation underestimation at very low-elevation sites include: (i) The 5.5 km grid size which cannot resolve some fine-scale land-ice differences near the lowest sites

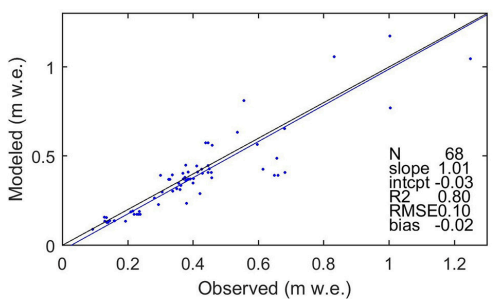

FIGURE 3 | Comparison of modeled and observed annual net accumulation (snowfall-minus-sublimation) for 68 ice cores with elevation greater than 1000 m a.s.l. The black line is 1:1 and the blue line is an orthogonal linear regression with statistics of the fit provided in the table. These are unitless except RMSE and bias (m w.e.).

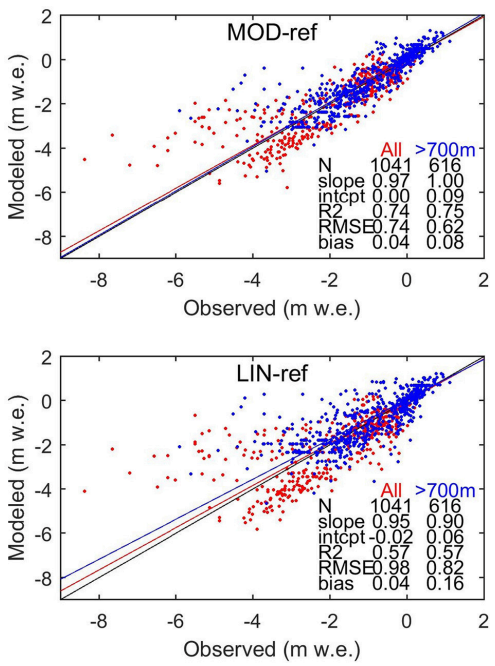

FIGURE 4 | Comparison of modeled and observed SMB at 351 ablation area sites providing a total of 1041 observations. Red dots are at sites below 700 m a.s.l. and blue above 700 m a.s.l. The red line (and the statistics in the "All" column) is an orthogonal linear fit to all 1041 observations, while the blue line is for sites above 700 m a.s.l. The statistics of the fits provided in the tables are unitless except RMSE and bias (m w.e.). The black line is 1:1. Units on the axes are in m w.e. and the observations cover uneven time intervals: some are a few months, some are 1 year and some are 2 years. Model numbers are integrated over the exact dates of the observation intervals.

(e.g., QAS_L); (ii) Jun-Aug observed vs. HIRHAM5 near-surface air temperatures at the L-sites indicate simulated cold biases of 2–3 degrees (Supplementary Table S3) giving biases in the air-to-surface temperature contrast typically of similar magnitude (ΔT bias Supplementary Table S3), which are expected to yield underestimated sensible heat input to the surface; (iii) A simplistic representation of surface roughness elements (crevasses, sub-grid undulations) may lead to underestimation of boundary layer turbulence and turbulent heat transfer (Fausto et al., 2016a,b); (iv) Average simulated albedo is overestimated at the low-level sites (Langen et al., 2015; Fausto et al., 2016b) as also shown in Supplementary Table S3. In the LIN case, the fixed bare-ice albedo of 0.4 is too high for sites like QAS_L where, for instance, July 2012 had an average *in situ* albedo of 0.21 (van As et al., 2013). Even in the MOD case, such a low value is not captured on the HIRHAM5 grid with a mean July 2012 value of 0.44 (Fausto et al., 2016b). Comparing Jun-Aug mean observed and simulated net incoming shortwave radiation (incoming minus reflected) over 2008-2014, QAS_L has model biases of −16 and −44% for MOD and LIN, respectively, as a result of positive mean albedo biases of 0.16 and 0.34 (Supplementary Table S3).

The U-sites also display a tendency for simulated near-surface air temperature cold biases but these are generally smaller than at the L-sites. At the KPC_U site (Northwest Greenland), however, where particularly the LIN case overestimates mass loss, there is a Jun-Aug mean 1.7 degree warm bias. The warm conditions allow a positive feedback between warming surface snow and lowered albedo to be activated resulting in a positive net incoming shortwave bias of 41%. Such a feedback is not active with the specified MOD albedo resulting in a small (−5%) net shortwave bias.

The 1988-2012 brightness temperature-derived melt days are compared to the simulations on the 25 km EASE grid to avoid artifacts of comparison of smoothly varying observations to finer scale variations in the model. Daily simulated fields of melt (value 1) vs. no-melt (value 0) on the 5 km HIRHAM5 grid (defined by daily total melt above 5 mm w.e. as in MAR and RACMO) are bi-linearly interpolated to the 25 km EASE grid and the resulting fractional (0–1) field is converted to melt vs. no-melt using a threshold of 0.5. Counting the melt days annually gives 25 2D fields which are compared between observations and simulations in cells where both have ice. In **Table 3**, "Bias" shows the long-term mean, ice sheet-wide sum of melt day counts as simulated relative to observation. The "Spatial" correlation and slope of orthogonal linear regression is found by calculating the long-term mean field of annual melt day counts, and the statistics are done on grid cells where either observations or model show melt (shown in **Figure 5**). The "Temporal" statistics are calculated by summing each year the melt day counts across the entire ice sheet.

The MOD versions have ∼18% too low long-term mean, ice sheet-wide melt day totals, while the LIN versions match observations closely (bias −4 to +2%). In all models, inter-annual variability in ice sheet-wide sums of melt day counts shows high correlation coefficient (∼0.9) but with too shallow slope (∼0.7) indicating that year-to-year differences are underestimated. The time-mean spatial pattern compares well in terms of correlation coefficient (∼0.9) but with too steep slopes (∼1.2), indicating too large differences between high and low melt day counts. **Figure 5** illustrates the spatial patterns and statistics of the long-term average fields. The simulated patterns are similar to observations, with the main differences related to the steep spatial regression slopes: The model tends to have too few points with few melt days and too many points with many melt days.

TABLE 3 | Statistics of comparison between observed (Mote, 2014) and simulated annual melt day counts (see text for details) over the period 1988-2012.

1988-2012		Spatial $N = 2683$		Temporal $N = 25$	
Experiment	**Bias (%)**	***r***	**Slope**	***r***	**Slope**
MOD-ref	−18	0.89	1.18	0.89	0.71
MOD-w01	−18	0.89	1.18	0.89	0.71
MOD-Swi02	−19	0.89	1.17	0.89	0.71
MOD-NoDarcy	−18	0.89	1.18	0.89	0.71
LIN-ref	+2	0.93	1.22	0.90	0.73
LIN-Swi02	−4	0.93	1.18	0.91	0.69

Slopes are for orthogonal linear fits and r denotes the correlation coefficient.

Comparing the LIN and MOD models, correlation coefficients (spatial and temporal) and slopes (spatial and temporal) are very similar, while the LIN models have a better match in terms of mean, ice sheet-wide totals. Within the LIN and MOD groups the statistics do not give a clear winner.

Subsurface Temperature and Density

Figure 6 shows the 8–10 m depth observed and simulated subsurface temperature records at the percolation area site KAN-U 1840 m above sea level (**Figure 2**). The subsurface model is generally too warm at these depths during winter (**Figure 6**) due to some combination of (i) a surface temperature warm bias (not shown) and (ii) excessive retention in the top 5 m which heats the modeled subsurface during winter. Given that the Swi02 versions of the experiments (which have a fixed S_{wi} of 0.02) display the same warm bias (not shown), excessive retained water is likely not the primary cause. In the early melt season, modeled temperatures are too low, indicating that the simulated wetting front advance is too slow. Once the wetting front has reached its maximum depth, the early-season cold bias subsides. The MOD-Swi02 and LIN-Swi02 experiments (not shown) allow, as discussed in the next section, a more rapid percolation to depth and the early melt season cold bias is less pronounced.

Two main differences between MOD-ref and LIN-ref at KAN-U are that the latter has a larger surface meltwater supply and produces a perched ice layer near 6 m depth beginning in summer 2011 (see **Figure 8**). Prior to that, the LIN experiment has a warm bias throughout the year below 5 m, while the MOD experiment is colder. In the summers following the ice layer formation in 2011, the LIN experiment is more in line with observations while the MOD experiment is too warm at depth. This difference agrees with the observed existence of an ice layer at the site in those years (Machguth et al., 2016a).

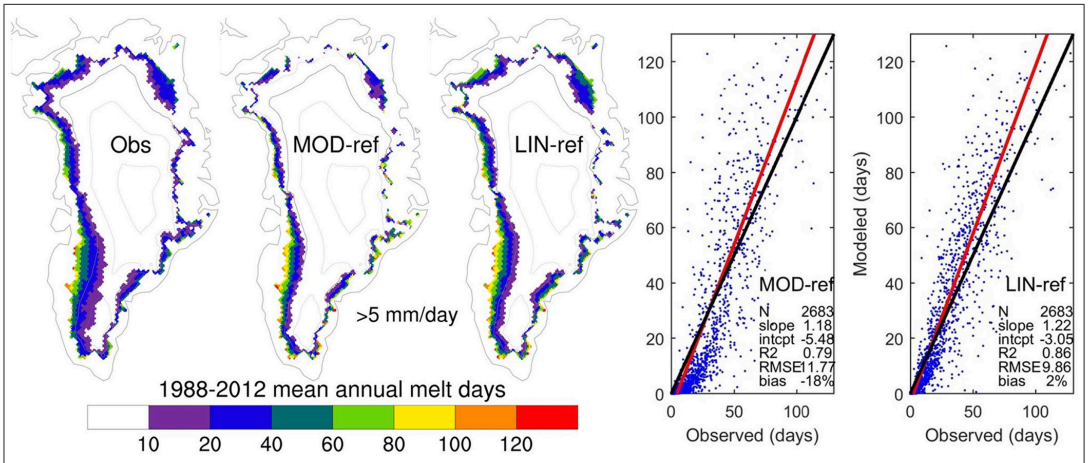

FIGURE 5 | Comparison of 1988-2012 mean observed and modeled spatial distribution of annual melt day counts on the 25 km EASE-grid (see text for details). The maps show melt day counts in grid cells where both the observed and interpolated model fields have ice. The scatter plots include only points where either observations or model show melt. The black line is 1:1 and the red line is an orthogonal linear regression with statistics of the fit provided in the table. These are unitless except RMSE (m w.e.).

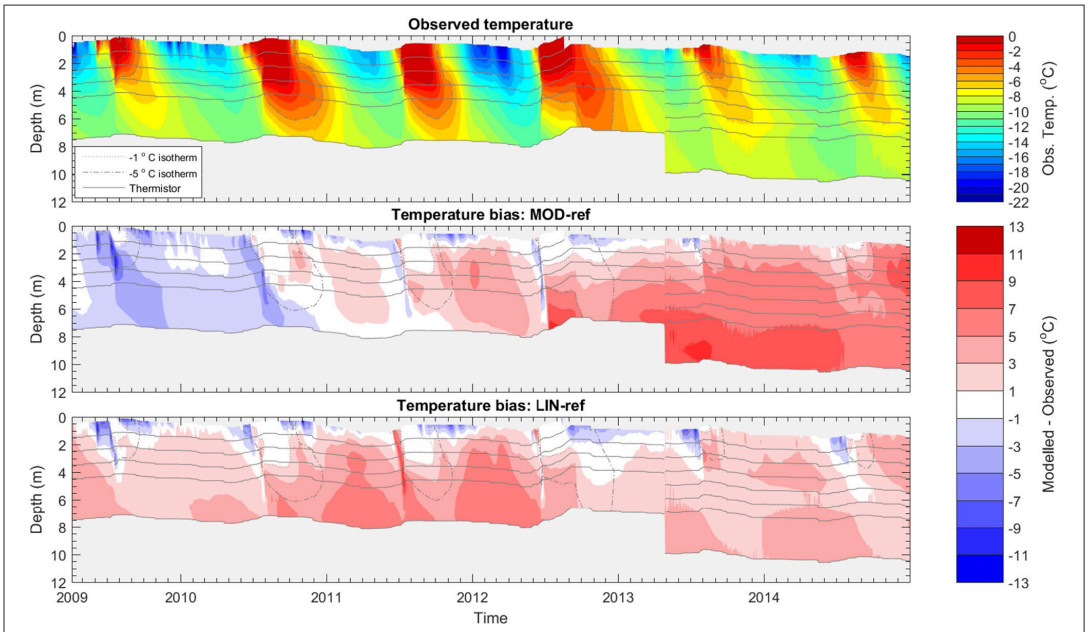

FIGURE 6 | Comparison between modeled and observed subsurface temperatures at KAN-U for 2009-2014. The positions of the thermistors are indicated by solid gray lines. In the lower panels, showing the difference between modeled and observed temperatures, the −1 and −5°C isotherms from the top panel are repeated for reference. Major ticks mark the beginning of the year.

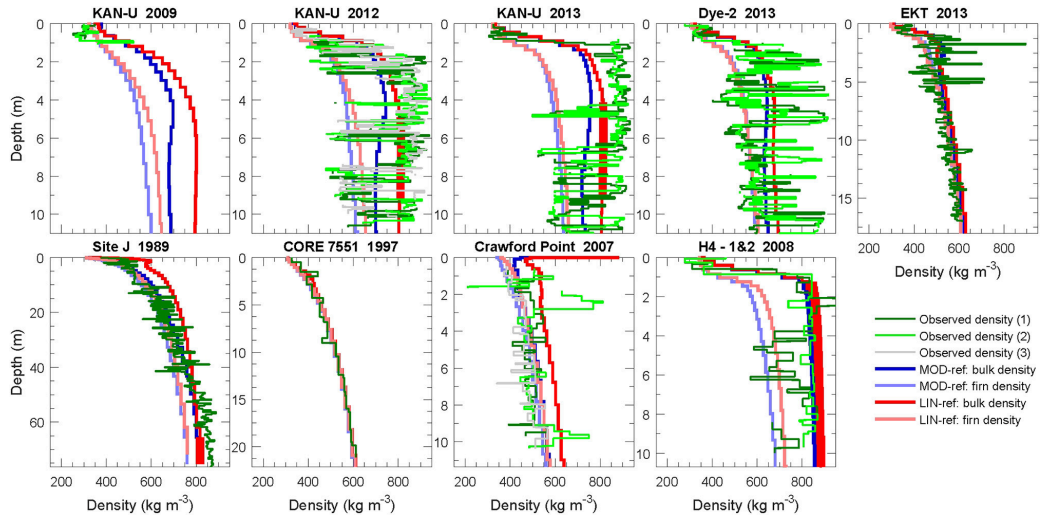

FIGURE 7 | Comparison between observed (green, light green, and gray) and modeled (blue for MOD-ref, red for LIN-ref) density profiles. Modeled bulk densities, ρ_{bulk} (Equation 12), are shown in darker blue or red while dry firn density, ρ_S, is shown in lighter shades. Modeled densities exceeding pore close-off density (810 kg m^{-3}) are shown with thicker lines.

Figure 7 shows nine comparisons of simulated and observed density profiles from MOD-ref and LIN-ref. More cores are presented in Supplementary Figures S1 and S2, showing that the following discussions apply more generally. The model gives realistic density profiles in dry snow areas such as core 7551 in **Figure 7**. In these areas, MOD-ref and LIN-ref give similar results due to limited melt.

In areas where more melt and refreezing occurs (all other panels in **Figure 7**), ice lenses of various thicknesses appear in the firn, and density profiles no longer increase monotonically with depth. At Site J for example, the smooth dry compaction profile is superimposed with sequences of higher and lower density peaks. Due to the model vertical resolution, it is not possible to recreate these thin features. However, agreement between the smoothed observed density (not shown) and modeled bulk density allows the model to accurately translate mass loss to surface lowering and calculate the thermal properties of the firn for that given resolution. On the other hand, the modeled firn density (shown in lighter shades) should match the ice-free sections of the observed density profile. In many cases, observed density profiles have low peak densities that are smaller than the modeled values, but with measurement uncertainty this overestimation of ice-free firn densities is perhaps less clear.

Wherever surface melt occurs, LIN-ref tends to give higher densities than MOD-ref because of the differences in meltwater input. In some cases it allows the LIN-ref model to reproduce observed ice lenses as shown with thick lines at KAN-U in 2012 and 2013. At other sites, such as Site J, LIN-ref clearly overestimates subsurface densities while MOD-ref fits the observed profile better.

The KAN-U core from 2009 only recorded densities to 1 m depth and stratigraphy down to 3 m and did not show any major ice lenses at shallow depth. In the cores from spring 2012, numerous ice layers are observed with some spatial variability (differences between multiple observed profiles). There, LIN-ref has reached pore close off at 5 m depth and replicates this densification process. The cores from spring 2013 show how the ice lens complexes had merged into a consistent ice layer. Accordingly the impermeable layer in LIN-ref also increased in thickness. A good spatial match is also visible on the EGIG line (first 15 panels in Supplementary Figure S2, ordered in decreasing altitude). The LIN-ref model reaches pore close off at the same sites where ice lenses and higher densities become frequent in the cores (from GGU163 to H2-1, differing only by 100 m in altitude). The MOD-ref model, however, reaches pore close off lower on this transect.

The observed density profiles at DYE-2 show a similar stratigraphy to what was observed at KAN-U before saturation of the near-surface firn and may potentially undergo a similar transformation. The EKT and Crawford Point cores also show increased ice features and density near the surface and can also potentially follow the same path. It is satisfactory to see the simulated density profile represent this near-surface densification due to increased refreezing in recent years. On the other end of the spectrum, sites like H4 show a stratigraphy where meltwater refreezing has filled most pore space except for isolated firn pockets at depth. Accordingly, simulated densities have reached pore close off at that site and surface melt is unable to percolate to depth.

SENSITIVITY RESULTS

Subsurface Temperature and Water Profiles

Figure 8 shows the simulated development of the subsurface (uppermost 10 m) temperature at KAN-U in different experiments. The long term variability in MOD-ref indicates relatively cold conditions in the 1990s, a somewhat warmer subsurface in the 2000s and widespread near-temperate conditions throughout the top 10 m in the 2010s. The 2000s heating is even more pronounced in the MOD-Swi02 experiment which differs from MOD-ref only in the parameterization for S_{wi} allowing considerably less water to be retained by capillary forces. As a result, surface meltwater is transferred more readily to depth thereby eroding the cold content. The MOD-NoDarcy experiment has the same irreducible saturation as MOD-ref but allows instantaneous downward percolation of water in excess of irreducible saturation. While this leads to differences between the two experiments on daily timescales (evident for liquid water content in the zoomed **Figure 9**), their resulting temperature structures are practically indistinguishable in **Figure 8**, even though daily values are, in fact, plotted.

Using the LIN albedo results in a larger meltwater supply at the KAN-U site leading to higher subsurface temperatures than in the corresponding MOD experiments, i.e., LIN-ref is warmer than MOD-ref and LIN-Swi02 is warmer than MOD-Swi02. The deeper penetration of latent heating with Swi02 than with SwiCL is seen also for LIN in the summers 2008-2010. In July 2011, however, a drastic difference emerges in that the 810 kg m^{-3} contour becomes visible in LIN-ref indicating the presence of impermeable layers. The larger capacity of the SwiCL formulation to retain water allows enough of the percolating meltwater to refreeze and initiate an ice layer. As the season progresses with latent heat supply cut off from above, the ice layer can grow from below from retained meltwater supplied before it was formed. In the following winter, the layer is gradually cooled and buried by snow accumulation. However, when the 2012 meltwater front reaches the layer, the thickness grows again from above. The subsequent summers 2013 and 2014 add further mass to the layer from above (in accordance with observations; Machguth et al., 2016a) but not enough to compensate the winter burial. The net effect is therefore a downward motion of the ice layer after the end of the 2012 melt season.

Figure 9 illustrates the differences in subsurface liquid water content ($L = p_w/p_s$) arising due to the presence of the perched ice layer in LIN-ref but also to different choices of w_h/w_{ice} and Darcy vs. NoDarcy. The presence of the ice layer in LIN-ref leads to an accumulation of liquid water on top which increases as long as supply from percolation continues. Two large melt events took place in July 2012 (Fausto et al., 2016b) during which this accumulation of liquid water is evident. In the intervening period, July 12 (day 194) to July 26 (day 208), runoff from the column lowers the liquid water level. The high levels of water in excess of the irreducible saturation leads to runoff from the time water starts accumulating atop the ice layer until late in the autumn season rather than being distributed over large depths as in the three left panels.

The distribution of liquid water content in MOD-ref vs. MOD-w01 shows the impact of reducing the hydraulic conductivity of the layers. Reduced conductivity in MOD-w01 slows the downward flow and allows for greater vertical gradients in liquid water to build up before being released. Such buildup of vertical gradients leads to a more intermittent downward flow

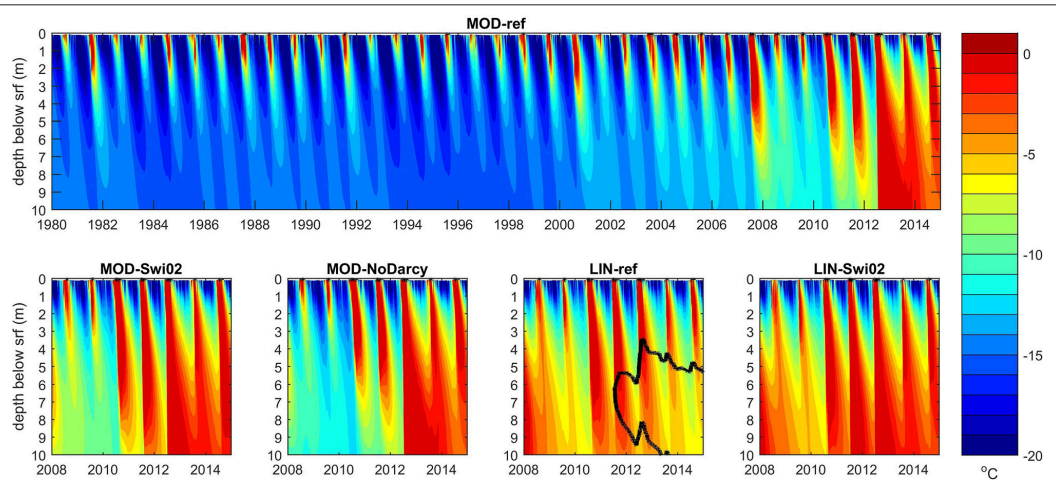

FIGURE 8 | Daily mean temperature at KAN-U of the upper 10 m for 1980-2014 for MOD-ref and for 2008-2014 for other selected experiments. The black solid line marks the $\rho_{bulk} = 810$ kg m^{-3} contour indicating the presence of impermeable layers.

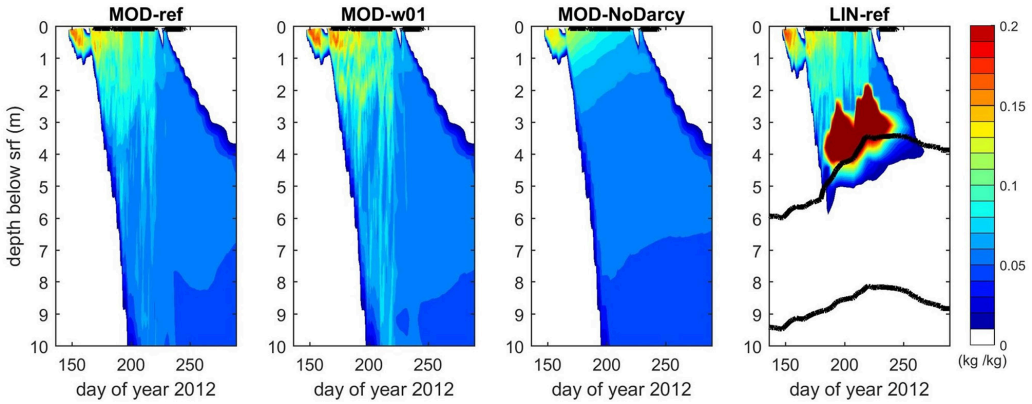

FIGURE 9 | Mass liquid water content ($L = p_w/p_s$) of the upper 10 m at KAN-U for days 136–289 (May 15–Oct 15) of 2012 for selected experiments. The black solid lines mark the $\rho_{bulk} = 810\,kg\,m^{-3}$ contour indicating the presence of impermeable layers. In the rightmost panel, the accumulating water leads to values of up to 0.5, beyond the range of the color bar.

pattern but not to formation of an impermeable layer. Opposite is the MOD-NoDarcy experiment in which excess water percolates instantaneously, leading to a gradual rather than intermittent evolution of the water field.

Since surface accumulation and percolation leads to simulated vertical shifting of mass, an ice layer effectively diffuses with time if no new mass is top-accreted after formation. A greater amount of meltwater is thus needed for the buildup of an ice layer that can survive the winter and still block percolation the next melt season. This could explain why MOD models do not form a sustainable ice layer at KAN-U.

Large-Scale Patterns of Perched Ice, Liquid Water, and Runoff

Figure 10 shows the distribution of perched ice layers over the years 2012-2014 along with the April 2014 distribution of perennial firn aquifers. Perched ice layers are identified from the three-dimensional field of ρ_{bulk} averaged over April: searching from the surface and downward, if one or more layers have $\rho_{bulk} \geq 810\,kg\,m^{-3}$ followed by $\rho_{bulk} < 810\,kg\,m^{-3}$, then that grid cell has an identified perched ice layer. Perched ice layers determined in this manner are present in a narrow band (typically 3–6 grid cells) going from the southwest up the west coast and around the north and northeast, and in some cases interrupted in the west and northwest by perennial firn aquifers.

The spatial distribution of perennial firn aquifers in the south matches qualitatively that found by Forster et al. (2014) in firn cores, airborne radar surveys and the regional climate model RACMO2. As in RACMO2, the modeled perennial firn aquifers consist entirely of water held within the irreducible saturation, since excess water has percolated further and refrozen or run off during autumn. The column total water content is thus tightly controlled by the parameterization of S_{wi} and our Swi02 experiments are directly comparable to the RACMO2 results. As discussed by Kuipers Munneke et al. (2014), the existence of perennial firn aquifers requires high annual accumulation rates and moderate to high summer melt or rainfall. In addition to the areas in the southeast discussed by Forster et al. (2014), our model simulates these conditions also in several places in the west and northwest.

Comparing cases with SwiCL and Swi02 (i.e., MOD-ref vs. MOD-Swi02 and LIN-ref vs. LIN-Swi02), the perched ice layers are more widespread with SwiCL. The KAN-U site is, as illustrated in **Figure 8**, one such location where SwiCL, but not Swi02, allows an ice layer to emerge (in the LIN case). The higher retention of water in still cool near-surface layers apparently favors the formation of the perched ice layer.

Even though **Figure 9** showed how daily variations in the subsurface water field and downward flow depend crucially on the implementation of hydraulic conductivity (MOD-ref vs. MOD-w01 vs. MOD-NoDarcy), it is apparently not important for the large-scale distribution of perched ice layers and perennial firn aquifers. It appears that the seasonal supply of meltwater, accumulation and irreducible saturation are important and not the exact timing of the downward flow on time-scales of days. This is a useful result for climate models, as it implies that capturing short-term variability is not as important as accurately capturing longer-term precipitation and snowpack processes.

Figure 11 shows differences in total runoff averaged over the years 2012-2014 arising due to the different model implementations. The top row shows the runoff in the MOD-ref and LIN-ref experiments and below is shown the difference between them. The LIN albedo promotes higher melting across the north, likely contributing to the more widespread occurrence of perched ice layers in that area in LIN-ref (**Figure 10**). In most of the west, south and east, however, the MOD experiment produces larger runoff rates. One exception is the green band

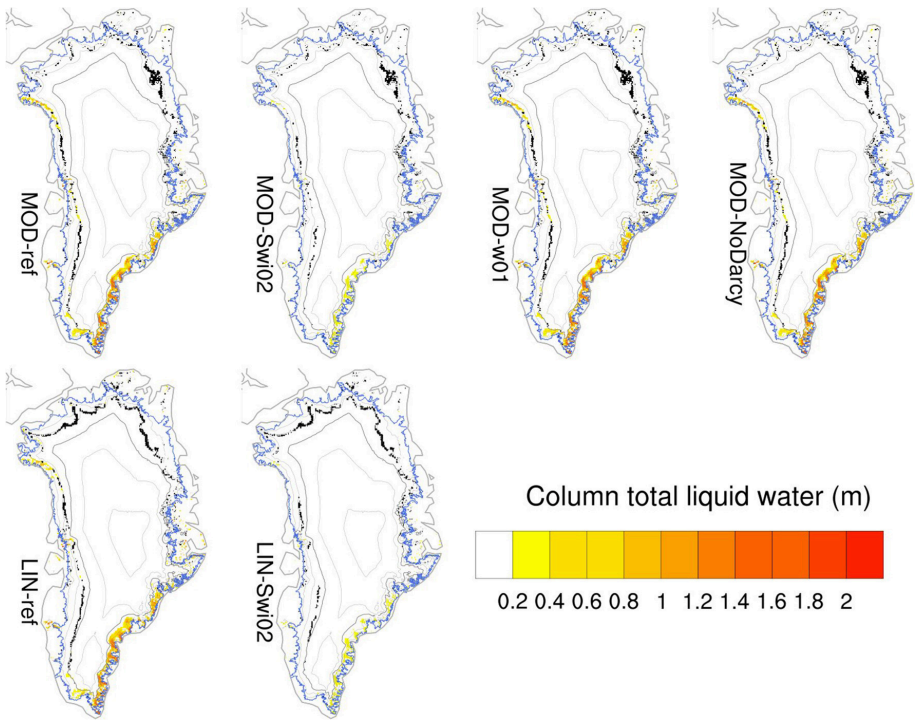

FIGURE 10 | Distribution of ice layers (i.e., existence of layers with $\rho_{bulk} \geq 810\,kg\,m^{-3}$ above less dense layers) in April of years 2012-2014 in black, and distribution of total column liquid water in April 2014 in reds. All panels include elevation contours (1000–3000 m a.s.l. in steps of 500 m with 2000 m a.s.l. highlighted) and outline of the contiguous ice sheet (blue).

inland of the yellow band in the west, indicating a higher runoff line in the LIN case.

The choice of albedo implementation is by far the most important factor for runoff. This is illustrated by the three remaining panels which have been multiplied by a factor of 10 for differences to appear. Again, the choice of Darcy vs. NoDarcy is particularly unimportant. In both the MOD (bottom left) and LIN (bottom right) cases, the choice of SwiCL vs. Swi02 has some impact. With exceptions, there is a general pattern of areas with perennial firn aquifers (south and southeast) giving less runoff with SwiCL and areas with perched ice layers (west and north) giving more runoff with SwiCL. This is to be expected since, in the absence of an ice layer, a higher S_{wi} allows more water to be retained in the column and refrozen during the following winter. In the presence of an ice layer, the meltwater accumulating on top (as seen in **Figure 9**) leads to runoff rather than deep percolation.

Greenland-wide time-series of calendar-year total runoff and SMB are shown in **Figure 12**. Clearly discernible are the differences between the MOD and LIN cases, while the differences between SwiCL and Swi02 are very small. This is due both to the smallness of the differences in the lower row of **Figure 11** (multiplied by a factor of 10) but also the competing effects from the perennial firn aquifer and perched ice layer areas. The MODIS-driven experiments employ an average 2000-2006 daily albedo climatology in the period before 2000. This reduces the inter-annual variability and leads to larger differences from the LIN experiments in runoff (and, consequently, SMB) in the pre-2000 period. In the post-2000 period with direct MODIS-derived albedos, there is better agreement on the variability.

CONCLUSIONS

The subsurface scheme of the regional climate model HIRHAM5 has been extended to include firn densification, grain size growth, snow state-dependent hydraulic conductivity and irreducible water saturation as well as retention of water in excess of the irreducible saturation and superimposed ice formation. Sensitivity experiments have been performed to gauge both small- and large-scale effects of these additions as well as the impact of different parameterization choices.

The model results compare favorably with 68 ice core-derived annual net accumulation rates (spatial correlation coefficient

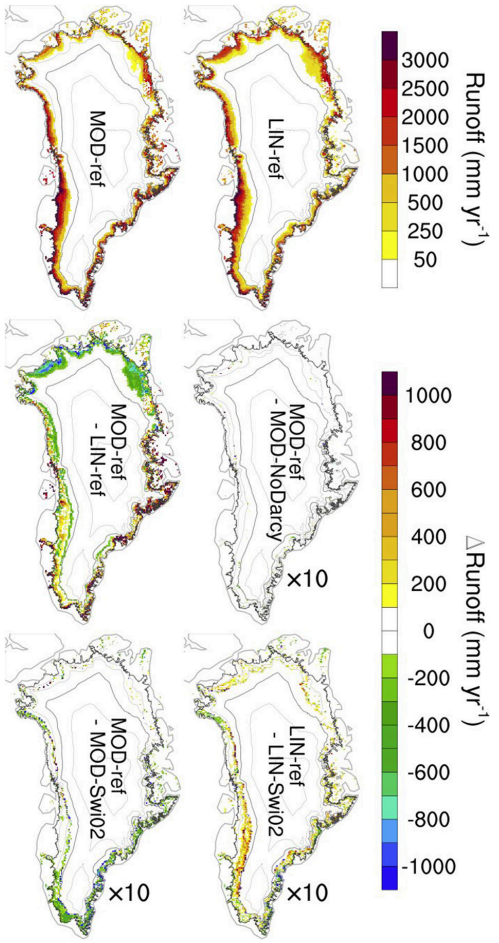

FIGURE 11 | (Upper row) Annual runoff (averaged over years 2012-2014) for experiments MOD-ref and LIN-ref. (Lower rows) Runoff differences between selected experiments. The last three have been multiplied by 10 to aid visualization. All panels include elevation contours (1000–3000 m a.s.l. in steps of 500 m with 2000 m a.s.l. highlighted) and outline of the contiguous ice sheet.

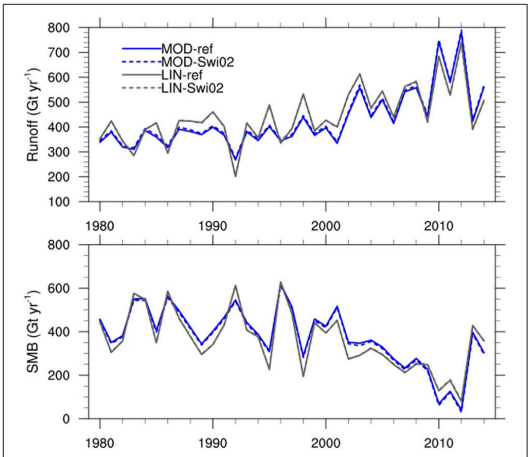

FIGURE 12 | Greenland-wide annual runoff and SMB from selected experiments.

of 0.90 and mean bias −5%). In the ablation area, simulated SMBs compare very well with 1041 observations with regression slopes of 0.97 and 0.95, and correlation coefficients of 0.86 and 0.75 for MOD-ref and LIN-ref, respectively. Mean biases are −3%, indicating only slightly underestimated net mass loss rates. The low mean bias is, however, partially due to a cancelation of under- and overestimates at high and low elevation sites. Splitting the sites between those above and below 700 m a.s.l. and weighting the resulting biases with the amount of runoff deriving from low vs. higher elevations results in weighted ice sheet-wide mass loss biases in the ablation area of −5 and −7% for MOD and LIN, respectively. These numbers do not depend significantly on other model choices (Darcy, S_{wi} and w_h/w_{ice}).

Comparing observed and simulated annual melt day counts shows that the spatial and temporal patterns of variability are reliably represented in the model, while it tends to underestimate the magnitude of inter-annual variability and overestimate that of spatial variability. As for the SMB comparison, the choice of albedo dominates the differences and the statistics do not allow for a best choice of the other model settings to be determined.

The mechanism for vertical flow (Darcy vs. NoDarcy and w_h/w_{ice} set to 1 vs. 0.1) has an impact on short time-scale features of the subsurface liquid water field, but appears unimportant for the seasonal-scale temperature structure and for the large-scale mass balance field.

Two model choices do influence the subsurface temperature at KAN-U on longer time-scales, namely albedo and S_{wi}. Prior to the formation of the ice lens, a larger meltwater production in LIN leads to a perennial warm bias below 5 m. Setting S_{wi} to 0.02, rather than parameterized according to Coleou and Lesaffre (1998), allows water to percolate more readily to depth in the early melt season and reduces the cold bias otherwise present in the model at that time of year with both LIN and MOD. On the other hand, using the Coleou and Lesaffre (1998) parameterization in combination with LIN albedo allows for formation of an ice layer in agreement with observations (**Figure 7** and Machguth et al., 2016a). This, in turn, shields the deeper part from latent heating from refreezing and reduces the warm bias at depth.

The model combinations without a perched ice layer at KAN-U do not produce runoff there over the 2009-2014 period, while LIN-ref generates 132 mm in 2010 and 583 mm in 2012. This agrees with the 690 ± 150 mm runoff in 2012 derived from

comparison of spring 2012 and 2013 firn core stratigraphies by Machguth et al. (2016a) at KAN-U. This increase in runoff line altitude with the LIN-ref combination (also seen in **Figure 11**) is a direct consequence of the perched ice layer formation, and modeling this accurately appears crucial in a warming climate where more meltwater would be available in the percolation area. While the appearance of the perched ice layer at KAN-U is in line with observations, this does not necessarily imply that the LIN-ref combination is better than the others. As seen in **Figure 10**, perched ice layers do form also with MOD and Swi02 in different combinations; just not exactly at KAN-U.

Perennial firn aquifers occur in the south and southeast in patterns corresponding to those found by Forster et al. (2014) and continue up the west coast interrupted by areas with perched ice layers. These areas with perennial firn aquifers are not much impacted by the choice of SwiCL vs. Swi02, but the total amount of water in the aquifers is. This is because the perennial firn aquifer water consists entirely of water held within the irreducible saturation. In areas of perennial firn aquifers, SwiCL generally leads to less runoff because more water is held back against runoff in the summer and fall and remains available for refreezing in winter.

The fact that water exits the model domain once it runs off from a column may influence our results. If water instead flowed to neighboring grid columns (at the surface or at the depth from which it runs off), it would become part of the water budget of that cell. This could potentially increase the magnitude or areal extent of both perched ice layers and perennial firn aquifers. Addition of a representation of lateral flow and routing of water along with vertical piping could potentially alter the current conclusions and should be the focus of further developments.

As perched ice layers form, water which would otherwise have percolated and refrozen at deeper levels end up contributing to runoff instead. This is visible in large-scale runoff maps, but in a Greenland-wide accumulated sense, this is more or less negligible in the model's current climate. In general, the same is true for details of the percolation mechanism and retention parameterizations: they matter for local-scale subsurface temperature, snow, ice and water fields; but for the Greenland-wide runoff and SMB, the major impact is from the choice of albedo implementation. Whether the large-scale effects of perennial firn aquifers and perched ice layers will change in a warmer climate is not yet clear.

AUTHOR CONTRIBUTIONS

PL led the development of the subsurface model, performed the subsurface experiments and led writing of the manuscript. RF, BV, and RM contributed to development of the subsurface model and RM performed the HIRHAM5 atmospheric model experiment. PL, BV, and JB performed comparisons of model output to observations. All authors contributed to discussions and writing of the manuscript.

FUNDING

This work is supported by the Retain project, funded by the Danish Council for Independent research (Grant no. 4002-00234).

ACKNOWLEDGMENTS

We are grateful to the three reviewers for their thorough and insightful input that lead to considerable improvements of the paper. We thank J. Harper, T. Kameda, M. Macferrin, H. Machguth, E. Mosley-Thompson, and D. van As for providing density profiles. The PARCA cores are available at http://research.bpcrc.osu.edu/Icecore/data/ and their collection was supported by NASA grants NAG5-5032 and 6817 to the Ohio State University, NASA grants NAG5-5031 and 6779 to the University of Arizona, and NASA grant NAGW-4248 and NSF/OPP grant 9423530 to the University of Colorado. The ACT campaigns were supported by NASA (grant NNX10AR76G), by the Greenland Analog Project (GAP), by the REFREEZE project, by the RETAIN project (DFF grant 4002-00234) and by the Programme for Monitoring of the Greenland Ice Sheet (PROMICE). PROMICE data are freely accessible at http://promice.org as is HIRHAM5 output at http://prudence.dmi.dk/data/temp/RUM/HIRHAM/GL2.

SUPPLEMENTARY MATERIAL

The Supplementary Material for this article can be found online at: http://journal.frontiersin.org/article/10.3389/feart.2016.00110/full#supplementary-material

REFERENCES

Ahlstrøm, A., Gravesen, P., Andersen, S., Van As, D., Citterio, M., Fausto, R., et al. (2008). A new programme for monitoring the mass loss of the Greenland ice sheet. *Geol. Surv. Den. Greenland Bull.* 15, 61–64. Available online at: http://www.geus.dk/DK/publications/geol-survey-dk-gl-bull/15/Documents/nr15_p61-64.pdf

Benson, C. S. (1962). *Stratigraphic Studies in the Snow and Firn of the Greenland Ice Sheet*. SIPRE, (CRREL) Research Report 70, reprinted with revisions by CRREL, 1996.

Box, J. E., Cressie, N., Bromwich, D. H., Jung, J.-H., van den Broeke, M., van Angelen, J. H., et al. (2013). Greenland ice sheet mass balance reconstruction. Part I: net snow accumulation (1600–2009). *J. Climate* 26, 3919–3934. doi: 10.1175/JCLI-D-12-00373.1

Box, J. E., Fettweis, X., Stroeve, J. C., Tedesco, M., Hall, D. K., and Steffen, K. (2012). Greenland ice sheet albedo feedback: thermodynamics and atmospheric drivers. *Cryosphere* 6, 821–839. doi: 10.5194/tc-6-821-2012

Braithwaite, R. J., W. Tad Pfeffer, Blatter, A., and Humphrey, N. F. (1992). "Meltwater refreezing in the accumulation area of the Greenland Ice Sheet, Pakitsoq Region, Summer 1991," in *Current Research, Greenland Geological Survey Report of Activities,* Report No. 155, 13–17.

Braithwaite, R., Laternser, M., and Pfeffer, W. (1994). Variations of near-surface firn density in the lower accumulation area of the Greenland ice sheet, Pakitsoq, West Greenland. *J. Glaciol.* 40, 477–485.

Brun, E. (1989). Investigation on wet-snow metamorphism in respect of liquid-water content. *Ann. Glaciol.* 13, 22–26.

Calonne, N., Geindreau, C., Flin, F., Morin, S., Lesaffre, B., Rolland du Roscoat, S., et al. (2012). 3-D image-based numerical computations of snow permeability: links to specific surface area, density, and microstructural anisotropy. *Cryosphere* 6, 939–951. doi: 10.5194/tc-6-939-2012

Charalampidis, C., van As, D., Box, J. E., van den Broeke, M. R., Colgan, W. T., Doyle, S. H., et al. (2015). Changing surface–atmosphere energy exchange and refreezing capacity of the lower accumulation area, West Greenland. *Cryosphere* 9, 2163–2181. doi: 10.5194/tc-9-2163-2015

Christensen, O., Drews, M., Christensen, J., Dethloff, K., Ketelsen, K., Hebestadt, I., et al. (2006). *The HIRHAM Regional Climate Model, Version 5*. Available online at: http://www.dmi.dk/fileadmin/Rapporter/TR/tr06-17.pdf

Church, J. A., Clark, P. U., Cazenave, A., Gregory, J. M., Jevrejeva, S., Levermann, A., et al. (2013). "Sea level change," in *Climate Change 2013: The Physical Science Basis. Contribution of Working Group I to the Fifth Assessment Report of the Intergovernmental Panel on Climate Change*, eds T. F. Stocker, D. Qin, G.-K. Plattner, M. M. B. Tignor, S. K. Allen, J. Boschung, A. Nauels, Y. Xia, V. Bex, and P. M. Midgley (Cambridge; New York, NY: Cambridge University Press), 1137–1216. Available online at: www.climatechange2013.org

Cogley, J. G., Hock, R., Rasmussen, L. A., Arendt, A. A., Bauder, A., Braithwaite, R. J., et al. (2011). *Glossary of Glacier Mass Balance and Related Terms*. IHP-VII Technical Documents in Hydrology No. 86, IACS Contribution No. 2, UNESCO-IHP, Paris.

Colbeck, S. (1972). A theory of water percolation in snow. *J. Glaciol.* 11, 369–385.

Colbeck, S. (1974). The capillary effects on water percolation in homogeneous snow. *J. Glaciol.* 13, 85–97.

Colbeck, S. (1975). A theory for water flow through a layered snowpack. *Water Resour. Res.* 11, 261–266. doi: 10.1029/WR011i002p00261

Coleou, C., and Lesaffre, B. (1998). Irreducible water saturation in snow: experimental results in a cold laboratory. *Ann. Glaciol.* 26, 64–68.

Cuffey, K. M., and Paterson, W. S. B. (2010). *The Physics of Glaciers*. Amsterdam: Elsevier Science, 704.

Dee, D. P., Uppala, S. M., Simmons, A. J., Berrisford, P., Poli, P., Kobayashi, S., et al. (2011). The ERA-Interim reanalysis: configuration and performance of the data assimilation system. *Q. J. R. Meteorol. Soc.* 137, 553–597. doi: 10.1002/qj.828

de la Peña, S., Howat, I. M., Nienow, P. W., van den Broeke, M. R., Mosley-Thompson, E., Price, S. F., et al. (2015). Changes in the firn structure of the western Greenland Ice Sheet caused by recent warming. *Cryosphere* 9, 1203–1211. doi: 10.5194/tc-9-1203-2015

Dumont, M., Brun, E., Picard, G., Michou, M., Libois, Q., Petit, J.-R., et al. (2014). Contribution of light-absorbing impurities in snow to Greenland's darkening since 2009. *Nat. Geosci* 7, 509–512. doi: 10.1038/ngeo2180

Eerola, K. (2006). About the performance of HIRLAM version 7.0. *HIRLAM Newslett.* 51, 93–102. Available online at: http://hirlam.org/index.php/hirlam-documentation/doc_view/473-hirlam-newsletter-no-51-article14-eerola-performance-hirlam7-0

Fausto, R. S., van As, D., Box, J. E., Colgan, W., and Langen, P. L. (2016a). Quantifying the surface energy fluxes in south Greenland during the 2012 high melt episodes using *in situ* observations. *Front. Earth Sci.* 4:82. doi: 10.3389/feart.2016.00082

Fausto, R. S., van As, D., Box, J. E., Colgan, W., Langen, P. L., and Mottram, R. H. (2016b). The implication of nonradiative energy fluxes dominating Greenland ice sheet exceptional ablation area surface melt in 2012. *Geophys. Res. Lett.* 43, 2649–2658. doi: 10.1002/2016GL067720

Fettweis, X. (2007). Reconstruction of the 1979–2006 Greenland ice sheet surface mass balance using the regional climate model MAR. *Cryosphere* 1, 21–40. doi: 10.5194/tc-1-21-2007

Forster, R. R., Box, J. E., van den Broeke, M. R., Miege, C., Burgess, E. W., van Angelen, J. H., et al. (2014). Extensive liquid meltwater storage in firn within the Greenland ice sheet. *Nat. Geosci.* 7, 95–98. doi: 10.1038/ngeo2043

Gascon, G., Sharp, M., Burgess, D., Bezeau, P., and Bush, A. B. G. (2013). Changes in accumulation-area firn stratigraphy and meltwater flow during a period of climate warming: Devon Ice Cap, Nunavut, Canada. *J. Geophys. Res. Earth Surf.* 118, 2380–2391. doi: 10.1002/2013jf002838

Gregory, J. M., White, N. J., Church, J. A., Bierkens, M. F. P., Box, J. E., van den Broeke, M. R., et al. (2013). Twentieth-century global-mean sea level rise: is the whole greater than the sum of the parts? *J. Climate* 26, 4476–4499. doi: 10.1175/JCLI-D-12-00319.1

Gregory, S. A., Albert, M. R., and Baker, I. (2014). Impact of physical properties and accumulation rate on pore close-off in layered firn. *Cryosphere* 8, 91–105. doi: 10.5194/tc-8-91-2014

Harper, J., Humphrey, N., Pfeffer, W. T., Brown, J., and Fettweis, X. (2012). Greenland ice-sheet contribution to sea-level rise buffered by meltwater storage in firn. *Nature* 491, 240–243. doi: 10.1038/nature11566

Hirashima, H., Yamaguchi, S., Sato, A., and Lehning, M. (2010). Numerical modeling of liquid water movement through layered snow based on new measurements of the water retention curve. *Cold Regions Sci. Technol.* 64, 94–103. doi: 10.1016/j.coldregions.2010.09.003

Howat, I. M., de la Peña, S., van Angelen, J. H., Lenaerts, J. T. M., and van den Broeke, M. R. (2013). Brief Communication "Expansion of meltwater lakes on the Greenland Ice Sheet." *Cryosphere* 7, 201–204. doi: 10.5194/tc-7-201-2013

Humphrey, N. F., Harper, J. T., and Pfeffer, W. T. (2012). Thermal tracking of meltwater retention in Greenland's accumulation area. *J. Geophys. Res. Earth Surf.* 117:F01010. doi: 10.1029/2011jf002083

Janssens, I., and Huybrechts, P. (2000). The treatment of meltwater retention in mass-balance parameterisations of the Greenland ice sheet. *Ann. Glaciol.* 31, 133–140. doi: 10.3189/172756400781819941

Kameda, T., Narita, H., Shoji, H., Nishio, F., Fujii, Y., and Watanabe, O. (1995). Melt features in ice cores from Site J, southern Greenland: some implications for summer climate since AD 1550. *Ann. Glaciol.* 21, 51–58.

Katsushima, T., Kumakura, T., and Takeuchi, Y. (2009). A multiple snow layer model including a parameterization of vertical water channel process in snowpack. *Cold Regions Sci. Technol.* 59, 143–151. doi: 10.1016/j.coldregions.2009.09.002

Keegan, K. M., Albert, M. R., McConnell, J. R., and Baker, I. (2014). Climate change and forest fires synergistically drive widespread melt events of the Greenland Ice Sheet. *Proc. Natl. Acad. Sci. U.S.A.* 111, 7964–7967. doi: 10.1073/pnas.1405397111

Koenig, L. S., Miège, C., Forster, R. R., and Brucker, L. (2014). Initial *in situ* measurements of perennial meltwater storage in the Greenland firn aquifer. *Geophys. Res. Lett.* 41, 81–85. doi: 10.1002/2013GL058083

Kuipers Munneke, P. M., Ligtenberg, S. R., van den Broeke, M. R., van Angelen, J. H., and Forster, R. R. (2014). Explaining the presence of perennial liquid water bodies in the firn of the Greenland Ice Sheet. *Geophys. Res. Lett.* 41, 476–483. doi: 10.1002/2013GL058389

Langen, P. L., Mottram, R. H., Christensen, J. H., Boberg, F., Rodehacke, C. B., Stendel, M., et al. (2015). Quantifying energy and mass fluxes controlling Godthåbsfjord freshwater input in a 5 km simulation (1991–2012). *J. Climate.* 28, 3694–3713. doi: 10.1175/jcli-d-14-00271.1

Lefebre, F., Gallée, H., van Ypersele, J.-P., and Greuell, W. (2003). Modeling of snow and ice melt at ETH Camp (West Greenland): a study of surface albedo. *J. Geophys. Res.* 108:4231. doi: 10.1029/2001jd001160

Ligtenberg, S. R. M., Helsen, M. M., and van den Broeke, M. R. (2011). An improved semi-empirical model for the densification of Antarctic firn. *Cryosphere* 5, 809–819. doi: 10.5194/tc-5-809-2011

Lucas-Picher, P., Wulff-Nielsen, M., Christensen, J. H., Ağalgeirsdóttir, G., Mottram, R., and Simonsen, S. B. (2012). Very high resolution regional climate model simulations over Greenland: identifying added value. *J. Geophys. Res.* 117:D02108. doi: 10.1029/2011jd016267

Machguth, H., MacFerrin, M., van As, D., Box, J. E., Charalampidis, C., Colgan, W., et al. (2016a). Greenland meltwater storage in firn limited by near-surface ice formation. *Nature Clim. Change* 6, 390–393. doi: 10.1038/nclimate2899

Machguth, H., Thomsen, H. H., Weidick, A., Ahlstrøm, A. P., Abermann, J., Andersen, M. L., et al. (2016b). Greenland surface mass-balance observations from the ice-sheet ablation area and local glaciers. *J. Glaciol.* 62, 861–887. doi: 10.1017/jog.2016.75

Mosley-Thompson, E., McConnell, J. R., Bales, R. C., Li, Z., Lin, P.-N., Steffen, K., et al. (2001). Local to regional-scale variability of annual net accumulation on the Greenland ice sheet from PARCA cores. *J. Geophys. Res.* 106, 33839–33851. doi: 10.1029/2001JD900067

Mote, T. L. (2007). Greenland surface melt trends 1973–2007: evidence of a large increase in 2007. *Geophys. Res. Lett.* 34, L22507. doi: 10.1029/2007GL031976

Mote, T. L. (2014). MEaSUREs Greenland Surface Melt Daily 25km EASE-Grid 2.0. Boulder, CO: NASA DAAC at the National Snow and Ice Data Center. doi: 10.5067/MEASURES/CRYOSPHERE/nsidc-0533.001

Mote, T. L., and Anderson, M. R. (1995). Variations in snowpack melt on the Greenland ice sheet based on passive microwave measurements. *J. Glaciol.* 41, 51–60.

Müller, F. (1976). On the thermal regime of a high arctic valley glacier. *J. Glaciol.* 16, 119–133.

Oerlemans, J., and Knap, W. (1998). 1 year record of global radiation and albedo in the ablation zone of Morteratschgletscher, Switzerland. *J. Glaciol.* 44, 231–238.

Parry, V., Nienow, P., Mair, D., Scott, J., Hubbard, B., Steffen, K., et al. (2007). Investigations of meltwater refreezing and density variations in the snowpack and firn within the percolation zone of the Greenland ice sheet. *Ann. Glaciol.* 46, 61–68. doi: 10.3189/172756407782871332

Pfeffer, W. T., Meier, M. F., and Illangasekare, T. H. (1991). Retention of Greenland runoff by refreezing: implications for projected future sea level change. *J. Geophys. Res.* 96, 22117–22124. doi: 10.1029/91JC02502

Polashenski, C., Courville, Z., Benson, C., Wagner, A., Chen, J., Wong, G., et al. (2014). Observations of pronounced Greenland ice sheet firn warming and implications for runoff production. *Geophys. Res. Lett.* 41:2014GL059806. doi: 10.1002/2014GL059806

Reeh, N. (1989). Parameterization of melt rate and surface temperature on the Greenland ice sheet. *Polarforschung* 59, 113–128.

Reijmer, C. H., van den Broeke, M. R., Fettweis, X., Ettema, J., and Stap, L. B. (2012). Refreezing on the Greenland ice sheet: a comparison of parameterizations. *Cryosphere* 6, 743–762. doi: 10.5194/tc-6-743-2012

Roeckner, E., Bäuml, G., Bonaventura, L., Brokopf, R., Esch, M., Giorgetta, M., et al. (2003). *The Atmospheric General Circulation Model ECHAM5. Part I: Model Description*. Available online at: http://www.mpimet.mpg.de/fileadmin/publikationen/Reports/max_scirep_349.pdf

Shimizu, H. (1970). Air permeability of deposited snow. *Contribut. Instit. Low Temp. Sci.* A22, 1–32.

Tedesco, M., Doherty, S., Fettweis, X., Alexander, P., Jeyaratnam, J., and Stroeve, J. (2016). The darkening of the Greenland ice sheet: trends, drivers, and projections (1981–2100). *Cryosphere* 10, 477–496. doi: 10.5194/tc-10-477-2016

van Angelen, J. H., Lenaerts, J. T. M., Lhermitte, S., Fettweis, X., Kuipers Munneke, P., van den Broeke, M. R., et al. (2012). Sensitivity of Greenland Ice Sheet surface mass balance to surface albedo parameterization: a study with a regional climate model. *Cryosphere* 6, 1175–1186. doi: 10.5194/tc-6-1175-2012

van Angelen, J. H. M., Lenaerts, J. T., van den Broeke, M. R., Fettweis, X., and van Meijgaard, E. (2013). Rapid loss of firn pore space accelerates 21st century Greenland mass loss. *Geophys. Res. Lett.* 40, 2109–2113. doi: 10.1002/grl.50490

van Angelen, J. H., van den Broeke, M. R., Wouters, B., and Lenaerts, J. T. M. (2014). Contemporary (1960–2012) evolution of the climate and surface mass balance of the Greenland Ice Sheet. *Surv. Geophysi.* 35, 1155–1174. doi: 10.1007/s10712-013-9261-z

van As, D., Box, J., and Fausto, R. (2016). Challenges of quantifying meltwater retention in snow and firn: an expert elicitation. *Front. Earth Sci.* 4:101. doi: 10.3389/feart.2016.00101

van As, D., Fausto, R., Colgan, W., Box, J., and PROMICE Project Team (2013). Darkening of the Greenland ice sheet due to the meltalbedo feedback observed at PROMICE weather stations. *Geol. Sur. Den. Greenland Bull.* 28, 69–72. Available online at: http://www.geus.dk/publications/bull/nr28/nr28_p69-72.pdf

van den Broeke, M., Bamber, J., Ettema, J., Rignot, E., Schrama, E., van de Berg, W. J., et al. (2009). Partitioning recent greenland mass loss. *Science* 326, 984–986. doi: 10.1126/science.1178176

van Genuchten, M. T. (1980). A closed-form equation for predicting the hydraulic conductivity of unsaturated soil. *Soil Sci. Soc. Am. J.* 44, 892–898. doi: 10.2136/sssaj1980.03615995004400050002x

Vernon, C. L., Bamber, J. L., Box, J. E., van den Broeke, M. R., Fettweis, X., Hanna, E., et al. (2013). Surface mass balance model intercomparison for the Greenland ice sheet. *Cryosphere* 7, 599–614. doi: 10.5194/tc-7-599-2013

Vionnet, V., Brun, E., Morin, S., Boone, A., Faroux, S., Le Moigne, P., et al. (2012). The detailed snowpack scheme Crocus and its implementation in SURFEX v7.2. *Geosci. Model Dev.* 5, 773–791. doi: 10.5194/gmd-5-773-2012

Wever, N., Schmid, L., Heilig, A., Eisen, O., Fierz, C., and Lehning, M. (2015). Verification of the multi-layer SNOWPACK model with different water transport schemes. *Cryosphere* 9, 2271–2293. doi: 10.5194/tc-9-2271-2015

Wright, A. P., Wadham, J. L., Siegert, M. J., Luckman, A., Kohler, J., and Nuttall, A. M. (2007). Modeling the refreezing of meltwater as superimposed ice on a high Arctic glacier: a comparison of approaches. *J. Geophys. Res.* 112:F04016. doi: 10.1029/2007JF000818

Yamaguchi, S., Katsushima, T., Sato, A., and Kumakura, T. (2010). Water retention curve of snow with different grain sizes. *Cold Regions Sci. Technol.* 64, 87–93. doi: 10.1016/j.coldregions.2010.05.008

Yen, Y. (1981). *Review of Thermal Properties of Snow, Ice and Sea Ice*. Hanover, NH: United States Army Cold Regions Research and Engineering Laboratory. Report number: CRREL Report 81-10.

Zuo, Z., and Oerlemans, J. (1996). Modelling albedo and specific balance of the Greenland ice sheet: calculations for the Søndre Strømfjord transect. *J. Glaciol.* 42, 305–317.

Conflict of Interest Statement: The authors declare that the research was conducted in the absence of any commercial or financial relationships that could be construed as a potential conflict of interest.

The reviewer PA and handling Editor declared their shared affiliation, and the handling Editor states that the process nevertheless met the standards of a fair and objective review.

APPENDIX E

Paper V

Journal of Geophysical Research: Earth Surface

RESEARCH ARTICLE
10.1029/2017JF004597

Drivers of Firn Density on the Greenland Ice Sheet Revealed by Weather Station Observations and Modeling

B. Vandecrux[1,2], R. S. Fausto[1], P. L. Langen[3], D. van As[1], M. MacFerrin[4], W. T. Colgan[1], T. Ingeman-Nielsen[2], K. Steffen[5], N. S. Jensen[6], M. T. Møller[6], and J. E. Box[1]

[1]Geological Survey of Denmark and Greenland, Copenhagen, Denmark, [2]Department of Civil Engineering, Technical University of Denmark, Kgs. Lyngby, Denmark, [3]Climate and Arctic Research, Danish Meteorological Institute, Copenhagen, Denmark, [4]Cooperative Institute for Research in Environmental Sciences, University of Colorado Boulder, Boulder, CO, USA, [5]Swiss Federal Institute for Forest, Snow, and Landscape Research (WSL), Birmensdorf, Switzerland, [6]Department of Environmental Engineering, Technical University of Denmark, Kgs. Lyngby, Denmark

Abstract Recent Arctic atmospheric warming induces more frequent surface melt in the accumulation area of the Greenland ice sheet. This increased melting modifies the near-surface firn structure and density and may reduce the firn's capacity to retain meltwater. Yet few long-term observational records are available to determine the evolution and drivers of firn density. In this study, we compile and gap-fill Greenland Climate Network (GC-Net) automatic weather station data from Crawford Point, Dye-2, NASA-SE, and Summit between 1998 and 2015. These records then force a coupled surface energy balance and firn evolution model. We find at all sites except Summit that increasing summer turbulent heat fluxes to the surface are compensated by decreasing net radiative fluxes. After evaluating the model against firn cores, we find that, starting from 2006, the density of the top 20 m of firn at Dye-2 increased by 11%, decreasing the pore volume by 18%. Crawford Point and Summit show stable near-surface firn density over 1998–2010 and 2000–2015 respectively, while we calculate a 4% decrease of firn density at NASA-SE over 1998–2015. For each year, the model identifies the drivers of density change in the top 20-m firn and quantifies their contributions. The key driver, snowfall, explains alone 72 to 92% of the variance in day-to-day change in firn density while melt explains from 7 to 33%. Our result indicates that correct estimates of the magnitude and variability of precipitation are necessary to interpret or simulate the evolution of the firn.

Plain Language Summary Arctic warming has led to more intense melt on the Greenland ice sheet. In recent decades this melt moved upglacier and started to alter the structure of perennial snow, or firn, in areas where melt was rarely recorded. In this study, we process 12–17 years of observations from four weather stations located in the vast high-elevation area of the ice sheet. From these climate records, we calculate how much melt occurred each summer and why (e.g., warm air or sunlight absorption). We found that heat transfer from the air to the surface has become more intense but is compensated by a brightening of the surface, causing less sunlight to be absorbed and used for melting. We use a computer model that simulates firn evolution and shows a good match with independent observations of the firn density. Our simulations identify increasing firn density at a first site, stable density at two sites, and decreasing firn density at the last one. Day-to-day and year-to-year changes in the density of the top 20 m of firn were mostly due to the snowfall variability followed by surface melt. This work underlines the importance of accurate precipitation estimates in order to understand firn evolution.

Key Points:
- We gathered, processed, and gap-filled underexploited climate observations at four sites from the Greenland ice sheet accumulation area
- Increasing turbulent heat fluxes were found at three sites over the 1998–2015 period, compensated by decreasing net radiative fluxes
- Our simulation of near-surface firn density quantifies the role of its climatic drivers among which snowfall and surface melt are dominant

Supporting Information:
- Supporting Information S1

Correspondence to:
B. Vandecrux,
bava@byg.dtu.dk

Citation:
Vandecrux, B., Fausto, R. S., Langen, P. L., van As, D., MacFerrin, M., Colgan, W. T., et al. (2018). Drivers of firn density on the Greenland ice sheet revealed by weather station observations and modeling. *Journal of Geophysical Research: Earth Surface*, *123*. https://doi.org/10.1029/2017JF004597

Received 27 DEC 2017
Accepted 23 SEP 2018
Accepted article online 27 SEP 2018

1. Introduction

Over the past two decades, the Greenland ice sheet has experienced significant atmospheric warming (e.g., Box, 2013; Hanna et al., 2008). As a result, the ice sheet loses mass at an increasing rate (e.g., Khan et al., 2015; van den Broeke et al., 2016) due to increasing meltwater runoff and accelerated ice flow discharge to the sea (e.g., Enderlin et al., 2014). Surface melt is common at the ice sheet margin, but has reached high elevations in the past decade (Fettweis et al., 2011; Nghiem et al., 2012; Tedesco et al., 2011). Beyond increasing air temperatures resulting in enhanced turbulent heat fluxes (Fausto et al., 2016), increasing melt can also be attributed to lower surface albedo yielding increased solar absorption (Box et al., 2012), and changes in cloud conditions (Hofer et al., 2017; Orsi et al., 2017; van Tricht et al., 2016). The complexity of ice sheet melt makes the full energy balance approach necessary to diagnose the drivers of that melt.

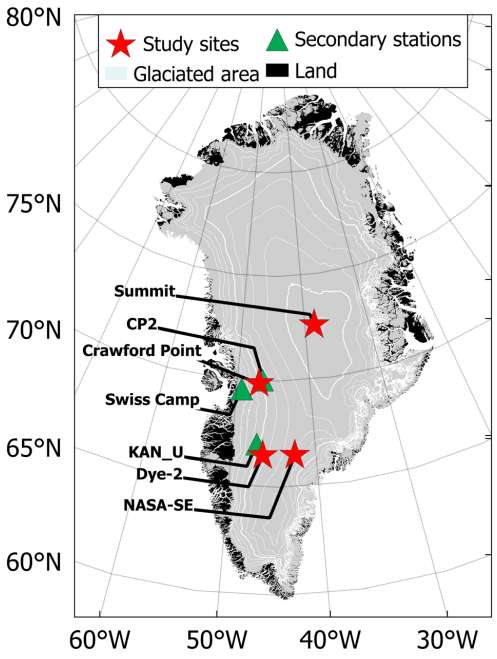

Figure 1. Locations of the study sites and secondary weather stations used for gap-filling. Ice sheet elevation contours are shown every 250 m with thicker lines indicating the 2,000- and 3,000-m elevations above sea level.

The upward migration of melt area presents an additional challenge owing to the limited observational climate records available for calculating the surface energy and mass balances in the accumulation area, over decadal time scales. The firn covering these regions also has the ability to retain surface meltwater (Pfeffer et al., 1991), complicating runoff calculations compared to over bare ice in the ablation area where meltwater is typically assumed to run off. Recent studies have investigated processes influencing firn structure and porosity in the accumulation area of the ice sheet (de la Peña et al., 2015; Forster et al., 2014; Harper et al., 2012; Machguth et al., 2016; van Angelen et al., 2013). Among them, De la Peña et al. (2015) and Machguth et al. (2016) reported an increase in near-surface firn density and ice content as a consequence of increased meltwater production. However, no observed climate histories were available at their sites, making it difficult to investigate the drivers of firn densification thoroughly.

Recent advances in firn modeling facilitated a move from empirical parameterizations of meltwater retention based on few climate parameter (Janssens & Huybrechts, 2000; Reijmer et al., 2012) to physical multilayer snow and firn models resolving multiple subsurface processes driven by weather observations (Charalampidis et al., 2015; Marchenko et al., 2017; Wever et al., 2014; Wever et al., 2016) or regional climate models (Langen et al., 2017; Steger et al., 2017). These models now allow identifying the contributions of various subsurface processes to a net observable change in firn structure and density and therefore allow a better understanding of the surface of the Greenland ice sheet and of its response to climate warming. Yet these firn models have seldom been forced by observed climate and validated against field measurements on the Greenland ice sheet. As a result, though the drivers of changes in the firn have been known for decades, the exact magnitude of their contribution to the near-surface firn density evolution remained unknown.

In this study, we identify and quantify the action of the main drivers of firn density at four sites located in different climate zones of the accumulation area of the Greenland ice sheet, using a multilayer firn model that simulates the processes affecting firn density. The model is forced by the surface mass and energy fluxes calculated from processed and gap-filled automatic weather station data. To ensure the reliability of the firn model, its results are validated against independent observations of density in 22 firn cores. Evolution of the surface climate and energy fluxes are also discussed.

2. Methods

2.1. Climate Station Data and Gap Filling

The observational data that drive the surface energy balance model are gathered by four Greenland Climate Network (GC-Net) stations (Steffen et al., 1996; Steffen & Box, 2001): Crawford Point, Dye-2, NASA-SE, and Summit (Figure 1 and Table 1). We use hourly values for net shortwave radiation fluxes, air temperature, humidity, and wind speed at one of the two levels available on GC-Net stations. We use primarily the higher-level instruments, less prone to be buried under accumulating snow, and use the lower-level instruments only when data from the upper instruments are unavailable. We do not use data recorded at less than 0.5 m from the surface or at unknown height. Due to the harsh climate and 1–2-year revisit times, GC-Net station data can be subject to prolonged multimonth gaps due to instrument or power failures. The data availability after discarding erroneous values is listed in Table 2. We interpolated over gaps under 6 hr, but for larger gaps in temperature, relative humidity, wind speed, and downward shortwave radiation, secondary weather station data were used (Figure 1 and Table 1). Third-level gap filling, when necessary values were unavailable from secondary stations, data from the closest grid cell of the high resolution (0.05° × 0.05°) HIRHAM5 regional climate model (Lucas-Picher et al., 2012) forced by ERA-Interim reanalysis data set (Dee et al., 2011) are used as our best estimation of climate variable at the main station.

Table 1
Overview of Study Site Locations, Periods Considered in This Study, and Secondary Weather Stations Used for the Gap-Filling Procedure

Name	Latitude (°N)	Longitude (°W)	Elevation (m a.s.l.)	Period	Main station (distance)
Crawford Point	69.879	46.986	2022	1998–2010	
Dye-2	66.480	46.279	2165	1998–2015	
NASA-SE	66.481	42.322	2360	1998–2015	
Summit	72.580	38.504	3208	2000–2015	
CP2	69.879	46.986	1990	1997–1999	Crawford Point (6.5 km)
Swiss Camp	69.568	49.316	1149	1994–2015	Crawford Point (97 km)
KAN_U[a]	67.000	47.024	1840	2009–2015	Dye-2 (67 km)

[a]Station from the Greenland analogue project (GAP) and Programme for monitoring of the Greenland ice sheet (PROMICE) network (Ahlstrøm et al., 2008).

Because they come from different locations, heights or sources, each variable in the auxiliary data (secondary station or HIRHAM5) needs adjustment, to match at best the available data from the main station, before they are used for gap-filling. Other studies have used linear functions (Charalampidis et al., 2015; Tardivo & Berti, 2012), but this approach applies the same linear function on all values of the variable to be adjusted and can lead to unrealistic adjusted values (see supporting information). To allow more flexibility, we adjust the auxiliary data using piecewise spline functions so that adjustment is done differently for six intervals spanning from the lowest to the highest value of the auxiliary data. Auxiliary data adjusted using piecewise spline functions give a better match to the available data from the main station than auxiliary data adjusted using linear functions. We therefore believe that our approach will give more realistic values over the periods when they are used to gap-fill the main station records. More information is available in the supporting information.

Gaps in upward shortwave radiation are dealt with differently as surface albedo depends strongly on the local conditions of the snow (grain size, frequency of precipitation, or melt events). Therefore, we use daily surface albedo from the nearest cell in the Moderate Resolution Imaging Spectroradiometer (MODIS) MOD10A1 data after Box et al. (2017) and multiply it by downward shortwave radiation to get the upward radiative flux. Before year 2000, when MOD10A1 data are unavailable, we use the daily averaged climatological albedo value from the MOD10A1 data set for gap filling.

Downward longwave radiation is not measured by the GC-NET stations. It is therefore reconstructed from HIRHAM5 data for the entire period. We found that HIRHAM5 underestimates downward longwave radiation at all 21 stations from the Programme for Monitoring of the Greenland Ice Sheet (PROMICE) (Ahlstrøm et al., 2008). All PROMICE stations are located on the margin of the ice sheet and at low elevation ($<$1300 m a.s.l. except KAN_U at 1,840 m a.s.l.) and in the absence of distributed longwave radiation measurement in the interior of the ice sheet the mean bias at PROMICE sites (-14 ± 5 W/m^2) is used to correct the HIRHAM5 downward longwave radiation at all study sites.

The gap-filled data are presented in Figures S2–S5 in the supporting information, and gap-filling statistics are given in Table S1.

Table 2
Data Availability at the Four Weather Station Sites (%)

	Crawford point	Dye-2	NASA-SE	Summit
Downward shortwave radiation	86	87	84	84
Upward shortwave radiation	78	76	79	81
Air temperature	90	95	82	92
Relative humidity	90	95	79	91
Air pressure	1.5	33	82	86
Wind speed	88	88	74	84
Surface height	96[a]	93	80	96

[a]Including surface height record from CP2.

The weather stations also measure surface height change which can be used to calculate hourly solid precipitation (Charalampidis et al., 2015). This method consists in smoothing the surface height record to remove transient deposition and erosion events and considers every sustained increment in surface height as a new layer of snow. The density of the snow that composes these increments was assumed to be 315 kg/m^3 after Fausto et al. (2018). However, the addition of new snow at the surface immediately triggers compaction within the deposited snow and in the underlying snow and firn, which means that the increment seen by the weather station is only part of what has been deposited. The calculated accumulation record thus underestimates snowfall. This was confirmed by comparing the cumulated snowfall calculated at the station to the end-of-winter snow water equivalent (SWE) surveyed occasionally at the study sites (see Figure S6 in the supporting information). Charalampidis

et al. (2015) compensated this underestimation using higher new snow density (400 kg/m^3) but the data available at each site and in Fausto et al. (2018) indicate that such near-surface snow density is not realistic. We, on the contrary, attribute this underestimation to the compaction of snow and firn below a newly deposited snow layer and apply a correction factor to each increment found in the snow height record. This correction factor is tuned at each site so that the weather station-derived end-of-winter SWE matches the ones reported in snow pits (see Figure S6 in the supporting information). During data gaps (see Table 2) snowfall from HIRHAM5 output, multiplied by a correction factor to match the available station-derived accumulation, is used instead.

2.2. Surface Energy Balance Model

Surface energy and mass fluxes are calculated using the model by van As et al. (2005) which has been previously used on weather station data on the Greenland ice sheet (Charalampidis et al., 2015; van As et al., 2017). At each hourly time step, it calculates the turbulent latent and sensible heat fluxes from near-surface gradients in air temperature, humidity, and wind speed using Monin-Obukhov similarity theory accounting for thermal stratification effects on the logarithmic wind speed profile. Surface roughness length scales are parameterized as a function of surface snow density (Andreas, 1987; Lefebre et al., 2003). The model iteratively searches for a surface temperature below or equal to 0 °C for which all surface energy fluxes are in balance. Upwelling longwave radiation is calculated from simulated surface temperature using Stefan-Boltzmann's law with an emissivity of 0.98. Conductive heat flux into the subsurface is calculated from the temperature gradient across the first layer in the firn model (see next section). Since the surface is composed of snow or ice, the surface temperature is limited to 0 °C, and any excess energy required to close the energy budget is used to melt of snow or ice. Sublimation and deposition are calculated from the latent heat flux.

2.3. Firn Evolution Model

The snow and firn model employed here was first presented by Langen et al. (2015), and was updated in Langen et al. (2017). In this section, we give a brief summary of the model from Langen et al. (2017) and describe further improvements made to the model since then.

2.3.1. Discretization

The firn column is here composed of 200 layers, each of which consists of three compartments: snow, pure ice, and liquid water. Layer temperature, firn grain size, and firn density are calculated for each layer. Langen et al. (2017) implemented an Eulerian approach, whereby added or removed mass was going through fixed layers of constant mass. This resulted in systematic averaging of the firn properties. In this study, we have updated the discretization scheme to allow layers to be advected downward or upward in a Lagrangian fashion. New layers containing snow can be created at the surface during precipitation events. New ice layers can be added at the bottom of the column if the thickness of the entire column drops below 20 m water equivalent (w.eq.). Surface layers can also disappear as the surface melts, while the deepest layer can be removed once buried too deep. To maintain a constant number of layers, the creation (respectively, deletion) of a layer is balanced by merging (respectively, splitting) of layers elsewhere in the column. Merging or splitting layers are done so that vertical resolution is higher close to the surface and that layers having significantly different characteristics (in temperature, density, ice and water content, grain size) than neighboring layers are less likely to be merged with others.

2.3.2. Mass Fluxes

An update since Langen et al. (2017) is that new material from snowfall or deposition is now first kept in a fresh snow bucket, and only when this bucket reaches a specified threshold (4 cm w.eq.), a new layer is created. The fresh snow bucket is used to distinguish fresh snow from old snow, information needed for the parameterization of surface roughness length from Lefebre et al. (2003). A fresh snow density of 315 kg/m^3 after Fausto et al. (2018), which already accounts for the effect of wind, is preferred to the parameterization used in Langen et al. (2017). Grain size of fresh snow is set to 0.1 mm as in Langen et al. (2017) and Katsushima et al. (2009). When sublimating or melting material, it is first taken from the fresh snow bucket and then from the first layer of the column. Melting at the surface triggers the transfer of the content of the fresh snow bucket to the first layer and thereafter shifts mass from the snow and ice compartments to the liquid water compartment.

2.3.3. Meltwater Percolation and Refreezing

The way water is passed from one layer to the next is unchanged from Langen et al. (2017). After calculating what can be retained by capillary forces, the excess water is available for downward movement following Darcy's law and depending on the conditions (density, grain size, and ice content) that are present in the two considered layers. Once the water movement is calculated for the whole column, the cold content of the subfreezing layers is used to refreeze the liquid water (including as superimposed ice). Firn compaction and grain growth are also unchanged since Langen et al. (2017).

As a minor update, we chose to use the formulation of saturated hydraulic conductivity after Calonne et al. (2012) and use the parameterization of heat capacity and thermal conductivity from firn density after Yen (1981). Finally, the parameterization from Colbeck (1975) is used to describe how discontinuous ice lenses decrease the snow hydraulic conductivity. The scheme requires a standard ratio between the width of gaps separating ice lenses and the width of ice lenses, $\frac{w_h}{w_{ice}}$, and although Langen et al. (2017) used both 1 and 0.1, they did not provide any justification. Here we argue that $\frac{w_h}{w_{ice}} = 0.1$ is more meaningful as it allows a layer filled by ice to have a hydraulic conductivity one order of magnitude lower than ice-free snow and therefore to be closer to observations of ice layer conductivity in natural snowpacks (Albert & Perron, 2000).

2.3.4. Model Initialization

The model starts with an initial column of 40 m w.eq. We use the closest available firn cores in time and space to initiate the firn density. At Dye-2 and NASA-SE, we use core Dye-2 A&B and core 6642 (120 and 20.13 m long, respectively) from Mosley-Thompson et al. (2001). At Crawford Point, no core drilled at that site in the 1990s was available. We therefore use the 18.55-m-long core 6945 drilled in 1998, 125 km southeast of the site, and 189 m higher on the ice sheet (Mosley-Thompson et al., 2001). The two locations are assumed to have the same firn condition. It is corroborated by other studies that already compared core 6945 to snow pits from the surroundings of Crawford Point (de la Peña et al., 2015). At Summit the initial density was taken from a 6-m-deep snow pit by Mayewski and Whitlow (2016) and the GRIP core (Spencer et al., 2001), both from 1990, when usable station data only start in 2000. Nevertheless, an ~2-m snow pit from 2000 by Albert and Shultz (2002) (see Figure S8 in the supporting information) indicates that shallow firn densities were similar in 1990 and 2000 and justifies our choice of initial condition. For Crawford Point and NASA-SE the density from the end of the available core to the bottom of the column is calculated by fitting a second-degree polynomial to the available density and to a pore close off density (830 kg/m^3) at 30 m w. eq. (~60 m) below the surface and then constant from there.

The initial temperature profile was taken as the first valid reading of the temperature strings that are installed at the GC-Net stations. Since the lowest-temperature sensor is located at ~10-m depth, the rest of the temperature profile is calculated using a second-degree polynomial to link the lowest available temperature to the bottom temperature. This bottom temperature is kept constant throughout the simulation and is set to the average firn temperature at 10-m depth observed by the thermistor string installed at each station: −17.4 °C at Crawford Point, −16.0 °C at Dye-2, −19.2 °C at NASA-SE, and −31.0 °C at Summit station.

3. Results

3.1. Climate Forcing, Energy, Mass, and Water Budget

We have compiled 12 to 17 years of climate data per study site, which give unprecedented insight into the evolution of the climate in the accumulation area of the Greenland ice sheet. Clear trends were seldom found throughout all variables monitored by the stations. For all study periods, the GC-Net stations show slight increase in annual and summer mean air temperature, congruent with climate change induced trends found, among others, by Hanna et al. (2008). However, probably due to the length of the considered records with respect to the natural variability, these trends cannot be proven statistically different from zero (all of them have p value >0.1; see Table S2 in the supporting information). The warming was noticeably more pronounced (higher slopes, smaller p values) for summer averages than for annual means.

As a key parameter of the surface energy balance, the evolution of the surface albedo was also investigated. The June through August average albedo was consistent between the sites (~0.83) and stable at Dye-2, NASA-SE, and Summit (Figure S7 in the supporting information). Yet albedo during the summer of 2012

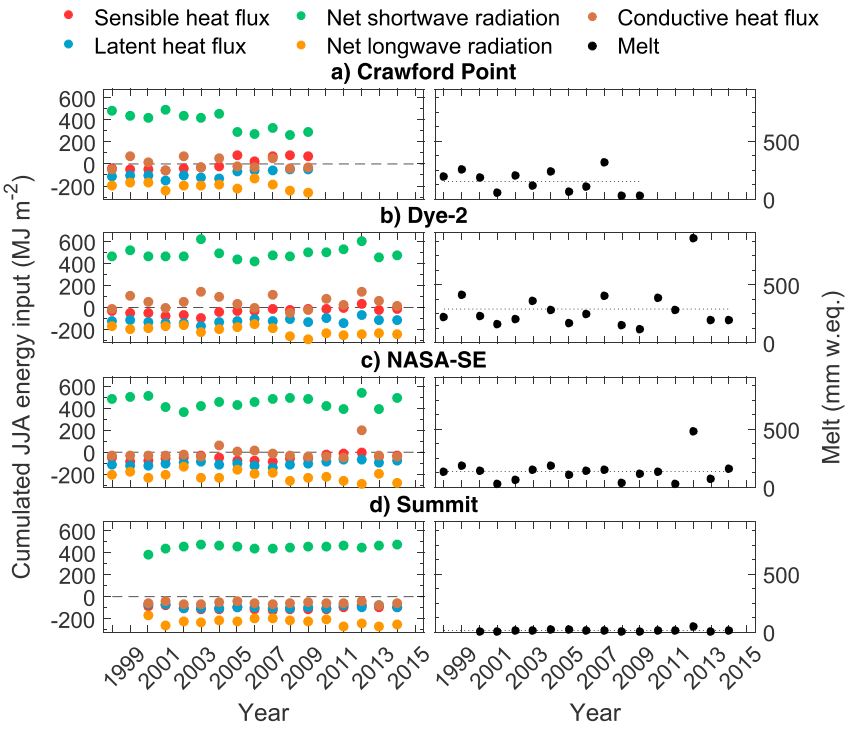

Figure 2. (left panels) Surface energy input summed June through August (JJA) each year. (right panels) Cumulated yearly surface melt. Dashed line on the left indicates zero energy input to the surface and segregate energy sinks (negative input) from energy sources (positive input). Dotted line on the right shows the average annual melt amount at each site. The similar magnitudes of latent and sensible heat fluxes at summit (d) cause the overlap of their markers.

was record-low at Dye-2 (0.75 ± 0.05) and NASA-SE (with 0.78 ± 0.05). At Crawford Point, summer albedo was on average 0.05 higher during 2005–2009 compared to 1998–2004 translating into a decreasing energy input of net shortwave radiation to the surface (Figure 2 and Table 3). This increase was not found in MODIS summer albedo; however, no malfunction was reported for that period in the station data. It is therefore difficult to ascertain the origin of this increase.

The calculated surface energy balance, illustrated in Figure 2, reveals the diversity of processes that govern the surface energy and mass budgets. For all sites, net shortwave radiation is the largest heat source and net longwave radiation is the largest heat sink for the surface during summer (Figure 2). In 2012, both at Dye-2 and

Table 3
Trends in the Components of the Surface Energy Balance

	Sensible Heat Flux	Latent Heat Flux	Net Shortwave Radiation	Net Longwave Radiation	Conductive Heat Flux
	Trends in cumulated JJA energy (MJ/m^2/year)				
Crawford Point	**14.09**	**7.25**	**−20.09**	−3.4	−2.16
Dye-2	**4.02**	**2.09**	1.25	**−5.28**	0.16
NASA-SE	**2.75**	**2.53**	−0.36	**−4.32**	2.38
Summit	0.02	−0.36	2.69	−3.10	−0.37

Note. Trends significantly different from zero (i.e., with associated p value <0.05) are shown in bold. Positive values indicate energy fluxes that heat the surface.

NASA-SE, surface melting led to lower albedo values (Figure S7 in the supporting information), causing increased shortwave radiation absorption (Figure 2) through the melt-albedo feedback (Box et al., 2012).

Our calculations of sensible and latent heat fluxes are in agreement with previous estimates using similar methods (Box & Steffen, 2001), and their cumulated June through August values are increasing at all sites except Summit (Table 3). However, Box and Steffen (2001) also described a possible negative bias when calculating sublimation from a single height above the surface. Using more advanced methods, such as the so-called eddy covariance method would be indeed preferable, but is hampered by the scarceness of periods where temperature, humidity, and wind speeds are available at two levels above the surface.

Longwave radiation fluxes are decreasing at all sites. But since downward longwave radiation is provided by HIRHAM5, this result is not based on direct observations from the weather stations. Conductive heat fluxes through the uppermost snow layer show a more mixed picture, and it seems that the capacity of the near-surface firn to accept heat from the surface did not drastically change at any site over the study period. Investigation of the heat conducted through the model column showed that only the near-surface firn was thermally active. Subsequently, the assigned bottom temperature, which could in theory act as an infinite source or sink of heat, did not interfere with the near-surface heat fluxes and latent heat release from refreezing.

Higher surface melt was calculated over the last decade (Figure 2), especially during the known extreme melt events of 2007 (Mote, 2007), 2010 (van As et al., 2012), and 2012 (Nghiem et al., 2012). The relatively short span of our records prevents from calculating trends representative of current climate evolution. However, a recent ice core study by Graeter et al. (2018) found that melt indeed increased at Crawford Point and Dye-2 over the last 50 years. But while Graeter et al. (2018) estimated surface melt from ice content in firn cores, subject to high spatial variability, our calculation of surface melt from the weather station data presents a more robust estimate.

Mean annual snowfall was respectively 564, 421, 731, and 303 mm w.eq. at Crawford Point, Dye-2, NASA-SE, and Summit over their respective study periods. At all sites, the meltwater is entirely refrozen in the snow and firn. The only modeled process removing mass from the firn column is sublimation, which on average sublimated 6.7%, 12.8%, 6.8%, and 12.2% of annual snowfall at Crawford Point, Dye-2, NASA-SE, and Summit, respectively. We calculate an average annual mass balance of 526, 367, 681, and 266 mm w.eq. at Crawford Point, Dye-2, NASA-SE, and Summit, respectively.

3.2. Firn Evolution and Densification

At sites where surface melt is frequent such as Crawford Point, Dye-2, and NASA-SE, ice layers are being formed from meltwater refreezing every summer. This is visible in Figure 3 as layers of higher density. Snow densifies with time as it gets buried under new material, with fastest compaction rates in the few months following snowfall. Additionally, Crawford Point and Dye-2 start with very few high-density layers in the upper 10 m while they end their respective study periods with a higher number of them in the near-surface firn. Seemingly abrupt changes in density at depth in Figure 3 are the result of the model layers merging in order to add new ones at the top.

4. Discussion

4.1. Evaluation Against Firn Cores

Before we further discuss the simulated evolution of the firn we need to assess the accuracy of the model. Errors on the initial conditions, from the climate forcing and limitations of the model formulation, affect the ability of the model to simulate the firn evolution. We assess the net effect of all these inaccuracies by comparing the modeled densities to 22 firn density observations. Among them 14 were already published (Albert & Shultz, 2002; Harper et al., 2012; Lomonaco et al., 2011; Machguth et al., 2016) while 8 are being presented for the first time (core 3 to 6 at NASA-SE and 22 to 25 at Summit; see Figure S8 in the supporting information) and have a 10-cm resolution in density.

For each core we calculate the average density for the whole core, for its upper section (above 5-m depth) and for its lower section (below 5-m depth) and compare it to the average densities given by the model at the same date and same depth range. When compared to the full cores, the simulations give a satisfactory

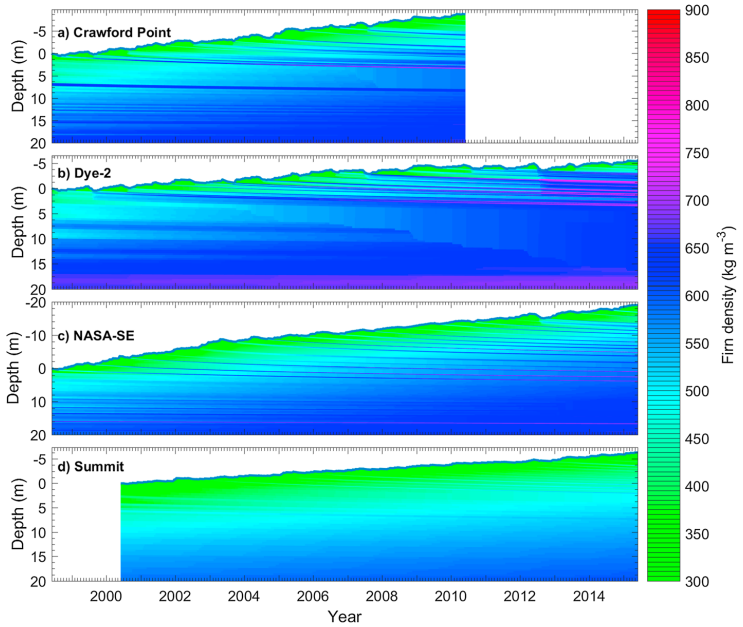

Figure 3. Evolution of simulated firn density at four GC-Net sites. Steps in density evolution between 5 and 10 m deep at Crawford point and Dye-2 are due to the model merging layers and to the averaging of their density. It is done so that new layers are available closer to the surface.

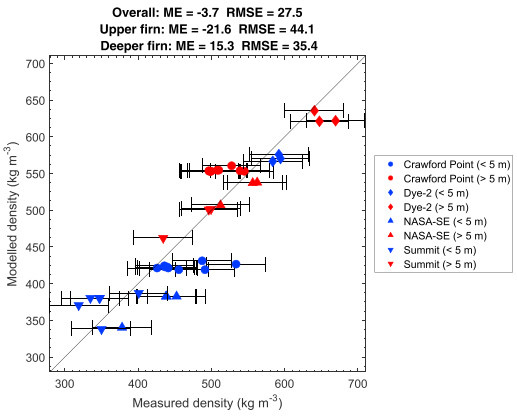

Figure 4. Evaluation of modeled and observed average firn density for the four sites for shallow (<5 m; in blue) and deep (>5 m; in red) firn. Mean error (ME) and root-mean-square error (RMSE) on the average densities are given for the whole depth range covered by the cores (overall), for the core sections within 5 m from the surface (upper firn), and for the core sections below 5-m depth (deeper firn).

mean error (ME) of −3.7 kg/m^3 and root-mean-square error of 27.5 kg/m^3 (Figure 4). However, the model on average underestimates the upper-firn average density by −21.6 kg/m^3 and overestimates the deeper-firn average density by 15.3 kg/m^3 (Figure 4). These discrepancies are most likely due to the densification scheme (Vionnet et al., 2012) that was designed for seasonal snowpack and not for polar firn, but also to inaccurate melt or snowfall at the surface or limitations in the meltwater percolation scheme in the firn model. Nevertheless, deviations between modeled and observed average firn densities are well within the natural variation of firn density at local scale due to spatial heterogeneities (standard deviation of the average densities from nine cores drilled in 2007 at Crawford Point is 23.1 kg/m^3).

The comparison of the modeled and observed full-depth density profiles (Figure S8 in the supporting information) confirms the agreement of average density and also shows that the model can reproduce denser melt layers within the firn. The model fails, however, to reproduce the exact depth and thickness of these layers. In addition to the sources of discrepancies listed above, the mismatch between modeled and observed ice layers can be due to the inability of the model to account for heterogeneous percolation (Marsh & Woo, 1984). Nonetheless, the objective of this study is to simulate the evolution of the average density of the near-surface firn and to quantify the contributions of surface processes to these changes. We consider that inaccuracies in the modeled depth of the ice layers are not relevant. Indeed, our simulations match reasonably well with observed firn density profiles and represent a likely evolution of the firn in

Table 4
Evolution of Firn Density at the Study Sites From Observations in Firn Cores and From the Model

Site	Period	Depth Range	Density Change (kg/m^3)	
			Observed	Modeled
Crawford Point	1998–2007[a]	0–10.4 m	+24	+16
	1998–2010	0–20 m	–	+ 10
Dye-2	1998–2013[a]	0–16.6 m	+109	+78
	2013[a]–2015[a]	0–16.6 m	−23	0
	1998–2015	0–20 m	–	+ 59
NASA-SE	1998–2015	0–16.6 m	+13	−21
	1998–2015	0–20 m	–	−19
Summit	2000[b]–2007	0–20 m	+8	+5
	2007–2015[a]	0–15.9 m	−19	−1
	2000–2015	0–20 m	–	+1

[a]Average of multiple cores. [b]In fact using the 1990 cores from Spencer et al. (2001) and Mayewski and Whitlow (2016) that appear to match with a 2-m pit from 2000 (Figure S8 in the supporting information).

the vicinity of the weather station. Substantial improvement in climate observation, energy balance modeling, and firn modeling as well as in our understanding of spatial heterogeneity will be needed before we can aim at replicating a mirror image of one specific measurement of density profile.

Beyond the comparison of density profiles at specific dates, it is also important to assess whether the model is able to reproduce the changes observed in firn between two measurements of firn density. Firn cores indicate that the highest densification took place at Dye-2 over the 1998–2013 period (Table 4). However, all the other density changes derived from firn core comparison are rather low compared to the natural spatial variability in firn density. Nevertheless, we believe that, despite spatial heterogeneity, if similar changes in density can be seen between two firn cores and in our simulation (which is the product of our current understanding of the firn processes applied to observed climate data), then there is a higher chance that both reflect the true evolution of the firn. When changes in density given by firn cores and by our simulations differ either in sign or magnitude then we cannot distinguish between potential anomaly in the observations and errors in the forcing or formulation of the firn model. Our firn model captures the sign and magnitude of observed changes: highest increase in density at Dye-2, mild increase at Crawford Point, and little changes at Summit (Table 4). Only at NASA-SE, the model indicates an overall decrease in density while the firn cores showed a small increase of firn density over the 1998–2015 period (Table 4).

4.2. Evolution of the Firn

After ensuring that the firn model gives a realistic estimate for the evolution of firn density, we can now focus on the temporal evolution of the average density of the upper 20 m of firn. This is a key parameter for the firn retention capacity. Simulations show the highest densification at the Dye-2 with an increase of +59 kg/m^3 (+11%) in the density of the upper 20 m of firn from 1 June 1998 to 1 June 2015, respectively (Table 4). The repeatedly positive annual changes of firn density in the second half of the study period (black line above 0 in Figure 5b) indicate that this increase in density started in 2006. Increasing density at Dye-2 causes the loss of 18% of the firn pore volume and represents a substantial decrease of the meltwater storage capacity of the firn. Crawford Point and Summit show rather stable densities (changes lower than 2%). However, no data are available at Crawford Point after 2010 and considering the similarities of their location (in western Greenland, ~2,000 m a.s.l.), it cannot be excluded that the site underwent the same densification, and loss of pore volume, as Dye-2 over the 2010–2015 period.

More surprisingly, our simulation at NASA-SE shows a 19 kg/m^3 (4%) decrease of firn density. The decrease in near-surface firn density primary occurs between 1998 and 2003 and is followed by a period of stable firn densities (Figure S9 in the supporting information). Calculated year-to-year changes in firn density (Figure 5, black line) indicate that this decrease can be attributed to higher precipitation than average. No major issue potentially affecting the station-derived precipitation was reported over that period, and unfortunately, no firn core was drilled at NASA-SE between 1998 and 2015 to assess whether this decrease of firn density indeed took place.

Although the firn core observations used for the initialization of the firn density cover the upper 20 m at all sites, our analysis naturally depends on the uncertainty present in these initial profiles. Nevertheless, the effect of any measurement error within these profiles would decrease throughout the simulation as the anomalous firn section is advected out of the upper 20 m of firn. Measurement errors put aside, the natural spatial heterogeneity of firn raises the question of representativity of the initial profiles that were used. In the absence of clear understanding of spatial heterogeneity and of its potential controls, we can only aim at simulating the likely evolution of the firn at the specific location where the initial density profiles were observed.

4.3. Drivers of Firn Density

It is known that near-surface firn density tends to decrease in periods of high precipitation and/or low melt (e.g., at NASA-SE during 1998–2003; Figure S9 in the supporting information) and to increase in periods of

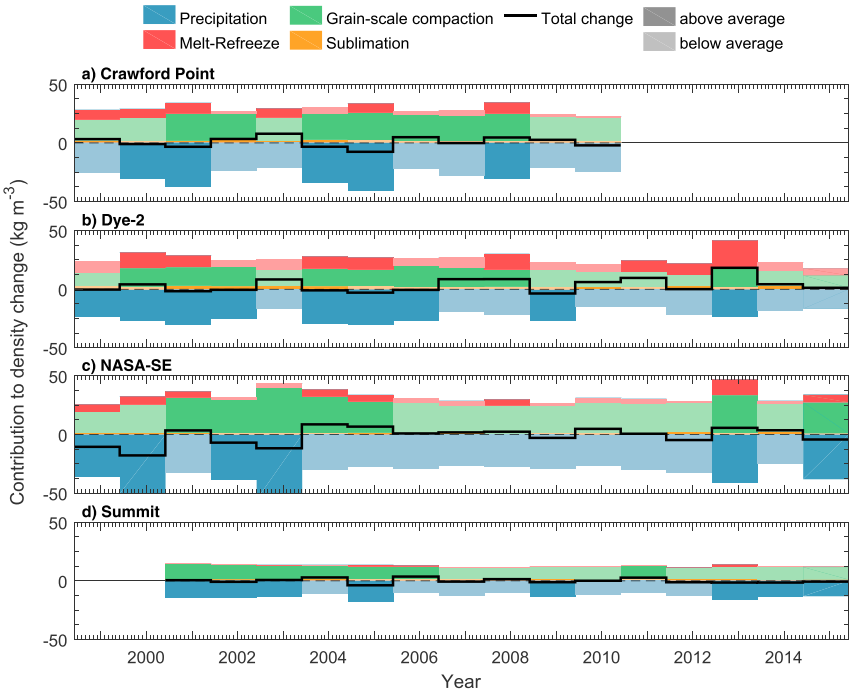

Figure 5. Temporal evolution of the near-surface firn (upper 20 m) density and of its drivers at (a) Crawford point, (b) Dye-2, (c) NASA-SE, and (d) Summit. Annual change in 20-m firn density (from 1 June to 1 June) is shown in black line, and the contribution of densification processes are shown in stacked colored areas (with darker colors when contributions are above whole-period average).

lower precipitation and/or higher melt (e.g., at Dye-2 over the 2007–2015; Figure S9 in the supporting information). Snowfall adds less dense fresh snow at the top of the firn column subsequently decreasing the average density of the upper 20 m of firn. On the contrary, surface melt transforms less dense surface snow into ice layers at depth thereby increasing the firn density. Two other processes affect near-surface firn density: the grain-scale compaction, which sinters and recrystallizes snow grains in response to the overburden pressure (and thereby to precipitation and melt history), subsurface temperature and water content (calculated after Vionnet et al., 2012) and sublimation at the surface, which by removing less dense surface snow will increase the average density of the upper 20 m of firn that remains. The firn model brings new insights by giving the magnitude of the near-surface density change related to precipitation, melt, compaction, or sublimation at each time step.

First, the hourly contributions can be aggregated into yearly contributions (i.e., from 1 June to 1 June) so that we can identify, for each year, the main driver of changes in the near-surface firn density (Figure 5). In addition to the magnitude of the contributions, we also show in Figure 5 whether that contribution is below (lighter color) or above (deeper color) the average contribution for the whole period. From Figure 5, we can therefore investigate and quantify, for each year, each driver's contribution the interannual change in near-surface firn density.

The role of precipitation for all sites is evident as shown in Figure 5. Year-to-year decrease in firn density (black line below zero in Figure 5) only comes with above-average precipitation (deep blue colored areas in Figure 5). On the contrary, below-average precipitation always leads to increasing firn densities. These two statements have one exception: at NASA-SE over 2010–2011, but are otherwise supported by 53 combined -station-years.

Table 5
Part of the Variance in Near-Surface Density Change Explained by the Contribution of Each Driver of the Top 20-m Firn Density, Calculated Both on Daily and Yearly Values (From 1 June to 1 June)

		Part (%) of the Variance in Near-Surface Density Change Explained by the Individual Contribution of			
Site	Temporal Scale	Precipitation	Melt	Grain-Scale Compaction	Sublimation
Crawford Point	Daily	84	19	9	7
	Yearly	68	1	14	1
Dye-2	Daily	72	33	17	6
	Yearly	29	43	3	11
NASA-SE	Daily	92	11	5	5
	Yearly	55	3	1	0
Summit	Daily	92	7	3	7
	Yearly	74	6	6	0

Note. Values for each site do not add up to 100 because of covariance between drivers.

While precipitation decreases near-surface firn density, on average by −13 to −34 kg/m^3 each year, it is partly compensated by the grain-scale compaction that densifies the near-surface firn on average by 11 to 26 kg/m^3. The formula by Vionnet et al. (2012) implies that grain-scale compaction decreases exponentially with increasing densities. Therefore, years with more precipitation bring more low-density snow to a site and leads greater grain-scale compaction (Figure 5). The grain-scale compaction is therefore the second contributor to firn density changes in magnitude. Nevertheless, and as detailed in the next section, the response of grain-scale compaction to precipitation is dampened. The variance of the contribution of grain-scale compaction is indeed between 4 and 11 times smaller than the one of snowfall. Therefore, we see that grain-scale compaction moderately counterbalances the contribution of precipitation and does not drive changes in the near-surface firn density over our study periods.

Due to the different locations of the stations, melting and subsequently melt-driven densification does not occur every year at all sites. At Crawford Point and Dye-2, melt and refreezing are responsible for an important part of the increase of near-surface firn density from one year to the next: 20 and 37% of all positive contributions to firn density change on average, respectively. At these sites the variability in melt also has its importance since above average melt years (Figure 5) generally (for 80% of such station-years) cause a positive change on the near-surface density change. At Summit, melt occurs rarely and does not have a significant effect on near-surface firn density. At NASA-SE, however, the contribution of melt and refreezing to the overall densification only becomes important during extreme melt events such as in 2012, when it accounted for a +14 kg/m^3 increase of density which was in turn compensated by an above-average contribution from snowfall.

The role of sublimation is minor for all sites and all years with an average annual contribution of +1.4 to +2.2 kg/m^3 depending on the site.

4.4. Effect of the Temporal Scale on the Drivers of Densification

Another approach to describe the role of precipitation, melt, grain-scale compaction, and sublimation into the evolution of the near-surface firn density is to see how much of the variability, or variance, in the density change can be explained by each driver (Table 5). This is done by calculating the coefficient of determination (R^2) of the linear regression between each driver's contribution and the overall density change.

Figure 5 indicates that precipitation is responsible for the largest and most variable contribution to the interannual evolution of the near-surface firn density. Precipitation also appears to be the main driver of the day-to-day variance in the firn density (Table 5). Due to the difference in average summer melt between the sites, the explanatory power of precipitation decreases, and the one of melt increases, as we move from colder sites (Summit, NASA-SE) to warmer sites (Crawford Point, Dye-2).

The higher values of explained variance at daily resolution, for all drivers of density, comes from the fact that on a day-to-day basis, the changes in density can be more easily linked to one single driver (for example, day of snowfall in absence of melt or melt day without snowfall). On yearly values, however, the drivers explain less of the variability in density (Table 5). This comes from the fact that over annual time scales, drivers contribute simultaneously to interannual changes in the firn density and cannot be separated into their individual contribution. Only at Dye-2 the yearly contribution of melt is still very important and explains 43% of the variance in annual changes in firn density. Yet precipitation alone still explains more than half of the variance in interannual changes of density at all the other sites.

Another argument for the dominant role of precipitation in near-surface density change, is that extreme precipitation events lead to much more drastic changes in the near-surface firn density (from −2 to −6 kg/m^3 within a day due to extreme snowfall) than the extreme melt events (+1.3 kg/m^3 during the strongest melt day at Dye-2). Therefore, when aiming at simulating the daily evolution of firn density, capturing these precipitation events appears to be more important than capturing the variability in any other drivers of densification.

Our conclusions are strengthened by the fact that precipitation and, in a less direct way, melt are calculated from the weather station data and therefore represent our closest estimates of true surface conditions. Additionally, the calculation of their contributions to near-surface firn density change is rather straightforward (adding new snow at the top for precipitation and transforming surface snow to ice for melt) and depends on a limited number of observation-derived assumptions: fresh snow density is taken from Fausto et al. (2018) and no runoff was reported at any of our study sites over the considered periods.

Another interesting finding is the relatively minor importance of the contributions of grain-scale compaction and sublimation into daily and yearly changes in the near-surface firn density (Table 5). It indicates that at our sites, over periods of ~15 years, grain-scale compaction and sublimation (as they are formulated in the firn model) do not vary sufficiently to have a noticeable impact on the evolution of the density of the upper 20 m of firn. Table 5 indicates that the contributions of grain-scale compaction and densification could be replaced by their mean values without losing much explanatory power. This finding is more dependent on the formulation of grain-scale compaction in the model, and on its sensitivity to changes in accumulation, temperature, or water content. It should therefore be used with caution.

All our results indicate the importance of precipitation, and its variability at different temporal scales to estimate the evolution of the near-surface firn density. This highlights the difficulty with attributing observed density changes to changes in melt alone (de la Peña et al., 2015; Graeter et al., 2018).

5. Conclusions

Climate data covering 12–17 years at Crawford Point, Dye-2, NASA-SE, and Summit automatic weather stations and adjusted data from nearby weather stations and HIRHAM5 regional climate model output were combined in continuous hourly time series. A surface energy and mass balance model driven by these data enabled the estimation of the relative contributions of the different surface energy and mass fluxes to the surface. We find that sensible and latent heat fluxes have increased at most sites but were partly compensated by a decrease in radiative fluxes. Melt was seen to be highest at the end of our study period with the occurrence of the 2007, 2010, and 2012 extreme melt events. Our updated snow and firn model revealed that the density of the top 20 m of firn has increased by 11% at Dye-2, subsequently decreasing the firn pore space by 18%. No near-surface firn density increase was found at Crawford Point and Summit while a 4% decrease was found at NASA-SE. Modeled densification is corroborated by comparison with firn cores. We find that precipitation changes are primarily responsible for the modeled variations of firn density at our study sites. Indeed, its contribution to changes in near-surface firn density change is both the highest in magnitude and the most variable of all drivers of firn densification. Precipitation can therefore explain alone 72 to 92% of the variance in day-to-day firn density change while melt can only explain 7 to 33% alone. When looking at year-to-year changes in firn density, precipitation is still the main driver followed by melt, however it is then their interaction that is necessary to explain the evolution of firn density. Contributions of grain-scale compaction and sublimation to the changes in firn density are less important and could not explain much of the variance in firn density change. We nevertheless expect this last finding to be more dependent on the model formulation of grain-scale compaction. Our results are of prime importance for the climate modeling community and provide a strong impetus to reproduce the observed magnitude and variability of precipitation in order to better estimate the past and future evolution of the firn on the Greenland ice sheet. It is also yet another reminder that observed changes in the firn density cannot be attributed entirely to changes in melt or temperatures without an accurate estimation of the precipitation history at that location. Eventually, should the decrease of pore space and buildup of ice layers at Dye-2 continue, its meltwater retention capacity could be eliminated as it has been reported at lower areas in the same region (Machguth et al., 2016), and meltwater generated there could participate to runoff. This possibility reaffirms the necessity of field campaigns and modeling efforts to understand ongoing changes in the firn of the Greenland ice sheet.

Acknowledgments
This work is part of the Retain project funded by the Danmarks Frie Forskningsfond (grant 4002-00234). We are grateful to J. Harper and E. Mosley-Thompson for providing some of the cores used in this study and to A. Heilig, J. Brown, and two anonymous reviewers for their useful comments on the manuscript. The GC-Net data are available at http://cires1.colorado.edu/steffen/gcnet. The data produced by this study (processed gap-filled hourly standardized weather data and SEB and firn model output) are available at http://doi.org/10.18739/A2TH8BM6X. The scripts used for this study are available at https://github.com/BaptisteVandecrux/SEB_Firn_model.git. The PARCA cores are available at http://research.bpcrc.osu.edu/Icecore/data/, and their collection was supported by NASA grants NAG5-5032, 6817, 5031, 6779, NAGW-4248, and NSF/OPP grant 9423530. KAN_U weather station data are funded by the Greenland Analogue Project (GAP), and made available through the Programme for Monitoring of the Greenland Ice Sheet (PROMICE). PROMICE data are freely accessible at http://promice.org. HIRHAM5 output is available at http://prudence.dmi.dk/data/temp/RUM/HIRHAM/.

References

Ahlstrøm, A., Gravesen, P., Andersen, S., van As, D., Citterio, M., Fausto, R., et al. (2008). A new programme for monitoring the mass loss of the Greenland ice sheet. *Geological Survey of Denmark and Greenland Bulletin*, *15*, 61–64.

Albert, M., & Shultz, E. (2002). Snow and firn properties and air–snow transport processes at summit, Greenland. *Atmospheric Environment*, *36*(15-16), 2789–2797. https://doi.org/10.1016/S1352-2310(02)00119-X

Albert, M. R., & Perron, F. (2000). Ice layer and surface crust permeability in seasonal snow pack. *Hydrological Processes*, *14*(18), 3207–3214. https://doi.org/10.1002/1099-1085(20001230)14:18<3207::AID-HYP196>3.0.CO;2-C

Andreas, E. L. (1987). A theory for the scalar roughness and the scalar transfer coefficients over snow and sea ice. *Boundary LayerMeteorol*, *38*(1-2), 159–184. https://doi.org/10.1007/BF00121562

Box, J. (2013). Greenland ice sheet mass balance reconstruction. Part II: Surface mass balance (1840–2010). *Journal of Climate*, *26*(18), 6974–6989. https://doi.org/10.1175/JCLI-D-12-00518.1

Box, J., & Steffen, K. (2001). Sublimation on the Greenland ice sheet from automated weather station observations. *Journal of Geophysical Research*, *106*(D24), 33,965–33,981. https://doi.org/10.1029/2001JD900219

Box, J. E., Fettweis, X., Stroeve, J. C., Tedesco, M., Hall, D. K., & Steffen, K. (2012). Greenland ice sheet albedo feedback: Thermodynamics and atmospheric drivers. *The Cryosphere*, *6*(4), 821–839. https://doi.org/10.5194/tc-6-821-2012

Box, J. E., van As, D., Steffen, K., & the PROMICE team (2017). Greenland, Canadian and Icelandic land-ice albedo grids (2000–2016). *Geological Survey of Denmark and Greenland Bulletin*, *38*, 53–56.

Calonne, N., Geindreau, C., Flin, F., Morin, S., Lesaffre, B., Roscoat, S. R., & Charrier, P. (2012). 3-D image-based numerical computations of snow permeability: Links to specific surface area, density, and microstructural anisotropy. *The Cryosphere*, *6*(5), 939–951. https://doi.org/10.5194/tc-6-939-2012

Charalampidis, C., van As, D., Box, J. E., van den Broeke, M. R., Colgan, L. T., Doyle, S. H., et al. (2015). Changing surface-atmosphere energy exchange and refreezing capacity of the lower accumulation area, West Greenland. *The Cryosphere*, *9*(6), 2163–2181. https://doi.org/10.5194/tc-9-2163-2015

Colbeck, S. (1975). A theory of water flow through a layered snowpack. *Water Resources Research*, *11*(2), 261–266. https://doi.org/10.1029/WR011i002p00261

de la Peña, S., Howat, I. M., Nienow, P. W., van den Broeke, M. R., Mosley-Thompson, E., Price, S. F., et al. (2015). Changes in the firn structure of the western Greenland ice sheet caused by recent warming. *The Cryosphere*, *9*(3), 1203–1211. https://doi.org/10.5194/tc-9-1203-2015

Dee, D. P., Uppala, S. M., Simmons, A. J., Berrisford, P., Poli, P., Kobayashi, S., et al. (2011). The ERA-interim reanalysis: Configuration and performance of the data assimilation system. *Quarterly Journal of the Royal Meteorological Society*, *137*(656), 553–597. https://doi.org/10.1002/qj.828

Enderlin, E., Howat, I. M., Jeong, S., Noh, M.-J., van Angelen, J., & van den Broeke, M. (2014). An improved mass budget for the Greenland ice sheet. *Geophysical Research Letters*, *41*, 866–872. https://doi.org/10.1002/2013GL059010

Fausto, R. S., Box, J. E., Vandecrux, B., van As, D., Steffen, K., MacFerrin, M., et al. (2018). A snow density dataset for improving surface boundary conditions in Greenland ice sheet firn modelling. *Frontiers in Earth Science*, *6*(51). https://doi.org/10.3389/feart.2018.00051

Fausto, R. S., van As, D., Box, J. E., Colgan, W., Langen, P. L., & Mottram, R. H. (2016). The implication of nonradiative energy fluxes dominating Greenland ice sheet exceptional ablation area surface melt in 2012. *Geophysical Research Letters*, *43*, 2649–2658. https://doi.org/10.1002/2016GL067720

Fettweis, X., Tedesco, M., van den Broeke, M., & Ettema, J. (2011). Melting trends over the Greenland ice sheet (1958–2009) from spaceborne microwave data and regional climate models. *The Cryosphere*, *5*(2), 359–375. https://doi.org/10.5194/tc-5-359-2011

Forster, R. R., Box, J. E., van den Broeke, M. R., Miège, C., Burgess, E. W., van Angelen, J. H., et al. (2014). Extensive liquid meltwater storage in firn within the Greenland ice sheet. *Nature Geoscience*, *7*(2), 95–98. https://doi.org/10.1038/NGEO2043

Graeter, K. A., Osterberg, E., Ferris, D. G., Hawley, R. L., Marshall, H. P., Lewis, G., et al. (2018). Ice core records of West Greenland melt and climate forcing. *Geophysical Research Letters*, *45*, 3164–3172. https://doi.org/10.1002/2017GL076641

Hanna, E., Huybrechts, P., Steffen, K., Cappelen, J., Huff, R., Shuman, C., et al. (2008). Increased runoff from melt from the Greenland ice sheet: A response to global warming. *Journal of Climate*, *21*(2), 331–341. https://doi.org/10.1175/2007JCLI1964.1

Harper, J., Humphrey, N., Pfeffer, W. T., Brown, J., & Fettweis, X. (2012). Greenland ice-sheet contribution to sea-level rise buffered by meltwater storage in firn. *Nature*, *491*(7423), 240–243. https://doi.org/10.1038/nature11566

Hofer, S., Tedstone, A. J., Fettweis, X., & Bamber, J. L. (2017). Decreasing cloud cover drives the recent mass loss on the Greenland ice sheet. *Science Advances*, *3*(6), e1700584. https://doi.org/10.1126/sciadv.1700584

Janssens, I., & Huybrechts, P. (2000). The treatment of meltwater retention in mass-balance parametrization of the Greenland ice sheet. *Annals of Glaciology*, *31*, 133–140. https://doi.org/10.3189/172756400781819941

Katsushima, T., Kumakura, T., & Takeuchi, Y. (2009). A multiple snow layer model including a parameterization of vertical water channel process in snowpack. *Cold Regions Science and Technology*, *59*(2-3), 143–151. https://doi.org/10.1016/j.coldregions.2009.09.002

Khan, S., Aschwanden, A., Bjork, A., Wahr, J., Kjeldsen, K., & Kjaer, K. (2015). Greenland ice sheet mass balance: A review. *Reports on Progress in Physics*, *78*(4), 046801. https://doi.org/10.1088/0034-4885/78/4/046801

Langen, P., Fausto, R. S., Vandecrux, B., Mottram, R. H., & Box, J. E. (2017). Liquid water flow and retention on the Greenland ice sheet in the regional climate model HIRHAM5: Local and large-scale impacts. *Frontiers in Earth Science*, *4*(110). https://doi.org/10.3389/feart.2016.00110

Langen, P., Mottram, R., Christensen, J., Boberg, F., Rodehacke, C., Stendel, M., et al. (2015). Quantifying energy and mass fluxes controlling Godthåbsfjord freshwater input in a 5-km simulation (1991–2012). *Journal of Climate*, *28*(9), 3694–3713. https://doi.org/10.1175/JCLI-D-14-00271.1

Lefebre, F., Gallée, H., van Ypersele, J., & Greuell, W. (2003). Modelling of snow and ice melt at ETH camp (West Greenland): A study of surface albedo. *Journal of Geophysical Research*, *108*(D8), 4231. https://doi.org/10.1029/2001JD001160

Lomonaco, R., Albert, M., & Baker, I. (2011). Microstructural evolution of fine-grained layers through the firn column at summit, Greenland. *Journal of Glaciology*, *57*(204), 755–762. https://doi.org/10.3189/002214311797409730

Lucas-Picher, P., Wulff-Nielsen, M., Christensen, J. H., Aðalgeirsdóttir, G., Mottram, R., & Simonsen, S. (2012). Very high resolution in regional climate model simulations for Greenland: Identifying added value. *Journal of Geophysical Research*, *117*, D02108. https://doi.org/10.1029/2011JD016267

Machguth, H., MacFerrin, M., van As, D., Box, J. E., Charalampidis, C., Colgan, W., et al. (2016). Greenland meltwater storage in firn limited by near-surface ice formation. *Nature Climate Change*, *6*(4), 390–393. https://doi.org/10.1038/nclimate2899

Marchenko, S., van Pelt, W., Claremar, B., Machguth, H., Reijmer, C., Pettersson, R., & Pohjola, V. (2017). Parameterizing deep water percolation improves subsurface temperature simulations by a multilayer firn model. *Frontiers in Earth Science*, *5*(16). https://doi.org/10.3389/feart.2017.00016

Marsh, P., & Woo, M. (1984). Wetting front advance and freezing of meltwater within a snow cover. 1. Observations in the Canadian Arctic. *Water Resources Research*, *20*(12), 1853–1864. https://doi.org/10.1029/WR020i012p01853

Mayewski, P., & Whitlow, S. (2016). Snow pit data from Greenland summit, 1989 to 1993. *NSF Arctic Data Center*. https://doi.org/10.5065/D6NP22KX

Mosley-Thompson, E., McConnell, J., Bales, R., Li, Z., Lin, P.-N., & Steffen, K. (2001). Local to regional-scale variability of annual net accumulation on the Greenlandice sheet from PARCA cores. *Journal of Glaciology*, *106*(D24), 33,839–33,851. https://doi.org/10.1029/2001JD900067

Mote, T. L. (2007). Greenland surface melt trends 1973–2007: Evidence of a large increase in 2007. *Geophysical Research Letters*, *34*, L22507. https://doi.org/10.1029/2007GL031976

Nghiem, S. V., Hall, D. K., Mote, T. L., Tedesco, M., Albert, M. R., Keegan, K., et al. (2012). The extreme melt across the Greenland ice sheet in 2012. *Geophysical Research Letters*, *39*, L20502. https://doi.org/10.1029/2012GL053611

Orsi, A., Kawamura, K., Masson-Delmotte, V., Fettweis, X., Box, J. E., Dahl-Jensen, D., et al. (2017). The recent warming trend in North Greenland. *Geophysical Research Letters*, *44*, 6235–6243. https://doi.org/10.1002/2016GL072212

Pfeffer, W. T., Meier, M. F., & Illangaskare, T. (1991). Retention of Greenland runoff by refreezing: Implication for projected future sea level change. *Journal of Glaciology*, *96*(C12), 22,117–22,124.

Reijmer, C. H., van den Broeke, M. R., Fettweis, X., Ettema, J., & Stap, L. B. (2012). Refreezing on the Greenland ice sheet: A comparison of parameterizations. *The Cryosphere*, *6*(4), 743–762. https://doi.org/10.5194/tc-6-743-2012

Spencer, M. K., Alley, R. B., & Creyts, T. T. (2001). Preliminary firn-densification model with 38-site dataset. *Journal of Glaciology*, *96*(C12), 671–676. https://doi.org/10.1029/91JC02502

Steffen, K., & Box, J. E. (2001). Surface climatology of the Greenland ice sheet: Greenland climate network 1995–1999. *Journal of Glaciology*, *106*(D24), 33,951–33,964. https://doi.org/10.1029/2001JD900161

Steffen, K., Box, J. E., & Abdalati, W. (1996). Greenland climate network: GC-net. In S. C. Colbeck (Ed.), *Special Report on Glaciers, Ice Sheets and Volcanoes, trib. to M. Meier*, (pp. 98–103). CRREL 96–27. Hanover, NH.

Steger, C. R., Reijmer, C. H., & van den Broeke, M. R. (2017). The modelled liquid water balance of the Greenland ice sheet. *The Cryosphere*, *11*(6), 2507–2526. https://doi.org/10.5194/tc-11-2507-2017

Tardivo, G., & Berti, A. (2012). A dynamic method for gap filling in daily temperature datasets. *Journal of Applied Meteorology*, *51*(6), 1079–1086. https://doi.org/10.1175/JAMC-D-11-0117.1

Tedesco, M., Fettweis, X., van den Broeke, M. R., van de Wal, R. S., Smeets, C. J., van de Berg, W. J., et al. (2011). The role of albedo and accumulation in the 2010 melting record in Greenland. *Environmental Research Letters*, *6*(1). https://doi.org/10.1088/1748-9326/6/1/014005

van Angelen, J. H., Lenaerts, J., van den Broeke, M. R., Fettweis, X., & van Meijgaard, E. (2013). Rapid loss of firn pore space accelerates 21st century Greenland mass loss. *Geophysical Research Letters*, *40*, 2109–2113. https://doi.org/10.1002/grl.50490

van As, D., Hubbard, A. L., Hasholt, B., Mikkelsen, A. B., van den Broeke, M. R., & Fausto, R. S. (2012). Large surface meltwater discharge from the Kangerlussuaq sector of the Greenland ice sheet during the record-warm year 2010 explained by detailed energy balance observations. *The Cryosphere*, *6*(1), 199–209. https://doi.org/10.5194/tc-6-199-2012

van As, D., Mikkelsen, A. B., Nielsen, M. H., Box, J. E., Liljedahl, L. C., Lindbäck, K., et al. (2017). Hypsometric amplification and routing moderation of Greenland ice sheet meltwater release. *The Cryosphere, 11*(3), 1371–1386. https://doi.org/10.5194/tc-11-1371-2017

van As, D., van den Broeke, M., Reijmer, C., & van de Wal, R. (2005). The summer surface energy balance of the high Antartic plateau. *Boundary-Layer Meteorology*, *115*(2), 289–317. https://doi.org/10.1007/s10546-004-4631-1

van den Broeke, M. R., Enderlin, E. M., Howat, I. M., Kuipers Munneke, P., Noël, B. P., van de Berg, W. J., et al. (2016). On the recent contribution of the Greenland ice sheet to sea level change. *The Cryosphere*, *10*(5), 1933–1946. https://doi.org/10.5194/tc-10-1933-2016

van Tricht, K., Lhermitte, S., Lenaerts, J. T., Gorodetskaya, I. V., L'Ecuyer, T. S., Noël, B., et al. (2016). Clouds enhance Greenland ice sheet meltwater runoff. *Nature Communications*, *7*, 10266. https://doi.org/10.1038/ncomms10266

Vionnet, V., Brun, E. S., Eisen, A., Fierz, C., & Lehning, M. (2012). The detailed snowpack scheme Crocus and its implementation in SURFEXv7.2. *Geoscientific Model Development*, *5*(3), 773–791. https://doi.org/10.5194/gmd-5-773-2012

Wever, N., Fierz, C., Mitterer, C., Hirashima, H., & Lehning, M. (2014). Solving Richards equation for snow improves snowpack meltwater runoff estimations in detailed multi-layer snowpack model. *The Cryosphere*, *8*(1), 257–274. https://doi.org/10.5194/tc-8-257-2014

Wever, N., Würzer, S., Fierz, C., & Lehning, M. (2016). Simulating ice layer formation under the presence of preferential flow in layered snowpacks. *The Cryosphere*, *10*(6), 2731–2744. https://doi.org/10.5194/tc-10-2731-2016

Yen, Y. (1981). *Review of Thermal Properties of Snow, Ice and Sea Ice*. Hanover,NH: United States Army Cold Regions Research and Engineering Laboratory.

APPENDIX F

Paper VI

The Cryosphere, 13, 845–859, 2019
https://doi.org/10.5194/tc-13-845-2019

The Cryosphere Open Access EGU

Firn data compilation reveals widespread decrease of firn air content in western Greenland

Baptiste Vandecrux[1,2], Michael MacFerrin[3], Horst Machguth[4,5], William T. Colgan[1], Dirk van As[1], Achim Heilig[6], C. Max Stevens[7], Charalampos Charalampidis[8], Robert S. Fausto[1], Elizabeth M. Morris[9], Ellen Mosley-Thompson[10], Lora Koenig[11], Lynn N. Montgomery[11], Clément Miège[12], Sebastian B. Simonsen[13], Thomas Ingeman-Nielsen[2], and Jason E. Box[1]

[1]Department of Glaciology and Climate, Geological Survey of Denmark and Greenland, Copenhagen, Denmark
[2]Department of Civil Engineering, Technical University of Denmark, Kongens Lyngby, Denmark
[3]Cooperative Institute for Research in Environmental Sciences, University of Colorado, Boulder, CO, USA
[4]Department of Geosciences, University of Fribourg, Fribourg, Switzerland
[5]Department of Geography, University of Zurich, Zurich, Switzerland
[6]Department of Earth and Environmental Sciences, Ludwig Maximilian University, Munich, Germany
[7]Department of Earth and Space Sciences, University of Washington, Seattle, WA, USA
[8]Bavarian Academy of Sciences and Humanities, Munich, Germany
[9]Scott Polar Research Institute, Cambridge University, Cambridge, UK
[10]Byrd Polar and Climate Research Center and Department of Geography, Ohio State University, Columbus, OH, USA
[11]National Snow and Ice Data Center, University of Colorado, Boulder, CO, USA
[12]Department of Geography, Rutgers University, Piscataway, NJ, USA
[13]DTU Space, National Space Institute, Department of Geodynamics, Technical University of Denmark, Kongens Lyngby, Denmark

Correspondence: Baptiste Vandecrux (bava@byg.dtu.dk)

Received: 21 August 2018 – Discussion started: 28 August 2018
Revised: 29 January 2019 – Accepted: 2 February 2019 – Published: 11 March 2019

Abstract. A porous layer of multi-year snow known as firn covers the Greenland-ice-sheet interior. The firn layer buffers the ice-sheet contribution to sea-level rise by retaining a fraction of summer melt as liquid water and refrozen ice. In this study we quantify the Greenland ice-sheet firn air content (FAC), an indicator of meltwater retention capacity, based on 360 point observations. We quantify FAC in both the uppermost 10 m and the entire firn column before interpolating FAC over the entire ice-sheet firn area as an empirical function of long-term mean air temperature ($\overline{T_a}$) and net snow accumulation ($\bar{c}$). We estimate a total ice-sheet-wide FAC of $26\,800 \pm 1840\,km^3$, of which $6500 \pm 450\,km^3$ resides within the uppermost 10 m of firn, for the 2010–2017 period. In the dry snow area ($\overline{T_a} \leq -19\,°C$), FAC has not changed significantly since 1953. In the low-accumulation percolation area ($\overline{T_a} > -19\,°C$ and $\bar{c} \leq 600\,mm\,w.e.\,yr^{-1}$), FAC has decreased by $23 \pm 16\,\%$ between 1998–2008 and 2010–2017. This reflects a loss of firn retention capacity of between $150 \pm 100\,Gt$ and $540 \pm 440\,Gt$, respectively, from the top 10 m and entire firn column. The top 10 m FACs simulated by three regional climate models (HIRHAM5, RACMO2.3p2, and MARv3.9) agree within 12 % with observations. However, model biases in the total FAC and marked regional differences highlight the need for caution when using models to quantify the current and future FAC and firn retention capacity.

1 Introduction

As a consequence of the atmospheric and oceanic warming associated with anthropogenic climate change, the Greenland ice sheet (GrIS) is losing mass at an accelerating rate. The GrIS is now responsible for approximately 20 % of con-

Published by Copernicus Publications on behalf of the European Geosciences Union.

temporary sea-level rise (Bindoff et al., 2013; Nerem et al., 2018). Over half of this GrIS mass loss stems from summer surface melt and subsequent meltwater runoff into the ocean (van den Broeke et al., 2016). While most meltwater runoff originates from the low-elevation ablation area, the surface melt area is now expanding into the high-elevation firn-covered interior of the GrIS (Mote et al., 2007; Nghiem et al., 2012). Rather than flowing horizontally, most of the meltwater produced at the surface of the firn area percolates vertically into the underlying firn where it refreezes and thereby does not contribute to sea-level rise (Harper et al., 2012). Hence, the meltwater retention capacity of Greenland's firn is a non-trivial parameter in the sea-level budget.

Assessing meltwater retention capacity of the firn in Greenland requires knowledge of both the extent of the firn area, as well as the spatial distribution of depth-integrated firn porosity or firn air content (FAC). The extent of the firn area can be tracked using the firn line, which Benson (1962) described as "the highest elevation to which the annual snow cover recedes during the melt season". Recently, Fausto et al. (2018a) updated the methods from Fausto et al. (2007) and presented maps of remotely sensed end-of-summer snow lines over the 2000–2017 period. These maps effectively provide an annual delineation of Greenland's firn area. FAC is the integrated volume of air contained within the firn from the surface to a certain depth per unit area (van Angelen et al., 2013; Ligtenberg et al., 2018). FAC quantifies the maximum pore volume available per unit area to retain percolating meltwater, either in liquid or refrozen form (Harper et al., 2012; van Angelen et al., 2013). Previously, ice-sheet-wide firn retention capacity has been estimated using simplifying assumptions (Pfeffer et al., 1991) or unconstrained regional climate model (RCM) simulations (van Angelen et al., 2013). Harper et al. (2012) provided the first empirical estimate of the firn's meltwater retention capacity in the GrIS percolation area using 3 years of observations (2007–2009) at 15 sites in western Greenland. While pioneering, their approach did not acknowledge the GrIS's diverse firn regimes (Forster et al., 2014; Machguth et al., 2016). Ligtenberg et al. (2018) provided an RCM simulation of FAC that generally compares well against observations in 62 firn cores but substantially underestimated FAC in the western percolation area.

The depth to which meltwater may percolate, and therefore the depth range over which FAC must be integrated to constrain meltwater retention capacity, varies with melt intensity and firn permeability (Pfeffer et al., 1991). This makes the maximum depth of meltwater percolation both temporally and spatially variable, as highlighted by the following studies. Braithwaite et al. (1994) and Heilig et al. (2018) reported meltwater refreezing within the top 4 m of firn in western Greenland, respectively, at $\sim$ 1500 m a.s.l. during the summer of 1991 and at 2120 m a.s.l. during the 2016 melt season. Both studies indicate that, at specific sites and years, meltwater is stored in near-surface firn. However, firn temperature measurements in 2007–2009 at 1555 m a.s.l. in western Greenland (Humphrey et al., 2012) as well as the presence of firn aquifer at a depth greater than 10 m in south-eastern Greenland (Miège et al., 2016) both show that meltwater can percolate below 10 m depth in the firn. This deep percolation implies that, for certain firn conditions and given sufficient meltwater, the FAC of the total firn column, from the surface to the firn–ice transition, may be used for meltwater retention. Finally, Machguth et al. (2016) show that percolation depth may not increase linearly with meltwater production, and instead low-permeability ice layers can limit even abundant meltwater from percolating into the entire firn column. Given the complexity of meltwater percolation and the paucity of percolation observations, reasonable upper and lower bounds of the meltwater retention capacity of firn can be estimated by determining FAC through the total firn column (FAC_{tot}) and within the uppermost 10 m of firn column (FAC_{10}), respectively (Harper et al., 2012). FAC_{tot} is also valuable information to convert remotely sensed surface height changes into mass changes (Sørensen et al., 2011; Simonsen et al., 2013; Kuipers Munneke et al., 2015a).

In this study, we first compile a dataset of 360 firn density profiles, collected between 1953 and 2017, and quantify the observed FAC. We then extrapolate these point-scale observations across the entire GrIS firn area as empirical functions of long-term mean air temperature and mean snow accumulation. The point observations are thereby used to resolve the spatial distribution of FAC but also, where possible, its temporal evolution. We use a simple extrapolation to estimate FAC_{tot} from FAC_{10} where firn cores do not extend to the firn–ice transition. Spatial integration of FAC_{10} and FAC_{tot} over the firn area permits the estimation of the lower and upper bounds, respectively, of the GrIS firn meltwater retention capacity. Finally, we evaluate the FAC simulated by three RCMs that are commonly used to evaluate ice-sheet-wide firn meltwater retention capacity but that have never been compared to such an extensive firn dataset.

2 Data and methods

2.1 Firn core dataset and firn area delineation

We compiled 340 previously published GrIS firn density profiles of at least 5 m in depth (Table 1). To these, we added an additional 20 cores extracted in 2016 and 2017, for which firn density was measured at a 10 cm resolution following the same procedure as Machguth et al. (2016). When near-surface snow densities were missing, we assigned a density of 315 kg m^{-3} (Fausto et al., 2018b) to the top centimetre and interpolated over the remaining gaps in density profiles using a logarithmic function of depth fitted to the available densities.

We use the end-of-summer snow lines from Fausto et al. (2018a) to delineate the minimum firn area detected during the 2000–2017 period. This 1 405 500 km^2 area, where

Table 1. List of the publications presenting the firn cores used in this study.

Source	Number of cores
Albert and Shultz (2002)	1
Alley (1987)	1
Bader (1954)	1
Baker (2012)	1
Benson (1962)	55
Bolzan and Strobel (1999)	9
Buchardt et al. (2012)	8
Clausen et al. (1988)	8
Colgan et al. (2018)	1
Fischer et al. (1995)	14
Forster et al. (2014)	5
Hawley et al. (2014)	8
Harper et al. (2012)	32
Jezek (2012)	1
Kameda et al. (1995)	1
Koenig et al. (2014)	3
Kovacs et al. (1969)	1
Langway (1967)	1
Lomonaco et al. (2011)	1
Machguth et al. (2016)	28
Mayewski and Whitlow (2016a)	1
Mayewski and Whitlow (2016b)	1
Miège et al. (2013)	3
Morris and Wingham (2014)	66
Mosley-Thompson et al. (2001)	47
Porter and Mosley-Thompson (2014)	1
Reed (1966)	1
Renaud (1959)	7
Spencer et al. (2001)	8
Steen-Larsen et al. (2011)	1
Vallelonga et al. (2014)	1
Van der Veen et al. (2001)	10
Wilhelms (1996)	13
This study	20

snow is always detected during the 2000–2017 period, is taken to represent the GrIS's current firn area. Moving this firn line 1 km inward or outward, the resolution of the product from Fausto et al. (2018a) suggests an uncertainty of $\pm 17\,250\,\mathrm{km}^2$ ($\sim 1\,\%$). Additional uncertainty applies to the margin of the firn area where transient firn patches may exist outside of our delineation. Owing to the inherent thinness of firn at the lower elevation boundary of the firn area, we expect these omitted firn patches to play a negligible role in the overall meltwater retention capacity of the firn area.

2.2 Calculation of FAC_{10}

For a discrete density profile composed of N sections and reaching a depth z, the FAC in metres is calculated as follows:

$$\mathrm{FAC}_z = \sum_{k=1}^{N} m_k \left(\frac{1}{\rho_k} - \frac{1}{\rho_{\mathrm{ice}}} \right), \quad (1)$$

where, for each depth interval k, ρ_k is the firn density and m_k is the firn mass. ρ_{ice} is the density of the ice, assumed to be $917\,\mathrm{kg\,m^{-3}}$.

With 121 cores shorter than 10 m in our dataset, we extrapolate shallow measurements to a depth of 10 m. We do this by finding the core longer than 10 m that best matches the FAC-versus-depth profile of the core shorter than 10 m with the lowest root-mean-squared difference (RMSD) amongst all available cores. We then append the bottom section of this core longer than 10 m to the FAC profile of the core shorter than 10 m (see Fig. S1 of the Supplement). When testing this methodology on the available cores longer than 10 m, from which we remove the deepest 3 m of the FAC profile, we find a mean difference between extrapolated and real $\mathrm{FAC}_{10} < 1\,\%$ and an RMSD of 0.15 m.

We assess the accuracy of the firn density measurements, as well as the effect of spatial heterogeneity, by comparing FAC_{10} measurements located within 1 km and collected in the same year (Fig. S2). A standard deviation below 0.15 m is found in the majority of the co-located and contemporaneous FAC_{10} observations (20 of 27 groups of comparable observations). We correspondingly assign an uncertainty of ± 0.3 m, twice this standard deviation, to FAC_{10} measurements.

2.3 Zonation of firn air content

The FAC_{10} is calculated from firn density, which depends, among other parameters, on the local near-surface air temperature and snowfall rate (Shumskii, 1964). Air temperature is a proxy for summer melt and subsequent refreezing within the firn, as well as firn temperature and compaction rates. Through these processes, increasing air temperature acts to decrease FAC (Kuipers Munneke et al., 2015b). On the other hand, snow accumulation introduces low-density fresh snow at the surface. Increasing snowfall thus acts to increase FAC. To put our FAC_{10} measurements in their climatic context, we extract the long-term (1979–2014) average annual net snow accumulation $\overline{\dot{c}}$ (snowfall − sublimation) and air temperature $\overline{T_{\mathrm{a}}}$ for each FAC_{10} measurement location from the nearest $5\,\mathrm{km}^2$ cell of the Modèle Atmosphérique Régional (MARv3.5.2; Fettweis et al., 2017).

Following the terminology of Benson (1962), we define three regions where FAC_{10} shows distinct regimes: (1) the dry snow area (DSA, yellow area in Fig. 1a), (2) the low-accumulation percolation area (LAPA, red area in Fig. 1a) and (3) the high-accumulation percolation area (HAPA, green area in Fig. 1a). The DSA encompasses low temperature regions of high altitude and/or latitude where melt is uncommon and where FAC_{10} can be related by a linear function of $\overline{T_{\mathrm{a}}}$ (yellow markers in Fig. 1c). Two distinct firn regimes emerge towards higher $\overline{T_{\mathrm{a}}}$, meaning lower altitude and/or lat-

itude. Firstly, towards lower $\bar{\dot{c}}$, in the LAPA, more scatter appears in FAC_{10} and the slope of the FAC_{10} temperature dependency changes. Secondly, towards higher $\bar{\dot{c}}$, in the HAPA, the few available FAC_{10} observations describe a similar temperature dependency as in the DSA, even though they are in relatively warm regions where melt occurs. FAC_{10} observations in the HAPA are up to 5 times higher than at locations with similar $\overline{T_a}$ in the LAPA (Fig. 1c).

The boundary that delineates the cold (DSA) and warm regions (LAPA and HAPA) can be defined as the temperature where an inflection occurs in the linear dependency of FAC_{10} on $\overline{T_a}$ (Fig. 1c). We interpret the slope break in the temperature dependence of FAC_{10} as the upper limit of frequent meltwater percolation and refreezing within the firn which Benson et al. (1962) defined as the dry snow line. While the transition between cold and warm areas is gradual in practice, for our analysis we set this boundary to $\overline{T_a} = -19\,°C$. Our LAPA and HAPA here stretch from the dry snow line to the firn line and therefore also include the so-called wet snow facies defined by Benson et al. (1962). The snowfall boundary that delineates the low- and high-accumulation percolation areas is more difficult to characterise. There are insufficient firn observations available along the transition from LAPA to HAPA. The snowfall boundary could be anywhere between 543 mm w.e. yr^{-1} (the highest-accumulation LAPA core, Fig. 1b) and 647 mm w.e. yr^{-1} (the lowest-accumulation HAPA core, Fig. 1b). Acknowledging this uncertainty, we chose the round value of $\bar{\dot{c}} = 600$ mm w.e. yr^{-1} to separate LAPA and HAPA. The spatial delineations of the DSA, LAPA and HAPA are illustrated in Fig. 1a.

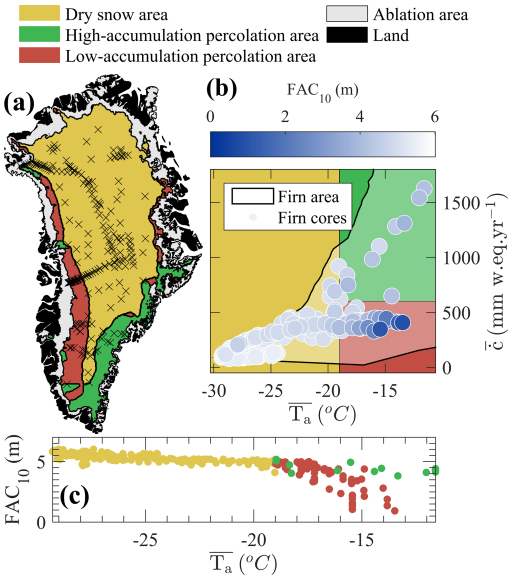

Figure 1. (a) Spatial distribution of the FAC_{10} dataset. The DSA, HAPA and LAPA are indicated using yellow, green and red areas, respectively. **(b)** Distribution of the dataset in the accumulation–temperature space ($\bar{\dot{c}}$ and $\overline{T_a}$). FAC_{10} value is indicated by a coloured marker. Black lines and shaded areas indicate the extent of firn in the accumulation–temperature space. **(c)** Temperature dependency of FAC_{10} in the DSA (yellow markers), LAPA (red markers) and HAPA (green markers).

2.4 FAC_{10} interpolation

To interpolate point-scale observations of FAC_{10} over the entire GrIS firn area, we describe FAC_{10} observations using empirical functions of long-term mean air temperature and net snowfall. The derivation of these empirical functions is described in the following sections and an overview of their general form as well as the data used to constrain them is presented in Table 2.

2.4.1 Dry snow area

In the DSA, the 259 FAC_{10} observations obtained between 1953 and 2017 can be approximated by a linear function of their local $\overline{T_a}$ (Fig. 1c). This dependency is the same for the 19 FAC_{10} observations from the upper HAPA available between 1981 and 2014. We consequently include these observations so that the linear relationship remains valid in the upper HAPA (Sect. 2.4.2). These 278 FAC_{10} observations are then binned into four equal $\overline{T_a}$ ranges to avoid the over-representation of clustered data (Fig. 2a). Eventually, a linear function of $\overline{T_a}$ is fitted to the bins' average FAC_{10} using a least-squares method to estimate the FAC_{10} in the DSA:

$$FAC_{10}\left(\overline{T_a}\right) = -0.08 \times \overline{T_a} + 3.27. \quad (2)$$

We assign to any FAC_{10} estimated in the DSA using Eq. (2) an uncertainty equal to twice the regression's RMSD: 0.4 m. Although FAC_{10} is also dependent on $\bar{\dot{c}}$, the residuals from Eq. (2) do not present any correlation with their respective $\bar{\dot{c}}$ values. It indicates that because of the intrinsic co-variability of $\bar{\dot{c}}$ and $\overline{T_a}$, most of the variations in observed FAC_{10} can be explained using either $\bar{\dot{c}}$ or $\overline{T_a}$. Insufficient data are available to separate the role of $\bar{\dot{c}}$ and $\overline{T_a}$ in FAC_{10} variations in the DSA. We therefore choose to use only $\overline{T_a}$ in Eq. (2).

2.4.2 Percolation areas

In the LAPA and in the HAPA, FAC_{10} observations exhibit a more complex dependency on $\bar{\dot{c}}$ and $\overline{T_a}$ (Fig. 1b and c). Additionally, observations are unevenly distributed in space and time. Thus, to reveal the temporal trends in FAC_{10}, the observation dataset is divided into two time slices that each contain enough FAC_{10} observations to describe the spatial pattern of FAC_{10} and constrain our empirical functions.

Table 2. Overview of the empirical functions fitted to FAC_{10} observations in each region of the firn area.

Area	Period	Form	Observations used for fitting
DSA and upper HAPA	1953–2017	Linear function of $\overline{T_a}$ (Eq. 2)	259 from the DSA 19 from the HAPA
LAPA and HAPA	2010–2017	Smoothed bilinear function of $\overline{T_a}$ and $\bar{c}$	25 from the LAPA 10 from the HAPA 6 selected from firn line in the HAPA
LAPA	1998–2008	Cannot exceed the FAC_{10} estimated with Eq. (2)	38 from the LAPA 1 from the HAPA 6 selected from the firn line in the HAPA

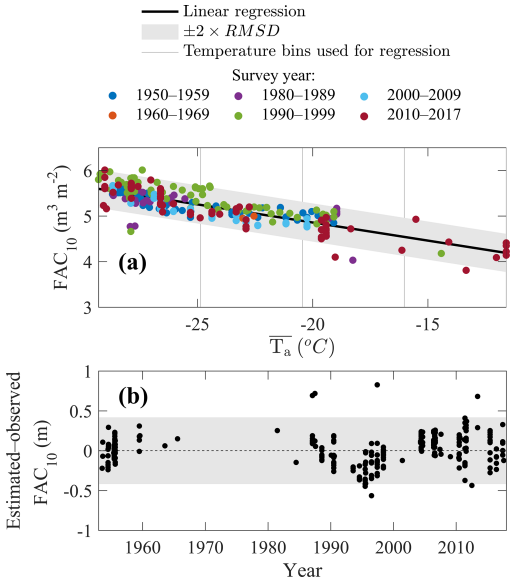

Figure 2. **(a)** Linear function of $\overline{T_a}$ fitted to FAC_{10} observations from the DSA and upper HAPA. **(b)** Residual between estimated (using linear regression) and observed FAC_{10} as a function of survey year.

Over the 2010–2017 period, 25 FAC_{10} observations were made in the LAPA, stretching from the upper boundary of the LAPA down to the vicinity of the firn line. During that same period, 10 firn cores were collected in the HAPA. Unfortunately, in addition to their small number, the cores are located relatively far into the interior of the ice sheet and do not describe how the FAC_{10} decreases in parts of the HAPA closer to the firn line. We consequently complement these firn cores with six sites, selected on the remotely sensed firn line, where FAC_{10} is assumed to be null (Fig. S3). FAC_{10} in the LAPA and HAPA during 2010–2017 is then described by a smoothed bilinear function of $\overline{T_a}$ and $\bar{c}$ fitted through least squares method to the available observations (Fig. 3b). We do not allow that function to exceed the linear function of $\overline{T_a}$ that describes FAC_{10} measurements in the DSA and in the upper HAPA (Eq. 2) or to predict FAC_{10} below 0 m.

Prior to 2010, insufficient data are available to document the FAC_{10} in the HAPA. In the LAPA, however, 35 observations were made between 2006 and 2008 and three cores were collected in 1998. These measurements are used to describe the FAC_{10} in LAPA during the 1998–2008 period by a smoothed bilinear function of $\overline{T_a}$ and $\bar{c}$. To ensure that our empirical function has realistic values towards the transition with the HAPA, we also include one core collected in the HAPA in 1998. We also include the previously described six locations from the firn line (Fig. 3a). Although observation locations in 1998–2008 and 2010–2017 can be different, few samples available at the same sites (e.g. Crawford Point, DYE-2) in both time slices confirm that FAC_{10} changes are more likely due to a temporal evolution rather than from the different spatial coverage of each period's constraining dataset.

The empirical functions used to estimate the FAC_{10} in the LAPA and HAPA (Fig. 3), when compared to FAC_{10} observations, have a RMSD of 0.28 m in the LAPA over the 1998–2008 period, 0.27 m in the LAPA over the 2010–2017 period and 0.17 m in the HAPA over the 2010–2017 period.

We investigate the robustness of our empirical functions in the HAPA and LAPA using, for each period separately, the following sensitivity analysis. For 1000 repetitions, we apply four types of perturbations to the FAC_{10} observations and then refit our empirical functions. The effect of the availability of measurements in the LAPA is tested by randomly excluding four observations in that region (16 % and 11 % of observations in 2010–2017 and 1998–2008, respectively). The effect of uncertainty in the firn line location in the $(\overline{T_a}, \bar{c})$ space is tested by adding a normally distributed noise with a mean of zero and standard deviation of 3 °C to the $\overline{T_a}$ of firn-line-derived FAC_{10} (illustrated in Fig. S3). The effect of the uncertain FAC_{10} value at the firn line is assessed by assigning to firn-line-derived points a random FAC_{10} value between 0

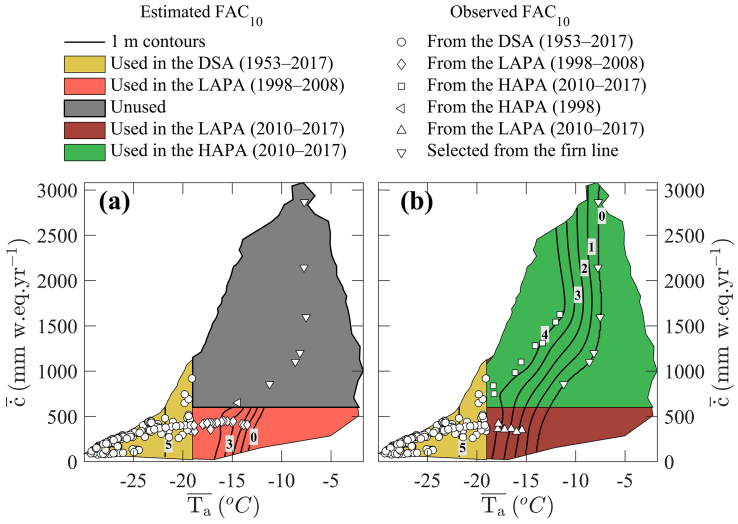

Figure 3. Contours (labelled black lines) of the empirical functions of $\overline{T_a}$ and $\bar{c}$ used to estimate FAC_{10} along with the FAC_{10} observations used to constrain the functions. Two functions could be constructed: **(a)** describing FAC_{10} in the LAPA during 1998–2008 and **(b)** describing FAC_{10} in the LAPA and HAPA during 2010–2017.

and 1 m. Finally, the effect of the smoothing applied to the bilinear interpolation of FAC_{10} measurements is assessed by modifying the amount of smoothing applied. Following 1000 repetitions of the above-mentioned four perturbations to the FAC_{10} observations, we then calculate the standard deviation of all empirically estimated FAC_{10} values within the ($\overline{T_a}$, $\bar{c}$) parameter space. We then double this standard deviation to approximate the 95 % uncertainty envelope for empirically estimated FAC_{10} in the LAPA and HAPA. We set 0.3 m, the uncertainty related to FAC measurements (Sect. 2.2), as the minimum possible uncertainty on any empirically estimated FAC_{10}.

2.5 Estimation of FAC_{tot}

FAC_{tot} should be integrated from the ice-sheet surface down to the depth where firn reaches the density of ice (Ligtenberg et al., 2018). This depth varies in space and time across the GrIS but is poorly documented. Additionally, the RCM HIRHAM5 (evaluated in Sect. 3.3) does not reach ice density at the bottom of its column in certain locations. We therefore calculate FAC_{tot} as the vertically integrate FAC from the surface to a standard 100 m depth. Only 29 of our 360 firn observations reach depths greater than 100 m. We therefore complement these core observations with 13 ground-penetrating radar observations of FAC_{tot} from Harper et al. (2012).Using the least squares method with an intercept of zero, we fit the following linear regression between FAC_{10} and FAC_{tot} (Fig. 4):

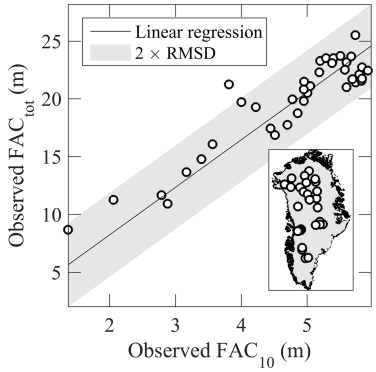

Figure 4. Linear regression used to estimate FAC_{tot} from FAC_{10}.

$$FAC_{tot} = 4.1 \times FAC_{10}. \quad (3)$$

This function infers that FAC_{tot} is approximately 410 % of FAC_{10}. While we acknowledge this relation is straightforward, we highlight that it is statistically robust. We assign 3.6 m, twice the RMSD of the linear regression, as the typical uncertainty for an estimated FAC_{tot} value that can, in theory, vary between 0 and $\sim$ 25 m.

As a result of deriving FAC_{tot} as a function of FAC_{10} (Eq. 3), any change in FAC_{10} between two dates implies a

proportional change in FAC_{tot} over the same time period. The use of this covariation neglects the fact that near-surface changes in the firn slowly propagate to greater depth with thermal conduction and downward mass advection (Kuipers Munneke et al., 2015b). We therefore note that, for a decreasing FAC_{10} (see Sect. 3.2.1), our estimated change in FAC_{tot} corresponds to the maximum possible change associated with the whole firn column having sufficient time to adapt to the new surface conditions.

2.6 Spatially integrated FAC and retention capacity

We define, for any ice-sheet region, the spatially integrated FAC as the cumulated volume of air within that region either in the top 10 m of firn or for the total firn column (top 100 m). The uncertainty associated with the empirically estimated FAC_{10} and FAC_{tot} at a given location is not independent of other locations because the same functions of $\overline{T_a}$ and $\bar{\bar{c}}$ are applied across the GrIS. Consequently, we consider that the uncertainty of the mean FAC in a specific region is the mean of FAC uncertainty values therein and that the uncertainty of spatially integrated FAC is the sum of the uncertainty values in the considered region.

We use the estimated FAC to calculate the meltwater retention capacity of the firn. Harper et al. (2012) defined the firn retention capacity as the amount of water that needs to be added to the firn to bring its density to $843\,kg\,m^{-3}$, the density of firn saturated by refrozen meltwater measured in firn cores.

2.7 Comparison with regional climate models

We compare our FAC_{10} observations and spatially integrated FAC estimates to the firn products available from three RCMs: HIRHAM5, RACMO2.3p2 and MARv3.9. HIRHAM5 output is available at 5.5 km spatial resolution and is presented in Langen et al. (2017). Two versions of HIRHAM5 are used: linear parameterisation of surface albedo (hereafter referred as HH_LIN) and MODIS-derived albedo (hereafter referred as HH_MOD). RACMO2.3p2, presented by Noël et al. (2018), provides FAC at a 5.5 km resolution. MARv3.9, presented in Fettweis et al. (2017), only simulates FAC_{10} because of its shallow subsurface domain and has a spatial resolution of 15 km.

3 Results and discussion

3.1 Spatio-temporal distribution of FAC

In the DSA, we consider the absence of a temporal trend in the deviation between measured FAC_{10} and FAC_{10} estimated using the linear function of $\overline{T_a}$ (Fig. 2b) as evidence of unchanging FAC_{10} in that area between 1953 and 2017. This inference of widespread stable FAC in the DSA is confirmed at point scale by firn cores in our dataset taken at the same sites but decades apart, showing the same FAC (e.g. Summit Station, Camp Century). This result is also corroborated by recent firn modelling at weather stations located in the DSA (Vandecrux et al., 2018).

Using the $5\,km \times 5\,km$ $\overline{T_a}$ and $\bar{\bar{c}}$ grids from Fettweis et al. (2017) and the empirical functions presented in Fig. 3, we map the FAC_{10} and its uncertainty across the GrIS firn area (Fig. 5). From these maps we calculate an average FAC_{10} of 5.2 ± 0.3 m in the DSA over the 1953–2017 period and of 3.0 ± 0.4 m in the HAPA during the 2010–2017 period. Within the LAPA, we calculate an average FAC_{10} of 3.9 ± 0.3 m during the 1998–2008 period, which decreases by 23 % to 3.0 ± 0.3 m in the 2010–2017 period. Spatially, the FAC_{10} loss in the LAPA is concentrated in a 60 km wide band above the firn line in western Greenland (Fig. 5b).

We find that during the 2010–2017 period, the entire firn area contained $6500 \pm 450\,km^3$ of air within the top 10 m and up to $26\,800 \pm 1840\,km^3$ within the whole firn column (Table 3). About 83 ± 5 % of this air content is found in the DSA, which represents 74 % of the firn area. The HAPA, covering 12 % of the firn area, contains 8 ± 1 % of GrIS FAC, both for the top 10 m and the whole firn column.

The LAPA, which comprises 14 % of the firn area, contained 9 ± 1 % of ice-sheet-wide firn air content in the period 2010–2017. Decreasing FAC_{10} between 1998–2008 and 2010–2017 yields a loss of $170 \pm 120\,km^3$ (23 ± 16 %) of air from the top 10 m of firn. The corresponding decrease in FAC_{tot} indicates that, as an upper estimate, $700 \pm 490\,km^3$ of air may have been lost from the total firn column. In this we assume that the FAC_{10} decrease propagated to the entire firn column (see Sect. 2.5), which might not be accurate. Insufficient data are available to determine precisely how much FAC was lost below 10 m and we can only give a hypothetical upper bound to the FAC_{tot} decrease.

Recent studies have identified increasing surface melt and meltwater refreezing as major contributors to increasing near-surface firn densities and subsequent loss of FAC (de la Peña et al., 2015; Charalampidis et al., 2015; Machguth et al., 2016; Graeter et al., 2018). However, firn density and FAC are also dependent on annual snowfall, with decreasing snowfall driving increasing firn density and decreasing FAC (e.g. Vandecrux et al., 2018). Nevertheless, the lack of widely distributed observations of snow accumulation for the 1998–2017 period and the contradicting trends in precipitation calculated by RCMs (Lucas-Picher et al., 2012; van den Broeke et al., 2016; Fettweis et al., 2017) complicate the partitioning of the melt and snowfall contributions to changes in GrIS FAC.

To investigate how uncertainties in $\overline{T_a}$ and $\bar{\bar{c}}$ impact our FAC_{10} maps, we repeat our procedure using the 1979–2014 $\overline{T_a}$ and $\bar{\bar{c}}$ estimated by Box (2013) and Box et al. (2013) (hereafter referred to as "Box13"). The Box13-derived FAC_{10} fits equally well ($RMSD < 0.3$ m) to the FAC_{10} observations, leading to spatially integrated FAC values within the uncertainty of the MAR-derived values. However, due to differ-

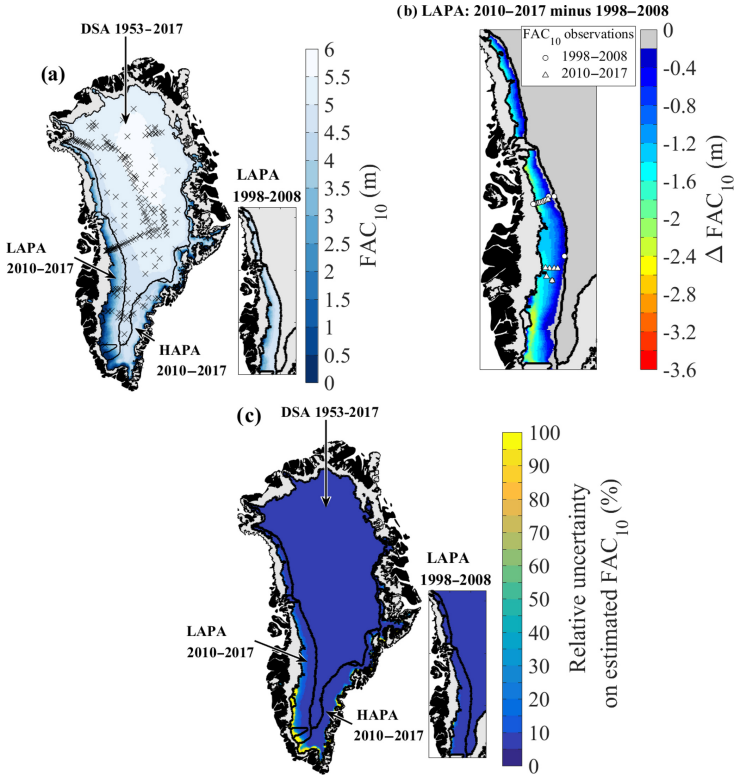

Figure 5. **(a)** FAC_{10} maps and location of the FAC_{10} measurements. **(b)** Change in FAC_{10} between 1998–2008 and 2010–2017 in the LAPA. **(c)** Maps of the relative uncertainty of the FAC_{10}.

Table 3. Spatially integrated FAC and firn retention capacity over each ice-sheet region.

Area	Period	Spatially integrated FAC (km^3)		Firn storage capacity (Gt)	
		Upper 10 m	Total firn column	Upper 10 m	Total firn column
DSA	1953–2017	5400 ± 310	$22\,300 \pm 1280$	4200 ± 290	$12\,800 \pm 1170$
LAPA	1998–2008	750 ± 60	3100 ± 240	550 ± 50	1490 ± 220
LAPA	2010–2017	580 ± 60	2400 ± 250	400 ± 50	950 ± 220
HAPA	2010–2017	530 ± 80	2200 ± 320	370 ± 70	960 ± 290
All	2010–2017	6500 ± 450	$26\,800 \pm 1840$	5000 ± 410	$14\,700 \pm 1600$

ing model formulations and atmospheric forcings, the spatial patterns of air temperature and snowfall are different between Box13 and MARv3.5.2 (detailed in Fettweis et al., 2017), especially in the southern and eastern regions of the firn area. This leads to different estimations of FAC_{10} in these regions (Fig. S4). Additionally, in these regions no firn observations are available to constrain our FAC_{10} estimates. More observations in the sparsely observed southern and eastern regions would improve FAC_{10} estimates and help better elucidate which $\overline{T_a}$ and $\bar{c}$ source best describes the spatial pattern in FAC_{10}.

3.2 Firn retention capacity

The decrease in FAC_{10} in the LAPA between 1998–2008 and 2010–2017 translates to a loss in meltwater retention capacity of 150 ± 100 Gt in the top 10 m of firn (Table 3). This lost

retention capacity represents 0.4 ± 0.3 mm sea-level equivalent (s.l.e.). For the total firn column, we estimate an associated upper bound loss of 540 ± 440 Gt (1.5 ± 1.2 mm s.l.e.). While these volumes are small compared to the average GrIS mass loss ($\sim 0.47 \pm 0.23$ mm s.l.e. yr^{-1} for 1991–2015 in van den Broeke, 2016), the impact of reduced retention capacity has an important time-integrated effect in amplifying meltwater runoff each year. This amplification can be non-linear as when, for instance, a succession of anomalously high melt years and reduced firn permeability resulted in an abrupt increase in western Greenland runoff in 2012 (Machguth et al., 2016).

Harper et al. (2012), using observations from 2007 to 2009, estimated that 150 000 km^2 of firn residing within the lower percolation area (as delineated in an earlier version of MAR) could potentially store between 322 ± 44 Gt of meltwater in the top 10 m of firn and 1289^{+388}_{-252} Gt within the entire firn column. We note that the Harper et al. (2012) estimate is based solely on observations in the LAPA, while 68 % of the percolation area to which they extrapolate is located in the HAPA. By contrast, we find that the warmest 150 000 km^2 of our firn area in 2010–2017 can retain only 150 ± 66 Gt of meltwater in the top 10 m of the firn. We estimate a total storage capacity of 310 ± 270 Gt within the whole firn column in this part of the firn area. Our relatively low estimate of the retention capacity might reflect the recent decrease of FAC in the LAPA but also, for the values derived from FAC_{tot}, our simplifying assumption that this decrease has propagated through the whole firn column (Sect. 2.5). Yet, beyond these integrated values, our approach allows the quantification of the firn retention capacity and the corresponding uncertainty at any location of the firn area. Our product can therefore be used in combination with, for instance, remotely sensed melt extent to derive which areas of the firn actively retain meltwater and evaluate the retention capacity there.

We use the same infiltration ice density as Harper et al. (2012), 843 ± 36 kg m^{-3} as determined from firn core segments saturated by refrozen meltwater. However, Machguth et al. (2016) measured an infiltration ice density of 873 ± 25 kg m^{-3} with a similar technique in western Greenland. Using the latter value increases our estimated firn storage capacity of the top 10 m of firn by 8 % to 13 %, depending on the region, but remains within our uncertainty intervals (Table 3). Additional field measurements are needed to ascertain the spatial and temporal dependence of infiltration ice density on climatic drivers. Our definition of retention capacity assumes that retention occurs through the refreezing of meltwater and neglects potential liquid water retention seen in firn aquifers (Forster et al., 2014). Nevertheless, recent work in southeastern Greenland showed that meltwater resides for less than 30 years in the aquifer before it flows into nearby crevasses and eventually leaves the GrIS (Miller et al., 2018). Meltwater refrozen within the firn can be retained for much longer periods, until it is discharged at a marine-terminating outlet glacier or reaches the surface of the ablation area. By neglecting liquid water retention in firn, our study focuses on long-term meltwater retention.

3.3 Regional climate model evaluation

3.3.1 Comparison with FAC observations

All models reproduce the FAC_{10} observations in the DSA and HAPA with a bias ≤ 0.2 m and RMSD ≤ 0.4 m (Fig. 6, Table 4). RACMO2.3p2, MARv3.9 and HH_LIN tend to underestimate the FAC_{10} in the LAPA, while HH_MOD does not show a pronounced bias there. The RCMs all present a RMSD less than 12 % of the mean FAC_{10} for our entire dataset. The RCMs are also evaluated against the 29 directly observed FAC_{tot} (Fig. 6, Table 4). Both versions of HIRHAM5 overestimate FAC_{tot} in the DSA (bias > 3 m), while RACMO2.3p2 performs better in that area (bias $= 0.1$, RMSD $= 1.8$). HH_LIN and RACMO2.3p2 compare relatively well with the three FAC_{tot} observations available in the LAPA, while HH_MOD presents a larger positive bias. These three FAC_{tot} observations are located in the upper LAPA and therefore do not include regions where RCMs underestimate FAC_{10}. All models overestimate the only FAC_{tot} observation available in the HAPA by more than 3 m. Compared to all FAC_{tot} measurements, RACMO2.3p2 gives a RMSD equivalent to 9 % of the mean observed FAC_{tot} when HIRHAM5's RMSD reaches 20 % with HH_MOD. None of the RCMs therefore simulate both FAC_{10} and FAC_{tot} accurately.

3.3.2 Comparison with the spatially integrated FAC

Agreement between RCM-simulated and observation-derived spatially integrated FAC is model- and region-dependent (Fig. 7). RCMs simulate a spatially integrated FAC_{10} within the uncertainty of our observation-derived estimation in the DSA. Models also show lower spatially integrated FAC_{10} in the LAPA and higher values in the HAPA compared to our estimate (Fig. 7b–d). These regional differences cancel out when spatially integrating FAC_{10} over the entire firn area (Fig. 7a). Our estimation of spatially integrated FAC_{tot} is subject to more assumptions, as uncertainty is introduced in our conversion of FAC_{10} to FAC_{tot} (Sect. 2.5). In the DSA, HH_MOD simulates a spatially integrated FAC_{tot} 20 % higher than our estimation while RACMO2.3p2 simulates spatially integrated FAC_{tot} within our uncertainty range (Fig. 7e). In the LAPA, the decrease in spatially integrated FAC_{tot} is more pronounced in our estimate than in the RCMs. This might indicate that, in the RCMs, the FAC loss is concentrated in the near-surface firn and has not yet propagated through the entire firn column. Our estimate assumes that any change in FAC_{10} immediately propagates to the entire firn pack (see Sect. 2.5). In the HAPA, RCMs show higher spatially integrated FAC_{tot} val-

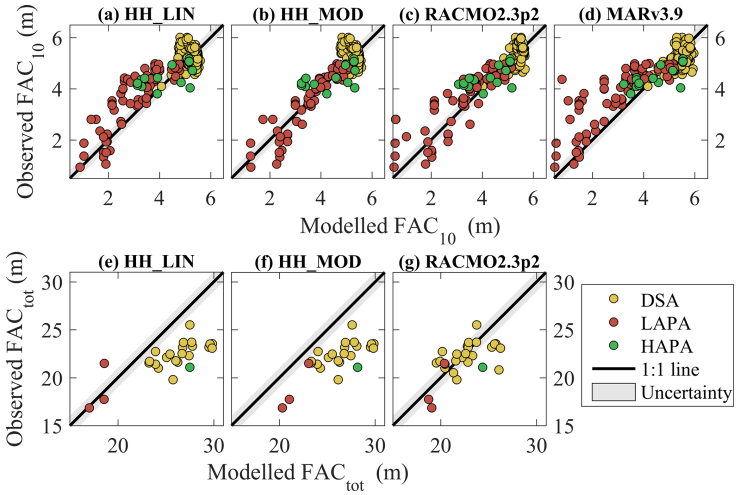

Figure 6. Comparison between the observed FAC_{10} and FAC_{tot} and the simulated FAC in the corresponding cells of three RCMs.

Table 4. Performance of the RCMs for FAC_{10} and FAC_{tot} in terms of bias (average difference between model and observations) and root-mean-squared difference (RMSD).

		DSA		LAPA		HAPA		All firn area	
		Bias (m)	RMSD (m)	Bias (m)	RMSD (m)	Bias (m)	RMSD (m)	Bias (m)	RMSD (m)
FAC_{10}	N_{obs}	259		82		19		360	
	HH_LIN	0.0	0.4	−0.5	0.8	0.1	0.6	−0.2	0.6
	HH_MOD	0.0	0.4	0.1	0.4	0.2	0.6	0.0	0.4
	RACMO2.3p2	0.1	0.3	−0.3	0.6	0.0	0.5	0.0	0.5
	MARv3.9	0.2	0.3	−0.6	1.0	0.2	0.6	0.0	0.6
FAC_{tot}	N_{obs}	25		3		1		29	
	HH_LIN	3.7	4.1	1.0	3.3	6.4	–	3.4	4.1
	HH_MOD	3.8	4.1	3.7	4.1	7.1	–	3.9	4.3
	RACMO2.3p2	0.1	1.8	1.0	1.6	3.3	–	0.4	1.9

ues than our estimate (Fig. 7h), contributing to the higher spatially integrated FAC_{tot} across the entire firn area in the RCMs compared to our estimation (Fig. 7e). This is partly due to the fact that in our estimation, FAC decreases with elevation and is set to zero at the firn line. In the RCMs, modelled FAC remains higher than our estimate in the lower HAPA and in the vicinity of the firn line. No FAC observations are available in the lower HAPA to confirm this. Future measurements will help to quantify FAC in the surroundings of the firn line, allowing for better evaluations of our assumptions and further assess to the RCMs' performance in that area.

The differences between RCM outputs may stem from their respective surface forcings. As an illustration, HH_MOD uses a higher albedo than HH_LIN and thus calculates less surface melt and refreezing and, as a consequence, higher FAC_{10} in the LAPA. Noël et al. (2018) found that the surface mass balance of RACMO2.3p2 in the accumulation area was on average slightly lower than observations, indicating excessive sublimation or runoff relative to snowfall in the model. This surface bias could explain the model's underestimation of FAC_{10} in the LAPA at point scale (Fig. 6, Table 4) and on spatially integrated values (Fig. 7). On the other hand, MARv3.9 has slight positive biases in surface mass balance compared to observations (Fettweis et al., 2017). And although this RCM simulates too much precipitation relative to melt, it also underestimates FAC_{10} in the LAPA. Surface forcing is therefore not the only factor influencing the FAC estimates by the RCMs.

Differences in RCM-simulated FAC_{10} can also be explained by the way firn densification is treated in the snow model of each RCM. For instance, the overestimation of

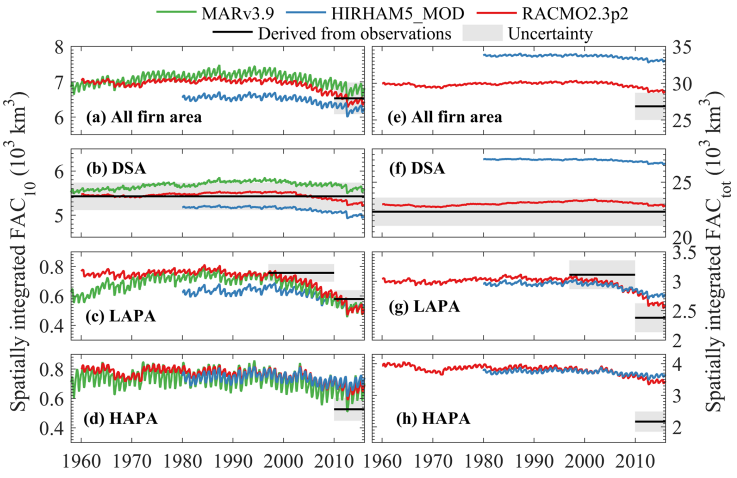

Figure 7. Spatially integrated FAC in the RCMs and from observation-derived estimates.

FAC_{tot} in the DSA by HIRHAM5 potentially arises from the use of a firn compaction law originally developed for seasonal snow (Vionnet et al., 2012). RACMO2.3p2 produces more realistic FAC_{tot} in the DSA, most likely because the densification law it uses has been tuned to match eight deep firn density observations (Kuipers Munneke et al., 2015a). It is nevertheless difficult to disentangle the roles of surface forcing and model formulation in the performance of RCMs.

In agreement with our observation-derived FAC_{10} estimates, the RCMs calculate a decreasing FAC_{10} in the LAPA (Fig. 7c) initiating in the early 2000s and accelerated during the extreme summers of 2010 and 2012. In the DSA, RCMs show a FAC_{10} decrease ranging from $-120\,km^3$ in MARv3.9 to $-282\,km^3$ in RACMO2.3p2 between 1998 and 2017. These decreases contradict our conclusion that FAC has not changed significantly in the DSA over that period (Sect. 3.1). The different FAC_{10} dynamics in our dataset and in RCMs could be due to (i) the RCMs not capturing an increase of snowfall in the DSA, which could in theory counterbalance the densification expected from the recent warming in the firn area (McGrath et al., 2014); (ii) an overestimated response of firn compaction rates to increasing temperatures in the models; or (iii) the spatial heterogeneity and uncertainty of FAC observations leading to spurious conclusions from our dataset. Yet, finding identical firn density profiles decades apart at several sites (e.g. Summit Station, Camp Century) adds confidence to our findings.

4 Conclusions

Using a collection of 360 firn density profiles spanning 65 years we quantified the firn air content (FAC) of the Greenland ice sheet as function of long-term air temperature and net snow accumulation averages ($\overline{T_a}$ and $\overline{\dot{c}}$). For the 2010–2017 period we calculate that the Greenland firn contained $26\,800 \pm 1840\,km^3$ of air, of which $6500 \pm 450\,km^3$ is in its top 10 m. We find that over the 1953–2017 period, FAC remained constant within uncertainty in the dry snow area (DSA, where $\overline{T_a} \leq -19\,°C$). We note that the vast majority of the ice sheet's FAC ($83 \pm 5\,\%$) resides within the DSA and represents a potential meltwater storage volume of $12\,800 \pm 1170\,Gt$. In the low-accumulation percolation area (LAPA, where $\overline{T_a} > -19\,°C$ and $\overline{\dot{c}} \leq 600\,mm\,w.e.\,yr^{-1}$), we calculate that the FAC decreased by $23 \pm 16\,\%$ between 1998–2008 and 2010–2017. This decrease translates into the loss of meltwater retention capacity of $150 \pm 100\,Gt$ ($0.4 \pm 0.3\,mm$ sea-level equivalent) in the top 10 m of the firn and potentially up to $540 \pm 440\,Gt$ ($1.5 \pm 1.2\,mm$ sea-level equivalent) in the entire vertical extent of the firn layer. This decreased FAC and meltwater retention capacity is focused in the lower-accumulation area of central western Greenland. Thus, in contrast to the relative stability of the DSA, the LAPA is the focal area of the firn's response to recent climate change. The firn in the high-accumulation percolation area (LAPA, where $\overline{T_a} > -19\,°C$ and $\overline{\dot{c}} > 600\,mm\,w.e.\,yr^{-1}$) has the capacity to store $370 \pm 70\,Gt$ in its top 10 m and up to $960 \pm 290\,Gt$ in its entire vertical extent. Yet, this area is covered by fewer observations and would highly benefit from future field surveys.

The outputs from three regional climate models (HIRHAM5, RACMO2.3p2 and MARv3.9) indicate that our calculated decrease in FAC may have been initiated in the early 2000s and accelerated after 2010. The RCMs also provide estimates of FAC in regions where no measurements are available. But the mismatch between RCMs and

our firn core dataset illustrates that RCMs should be used with caution when assessing meltwater retention capacity, or when converting ice-sheet volume changes into mass changes in the firn area. Finally, our study highlights the importance of assimilating in situ firn density measurements to document the climate response of ice-sheet firn as a non-trivial component of the sea-level budget. More broadly, this work illustrates how new insight can be obtained from the synthesis of historical data sources and thus emphasises the tremendous value of open-access data within the scientific community.

Code and data availability. The FAC dataset and maps, along with the firn area delineation, are available at https://doi.org/10.18739/A2V40JZ6C (Vandecrux, 2019a) and the majority of the original firn density measurements can be found in the SUMup dataset at https://doi.org/10.18739/A2JH3D23R (Koenig and Montgomery, 2018). The source code is available at https://doi.org/10.5281/zenodo.2578788 (Vandecrux, 2019b).

Supplement. The supplement related to this article is available online at: https://doi.org/10.5194/tc-13-845-2019-supplement.

Author contributions. BV, MM, HM, WTC, DvA, AH, CMS, CC, EMM, EMT, LK, LNM, CM and SBS collected firn density profiles either in the field or from previously published sources. BV, RSF, JEB and TIN designed the study. BV wrote the manuscript, to which all co-authors contributed.

Competing interests. The authors declare that they have no conflict of interest.

Acknowledgements. This work is part of the Retain project funded by Danmarks Frie Forskningsfond (grant no. 4002-00234) and the Programme for Monitoring of the Greenland ice sheet (http://PROMICE.dk, last access: 25 February 2019). The field campaigns were funded by the NASA grant NNX15AC62G in collaboration with the Greenland Analogue Project (GAP). Achim Heilig was supported by DFG grant HE 7501/1-1. We thank Hubertus Fischer from the Department of Climate and Environmental Physics at the University of Bern (Switzerland), for providing low-resolution density data from firn cores collected during the EGIG expeditions of 1990 and 1992. We are grateful to Peter Langen from the Danish Meteorological Institute, Stefan Ligtenberg from the Institute for Marine and Atmospheric Research at Utrecht University (IMAU) and Xavier Fettweis from the Laboratory of Climatology, Department of Geography, University of Liège, for providing the regional climate model output. We thank Sergey Marchenko and an anonymous reviewer for their suggestions, which greatly improved the manuscript.

Edited by: Michiel van den Broeke
Reviewed by: Sergey Marchenko and one anonymous referee

References

Albert, M. and Shultz, E.: Snow and firn properties and air–snow transport processes at Summit, Greenland, Atmos. Environ., 36, 2789–2797, https://doi.org/10.1016/S1352-2310(02)00119-X, 2002.

Alley, R.: Transformations in Polar Firn, PhD Thesis, University of Wisconsin, Madison, WI, USA, 1987.

Bader, H.: Sorge's law of densification of snow on high polar glaciers, J. Glaciol., 2, 15, 319–411, https://doi.org/10.3189/S0022143000025144, 1954.

Baker, I.: Density and permeability measurements with depth for the NEEM 2009S2 firn core, ACADIS Gateway, https://doi.org/10.18739/A2Q88G, 2012.

Benson, C. S.: Stratigraphic Studies in the Snow and Firn of the Greenland Ice Sheet, U.S. Army Snow, Ice and Permafrost Research Establishment (SIPRE–CRREL), Research Report 70, reprinted with revisions by CRREL, 1996, 1962.

Bindoff, N. L., Stott, P. A., AchutaRao, K. M., Allen, M. R., Gillett, N., Gutzler, D., Hansingo, K., Hegerl, G., Hu, Y., Jain, S., Mokhov, I. I., Overland, J., Perlwitz, J., Sebbari, R., and Zhang, X.: Detection and Attribution of Climate Change: from Global to Regional, in: Climate Change 2013: The Physical Science Basis, Contribution of Working Group I to the Fifth Assessment Report of the Intergovernmental Panel on Climate Change, edited by: Stocker, T. F., Qin, D., Plattner, G.-K., Tignor, M., Allen, S. K., Boschung, J., Nauels, A., Xia, Y., Bex, V., and Midgley, P. M., Cambridge University Press, Cambridge, UK, New York, NY, USA, 867–952, https://doi.org/10.1017/CBO9781107415324.022, 2013.

Bolzan, J. F. and Strobel, M.: Oxygen isotope data from snowpit at GISP2 Site 15, PANGAEA, https://doi.org/10.1594/PANGAEA.55511, 1999.

Box, J.: Greenland ice sheet mass balance reconstruction. Part II: Surface mass balance (1840–2010), J. Climate, 26, 6974–6989, https://doi.org/10.1175/JCLI-D-12-00518.1, 2013.

Box, J., Cressie, N., Bromwich, D. H., Jung, J.-H., van den Broeke, M. R., van Angelen, J., Forster, R. R., Miège, C., Mosley-Thompson, E., Vinther, B., and McConnell, J. R.: Greenland ice sheet mass balance reconstruction. Part I: Net snow accumulation (1600–2009), J. Climate, 26, 3919–3934, https://doi.org/10.1175/JCLI-D-12-00373.1, 2013.

Braithwaite, R., Laternser, M., and Pfeffer, W. T.: Variation of near-surface firn density in the lower accumulation area of the Greenland ice sheet, Pâkitsoq, West Greenland, J. Glaciol., 40, 477–485, https://doi.org/10.3189/S002214300001234X, 1994.

Buchardt, S. L., Clausen, H. B., Vinther, B. M., and Dahl-Jensen, D.: Investigating the past and recent δ^{18}O-accumulation relationship seen in Greenland ice cores, Clim. Past, 8, 2053–2059, https://doi.org/10.5194/cp-8-2053-2012, 2012.

Charalampidis, C., van As, D., Box, J. E., van den Broeke, M. R., Colgan, W. T., Doyle, S. H., Hubbard, A. L., MacFerrin, M., Machguth, H., and Smeets, C. J. P. P.: Changing surface–atmosphere energy exchange and refreezing capacity of the lower accumulation area, West Greenland, The Cryosphere, 9, 2163–2181, https://doi.org/10.5194/tc-9-2163-2015, 2015.

Clausen, H., Gundestrup, N. S., Johnsen, S. J., Bindschadler, R., and Zwally, J.: Glaciological investigations in the Crete area, Central Greenland: a search for a new deep-drilling Site, Ann. Glaciol., 10, 10–15, https://doi.org/10.3189/S0260305500004080, 1988.

Colgan, W., Pedersen, A., Binder, D., Machguth, H., Abermann, J., and Jayred, M.: Initial field activities of the Camp Century Climate Monitoring Programme in Greenland, Geol. Surv. Denmark Greenland Bull., 41, 75–78, 2018.

de la Peña, S., Howat, I. M., Nienow, P. W., van den Broeke, M. R., Mosley-Thompson, E., Price, S. F., Mair, D., Noël, B., and Sole, A. J.: Changes in the firn structure of the western Greenland Ice Sheet caused by recent warming, The Cryosphere, 9, 1203–1211, https://doi.org/10.5194/tc-9-1203-2015, 2015.

Fausto, R., Mayer, C., and Ahlstrøm, A.: Satellite-derived surface type and melt area of the Greenland ice sheet using MODIS data from 2000 to 2005, Ann. Glaciol., 46, 35–42, https://doi.org/10.3189/172756407782871422, 2007.

Fausto, R. S, Andersen, S. B., Ahlstrøm, A. P., van As, D., Box, J. E., Binder, D., Citterio, M., Colgan, W., Haubner, K., Hansen, K., Karlsson, N. B., Mankoff, K. D., Pedersen, A. Ø., Solgaard, A., and Vandecrux, B.: The Greenland ice sheet – snowline elevations at the end of the melt seasons from 2000 to 2017, Geol. Surv. Denmark Greenland Bull., 41, 71–74, 2018a.

Fausto, R. S., Box, J. E., Vandecrux, B., van As, D., Steffen, K., MacFerrin, M., Machguth H., Colgan W., Koenig L. S., McGrath D., Charalampidis, C., and Braithwaite, R. J.: A Snow Density Dataset for Improving Surface Boundary Conditions in Greenland Ice Sheet Firn Modeling, Front. Earth Sci., 6, 51 pp., https://doi.org/10.3389/feart.2018.00051, 2018b.

Fettweis, X., Box, J. E., Agosta, C., Amory, C., Kittel, C., Lang, C., van As, D., Machguth, H., and Gallée, H.: Reconstructions of the 1900–2015 Greenland ice sheet surface mass balance using the regional climate MAR model, The Cryosphere, 11, 1015–1033, https://doi.org/10.5194/tc-11-1015-2017, 2017.

Fischer, H., Wagenbach, D., Laternser, M., and Haeberli, W.: Glacio-meteorological and isotopic studies along the EGIG line, central Greenland, J. Glaciol., 41, 139, 515–527, https://doi.org/10.3189/S0022143000034857, 1995.

Forster, R. R., Box, J. E., van den Broeke, M. R., Miège, C., Burgess, E. W., Angelen, J. H., Lenaerts, J. T. M., Koenig, L. S., Paden, J., Lewis, C., Gogineni, S. P., Leuschen, C., and McConnell, J. R.: Extensive liquid meltwater storage in firn within the Greenland ice sheet, Nat. Geosci., 7, 95–98, 2014.

Graeter, K. A., Osterberg, E., Ferris, D. G., Hawley, R. L., Marshall, H. P., Lewis, G., Meehan, T., McCarthy, F., Overly, T., and Birkel, S. D.: Ice Core Records of West Greenland Melt and Climate Forcing, Geophys. Res. Lett., 45, 3164–3182, https://doi.org/10.1002/2017GL076641, 2018.

Harper, J., Humphrey, N., Pfeffer, W. T., Brown, J., and Fettweis, X.: Greenland ice-sheet contribution to sea-level rise buffered by meltwater storage in firn, Nature, 491, 240–243, https://doi.org/10.1038/nature11566, 2012.

Hawley, R. L., Courville, Z. R., Kehrl, L., Lutz, E., Osterberg, E., Overly, T. B., and Wong, G.: Recent accumulation variability in northwest Greenland from ground-penetrating radar and shallow cores along the Greenland Inland Traverse, J. Glaciol., 60, 375–382, https://doi.org/10.3189/2014JoG13J141, 2014.

Heilig, A., Eisen, O., MacFerrin, M., Tedesco, M., and Fettweis, X.: Seasonal monitoring of melt and accumulation within the deep percolation zone of the Greenland Ice Sheet and comparison with simulations of regional climate modeling, The Cryosphere, 12, 1851–1866, https://doi.org/10.5194/tc-12-1851-2018, 2018.

Humphrey, N. F., Harper, J. T., and Pfeffer, W. T.: Thermal tracking of meltwater retention in Greenland's accumulation area, J. Geophys. Res., 117, F01010, https://doi.org/10.1029/2011JF002083, 2012.

Jezek, K. C.: Surface Elevation and Velocity Changes on the South Central Greenland Ice Sheet: 1980–2011 – Data Summary, BPRC Technical Report No. 2012-01, Byrd Polar Research Center, The Ohio State University, Columbus, Ohio, 2012.

Kameda, T., Narita, H., Shoji, H., Nishio, F., Fuji, Y., and Watanabe, O.: Melt features in ice cores from Site J, southern Greenland: some implication for summer climate since AD 1550, Ann. Glaciol., 21, 51–58, https://doi.org/10.3189/S0260305500015597, 1995.

Koenig, L. and Montgomery, L.: Surface Mass Balance and Snow Depth on Sea Ice Working Group (SUMup) snow density subdataset, Greenland and Antartica, 1950–2018, Arctic Data Center, https://doi.org/10.18739/A2JH3D23R, 2018.

Koenig, L. S., Miège, C., Forster, R. R., and Brucker, L.: Initial in situ measurements of perennial meltwater storage in the Greenland firn aquifer, Geophys. Res. Lett., 41, 81–85, https://doi.org/10.1002/2013GL058083, 2014.

Kovacs, A., Weeks, W. F., and Michitti, F.: Variation of Some Mechanical Properties of Polar Snow, Camp Century, Greenland, CRREL Res. Rpt. 276, 1969.

Kuipers Munneke, P., Ligtenberg, S. R. M., Noël, B. P. Y., Howat, I. M., Box, J. E., Mosley-Thompson, E., McConnell, J. R., Steffen, K., Harper, J. T., Das, S. B., and van den Broeke, M. R.: Elevation change of the Greenland Ice Sheet due to surface mass balance and firn processes, 1960–2014, The Cryosphere, 9, 2009–2025, https://doi.org/10.5194/tc-9-2009-2015, 2015a.

Kuipers Munneke, P., Ligtenberg, S. R., Suder, E. A., and van den Broeke, M. R.: A model study of the response of dry and wet firn to climate change, Ann. Glaciol., 56, 1–8, https://doi.org/10.3189/2015AoG70A994, 2015b.

Langen, P., Fausto, R. S., Vandecrux, B., Mottram, R., and Box, J.: Liquid Water Flow and Retention on the Greenland Ice Sheet in the Regional Climate Model HIRHAM5: Local and Large-Scale Impacts, Front. Earth Sci., 4, 110 pp., https://doi.org/10.3389/feart.2016.00110, 2017.

Langway, C. C.: Stratigraphic analysis of a deep ice core from Greenland, CRREL Res. Rpt. 77, 1967.

Ligtenberg, S. R. M., Kuipers Munneke, P., Noël, B. P. Y., and van den Broeke, M. R.: Brief communication: Improved simulation of the present-day Greenland firn layer (1960–2016), The Cryosphere, 12, 1643–1649, https://doi.org/10.5194/tc-12-1643-2018, 2018.

Lomonaco, R., Albert, M., and Baker, I.: Microstructural evolution of fine-grained layers through the firn column at Summit, Greenland, J. Glaciol., 57, 204 pp., https://doi.org/10.3189/002214311797409730, 2011.

Lucas-Picher, P., Wulff-Nielsen, M., Christensen, J. H., Aðalgeirsdóttir, G., Mottram, R., and Simonsen, S. B.: Very high resolution in regional climate model simulations for Greenland: Identifying added value, J. Geophys. Res., 117, D02108, https://doi.org/10.1029/2011JD016267, 2012.

Machguth, H., MacFerrin, M., van As, D., Box, J., Charalampidis, C., Colgan, W., Fausto, R. S., Meijer, H. A., Mosley-Thompson, E., and van de Wal, R. S.: Greenland meltwater storage in firn

limited by near-surface ice formation, Nat. Clim. Change, 6, 390–395, https://doi.org/10.1038/NCLIMATE2899, 2016.

Mayewski, P. and Whitlow, S.: Snow Pit and Ice Core Data from Southern Greenland, 1984, NSF Arctic Data Center https://doi.org/10.5065/D6S180MH, 2016a.

Mayewski, P. and Whitlow S.: Snow Pit Data from Greenland Summit, 1989 to 1993, NSF Arctic Data Center, https://doi.org/10.5065/D6NP22KX, 2016b.

McGrath, D., Colgan, W., Bayou, N., Muto, A., and Steffen, K.: Recent warming at Summit, Greenland: Global context and implications, Geophys. Res. Lett., 40, 2091–2096, https://doi.org/10.1002/grl.50456, 2013.

Miège, C., Forster, R. R., Box, J. E., Burgess, E., McConnell, J., Pasteris, D., and Spikes, V. B.: Southeast Greenland high accumulation rates derived from firn cores and ground-penetrating radar, Ann. Glaciol., 54, 322–332, https://doi.org/10.3189/2013AoG63A358, 2013.

Miège, C., Forster, R. R., Brucker, L., Koenig, L. S., Solomon, D. K., Paden, J. D., Box, J. E., Burgess, E. W., Miller, J. Z., McNerney, L., Brautigam, N., Fausto, R. S., and Gogineni, S.: Spatial extent and temporal variability of Greenland firn aquifers detected by ground and airborne radars, J. Geophys. Res.-Earth, 121, 2381–2398, https://doi.org/10.1002/2016JF003869, 2016.

Morris, E. M. and Wingham, D. J.: Densification of polar snow: Measurements, modeling and implication for altimetry, J. Geophys. Res.-Earth, 119, 349–365, https://doi.org/10.1002/2013JF002898, 2014.

Mosley-Thompson, E., McConnell, J., Bales, R., Li, Z., Lin, P.-N., Steffen, K., Thompson, L. G., Edwards, R., and Bathke, D.: Local to regional-scale variability of annual net accumulation on the Greenland ice sheet from PARCA cores, J. Geophys. Res., 106, 33839–33851, https://doi.org/10.1029/2001JD900067, 2001.

Mote, T. L.: Greenland surface melt trends 1973–2007: Evidence of a large increase in 2007, Geophys. Res. Lett., 34, L22507, https://doi.org/10.1029/2007GL031976, 2007.

Nerem, R. S., Beckley, B. D., Fasullo, J. T., Hamlington, B. D., Masters, D., and Mitchum, G. T.: Climate-change-driven accelerated sea-level rise detected in the altimeter era, P. Natl. Acad. Sci. USA, 7, 201717312, https://doi.org/10.1073/pnas.1717312115, 2018.

Nghiem, S. V., Hall, D. K., Mote, T. L., Tedesco, M., Albert, M. R., Keegan, K., Shuman, C. A., DiGirolamo, N. E., and Neumann, G.: The extreme melt across the Greenland ice sheet in 2012, Geophys. Res. Lett., 39, L20502, https://doi.org/10.1029/2012GL053611, 2012.

Noël, B., van de Berg, W. J., van Wessem, J. M., van Meijgaard, E., van As, D., Lenaerts, J. T. M., Lhermitte, S., Kuipers Munneke, P., Smeets, C. J. P. P., van Ulft, L. H., van de Wal, R. S. W., and van den Broeke, M. R.: Modelling the climate and surface mass balance of polar ice sheets using RACMO2 – Part 1: Greenland (1958–2016), The Cryosphere, 12, 811–831, https://doi.org/10.5194/tc-12-811-2018, 2018.

Porter, S. and Mosley-Thompson, E.: Exploring seasonal accumulation bias in a west central Greenland ice core with observed and reanalyzed data, J. Glaciol., 60, 1065–1074, https://doi.org/10.3189/2014JoG13J233, 2014.

Reed, S.: Performance Study of the Dewline Ice Cap Stations, 1963, CRREL Special Report 72, 1966.

Renaud, A.: Etude physiques et chimiques sur la glace de l'inlandsis du Groenland, Medd. Groenland, 2, 100–107, 1959.

Shumskii, P. A.: Principles of structural glaciology: the petrography of fresh-water ice as a method of glaciological investigation, Dover Publications Inc., 1964.

Simonsen, S. B., Stenseng, L., Aðalgeirsdóttir, G., Fausto, R. S., Hvidberg, C. S., and Lucas-Picher, P.: Assessing a multilayered dynamic firn-compaction model for Greenland with ASIRAS radar measurements, J. Glaciol., 59, 545–558, https://doi.org/10.3189/2013JoG12J158, 2013.

Spencer, M. K., Alley, R. B., and Creyts, T. T.: Preliminary firn-densification model with 38-site dataset, J. Glaciol., 47, 671–676, https://doi.org/10.3189/172756501781831765, 2001.

Steen-Larsen, H. C., Masson-Delmotte, V., Sjolte, J., Johnsen, S. J., Vinther, B. M., Bréon, F. M., Clausen, H. B., Dahl-Jensen, D., Falourd, S., Fettweis, X., Gallée, H., Jouzel, J., Kageyama, M., Lerche, H., Minster, B., Picard, G., Punge, H. J., Risi, C., Salas, D., Schwander, J., Steffen, K., Sveinbjörnsdóttir, A. E., Svensson, A., and White, J.: Understanding the climatic signal in the water stable isotope records from the NEEM cores, J. Geophys. Res., 116, D06108, https://doi.org/10.1029/2010JD014311, 2011.

Sørensen, L. S., Simonsen, S. B., Nielsen, K., Lucas-Picher, P., Spada, G., Adalgeirsdottir, G., Forsberg, R., and Hvidberg, C. S.: Mass balance of the Greenland ice sheet (2003–2008) from ICESat data – the impact of interpolation, sampling and firn density, The Cryosphere, 5, 173–186, https://doi.org/10.5194/tc-5-173-2011, 2011.

Vallelonga, P., Christianson, K., Alley, R. B., Anandakrishnan, S., Christian, J. E. M., Dahl-Jensen, D., Gkinis, V., Holme, C., Jacobel, R. W., Karlsson, N. B., Keisling, B. A., Kipfstuhl, S., Kjær, H. A., Kristensen, M. E. L., Muto, A., Peters, L. E., Popp, T., Riverman, K. L., Svensson, A. M., Tibuleac, C., Vinther, B. M., Weng, Y., and Winstrup, M.: Initial results from geophysical surveys and shallow coring of the Northeast Greenland Ice Stream (NEGIS), The Cryosphere, 8, 1275–1287, https://doi.org/10.5194/tc-8-1275-2014, 2014.

van Angelen, J., Lenaerts, J. T., van den Broeke, M. R., Fettweis, X., and van Meijgaard, E.: Rapid loss of firn pore space accelerates 21st century Greenland mass loss, Geophys. Res. Lett., 40, 2109–2113, https://doi.org/10.1002/grl.50490, 2013.

Vandecrux, B., Fausto, R. S., Langen, P. L., Van As, D., MacFerrin, M., Colgan, W. T., Ingeman-Nielsen, T., Steffen, K., Jensen, N. S., Møller, M. T., and Box, J. E.: Drivers of Firn Density on the Greenland Ice Sheet Revealed by Weather Station Observations and Modeling, J. Geophys. Res.-Earth, 123, 2563–2576, https://doi.org/10.1029/2017JF004597, 2018.

Vandecrux, B.: Firn air content and firn area delineation on the Greenland ice sheet, Arctic Data Center, https://doi.org/10.18739/A2V40JZ6C, 2019a.

Vandecrux, B.: Greenland ice sheet firn air content analysis scripts (Version v1.0.1), Zenodo, https://doi.org/10.5281/zenodo.2578788, 2019b.

van den Broeke, M. R., Enderlin, E. M., Howat, I. M., Kuipers Munneke, P., Noël, B. P. Y., van de Berg, W. J., van Meijgaard, E., and Wouters, B.: On the recent contribution of the Greenland ice sheet to sea level change, The Cryosphere, 10, 1933–1946, https://doi.org/10.5194/tc-10-1933-2016, 2016.

van der Veen, C. J., Mosley-Thompson, E., Jezek, K. C., Whillans, I. M., and Bolzan, J. F.: Accumulation rates in South and Central Greenland, Polar Geography, 25, 79–162, https://doi.org/10.1080/10889370109377709, 2001.

Wilhelms, F.: Measuring the Conductivity and Density of Ice Cores, Ber. Polarforsch., 191 pp., 1996.

APPENDIX G

Paper VII

Heat budget of Greenland firn: observed and simulated changes from 1998-2015

B. Vandecrux[1,2], R. S. Fausto[2], D. van As[2], W. Colgan[2], P. L. Langen[3], K. Sampson[4], K. Steffen[5], K. Haubner[2,6] , T. Ingeman-Nielsen[1], M. Niwano[7], J.E. Box[2]

[1] Department of Civil Engineering, Technical University of Denmark, Lyngby, Denmark.
[2] Geological Survey of Denmark and Greenland, Copenhagen, Denmark.
[3] Climate and Arctic Research, Danish Meteorological Institute, Copenhagen, Denmark
[4] National Center for Atmospheric Research, Boulder, USA
[5] Swiss Federal Institute for Forest, Snow, and Landscape Research (WSL), Birmensdorf, Switzerland
[6] Université Libre de Bruxelles, Brussels, Belgium
[7] Climate Research Department, Meteorological Research Institute, Japan Meteorological Agency, Tsukuba, Japan

Correspondence to: B. Vandecrux (bava@byg.dtu .dk)

Abstract.

The Greenland land ice's accelerating mass loss contributes to 15-30% of the current sea level rise and mostly originates from increased surface melting and runoff. About 80% of the ice sheet is covered by perennial snow, a.k.a. firn, that retains part of the seasonal surface melt. Firn meltwater retention depends on its physical and thermal state which can be estimated from a firn model driven by weather station observations. We find that increasing air temperatures have driven increasing melt and firn heating at nine GC-Net stations between 1998 and 2015. Accounting for deep preferential meltwater percolation can: i) decrease the calculated melt by up to 8% by decreasing near-surface firn saturation; ii) hinder the transmission of heat from the firn to the atmosphere by routing the meltwater at depth where the released latent heat need more time to be conducted back to the surface; iii) improve the comparison of simulated firn temperatures to observations. We find that, in spite of increasing firn heat influx, the firn refreezing capacity is stable at all sites. At the two warmest sites, firn densification led to the loss of 13-15% of the firn retention capacity. The denser near-surface firn however requires more energy per unit volume to be brought to melting resulting in a stable refreezing capacity at these sites. We find either constant or slightly increasing ($\leq$ 5 %) refreezing capacity and retention capacity at colder sites.

1. Introduction

The Greenland ice sheet, the greatest freshwater reservoir in the Northern hemisphere, is losing mass at an accelerating rate as a response to climate warming in the arctic (Vaughan et al., 2013). This mass loss is responsible for a 0.46-0.77 mm rise of global mean sea level every year in the last decades, 15-30% of the observed

contemporary sea level rise (Box et al. 2018; Cazenave et al., 2018; Nerem et al., 2018). About half of the current ice sheet mass loss stems from surface melt and subsequent meltwater runoff which both increased over recent decades (van den Broeke et al., 2016). More intense melting in recent decades was accompanied by an increasing extent of surface melting (Mote, 2007; Nghiem et al., 2012). The firn area, increasingly affected by this expansion of melt, reacts in various ways to these new surface conditions: increasing ice content (de la Peña et al., 2015; Machguth et al., 2016; Graeter et al., 2018), increasing density (Vandecrux et al., 2018), decreasing pore space (van Angelen et al., 2013; Vandecrux et al., submitted) and firn warming (McGrath et al., 2013; Polashenski et al., 2014). All these consequences indicate a shrinking capacity of the firn to retain surface meltwater and buffer sea level rise (Pfeffer et al., 1991; Harper et al., 2012).

Snow and firn models are widely used in combination with Regional Climate Models (RCM) to simulate the snow and firn conditions across the Greenland ice sheet (e.g., van Angelen et al., 2013; Steger et al., 2016; Langen et al., 2017; Ligtenberg et al., 2018; Niwano et al., 2018). However, the validation of the subsurface outputs of these RCM-driven snow models remains difficult due to limited available subsurface data. No comprehensive validation dataset of firn temperature has been made available to this date. Additionally, given the imperfections of the RCM's simulated climatic conditions, it is necessary to test RCM's snow and firn models with in-situ observations to ensure the overall performance these snow models. At present, our understanding of firn processes is best evaluated by comparing firn models forced by weather station observation and in-situ firn observation (Humphrey et al., 2012; Charalampidis et al., 2015; Charalampidis et al., 2016; Miller et al., 2017; Vandecrux et al., 2018).

Although long known to operate in snow and firn (Benson, 1962; Colbeck, 1979; Marsh and Woo, 1984), preferential meltwater percolation was recently identified as potential improvement in current snow models (Machguth et al., 2018). In alpine snow packs, accounting for preferential flow enabled snow models to improve the timing of meltwater arrival at the base of the snowpack (Colbeck, 1979) or to reproduce thin ice layers observed in natural snow packs (Wever et al., 2016). Yet, these modelling approaches have not been tested in Greenland ice sheet either because of their computational cost or because of the lack of in-situ observations. As a result, the importance of heterogeneous percolation for the overall heat and mass balance of the firn that covers the Greenland ice sheet is still unclear. Marchenko et al. (2017) recently developed a deep percolation parametrization and found that it improved firn temperature simulation at a firn site in Svalbard. Still this parametrization has not been tested on the Greenland ice sheet.

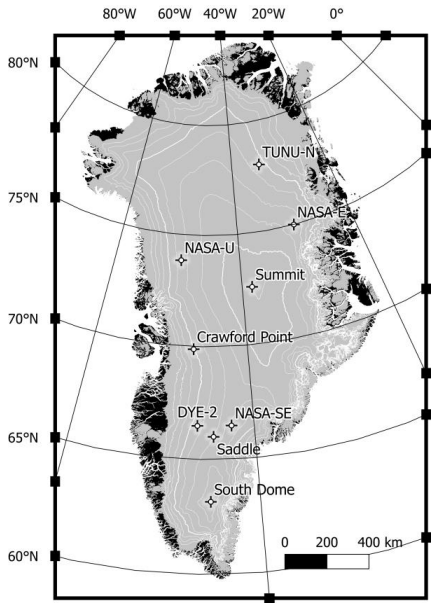

Figure 1. GC-Net automatic weather station locations providing data to this study

Here, we determine the heat budget of the firn at nine Greenland ice sheet accumulation area automatic weather station locations for the period 1998-2015 (Table 1, Figure 1) using observation-driven surface energy balance and firn modelling. We analyse the recent evolution of the surface energy budget and investigate the importance of accounting for deep percolation in the firn heat budget. We finally describe the recent changes of the firn refreezing capacity and the consequences for the overall meltwater retention capacity.

2. Methods

2.1. Weather data processing

GC-Net stations measure air temperature, relative humidity, wind speed, atmospheric pressure, down and upward shortwave irradiance. Since each GC-Net station has two measurement levels and our energy balance calculation requires data at a single level above the surface, we preferentially use the upper measurement because it is less often buried in snow. We follow the Vandecrux et al. (2018) outlier rejection and gap filling procedures: Gaps under 6 hours are interpolated using polynomial functions and larger gaps in air temperature, pressure, wind speed and relative humidity are filled using data from HIRHAM5 RCM (Lucas-Picher et al., 2012) adjusted to the available observations of each climate variable. Gaps in upward shortwave radiation are filled using the gap-filled downward

shortwave radiation and MODIS daily albedo grids after Box et al. (2017). Upward longwave irradiance is taken from HIRHAM5 after compensation of a negative bias found by Langen et al. (2017) as in Vandecrux et al. (2018).

Table 1. Station location and operational period.

Station	Latitude	Longitude	Elevation (m. a.s.l.)	Period
Crawford Point	69.88	-46.99	2022	1998 – 2010
DYE-2	66.48	-46.28	2165	1998 – 2015
NASA-SE	66.48	-42.50	2425	1996 – 2015
Summit	72.58	-38.50	3254	1996 – 2015
NASA-E	75.00	-30.00	2631	1997 – 2014
NASA-U	73.84	-49.50	2369	1996 – 2014
TUNU-N	78.02	-33.99	2113	1997 – 2014
South Dome	63.15	-44.82	2922	1997 – 2015
Saddle	66.00	-44.50	2559	1997 – 2015

Measured snow surface height is used to derive hourly snowfall rate after Vandecrux et al. (2018) in which any sustained increment in surface height is taken as a new snow layer of 315 kg m^{-3} density (Fausto et al., 2018). We then multiply the station-derived accumulation rate by a correction factor so that the annual winter accumulation matches with 32 snow pit derived annual accumulation observations to which we assign 10% as a rough estimate for sublimation loss.

At Crawford Point, suspiciously high albedo were measured by the station over the 2005-2010 period (Vandecrux et al., 2018). We here decided to discard the upward radiation measurements over that period and replace them by radiation calculated from the measured incoming radiation and the MODIS albedo associated to that station. Hence results for Crawford Point are different from what was reported in Vandecrux et al. (2018).

2.2. SEB calculation

The energy available for melt (M) is the total of the upward and downward shortwave irradiance(SR↑, SR↓), upward and downward longwave radiation flux (LR↑, LR↓), the turbulent sensible heat flux (SHF), the turbulent latent heat flux (LHF) and the conductive energy flux to or from the subsurface (G):

$$M = SR\downarrow - SR\uparrow + LR\downarrow - LR\uparrow + SHF + LHF + G \quad [1]$$

LR↑ is calculated from the surface temperature (T_s) using the Stefan-Boltzmann law with a constant surface emissivity of 0.98. G is calculated from T_s and from subsurface characteristics calculated by the firn model (next Section). Calculation of the turbulent heat fluxes also require T_s and are calculated using the bulk approach and

corrected for the stability of near-surface atmospheric stratification after van As et al. (2005) and Vandecrux et al., (2018). At each time step, Equation 1 is solved iteratively either for the subfreezing that balances Equation 1 in absence of melt; or by setting the surface to the melting point and allocating excess energy to melt.

2.3. Firn module

The conduction of heat from the surface down to depth (G) depends on the thermal, physical and hydrological characteristics of the firn. We use the firn model from Langen et al. (2017) and Vandecrux et al. (2018) briefly summarized in the following. The model has 200 vertical layers of varying thickness and a layer merging-splitting strategy that gives the highest resolution near the surface. The model starts with a 70 m thick firn column (40 m water equivalent) which is initialized with observed firn density profiles (Table 2) and with observed firn temperature (see section 2.4), when available. When these observed density and temperature profiles do not cover the entire model domain we extrapolate them using polynomial functions of depth until firn density reaches ice density from 60 m and below, and until firn temperature reaches the prescribed deep firn temperature (Table 2) at the bottom of the model.

For each layer, the model calculates the firn temperature accounting for the conduction, heat storage as well as latent heat release from meltwater refreezing. The heat capacity and thermal conductivity are calculated from firn temperature and density after Yen (1981). The firn density is updated at every time step accounting for firn compaction derived from overburden pressure (Vionnet et al., 2012) and for the ice originated from meltwater refreezing. Meltwater generated at the surface is transferred to underlying layers according to Darcy's law after Langen et al. (2017). If transferred to a subfreezing model layer, water is refrozen until the latent heat release brought the layer's temperature to 0^{o}C and the layer's ice content is updated. The vertical firn water flux depends on the firn irreducible water content (Coléou and Lesaffre, 1998), the firn's saturated (Calonne et al., 2012) and unsaturated (Hirashima et al., 2010) hydraulic conductivity which are modulated by a coefficient that accounts for the effect of ice content on the firn hydraulic conductivity (Colbeck, 1975). The evolution of grain size, needed to calculate these hydraulic conductivities, is calculated from firn temperature and water content according to Brun (1989). We do not account for firn ventilation (Albert, 1993).

In addition to this "standard" model, we use a similar set up in which deep percolation parametrization from Marchenko et al. (2017) is implemented. This parametrization allocates any newly produced meltwater directly at depth in an homogeneous fashion and until a maximum percolation depth of 5 m. The normal percolation routine is then used to compute further percolation of existing subsurface water.

Table 2. Boundary conditions of the firn model.

Station	Deep firn temperature (^{o}C)	Core used for initial firn density	Drilling year	Core depth (m)

5

Crawford Point	- 17.4	Core 6945	1998	18.6
DYE-2	-15.5	Core DYE-2 A&B	1998	120.0
NASA-SE	-19.2	Core 6642 (B)	1998	20.5
Summit	-31	GRIP core and shallow core from Mayewski (1990)	1990	>100
NASA-E	-30	NASA East Core A	1997	20.2
NASA-U	-23.5	NASA-U-1 1995	1995	>100
TUNU-N	-28.5	Tunu-1	1996	69
South Dome	-21	S. Dome Core A	1997	24.6
Saddle	-20	N. DYE 3 (Saddle) - A	1997	20.6

2.4. Firn temperature processing

GC-Net stations were equipped between 1995 and 2010 with type-T thermocouple strings having 1 m spacings from initially 0.1 to 9.1 m depth. Records are visually inspected to discard erroneous measurement and a 0.1σ variance filter was applied to reduce the impact of noise.

After installation, the depth of each sensor changes as a result of several surficial and internal processes: Snow accumulation during snowfall increases the sensor depths, while melt and sublimation removes surface snow thereby decreasing thermometer depths. Additionally, meltwater percolation and refreezing redistributes mass in the firn and also updates the sensors' positions relative to the surface. Finally, the firn in which the sensors are installed undergoes densification as a result of metamorphism and overburden pressure which changes the distance between the surface and the sensors and between the sensors. These processes are accounted for in our model, so we therefore track the sensors' installation depths in our simulation to estimate each sensor's depth at any point in time.

2.5. Firn retention capacity

Melt water can be retained within the snow and firn through refreezing when put in contact with subfreezing snow or by capillary retention in isothermal snow (Pfeffer et al., 1991). The refreezing capacity of a portion of firn can be defined as the amount of meltwater that can be refrozen before the subsequent latent heat release brings the firn to melting point. At each time step, we calculate the refreezing capacity of the top 20 m of firn (RC_{20}) in mm of water as:

$$RC_{20} = \frac{20\, c_i\, \rho_{20}}{L_f}\,(T_{20} - T_0) \qquad [2]$$

Where $c_i = 2.108\text{kJ kg}^{-1}\text{ K}^{-1}$ is the specific heat of ice, $L_f = 334\text{kJ kg}^{-1}$ the latent heat of fusion, ρ is the firn density, T_{20} the top 20 m average firn temperature and T_0 the ice melting point temperature.

Since the capillary water retained during the day can potentially be refrozen during night time, the repeated retention and refreezing cycles are limited by the pore volume available in the firn. The firn retention capacity can then be defined as the amount of water that needs to be refrozen within a volume of firn to bring the firn density to 843 kg m^{-3} at which meltwater admission is no longer possible (e.g. Harper et al., 2012). We calculate the firn retention capacity of the top 20 m of firn (FC_{20}) in mm of water as:

$$FC_{20} = 20 \times (843 - \rho_{20}) \quad [2]$$

where ρ_{20} is the average density of the top 20 m of firn.

3. Results and Discussion

3.1. Climatology

June through August (JJA) average 2 m air temperatures have increased at all sites at rates between +0.2 and +1.3 °C per decade (Table 3). The JJA air temperature increase is compensated by decreasing autumn and spring temperatures, resulting in smaller or even negative trends in annual air temperature (Table 3). Only some of the JJA air temperature trends reach statistical significance (P<0.1), mostly because the annual air temperature records hardly reach a sufficient span (13 to 19 years) compared to the year-to-year variability of JJA temperature. But the fact that the eight sites out of nine are showing similar trends increases our confidence in the existence of a positive trend in summer temperatures. McGrath et al. (2013) calculated trends similar to ours at Summit which they show to be statistically significant by putting them into a longer context.

Table 3. Trends in annual and June-July-August averages of 2 m air temperature (T) 2 m relative humidity (RH) and 10 m wind speeds (WS). Trends are calculate on each station's respective period (Table 1).

Variable	Crawford Point	DYE-2	NASA-E	NASA-SE	NASA-U	Saddle	South Dome	Summit	TUNU-N
Trends in annual averages									
T (°C dec.$^{-1}$)	0.01	0.35	-0.23	0.31	-0.74	-0.33	-0.07	0.28	0.41
RH (p.p. dec.$^{-1}$)	0.13	**-1.60**	0.18	0.45	-0.81	-0.12	-0.32	0.67	**0.80**
WS (m s^{-1} dec.$^{-1}$)	0.31	**0.84**	**0.47**	-0.01	-0.09	**-1.01**	0.27	-0.02	0.14
Trends in June-July-August averages									
T (°C dec.$^{-1}$)	0.91	0.60	0.42	0.81	**0.99**	0.22	0.78	**1.26**	**1.26**
RH (p.p. dec.$^{-1}$)	0.95	**-2.57**	0.30	**1.41**	0.16	-0.02	-0.93	**1.06**	**1.79**
WS (m s^{-1} dec.$^{-1}$)	**0.56**	**0.52**	0.39	-0.06	0.36	**-1.17**	-0.01	-0.03	0.23

3.2. Surface energy budget

Shortwave absorption is the main surface energy source. We find significant (P<0.1) negative temporal trends in downward shortwave radiation at Crawford Point, South Dome and TUNU-N (Table 4), potentially indicating more cloudy conditions at these sites as it was found by Orsi et al. (2018) at a site in North Greenland. In contrary, negative trends in downward longwave radiation at all sites except TUNU-N, adjusted from HIRHAM, suggest increasing clear sky conditions in the RCM which would also be consistent with regional observations of decreasing cloud cover (Hofer et al., 2017).

While the annual energy input from upward longwave radiation has decreased at all sites except DYE-2, TUNU-N and Summit, its JJA energy input increased at all sites except NASA-SE (Table 4). This increase indicates an increasing trend in summer surface temperatures which coincides with the increasing computed melt at all stations (Table 4). We find that summer SHF increases at seven out of nine sites. Further, the SHF at Crawford Point, DYE-2, NASA-SE switch from being a surface cooling mechanism before roughly 2004 to being a surface warming mechanism. Nevertheless, the small contribution of SHF to the surface energy budget and the uncertainty stemming from our bulk method to estimate them (Box and Steffen, 2001) make it hard to assess whether increasing SHF has a significant impact on the firn conditions.

During the record warm 2012 season with surface melting over almost the entire ice sheet (Nghiem et al. 2012), we find that the melting at all sites (Figure 2) coincided with record-low surface albedo at all sites except NASA-E and Summit (Supplementary Figure S10) due to the so-called melt-albedo feedback (Charalampidis et al. 2015).

Table 4. Trends in surface energy budget components. Positive trends are highlighted in orange while negative trends are highlighted in blue. Trends with associated P value lower than 0.1 are shown in bold.

Variable	Crawford Point	DYE-2	NASA-SE	NASA-U	Saddle	South Dome	NASA-E	Summit	TUNU-N
Trends in annual contribution (MJ dec.$^{-1}$)									
SHF	**205.51**	**148.04**	-18.57	-66.57	2.76	29.46	-21.07	21.91	29.21
LHF	**0.02**	0.00	**0.01**	**-0.01**	**0.01**	0.00	**-0.01**	**0.00**	0.00
SR↓	**-315.64**	-53.95	14.37	78.82	-38.71	**-108.23**	40.93	26.84	**-84.00**
SR↑	**-199.49**	-6.85	47.06	-26.75	-52.24	**-135.21**	-24.69	11.77	-47.63
LR↓	**-184.58**	-77.06	-89.34	-23.50	-106.83	-85.47	-27.28	-14.65	29.14
LR↑	-27.59	2.15	-104.32	-52.25	-64.15	-28.25	-2.81	8.74	36.86
GF	10.53	0.39	18.50	-4.08	11.48	-7.00	-0.31	**-24.29**	8.50
Melt energy	18.04	8.88	19.12	**16.09**	10.77	10.99	0.42	**1.68**	1.34
Trends in JJA contribution (MJ dec.$^{-1}$)									
SHF	**38.23**	**58.75**	13.50	-12.74	5.20	11.49	**-27.76**	9.33	10.55
LHF	**0.00**	0.00	**0.01**	**-0.01**	**0.00**	0.00	**-0.01**	0.00	**0.00**

SR↓	**-120.72**	-28.97	32.00	17.85	13.18	-18.45	10.50	22.64	**-58.85**
SR↑	**-127.09**	-43.51	20.67	-55.73	-27.11	**-64.91**	**-50.43**	2.35	-34.26
LR↓	-29.35	**-46.01**	**-64.13**	30.55	**-38.44**	-19.73	18.81	18.06	**52.34**
LR↑	27.52	4.64	-22.09	**38.51**	1.19	19.78	25.63	**42.68**	**35.28**
GF	9.84	-4.79	8.08	**-7.49**	-5.46	**-7.47**	-4.17	-5.89	-7.21
Melt energy	16.67	19.95	16.86	**17.85**	14.66	**13.52**	0.64	**1.62**	1.59

3.3. Snowfall and melt

We find increasing melt at all stations, although these melt trends seldom reach statistical significance (P>0.1) due to the short (13 to 19 years) length of the records with relative to year-to-year melt variability. On the other hand, we find decreasing snowfall at Crawford Point, DYE-2, NASA-SE, NASA-U and South Dome over their respective study period (Table 1). These negative trends have a magnitude ranging between -30 and -120 mm dec^{-1}. They are also rarely statistically significant (P>0.1) because of the high year-to-year snowfall variability compared to the span of our records. Increasing snow accumulation is seen at NASA-E and Summit.

Snow accumulation at the surface is derived from station surface height recordings, tuned to match the end-of-winter accumulation measured in 32 snow pits (Supplementary Figure S11). They can therefore be considered as best estimates for the accumulation at these sites. However, it is unsure whether these stations are representative for a greater region. For instance, Steffen and Box (2001) showed that the surface height change rate could differ by up to 36 cm yr^{-1} within tens of kilometres because of different snow deposition rates and drifting snow.

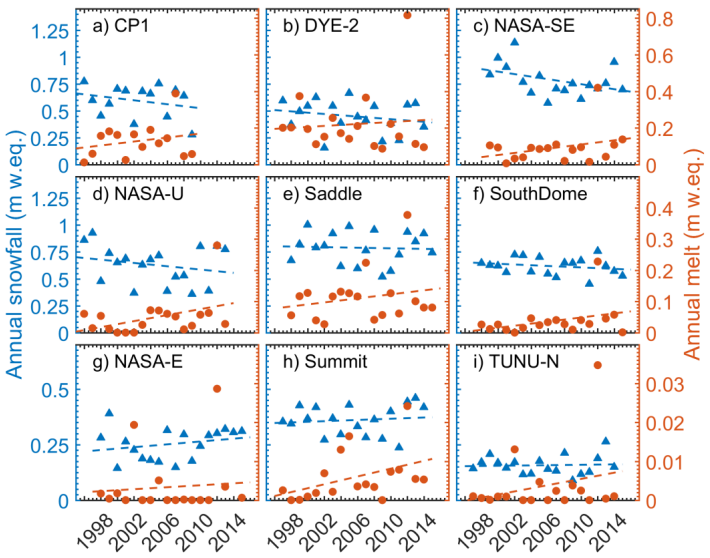

Figure 2. Annual snowfall and surface melt calculated at each site.

3.4. Subsurface temperature

The modelled firn temperature, either when using the uniform darcy-flow scheme from Langen et al. (2017) or the deep percolation scheme from Marchenko et al. (2017) is compared with the observed firn temperature at each site (Table 5). The modeled and observed firn temperatures are shown in Figure S13.

The standard model produces a cold bias in firn temperatures at all sites except NASA-U and Summit. Apart for this bias, the model reproduces the temporal variation (Table 5). However, R^2 as low as 0.54 are found at NASA-SE. Nevertheless, we calculate a RMSE below 1 ^{o}C at all sites except, again, at NASA-U and Summit. Accounting for deep percolation increases the R^2 at Crawford Point, DYE-2 and Saddle, sites where the highest annual melt is calculated and reduces the magnitude of the cold bias by 0.33 ^{o}C at Crawford Point, 0.78 ^{o}C at DYE-2 and 0.02 ^{o}C at Saddle.

Table 5. Performance of the simulated firn temperature.

	Crawford Point	DYE-2	NASA-SE	NASA-U	Saddle	South Dome	NASA-E	Summit	TUNU-N
Uniform wetting-front percolation scheme									
R^2	0.64	0.65	0.54	0.81	0.74	0.74	0.69	0.69	0.88
RMSE (^{o}C)	0.80	0.98	1.27	0.60	0.70	0.89	0.88	1.05	0.83
Bias (^{o}C)	-1.67	-1.58	-0.59	0.01	-0.71	-0.72	-0.63	0.60	-0.12
Deep percolation scheme									
R^2	0.67	0.69	0.54	0.81	0.75	0.74	0.69	0.69	0.88
RMSE (^{o}C)	0.83	0.93	1.27	0.60	0.69	0.89	0.88	1.05	0.83
Bias (^{o}C)	-1.34	-0.80	-0.59	0.01	-0.69	-0.72	-0.63	0.60	-0.12

3.5. Firn heat budget

In our model, the firn temperature is the result of two energy fluxes: the energy exchanged with the atmosphere through the surface and the energy exchanged with an ice sublayer of constant temperature located 40 m water-equivalent below the surface at model initiation. An additional internal energy source can be considered: latent heat release from refreezing meltwater. This energy is the excess energy flux from the atmosphere to the surface that, unable to further increase the surface temperature, generates meltwater and is later released where the meltwater is refrozen.

With the recent increase of melt at the surface (Figure 2), there is also an increasing heat released at depth (Figure 3). We find that about 1 340 MJ of latent heat were released into the firn of DYE-2, of which 267 MJ (20%) was released during the 2012 melt season (Figure 3).

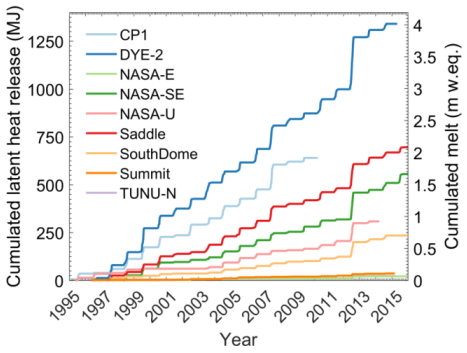

Figure 3. Cumulated melt and latent heat released in the firn at each site.

The heat fluxes from the subsurface to the surface (GF) a different role throughout the seasons. In winter, cold near-surface air temperature and radiative cooling decrease the surface temperature. During these months, the subsurface acts as a heat source for the surface and GF has a positive contribution to the surface energy budget. In summer, near-surface air temperatures warmer than the subsurface and peak seasonal absorbed solar radiation both raise the surface temperature, in which case, the subsurface acts as an energy sink and GF has a negative contribution to the surface heat budget. We calculate that the summer GF has been decreasing at all sites except Crawford Point and NASA-SE. This decrease indicates that the warming surface needs to transfer an increasing amount of energy to the subsurface.

The meltwater percolation scheme influences the firn energy budget in two ways. First, inefficient downward transfer of meltwater in the uniform wetting-front scheme allows more latent heat from refreezing to be conducted upward to the surface and radiated to the atmosphere (Figure S13). On the contrary, deep percolation releases latent heat deeper and longer time will be needed for the heat to be conducted from its release depth either back up to the surface or down to the bottom layer. As a result, we find that the cumulated GF is higher when using the standard percolation scheme compared to deep percolation, by 24% at Crawford Point and by 31% at DYE-2 (Figure 4a). We find other sites less suitable for such comparison as they do not receive enough melt to present marked differences depending on the choice of percolation.

Secondly, the deep percolation scheme distributes meltwater and therefore latent heat to a larger depth range below the surface. This wider redistribution increases the mass of subfreezing firn mobilized to cool and refreeze the meltwater. On the contrary, the standard percolation scheme concentrates the meltwater closer to the surface where a significant portion of the firn can become isothermal. As a consequence, the surface temperature remains higher overnight, is more easily brought to melting point the following day and more melt occurs than when using the deep percolation scheme, which drains more easily the near-surface firn and allows it to cool down at night. This indirect

feedback between melt and percolation depth is responsible for an additional 5% of melt at Crawford Point and 8% at DYE-2 when using the standard percolation scheme over deep percolation (Figure 4).

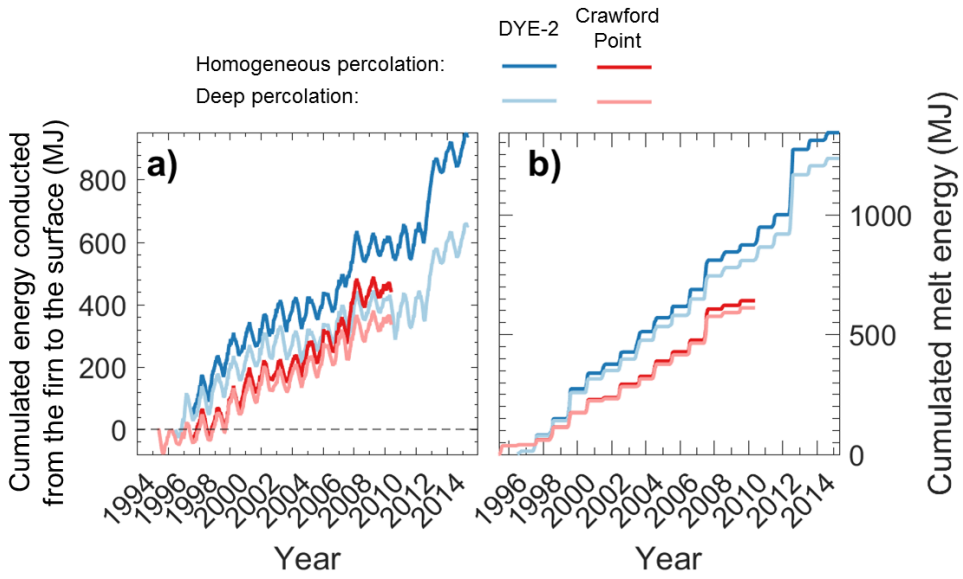

Figure 4. Cumulated energy transferred from the subsurface to the surface (a) and cumulated calculated melt energy (b) at DYE-2 and Crawford Point stations calculated using the homogeneous percolation or deep percolation scheme.

Finally, the simulated firn energy budget depends on the energy conducted from or to the model's bottom layer which is set to a constant temperature. This bottom layer can act as an unlimited source or sink of energy. The interpolation used for the deeper part of the initial temperature profile can lead to inaccurate firn temperature at the start of the simulation. When occurring, the initial energy excess or deficit are corrected within few months through energy conduction to the bottom layer (e.g. Saddle or NASA-E in Figure S14). The bottom layer thereafter does not transfer or receive energy from the rest of the firn, especially compared to the energy transferred through the top layer (Supplementary Figure S14).

3.6. Refreezing capacity and firn retention capacity

The refreezing capacity is seen to stable or slightly increasing (<+8%) at all sites (Figure 5). The positive trends in refreezing capacity can seem surprising when over the same period more heat has been conducted from the surface to the firn (Section 3.5). It is actually due to the increasing firn density at all sites, except again NASA-U and Summit. Indeed, at equal temperature, denser near-surface firn concentrates more mass in the top 20 m and requires

the refreezing of more water to reach melting temperature than less dense firn. While firn densification is generally interpreted as indicating a reduction of the firn retention capacity (van Angelen et al., 2013; Vandecrux et al., 2018), we show that at our stations densification can yet have a positive impact on the refreezing capacity and therefore enhance the retention capacity of the near-surface firn. Nevertheless, the firn capacity decreased by 15 % at Crawford Point, 13% at DYE-2, 10% at NASA-SE, ~5% at NASA-U, Saddle, South Dome, NASA-E while remaining stable at Summit and TUNU-N (Figure 5).

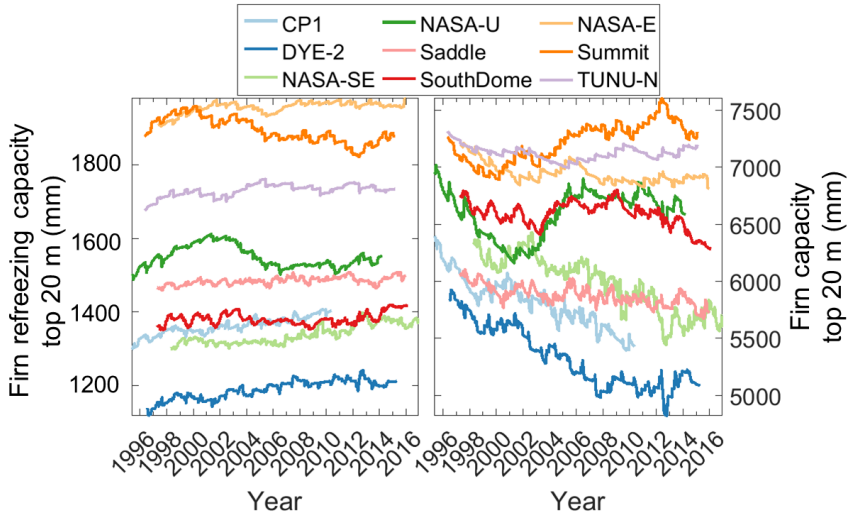

Figure 5. Evolution of the top 20 m firn refreezing capacity and firn capacity.

We also see in the positive impact of densification on the cold content the preliminary condition for firn saturation and potentially the emergence of low permeability ice slabs (Machguth et al., 2016; MacFerrin et al., 2018). We hypothesis that, as the near-surface firn densifies due to increased melting, refreezing and snowfall variability (Vandecrux et al., 2018), the simultaneous decrease of hydraulic conductivity and increase of available cold content in the near-surface firn promotes more intense refreezing into shallow ice features potentially coalescing into ice slabs if sufficient melt is provided. The role of deep percolation in the development of ice slabs yet remains unclear. Indeed, deep percolation can either route surface melt directly to the ice slab and thicken them, or on the contrary route the meltwater past these features using gaps or cracks in the ice slabs and to the underlying firn. More in-situ observations will be needed to quantify these two effects of meltwater deep percolation.

4. Conclusion

Between 1998 and 2015, summer 2m air temperature increased with rates ranging from 0.4 to 1.26 ^{o}C per decade at nine GC-Net firn sites. These warmer summer air temperatures were compensated by cooling spring and winter air

temperature leading to relatively stable annual air temperature. Using a coupled surface energy budget and firn model, we find at all sites except one that changes in the energy budget led to increasing summer surface temperature, elevated meltwater production and augmented heat transfer from the atmosphere to the firn between 1998 and 2015. Our choice of meltwater percolation scheme has an impact on the calculated heat fluxes between the firn and the atmosphere. Indeed accounting for deep percolation decreases by up to 8% the calculated melt and by 30% the energy transferred from the firn to the atmosphere. Parametrizing deep percolation, by providing a warmer simulated firn, also decreases the deviation of simulated firn temperatures from observed firn temperature. Finally, we find that although more heat has been transferred to the firn over the last two decades, the refreezing capacity of the top 20 m of firn has actually slightly increased due to the densifying near-surface firn which needs more energy to be brought to melting point. Yet, at most of our sites, the decrease of the firn capacity between 1998 and 2015 exceeds the slight increase in refreezing capacity and leads to an overall decrease of the meltwater retention capacity of the firn. Our work provides strong motivation to pursue climate and firn monitoring in the accumulation area as well as for further documentation of the effect of deep percolation on the heat balance of the firn so that it is accounted appropriately in coupled firn and climate models.

5. Bibliography

Albert, M. R.: Some numerical experiments on firn ventilation with heat transfer, Annals of Glaciology, doi:10.3189/S0260305500011435, 1993.

Benson, C. S.: Stratigraphic Studies in the Snow and Firn of the Greenland Ice Sheet, U.S. Army Snow, Ice and Permafrost Research Establishment. 1962.

Box, J.E., W.T. Colgan, B. Wouters, D.O. Burgess, S. O'Neel, L.I. Thomson, S.H. Mernild. Global sea-level contribution from Arctic land ice: 1971–2017, Environmental Research Letters, ERL-105795, https://doi.org/10.1088/1748-9326/aaf2ed, 2018.

Box, J. E., Fettweis, X., Stroeve, J. C., Tedesco, M., Hall, D. K., and Steffen, K.: Greenland ice sheet albedo feedback: thermodynamics and atmospheric drivers, The Cryosphere, 6, 821-839, doi:10.5194/tc-6-821-2012, 2012.

Box, J. E., van As, D., Steffen, K., and the PROMICE project team.: Greenland, Canadian and Icelandic land-ice albedo grids (2000-2016), Geological Survey of Denmark and Greenland Bulletin, 38, 53-56, 2017.

Box, J., and Steffen, K.: Sublimation on the Greenland ice sheet from automated weather station observations, Journal of Geophysical Research, 106, D34, 33965-33981, 2001.

Brun, E.: Investigation on wet-snow metamorphism in respect of liquid-water content, Annals of Glaciology, 22–26, doi:10.1017/S0260305500007576, 1989.

Calonne, N., Geindreau, C., Flin, F., Morin, S., Lesaffre, B., Roscoat, S. R., and Charrier, P.: 3-D image-based numerical computations of snow permeability: links to specific surface area, density, and microstructural anisotropy, Cryosphere, 6, 939-951, doi:10.5194/tc-6-939-2012, 2012.

Cazenave, A., Meyssignac, B., Ablain, M., Balmaseda, M., Bamber, J., Barletta, V., Beckley, B., Benveniste, J., Berthier, E., Blazquez, A., Boyer, T., Caceres, D., Chambers, D., Champollion, N., Chao, B., Chen, J., Cheng, L., Church, J. A., Chuter, S., Cogley, J. G., Dangendorf, S., Desbruyères, D., Döll, P., Domingues, C., Falk, U., Famiglietti, J., Fenoglio-Marc, L., Forsberg, R., Galassi, G., Gardner, A., Groh, A., Hamlington, B., Hogg, A., Horwath, M., Humphrey, V., Husson, L., Ishii, M., Jaeggi, A., Jevrejeva, S., Johnson, G., Kolodziejczyk, N., Kusche, J., Lambeck, K., Landerer, F., Leclercq, P., Legresy, B., Leuliette, E., Llovel, W., Longuevergne, L., Loomis, B. D., Luthcke, S. B., Marcos, M., Marzeion, B., Merchant, C., Merrifield, M., Milne, G., Mitchum, G., Mohajerani, Y., Monier, M., Monselesan, D., Nerem, S., Palanisamy, H., Paul, F., Perez, B., Piecuch, C. G., Ponte, R. M., Purkey, S. G., Reager, J. T., Rietbroek, R., Rignot, E., Riva, R., Roemmich, D. H., Sørensen, L. S., Sasgen, I., Schrama, E. J. O., Seneviratne, S. I., Shum, C. K., Spada, G., Stammer, D., van de Wal, R., Velicogna, I., Schuckmann, K. von, Wada, Y., Wang, Y., Watson, C., Wiese, D., Wijffels, S., Westaway, R., Woppelmann, G. and Wouters, B.: Global sea-level budget 1993-present, Earth System Science Data, 10(3), pp. 1551–1590. doi: 10.5194/essd-10-1551-2018, 2018.

Charalampidis, C., As, D. V., Colgan, W. T., Fausto, R. S., Macferrin, M., and Machguth, H.: Thermal tracing of retained meltwater in the lower accumulation area of the Southwestern Greenland ice sheet, Annals of Glaciology, 57, 72, 1-10, doi:10.1017/aog.2016.2, 2016.

Charalampidis, C., van As, D., Box, J. E., Van Den Broeke, M. R., Colgan, L. T., Doyle, S. H., . . . Smeets, C. J.: Changing surface-atmosphere energy exchange and refreezing capacity of the lower accumulation area, West Greenland, Cryosphere, 9, 6, 2163-2181, doi:10.5194/tc-9-2163-2015, 2015.

Colbeck, S. C.: A theory of water flow through a layered snowpack, Water Resources Research, 11, 2, 261-266, 1975.

Colbeck, S. C.: Water flow through heterogeneous snow, Cold Regions Science and Technology, 1, 1, 37–45, doi:10.1016/0165-232X(79)90017-X, 1979.

Coléou, C., and Lesaffre, B.: Irreducible water saturation in snow: experimental results in a cold laboratory, J. Glaciol., 26, 64-68, 1998.

de la Peña, S., Howat, I. M., Nienow, P. W., Broeke, M. R., Mosley-Thompson, E., Price, S. F., . . . Sole, A.: Changes in the firn structure of the western Greenland Ice Sheet caused by recent warming, The Cryosphere, 9, 1203-1211, doi:10.5194/tc-9-1203-2015, 2015.

Graeter, K. A., Osterberg, E., Ferris, D. G., Hawley, R. L., Marshall, H. P., Lewis, G., . . . Birkel, S.: Ice Core Records of West Greenland Melt and Climate Forcing, Geophysical Research Letters, 45, 7, doi:10.1002/2017GL076641, 2018.

Harper, J., Humphrey, N., Pfeffer, W. T., Brown, J., and Fettweis, X.: Greenland ice-sheet contribution to sea-level rise buffered by meltwater storage in firn, Nature, 491, 240-243, doi:doi:10.1038/nature11566, 2012.

Hirashima, H., Yamaguchi, S., Sato, A., and Lehning, M.: Numerical modeling of liquid water movement through layered snow based on new measurements of the water retention curve, Cold Regions Sci. Technol., 64, 94-103, doi:10.1016/j.coldregions.2010.09.003, 2010.

Humphrey, N. F., Harper, J. T., and Pfeffer, W. T.: Thermal tracking of meltwater retention in Greenland's accumulation area, Journal of Geophysical Research, 117, F01010, doi:10.1029/2011JF002083, 2012.

Langen, P., Fausto, R. S., Vandecrux, B., Mottram, R., and Box, J.: Liquid Water Flow and Retention on the Greenland Ice Sheet in the Regional Climate Model HIRHAM5: Local and Large-Scale Impacts., Front. Earth Sci., 4, 110, doi:10.3389/feart.2016.00110, 2017.

Ligtenberg, S. R., Kuipers Munneke, P., Noël, B. P., and . van den Broeke, M.: Improved simulation of the present-day Greenland firn layer (1960–2016), The Cryosphere Discussion, doi:10.5194/tc-2017-282,, 2018.

Lucas-Picher, P., Wulff-Nielsen, M., Christensen, J. H., Aðalgeirsdóttir, G., Mottram, R., and Simonsen, S.: Very high resolution in regional climate model simulations for Greenland: Identifying added value, J. Geophys. Res., 117, D02108, doi:10.1029/2011JD016267, 2012.

MacFerrin, M., Machguth, H., van As, D., Charalampidis, C., Stevens, C., Heilig, A., . . . Abdalati, W.: Rapid expansion of Greenland ' s low-permeability ice slabs, In review in Nature, 2018.

Machguth, H., Box, J., Fausto, R., and W.T.Pfeffer.: Editorial: Melt water retention processes in snow and firn on ice sheets and glaciers: Observation and modeling, Fronties in Earth Science, 2018.

Machguth, H., MacFerrin, M., As, D. v., Box, J., Charalampidis, C., Colgan, W., . . . Mosley-Thompson, E.: Greenland meltwater storage in firn limited by near-surface ice formation, Nature and Climate Change, 6, 390-395, doi:10.1038/NCLIMATE2899, 2016.

Marchenko, S., Pelt, W. v., Claremar, B., Machguth, h., Reijmer, C., Pettersson, R., and Pohjola, V.: Parametriing deep water percolation improves subsurface temperature simulations by a multilayer firn model, Frontiers in Earth Science, 5, 16, doi:0.3389/feart.2017.00016, 2017.

Marsh, P., and Woo, M.: Wetting Front Advance and Freezing of Meltwater Within a Snow Cover. 1. Observations in the Canadian Arctic, Water Ressources Research, 20, 12, 1853-1864, 1984.

McGrath, D., Colgan, W., Bayou, N., Muto, A., and Steffen, K.: Recent warming at Summit, Greenland: Global context and implications, Geophysical Research Letters, 40, 2091-2096, doi:10.1002/grl.50456, 2013.

Miège, C., Forster, R. R., Brucker, L., Koenig, L. S., Solomon, D. K., Paden, J. D., . . . Gogineni, S.: Spatial extent and temporal variability of Greenland firn a, Journal of Geophysical Research: Earth Surface, 2016.

Miller, N. B., Shupe, M. D., Cox, C. J., Noone, D., Persson, P. O., and Steffen, K.: Surface energy budget responses to radiative forcing at Summit, Greenland, Cryosphere, 11, 497-516, doi:10.5194/tc-11-497-2017, 2017, 2017.

Mote, T. L.: Greenland surface melt trends 1973–2007: Evidence of a large increase in 2007, Geophysical Research Letters, 34, 22, doi:10.1029/2007GL031976, 2007.

Nerem, R. S., Beckley, B. D., Fasullo, J. T., Hamlington, B. D., Masters, D., and Mitchum, G. T.: Climate-change–driven accelerated sea-level rise detected in the altimeter era, Proceedings of the National Academy of Sciences, doi:10.1073/pnas.171, 2018.

Nghiem, S. V., Hall, D. K., Mote, T. L., Tedesco, M., Albert, M. R., Keegan, K., . . . Neumann, G.: The extreme melt across the Greenland ice sheet in 2012, Geophysical Research Letter, 39, L20502, doi:10.1029/2012GL053611, 2012.

Niwano, M., Aoki, T., Hashimoto, A., Matoba, S., Yamaguchi, S., and Tanikawa, T.: NHM – SMAP : spatially and temporally high-resolution nonhydrostatic atmospheric model coupled with detailed snow process model for Greenland Ice Sheet, Cryosphere, 635–655, 2018.

Pfeffer, W. T., Meier, M. F., and Illangaskare, T.: Retention of Greenland Runoff by Refreezing: Implication for Projected Future Sea Level Change, Journal of Geophysical Research, 96, C12, 22117-22124, 1991.

Polashenski, C., Courville, Z., Benson, C., Wagner, A., Chen, J., Wong, G., . . . Hall, D.: Observations of pronounced Greenland ice sheet firn warming and implications for runoff production, Geophys. Res. Lett., 41, 4238–4246, doi:10.1002/2014G, 2014.

Steffen, K., Box, J. E., and Abdalati, W. 1996. Greenland Climate Network: GC-Net, In S. C. Colbeck (Ed.), *Special Report on Glaciers, Ice Sheets and Volcanoes, trib. to M. Meier* (pp. 98-103). CRREL 96-27.

Steger, C., Reijmer, C., Broeke, M. v., Wever, N., Forster, R., Koenig, L., . . . Noël, B.: Firn meltwater retention on the Greenland ice sheet: a model comparison, Front. Earth Sci., 5:3, doi:10.3389/feart.2017.00003, 2016.

van Angelen, J. H., Lenaerts, J., Broeke, M. v., Fettweis, X., and Meijgaard, E. v.: Rapid loss of firn pore space accelerates 21st century Greenland mass loss, Geophysical Research Letters, 40, 2109-2113, doi:10.1002/grl.50490, 2013.

van As, D., van den Broeke, M., Reijmer, C., and van de Wal, R.: The summer surface energy balance of the high antartic plateau, Boundary Layer Meteorol., 115, 289-317, doi:10.1007/s10546-004-4631-1, 2005.

van den Broeke, M. R., Enderlin, E. M., Howat, I. M., Kuipers Munneke, P., Noël, B. P., van de Berg, W. J., . . . Wouters, B.: On the recent contribution of the Greenland ice sheet to sea level change, Cryosphere, 10, 1933-1046, doi:doi:10.5194/tc-10-1933-2016, 2016.

Vandecrux, B., Fausto, R. S., Langen, P. L., As, D. V., MacFerrin, M., Colgan, W., . . . Box, J.: Drivers of Firn Density on the Greenland Ice Sheet Revealed by Weather Station Observations and Modelling, Journal of Geophysical Research: earth Surface, 2018.

Vaughan, D. G., Comiso, J. C., Allison, I., Carrasco, J., Kaser, G., Kwok, R., . . . Zhang, T. 2013. Observations: Cryosphere, In T. F. Stocker, D. Qin, G.-K. Plattner, M. Tignor, S. K. Allen, J. Boschung, . . . P. Midgley (Eds.), *Climate Change 2013: The physical Science Basis.* Cambridge University Press.

Vionnet, V., Brun, E. S., Eisen, A., Fierz, C., and Lehning, M.: The detailed snowpack scheme Crocus and its implementation in SURFEXv7.2, Geosci. Model Dev., 5, 773-791, doi:10.5194/gmd-5-773-2012, 2012.

Wever, N., Würzer, S., Fierz, C., and Lehning, M.: Simulating ice layer formation under the presence of preferential flow in layered snowpacks, The Cryosphere, 10, 2731-2744, doi:10.5194/tc-10-2731-2016, 2016.

Yen, Y.: Review of Thermal Properties of Snow, Ice and Sea Ice, Hanover,NH: United States Army Cold Regions Research and Engineering Laboratory. 1981.

While meltwater runoff from the Greenland ice sheet is a large contributor to current sea-level rise, the perennial snow, or firn, that covers 80 % of the ice sheet, retains meltwater and prevents it from reaching the ocean.

This PhD thesis links the publications of the PhD candidate Baptiste Vandecrux and relates his main results: the documentation of the low permeability ice slabs, climate observation and firn modelling at nine firn sites, and the description of the firn air content from a collection of firn cores.

DTU Civil Engineering

Brovej, Building 118
2800 Kongens Lyngby
Tlf. 45251700

8778775051